Université Bordeaux 1 C.E.N.B.G (CNRS - IN²P³ - UMR 5797)

THÈSE

présentée à

L'UNIVERSITÈ BORDEAUX 1

par

IULIA COMPANIS

pour obtenir le titre de DOCTEUR
Spécialité : Astrophysique, Plasmas, Nucléaire

DÉVELOPPEMENT D'UN DISPOSITIF EXPÉRIMENTAL DÉDIÉ À LA MESURE DES SECTIONS EFFICACES DE CAPTURE ET DE FISSION DE L'^{233}U DANS LE DOMAINE DES RÉSONANCES RÉSOLUES

Soutenue publiquement le 9/12/2013 devant un jury composé de :

Président	M. Phillipe Moretto	Professeur Univ. Bordeaux 1
Rapporteurs	M. Laurent Tassan-Got	Directeur de Recherche CNRS
	M. Olivier Serot	Physicien Chercheur CEA Cadarache
Examinateurs	M. Daniel Heuer	Directeur de Recherche CNRS
	M. Catalin Borcea	Directeur de Recherche IFIN-HH
Directeur de thèse	M. Igor Tsekhanovich	Professeur Univ. Bordeaux 1
Co-encadrant de thèse	M. Ludovic Mathieu	Chargé de Recherche CNRS

Numéro d'ordre : 000

Thèse réalisée au Centre d'Etude Nucléaire de Bordeaux Gradignan
Chemin du Solarium
Le Haut Vigneau
BP120
33175 GRADIGNAN Cedex

Tél : +33 5 57 12 08 04
Fax : +33 5 57 12 08 01

Web : http ://www.cenbg.in2p3.fr

Sous la direction de Dr. Igor Tsekhanovich tsekhano@cenbg.in2p3.fr

Co-encadrement Dr. Mourad Aiche aiche@cenbg.in2p3.fr
Dr. Ludovic Mathieu mathieu@cenbg.in2p3.fr

Financement Ministère de l'Enseignement Supérieur et de la Recherche

This work is supported by the CNRS program GEDEPEON/NEEDS and the EURATOM programs EFNUDAT (European Facilities for Nuclear Data Measurements) contract n° FP6-036434

Résumé

^{233}U est le noyau fissile produit dans le cycle du combustible $^{232}Th/^{233}U$ qui a été proposé comme une alternative plus sûre et plus propre du cycle $^{238}U/^{239}Pu$. La connaissance précise de la section efficace de capture de neutrons de cet isotope est requise avec une haute précision pour la conception et le développement de réacteurs utilisant ce cycle du combustible. Les deux seuls jeux de données expérimentales fiables pour la section efficace de capture de l'^{233}U montrent des écarts important allant jusqu'à 20%. Ces différences peuvent être dues à des incertitudes systématiques associées à l'efficacité du détecteur, la correction du temps mort, la soustraction du bruit de fond et le phénomène d'empilement de signaux causé par la forte activité α de l'échantillon. Un dispositif expérimental dédié a la mesure simultanée des sections efficaces de fission et de capture des noyaux fissiles radioactifs a été conçu, assemblé et optimisé au CENBG dans le cadre de ce travail. La mesure sera effectuée à l'installation de temps de vol de neutrons Gelina de l'IRMM, où les sections efficaces neutroniques peuvent être mesurées sur une large gamme d'énergie avec une haute résolution énergetique. Le détecteur de fission se compose d'une chambre à ionisation (CI) multi-plaque de haute efficacité. Les rayons γ produits dans les réactions de capture sont détectés par un ensemble de six scintillateurs C_6D_6 entourant la CI. Dans ces mesures, les rayons γ de la capture radiative sont masqués par le grand nombre de rayons γ de fission, ce qui représente le problème le plus delicat. Ces γ parasites doivent être soustraits par la détection des événements de fission avec une efficacité très bien connue (méthode de VETO). Une détermination précise de cette efficacité est assez difficile. Dans ce travail, nous avons soigneusement étudié la méthode des neutrons prompts de fission pour la mesure de l'efficacité de la CI, apportant un éclairage nouveau sur la méthode, ce qui a permi d'obtenir une excellente precision sur l'efficacité de détection des fission d'une source de ^{252}Cf. Avec cette même source, plusieurs paramètres (pression du gaz, haute tension et la distance entre les électrodes) ont été étudiés afin de déterminer le comportement de la CI et de trouver le point de fonctionnement idéal : une bonne séparation énergétique entre les particules α et les fragments de fission (FF) et une bonne résolution temporelle. Une bonne séparation α-FF a également été obtenue avec une cible d'^{233}U tres radioactive. De plus, l'analyse de forme de signaux entre les rayons γ et les neutrons dans les détecteurs C_6D_6 a été observée à Gelina dans des conditions expérimentales réalistes. Pour conclure, le dispositif expérimental et la méthode de VETO ont été soigneusement vérifiés et validés, ouvrant la voie à la mesure future des sections efficaces de capture et fission d'^{233}U.

Mots clés : cycle thorium, sections efficaces neutronique de fission et de capture, isotope fissile, développement d'un dispositif expérimental pour la détection des neutrons et γ, scintillateurs C_6D_6, chambre à ionisation, mesure de l'efficacité, méthode VETO, simulations Geant4.

Development of an experimental set-up for the measurement of the neutron-induced fission and capture cross section of ^{233}U in the resonance region

Abstract

^{233}U is the fissile nucleus produced in $^{232}Th/^{233}U$ fuel cycle which has been proposed as a safer and cleaner alternative to the $^{238}U/^{239}Pu$ cycle. The accurate knowledge of the neutron capture cross-section of this isotope is needed with high-precision for design and development of this fuel cycle. The only two reliable experimental data for the capture cross-section of ^{233}U show discrepancies up to 20%. These differences may be due to systematic uncertainties associated with the detector efficiency, dead-time effects, background subtraction and signal pile-up caused by the α-activity of the sample. A special experimental set-up for simultaneous measurement of fission and capture cross sections of radioactive fissile nuclei was designed, assembled and optimized at CENBG in the frame of this work. The measurement will be performed at the Gelina neutron time-of-flight facility at IRMM, where neutron cross sections can be measured over a wide energy range with high energy resolution. The fission detector consists of a multi-plate high-efficiency ionization chamber (IC). The γ-rays produced in capture reactions are detected by an array of six C_6D_6 scintillators surrounding the IC. In these measurements the radiative capture γ-rays are hidden in large background of fission γ-rays that represents a challenging issue. The latter has then to be subtracted by detecting fission events with a very well known efficiency (VETO method). An accurate determination of this efficiency is rather difficult. In this work we have thoroughly investigated the prompt-fission-neutrons method for the IC efficiency measurement, providing new insights on this method. Thanks to this study the IC efficiency was determined with a very low uncertainty. Using a ^{252}Cf source, several parameters (gas pressure, high voltage and the distance between the electrodes) have been studied to determine the behaviour of the IC in order to find the ideal operation point: a good energy separation between α-particles and fission fragments (FF) and a good timing resolution. A good α-FF separation has been obtained with a highly radioactive ^{233}U target. Also, the pulse-shape discrimination between γ-rays and neutrons in the C_6D_6 detectors was observed at Gelina under realistic experimental conditions. To conclude, the experimental set-up and the VETO method have been carefully checked and validated, opening the way to future measurements of the capture and fission cross sections of ^{233}U.

Keywords: thorium cycle, neutron-induced capture and fission cross sections, fissile isotope, development of experimental set-up for neutron and gamma detection, C_6D_6 scintillators, ionisation chamber, efficiency measurement, VETO method, Geant4 simulations.

Contents

Motivation and Objectives

Chapter 1

Context and purpose

Earth, the only planet we know to be capable of sustaining living beings (our home planet), does the whole complicated and dynamic mix of human-nature interactions come together in a way that encourages life. Over the decades our society has conducted several research, developed technologies and extended science and technology education to characterize, understand and predict variability and trends in Earth's system. In short, this allowed human population to grow. Sustainable development is supposed to focus on improving the quality of life while respecting the environment. Nevertheless, all over the world we see signs of stress on our interlocked global economic, environmental and social system.

For the evolution, the welfare and the prosperity of mankind and even for the world peace, a large amount of energy is needed. Choosing an energy source is not an easy task since an evaluation not only from the prospect of its resources, but also its impact on local and global environment [1] is required. From this standpoint, nuclear energy has many advantages.

The aim of this chapter is to give an overview of the world situation concerning the consumption and demand of energy in general and nuclear energy in particular. A brief introduction to nuclear power and nuclear waste will be given together with a short review of the different possible ways for energy production, with their advantages and limits. Finally, the role and need of nuclear data, such as the neutron cross-sections, is discussed.

1. Global environment refers to an environment about our nature and the surroundings where certain factors (political, economical, social and technological) influence worldwide scale.

1.1 World energy demand and outlook

One hundred thousand years ago there may have been fewer than a million human beings on the planet, indeed as few as 10,000. Today there are 7.1 billions and by 2050 this number will reach 9 billions [Nations 04]. In these circumstances, the use of electricity has been growing and gaining importance in everyday life. The world energy consumption is expected to increase by 53%, from 505 quadrillion British Thermal Unit (BTU) [2] in 2008 to 770 quadrillion Btu in 2050 as illustrated in Figure 1.1. Even though, an increase in the energy consumption is expected for the Organisation for Economic Co-operation and Development (OECD) member countries, the most significant growth in energy use is predicted for the non-OECD regions.

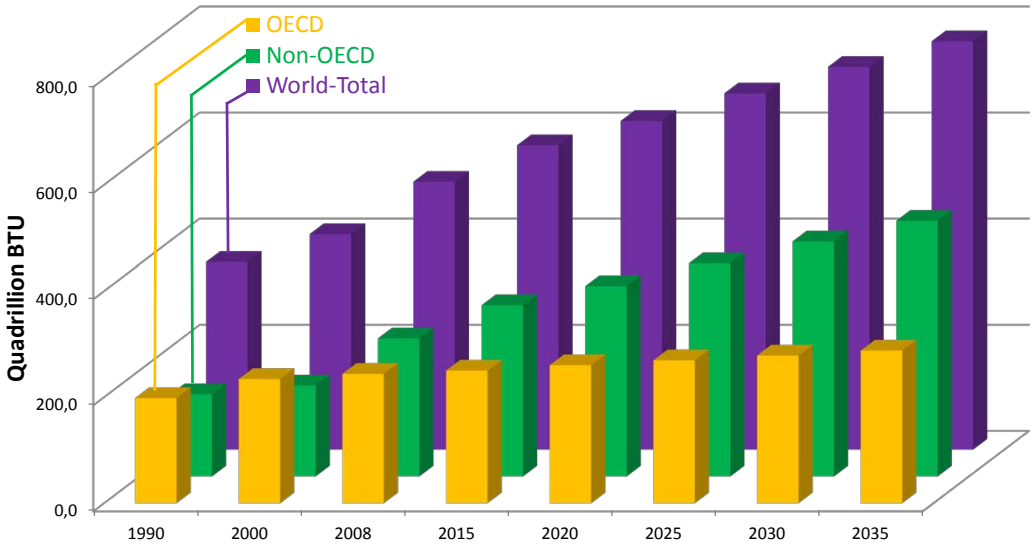

Figure 1.1: The world energy consumption 1990-2035 ([IEA 11b])

Development depends on energy, as energy is one of the main sources of life. We naturally seek to use energy to multiply our labor, increasing our productivity. And yet, globally, it is estimated that 40% of the global population (2.7 billion people) rely on traditional use of biomass for cooking [IEA 11a]. In addition, about 20% of the global population (1.4 billion people) lack access to the basic energy services, including electricity, clean cooking fuel, proper means of transportation and sanitary water [IEA 11a, WHO 08]. All of these could be provided easily and less expensively if energy was available. Without substantial enhanced actions in energy production, the environmental pollution and the proportion of the population without sufficient electricity will increase.

2. 100 quadrillion BTU is equivalent of 2.5Gtep (tonne of oil equivalent)

The most widely used energy source on Earth today comes from fossil fuels, and besides the fact that they could make global warming to keep going up, leading to an international conflict on economic prosperity and global pollution, they will also will run out (particularly oil and gas fuels) in the next hundred years [IPCC 12]. The most reasonable solution is the use of renewable energy sources. Biomass, water, wind, solar and geothermal energy sources are known as renewable energy, because they will last forever, or, at least as long as the Sun keeps shining. Earth's supplies of renewable energy are vast. A 3m high ocean wave has enough power per meter of its width to power 1000 light bulbs. If we could cover just 1% (90000 km^2) of the Sahara Desert with solar panels we could make more than enough electricity for our entire planet.

All over the world, concerns about energy security and environmental consequences of emission of greenhouse gases have spurred government policies to support projects for renewable energy sources. As a result, renewable energy sources are, and will be, the fastest growing sources for electricity generation with an expected rate of 3 % per year from 2008 to 2035. Hydroelectric and wind power represents more than 82% of the increase of the new renewable generation. 27% is the contribution of wind energy which has grown rapidly over the past decade and is estimated to continue in the future [IEA 11b].

Nowadays, the contribution of each energy source to the total energy generation by fuel varies significantly from country to country. Figure 1.2 shows the contribution of the different electricity production by various sources in the world in 2009. Coal (40.6%) and gas (21.4%) cover more than half of the world electricity generation, while the clean and renewable technologies are less than 20%. The contribution of the hydroelectric power stations represents 16.2% of the total electricity consumption in the world, while for the other renewable energy sources the production is less than 4%. Nuclear energy contributes to the world energy supply with about 13.4%, which represents only a modest part of the total produced energy because this energy source is used for electricity production that constitutes only 30% of the global energy needs. Clearly, this is not the case everywhere: in France, for example, 39% of the total energy [Nifenecker 03] and 75.9% of electricity production comes from nuclear power [CEA 12].

For economic and resource sustainability, sources of energy must be clean, affordable, environmental [3], reliable, safe and secure. Economic growth and development are the most important factors to be considered in further coming changes in the world energy consumption. Because emissions of carbon dioxide result primarily from the combustion of fossil fuels, energy consumption is at the center of the climate change debate.

3. Environmental implies more than clean, meaning not putting hazardous matter into our water, land and air. Activities like creating sink holes, mountaintop mining, release of toxic water from coal bed methan extraction, and drowning thousands of m^2 behind dams are obviously not environmentally practices.

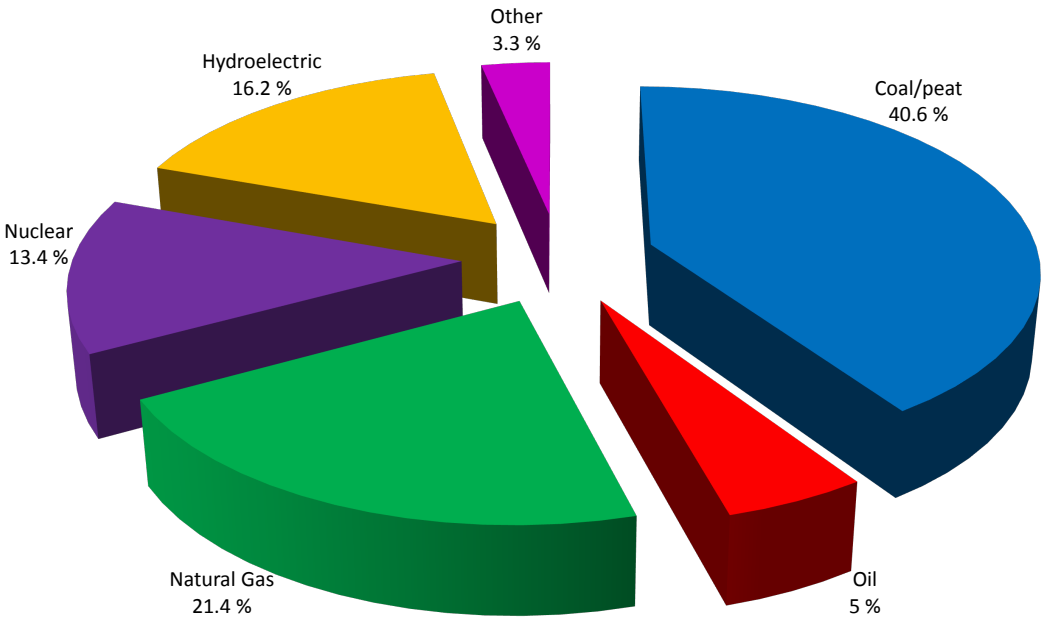

Figure 1.2: Contribution of energy sources to the world electricity production in 2009 ([IEA 11c]).

Thus, the European Union proposed the "20-20-20" technology plan, which requires a 20% reduction of CO_2 emissions, a 20% improvement in energy efficiency, and a 20% production from renewable energies by 2020 [Commission 08]. Together with the fact that many countries are facing prices excess of fossil fuel, combined with concerns about geopolitical risks and environmental consequences of global warming, the International Energy Agency (IEA) has renewed the support in the development of new nuclear facilities and renewable energy sources [IEA 11b]. Nuclear power plants could be considered environmentally clean because they do not emit CO_2, SO_2 or NO_X. Also there are no significant adverse effects to the water used for cooling because it does not come in contact with radioactive materials. Using nuclear energy in place of other energy sources will help keeping the air clean, preserve the earth's climate, avoid ground-level ozone formation, smog and prevent acid rain. However, the radioactive nuclear waste generated during the operation of nuclear power plants are and will remain the prior concern for this industry (see for more details Section 1.2.4).

1.2 Nuclear energy and sustainable development

Nuclear power and the technology behind it are bound up with several scientific and social developments in the twenty first century: not only power generation, but also medicine, geology, transport, warfare, food and agriculture, space and futuristic appli-

cations. After the substantial growth between the 1960's and 1970's, the nuclear industry fell out of disgrace for two decades, mainly because of safety and cost considerations. The reactor explosion at Chernobyl in 1986, which caused human deaths and environmental contamination contributed to the stagnation of nuclear development and to the shutting down of many nuclear power stations in Europe. Despite all these setbacks, nuclear power never completely fades away. On the contrary, during 1990s the third generation of new reactor design has been developed.

Before the devastating earthquake and tsunami at Fukushima on March 11, 2011, the worldwide prospects for nuclear power had improved considerably over the past few years. Since the disaster, many countries have changed their nuclear policies, planning to close their nuclear reactors and rejecting the idea of construction of new nuclear generating capacity [IEA 11b].

The future of nuclear energy is still uncertain, and a number of issues could slow the development of new nuclear power plants. How feasible is the nuclear option? What mistakes were made, and what lessons have we learnt? There is an ongoing debate about the use of nuclear energy. By examining the past and projecting into the future, answers and solutions are expected for efficient, safe, clean and affordable nuclear power for us and for the generations to come.

1.2.1 Outline history of nuclear energy

Several hundred thousand years ago, humans learned to turn stones into tools. This started a chain of events that made human being able to change his environment not only superficially, but in the very heart of matter. Artificial transmutation of elements was accomplished by Rutherford and coworkers in 1917 when converting nitrogen into oxygen through a nuclear reaction [Rutherford 19]. Soon after the discovery of the neutron by Chadwick in 1932 [Chadwick 32], physicists observed that the neutron was an ideal "bullet" for bombarding other nuclei. Hahn and Strassmann bombarded with neutrons the nucleus of uranium (atomic number 92), causing the formation of much lighter elements such as barium (atomic number 56) [Hahn 38, Hahn 39]. They contacted their collaborator Meitner that together with Frisch soon arrived at the idea of fission and explained for the first time in 1938 the nuclear fission process [Meitner 39]. Meitner used the Einstein's theory which demonstrates that mass can be converted into energy [Einstein 05]. This proved that the fission process occurred and also confirmed Einstein's work.

In 1940 the spontaneous fission was discovered by Flyorov and Petrzhak, this led to the notion of critical mass−minimum mass in which the sustained fission chain reaction can be carried out [Felder 09]. The unique feature of the fission process is that beside energy, few neutrons are released at the moment of fission, making a self-sustained chain

of exothermic nuclear reactions possible. From this point there was just a small step to start this astounding mechanism, and therefore to build a powerful bomb.

In 1942 Fermi and coworkers began building the world's first self-sustaining nuclear reactor and thereby initiated the controlled release of nuclear energy in Chicago [Fermi 46]. The goal of this experiment was to prove the fission chain reaction, but the task was the production of ^{239}Pu from ^{238}U in a reactor pile. That achievement led to the development of nuclear energy and the atomic bomb. However, the result of all these activities was the manufacture of the bombs dropped on Hiroshima and Nagasaki. The bombs devastating effects cast a fearsome shadow all over the world and nuclear energy was irrevocably associated with death and destruction. The potential negative consequences related to the misusage of nuclear-power shadowed the fact that uranium constitutes a valuable source of energy. Therefore, a new era was born by encouraging the development of nuclear energy for peaceful purposes and prosperity and to stop the proliferation of nuclear weapons. A major goal of nuclear science was to show that nuclear energy could produce energy for commercial use.

1.2.2 The nuclear option

The peacefull use of the nucleus became a symbol of progress and benefit to humanity, with hopes to provide the world with a least expensive and practically inexhaustible alternative source of energy [Carminati 93, Cuttler 09].

The first production of nuclear electricity was generated by a nuclear reactor on December 20, 1951, at the Experimental Breader Reactor (EBR-I), a breeder reactor (a reactor that could produce more fuel than it uses), at Argonne National Laboratory (ANL), which initially produced about 100 kW [Blokhintsev 55]. On June 27, 1954, the USSR's Obninsk nuclear power plant RBMK, became the world's first nuclear power plant to generate electricity for a power grid, and produced around 5 MW of electric power (MWe)[Semenov 83].

England opened in 1956 the Calder Hall nuclear-power station who delivered electricity in commercial quantities, having four Magnox reactors with an initial capacity of 60 MWe of power each [Cockcroft 56]. Magnox (magnesium non-oxidising) reactors are pressurised, carbon-dioxide cooled, graphite-moderated reactors using natural uranium as fuel and magnox alloy as fuel cladding.

Nuclear industry grew rapidly, this form of electricity production was seen at that time as economical, environmental clean and safe. During the 1960s nuclear power achieved the status of commercially viable energy source and by 1970 there were already 90 nuclear units operating in 15 countries with a total capacity of 16 500 MWe. Encouraged by the oil crisis in the early 1970s, electricity generation from nuclear power increased considerably worldwide, and by 1980s there were 253 operating nuclear power plants

with 135 000 MWe in 22 countries. In addition, about 230 units were under construction at that time. However, in the 1970s and 1980s, growth slowed because of the concern over nuclear issues, such as reactor safety, waste disposal, and other environmental considerations.

Obviously, the Chernobyl accident in 1986 showed that nuclear-power plants must be designed with increased safety constraints that guarantees automatic shutdown without human intervention.

Today's production of electricity from nuclear power stations is bigger than it was 55 years ago from all sources combined. They provide 13.4 percent of the world's electricity production in 2010, and in total, 13 countries rely on nuclear energy to supply at least one-quarter of their total electricity. France has the largest percentage (77.7%) of the electricity in 2011 from nuclear energy, followed by Slovakia (54.0%), Belgium (54.0%), and Ukraine (47.2%) [NEI 12a, NEI 12b].

However, the behaviour toward nuclear power varies between countries. Some countries maintained their vigorous programmes, and others started to phase out or cancel all their existing and future reactors, keeping them from expanding their nuclear power programme. The reasons were not only due to safety concern but to other factors as well, such as nuclear waste, financial constraints, reduced demand growth rates and issues like public and political acceptance. Finally, although the long-term implications of the disaster at the Japan's Fukushima Daiichi nuclear power plant for the world nuclear-power development are unknown, new policies indicate that some reduction in the projection for nuclear power should be expected.

1.2.3 Nuclear power plants

The mechanism of energy production in most of the nuclear power plants is comparable with the conventional thermal power plants (coal, gas and oil). The water is heated up and steam is produced, directly or indirectly, so it can drive a turbine that generates electricity. The main distinctive difference, which is also a very significant one, is that the heat is produced by a self-sustaining fission chain reaction.

Conventional nuclear power reactors are based on the fission process of ^{235}U and ^{239}Pu. While ^{235}U is fissile, the fertile uranium isotope ^{238}U produces the fissile element ^{239}Pu during the use of the fuel due to a neutron capture and subsequent β-decays. The following reactions are at the basis of the $^{238}U/^{239}Pu$ fuel cycle:

$$^{238}_{92}U + n \longrightarrow {}^{239}_{92}U \xrightarrow{\beta^-(23min)} {}^{239}_{93}Np \xrightarrow{\beta^-(2.4d)} {}^{239}_{94}Pu \tag{1.1}$$

The abundance of ^{235}U in natural uranium is about 0.7%. In order to be used in a thermal reactor, cooled with light water, an enrichment to about 3% is used in a typical reactor fuel, leaving a remaining 97 % of ^{238}U. To start operating a reactor, the core is loaded with a fissile fuel and requires an ignition source (radioactive material such as curium-beryllium (CmBe) or americium-beryllium (AmBe) sources) to initiate the reaction. The source is emitting neutrons that will start the fission chain reaction. This process is characterized by the emission of Fission Fragments (FF) and the release of neutrons and $\gamma-$rays from these FF and the subsequent absorption of some of these neutrons in the fissile fuel. The effectiveness of nuclear fuel is depending on the value of η, corresponding to the average number of fission neutrons produced for one neutron absorbed in the fuel and defined by:

$$\eta = \frac{\nu}{1+\alpha} \tag{1.2}$$

with ν the average number of neutrons produced per fission, $(1+\alpha)$ number of neutrons absorbed in the fuel to have one fission, and

$$\alpha(E_n) = \frac{\sigma_{capture}\,(E_n)}{\sigma_{fission}\,(E_n)} \tag{1.3}$$

where $\sigma_{capture}(E_n)$ is the capture cross section and $\sigma_{fission}(E_n)$ is the fission cross section as a function of neutron energy E_n, and the neutron is the one which has generated the fission process (see Section 2.3).

The condition for a chain reaction is expressed in terms of multiplication factor, k, which is defined as the ratio of number of fission neutrons produced in one generation over the fission neutrons from the previous generation. Every fission causes an average of one more fission, which implies a constant fission (and power) rate. Therefore, nuclear power plants operate with $k \cong 1$, named criticality. The remaining neutrons are either absorbed in a non-fission reaction or leave the system. The power level can be changed by playing with k: $k < 1$ (subcriticality), and the system can not sustain a chain reaction, and the power decreases, or $k > 1$ (supercriticality), and the number of reactions as well as the power increases.

Most of the existing nuclear reactors (88%) use enriched natural uranium and light water (LWR) to moderate neutrons to thermal velocity (2200 m/s) to increase the fission probability of ^{235}U. These are known as the Pressurized Water Reactors (PWR) that are cooled and moderated by high pressure water, or boiling reactors called Boilling Water Reactors (BWR), although only few of the latter are still functioning. Russia's Water-Water Power Reactor (VVER or WWER) are similar to PWR. Another common reactor type (10%) is the Pressurized Heavy Water Reactor (PHWR) that functions with natural uranium and is moderated with deuterium-oxide (heavy water), usually known as CANDU (CANada Deuterium Uranium). The other types of reactors are the

Advanced Gas Cooled Reactor (AGCR) using graphite as moderator and CO_2 as collant, and the Liquid Metal Fast Reactor (LMFR), an advanced type of nuclear reactor where the coolant is liquid sodium. Also the High Power Channel-type Reactor (RBMK) is the oldest commercial reactor design and still in wide operation. The reactor's flaws contributed to the 1986 Chernobyl disaster in which an RBMK exploded during an unsafe test.

1.2.4 Radioactive nuclear waste production

Radioactive material is usually generated during the operation of a nuclear power plant and by other applications of nuclear fission, such as research, or from the use of radioactive sources in medicine, agriculture and industry. Radioactive elements are harmful since some of the emitted radiation can easily penetrate deep inside the human body, damaging some of the biological cells of which the body is composed. This damage can cause a fatal cancer to develop, or if it occurs in reproductive cells, it can cause genetic defects in later generations of offspring.

The various types of radioactive waste produced vary considerably by their specific activity levels, emitted radiation, radiotoxicity, half-live, volumes and contents (fission products, scrap metal, resins, rubble, etc.). These characteristics associated with the treatment and storage of the radioactive waste set out a classification made by International Atomic Energy Agency (IAEA), that nowadays is internationally accepted [IAEA 09]. There are 5 principal waste classes: the Very Low Level Waste (VLLW), Low Level Long-Lived Waste (LLW-LL), Low and Intermediate Level Short-Lived Waste (LILW-SL), Intermediate-Level Long-Lived Waste (ILW-LL) and High Level Waste (HLW). This classification is presented in Table 1.1 and is based on two parameters:

- the activity expressed in terms of mass activity A_m in Bq/g and
- the half life ($T_{1/2}$) corresponding to the time that it takes for a given radioactive isotope to lose half of its radioactivity; the waste coming from short-lived radionuclides ($T_{1/2} \leq$30 years) is called Short-Lived Waste (SL) and Long-Lived Waste (LL) for the one coming from long-lived radionuclides ($T_{1/2}>$ 30 years).

Considering Table 1.1, one can see that the level of A_m can range from quite low to very high. The higher the level, the greater need to isolate the waste from biosphere. Also the radiological risks associated with the SL radionuclides are significantly reduced over a few hundred years by radioactive decay.

The HLW has the most dangerous level of radioactivity, from several billion to tens of billions of Bq/g. It contains different radionuclides SL and/or LL, some very LL such as ^{237}Np with $T_{1/2}\sim$2 million years. Limitations given the level of radioactivity and lifetime

of the HLW that need to be kept isolated into a final disposal will depend on radiological, physical, chemical and biological proprieties of the waste and the radionuclides type.

Apart from uranium isotopes, the high level radioactive waste consists of Fission Products (FP) and isotopes of plutonium and Minor Actinides (MA) like neptunium, americium and curium. They represent more than 95% of the total radioactivity produced during the nuclear electricity production and only 3% of the volume of all the radioactive waste.

Classification	Description	Origin	Disposal options
High Level Waste (HLW)	Fission Products and Minor Actinides $A_m > 10^9$Bq/g SL and/or LL	nuclear fuel reprocessing	under development: geological disposal and transmutation
Intermediate Level Long-Lived Waste (ILW-LL)	metal structures (cladding, hulls and end caps) $10^6 < A_m < 10^9$Bq/g	operation and maintenance of nuclear facilities	under development: geological disposal
Low and Intermediate Level Short-Lived Waste (LILW-SL)	clothes, tools, gloves, filters, paper, etc. $A_m < 10^6$ Bq/g	nuclear plant operating, research and medical labs decommissioning	surface / near surface (30m depth) storage
Low Level Long-Lived Waste (LLW-LL)	Graphite waste $10^4 < A_m < 10^6$Bq/g	nuclear plants decommissioning	under study temporary storage
Very Low Level Waste (VLLW)	scrap metal, plastics, concrete, bricks, earth, rubble, $A_m < 100$ Bq/g	decommissioning of nuclear installations	surface storage

Table 1.1: Nuclear waste classification ([IAEA 09, ANDRA 12]). The waste coming from short-lived radionuclides is called Short-Lived Waste (SL) and Long-Lived Waste (LL) for the one coming from long-lived radionuclides.

FP are generated by nuclear fission reactions, and even though most of them become stable shortly, some are radioactive and causing some difficulties with storage plans. While ^{90}Sr or ^{137}Cs with a $T_{1/2}$ of $\sim$30 years need to be stored for several hundred

years, ^{99}Tc or ^{129}I with $T_{1/2}$ higher than 200 000 years pose constraints on the features of geological disposal. On the other hand, some FP could be transmutated and transformed into stable nuclei, like for instance ^{99}Tc or ^{129}I (see Section 1.3).

MA are produced in neutron reactions such as (n, γ) on uranium and heavier isotopes. After the production of $^{239}_{94}Pu$ in the reactor core (see eq. 1.1) the neutron capture reactions will led to the formation of $^{241,243}_{94}Pu$ and after subsequent β-decay, to $^{241,243}_{95}Am$. Therefore, new isotopes with higher mass and atomic number are produced like neptunium, americium, curium and berkelium. These isotopes are characterised by relatively long $T_{1/2}$ and are much more radiotoxic [4] than the FP.

The main concern related to the HLW is the protection of people and environment. This means finding solutions for isolating or diluting the waste (practically to contain and manage it, since some waste clearly need deep and permanent burial), or reducing the radiotoxicity of HLW that could be achieved by partitioning and transmutating the MA and some FP or by using the $^{232}Th/^{233}U$ fuel cycle (see Sections 1.3 and 1.5).

1.3 Nuclear waste management

The HLW is one of the principal disadvantages of the currently operating nuclear power plants and requires sophisticated treatment and management to successfully isolate it from the biosphere. This treatment is followed by a long-term management strategy involving permanent storage, disposal or transformation of the waste into a less-radiotoxic form.

Due to their high radioactivity, the nuclear core waste generates heat. Before any treatment the spent fuel is stored in a water-filled pool for a couple of years, due to the α, β and γ radiations. This spent fuel is mainly composed of uranium (96%), TRansUranic (TRU) elements (1% of plutonium and traces of MA), and the rest are FP, remnants of zirconium or steel cladding and activation products. The remaining uranium and plutonium can be reinjected in the fuel cycle as mixed uranium-plutonium oxide (MOX). The reuse of a spent fuel allows the recovery of natural uranium resources (about 25%) necessary to operate the nuclear power plants, divides the waste volume by 5 and the radiotoxicity by 10 (compared to the choice of a direct storage spent fuel), and increases the time availability of the present ore reserve.

Sustainable management of radioactive materials and HLW implies the research for solutions concerning the partitioning (separation of various components of the used fuel) and transmutation (conversion of long-lived isotopes into short-lived ones by nuclear

4. The adverse health effects of a radioactive substance that is toxic to living cells or tissues due to its radioactivity.

reactions) so that the volume and radiotoxicity of HLW are reduced. The objective of several recent research projects is to study the impact of partitioning, transmutation and waste-reduction technologies in order to reduce significantly the risk and simplify the conditions of the final storage [IAEA 04, Lensa 08].

1.3.1 Nuclear waste transmutation

The processes that can be used for the transformation of a nuclide into one or several other nuclides (transmutation) are neutron-induced fission or capture reactions. When the transmutation is made by fission the process is rather known as incineration. The most effective nuclear process to be considered for transmutation or incineration of radiotoxic isotopes is neutron absorption, due to the small amount of energy required for the neutron to penetrate the nucleus. When irradiated with neutrons in a nuclear reactor, the TRU may undergo nuclear fission, destroying the original actinide isotope and producing FP with a wide variety of half-lives, mainly short-lived. The process is followed by energy release and the production of few neutrons, as for example in eq 1.4:

$$^{239}_{94}Pu + n \xrightarrow{fission} {}^{134}_{55}Cs\,(2years) + {}^{104}_{43}Ru\,(stable) + \nu \simeq 2 - 3n + E \simeq 200MeV \quad (1.4)$$

Transmutation of FP is also possible, but contrary to TRU, the process is neutron consuming, and requires a lot of them. As example, the two very long-lived radioactive isotopes that can be transmuted into less hazardous forms are ^{99}Tc and ^{129}I. They both require disposal strategies that will isolate them from the environment for long periods of time because they dissolve easily in groundwater and move through the ecosystem. After a neutron capture ^{99}Tc becomes ^{100}Tc, which decays into the stable ^{100}Ru within few seconds as indicated in equation 1.5. Taking also into account its ability to migrate in storage glasses, makes ^{99}Tc a particularly suited candidate for transmutation. Similarly, ^{129}I can be transformed into stable ^{130}Xe, as shown in equation 1.6. Due to technical challenges of isotopic enrichment of such radioactive isotopes this idea was abandoned.

$$^{99}_{43}Tc + n \xrightarrow{capture} {}^{100}_{43}Tc \xrightarrow{\beta^-(16s)} {}^{100}_{44}Ru \quad (1.5)$$

$$^{129}_{53}I + n \xrightarrow{capture} {}^{130}_{53}I \xrightarrow{\beta^-(12d)} {}^{130}_{54}Xe \quad (1.6)$$

Transmutation of TRU can occur in thermal, epithermal and fast reactors. The choice of the transmutation facility results from strategic studies to find the optimum combination of factors such as the manufacturing and remanufacturing of fuel, in all their aspects, availability of different types of reactors, the yields of transmutation/incineration and especially the significant reduction of the radiotoxic inventory of the nuclear waste.

OECD member countries, in general countries with heavy investment in nuclear power, have carried out extensive studies in order to identify an initial strategic approach.

In order to use all available neutrons for the transmutation process the best choice in critical systems is the use of reactors with excellent neutron economy, which are the Fast Reactors. Because of the severe constraints on the possible use of critical reactors (criticality conditions dependence of safe reactor operation on delayed neutrons) the quantity of MA which can be incinerated is limited. To solve this problem a subcritical system driven with an intense external source of neutrons called Accelerator-Driven System (ADS) has been proposed [Rubbia 95, **?**]. A part of the neutron flux is generated by a proton accelerator coupled with a spallation target and depends on the beam intensity, that allows a precise and almost instant control. The reactor being subcritical (k<1), the potential for unintended increase of reactivity is significantly reduced so that this type of reactor is much safer than the existing ones. The subcritical operation allow to obtain more flexibility in core design and fuel management opening new possibilities for transmutation.

From a waste management point of view, transmutation of MA eliminates the long-term radioactive hazard while producing a shorter-term radioactive hazard instead. Moreover, there exist studies on how to reduce the amount of nuclear waste, notably the heavier actinides, by using an alternative fuel cycle such as the $^{232}Th/^{233}U$ fuel cycle (see Section 1.5 and [Rubbia 95, **?**] for detailed concepts). The isotope ^{232}Th is not fissile but after a neutron capture followed by $\beta - decays$, the fissile isotope ^{233}U is formed. The MA generation is strongly suppresses, especially americium and curium, due to the lower atomic number of thorium with Z=90, instead of Z=92 for uranium. In this context, it has to be pointed out that partitioning and transmutation technologies will not eliminate the necessity of deep geological repositories in the future; rather will the radiotoxicity of the resulting materials be considerably reduced, hundred times and even more.

1.4 Is nuclear power safe and secure?

All sources of energy production are associated with a risk of accidents, health and environmental impacts. Although, several core melts and other nuclear accidents leading to the loss of human lives happened in the sixties, they were not considered during the seventies as a major impediment in the development of nuclear industry in the US and Europe. The turning point for nuclear expansion in many countries was in 1979 when the serious but non-fatal accident occurred in the Three Mile Island nuclear plant (USA). Even though no statistically significant correlation between dose and cancer rates has been possible to establish for the people in the most exposed areas, the fear of radioactive fallout from similar events damaged the nuclear industry's image and caused the shut down of many nuclear power stations.

The most severe nuclear accident, the Chernobyl disaster in 1986, was a direct consequence of the Cold War isolation and the resulting lack of any safety culture. Even today it is not clear how many people died or were exposed to radioactive contamination from the disaster. The accident has also raised concern about the design of nuclear power plants that should insure the automatic shut down. This highlights the simple fact that in the design of reactors one always must take into account that human operator may override the book of instructions. Gradually, all over the world it has been decided to close many nuclear power plants and to consider the exploitation of renewable energy sources. Despite all this regression, nuclear power did not disappear completely.

Considering the whole fuel cycle, from mining, transportation to waste management, according to [Burghrr 11], the impact of nuclear power accidents, in term of immediate death, is much lower than the accident risks due to oil, gas or coal fuel cycles. In addition, the emissions from nuclear power plants are kept to near zero [5]. Nuclear energy does have a tremendous potential adverse impact, but it has been the same for the last 40 years, which is why the nuclear plants are designed and operated with multiple levels of containment and safety and multiple backup systems.

Recent studies have quantified global-scale avoided greenhouse gas emissions due to nuclear power [Lenzen 12, Coleman 12]. Also recently, an estimation of historically prevented deaths and greenhouse gas emissions was performed [Kharecha 13], considering the data for global annual electricity generation by energy source from 1971 to 2009. Mortality was defined as deaths and greenhouse gas emissions as emissions per unit electric energy generated for relevant electricity sources as shown in Table 1.2. Taking also into account the Fukushima disaster, the study has concluded that nuclear power could prevent an average of 240 000 *to* 7.04 million deaths and 80 *to* 240 $GtCO_2$ equivalent emissions due to fossile fuels by midcentury. IEA emphasized that if nuclear power will significantly decline in the next few decades, heroic achievements will be require in the development of emerging low-carbon technologies, which have to be proven [IEA 11b]. The same conclusion was also strongly supported by National Aeronautics and Space Administration (NASA) [Kharecha 13].

Before the Fukushima disaster, surveys of public opinion showed that most people thought nuclear energy was reliable, and many countries were reevaluating their nuclear power programs to consider plant-life extensions or construction of new nuclear facilities [IEA 11b]. But once the radiation was emitted from the explosions at the Fukushima Daiichi nuclear power plant, the world suddenly seems a very different place. Demand for energy is growing strongly, fossil fuels are running out or are very polluting, and we all want affordable, clean and safe energy to run our economies and maintain our

5. No technology is truly zero emitting, including renewables, but if a technology can call itself "non-emitting", nuclear power certainly can.

standard of living. We cannot afford to turn our back on nuclear energy altogether, as there is no greater potential source of energy on the planet.

Electricity source	Mean Value (range)	Unit	Source
Coal	28.67 (7.15-114)	deaths/TWh	[Markandya 07]
	77(19.25-308)	deaths/TWh	[Markandya 07]
	1045(909-1182)	tCO_2-eq/GWh	[Jaramillo 07]
Natural gas	2.821(0.7-11.2)	deaths/TWh	[Markandya 07]
	602(386-818)	tCO_2-eq/GWh	[Jaramillo 07]
Nuclear	0.074 (range not given)	deaths/TWh	[Markandya 07]
	65(10-130)	tCO_2-eq/GWh	[Lenzen 08]

Table 1.2: Mortality and greenhouse gas emissions factors used in the most recent study made by NASA in 2013 [Kharecha 13]

The growing concern of the public opinion on nuclear waste and inherent safely operating nuclear energy systems has led to a variety of research activities. The use of thorium in nuclear in nuclear fuel cycle for either critical or subcritical systems is nowadays a topic of interest. A thorium reactor can be different from the Fukushima power plant design and also it will not have a Chernobyl-like 'melt-down', and we have known about this efficient technology for over 50 years [Briant 57, Rosental 70]!

However, there is still considerable uncertainty about the future of nuclear power, and a number of issues could slow the development of new nuclear power plants. In many countries, concerns about plant safety, radioactive waste disposal, and nuclear material proliferation may hinder plans for new installations.

1.5 The thorium cycle

1.5.1 Potential use of ^{232}Th /^{233}U cycle in the future energy production technology

The production of nuclear energy demands a nuclear-fuel that can be "burned" by nuclear fission to release energy. Among the nuclei found in nuclear-fuel composition there are the fissile nuclei, that are able to fission with high probability with all types of neutron spectra, and the fertile nuclei, which can be converted into fissile nuclei after a neutron capture followed by β-decays.

The main fissile isotopes are ^{233}U, ^{235}U, ^{239}Pu and ^{241}Pu. The principal source of nuclear energy production nowadays is based on ^{235}U. The two naturally-occurring and most abundant fertile nuclei on earth are ^{232}Th and ^{238}U. After a neutron absorption they are transformed into the fissile ^{233}U and respectively ^{239}Pu isotopes, generating two different fuel cycles.

The past 50 years of the nuclear industry has been dominated by the uranium fuel cycle, except for several test projects. Therefore, an alternative to this technically mature commercially fuel cycle has to demonstrate outstanding benefits in order to be adopted, as the benefits associated with the technology, security and safety, environmental efficiency, economics, sustainability, etc. The need to lower the production of HLW has led to renewed interest in the thorium-based fuel cycle. With its lower atomic and mass number relative to uranium, thorium reduces significantly the build-up of heavy transuranium isotopes, in particular plutonium and curium (see for more details [Rubbia 95, **?**]). This was also clearly demonstrated by detailed simulations on the isotopic composition of a thorium-based ADS system [Garcia-Sanz 99]. In Figure 1.3 a schematic view of the actinides produced in the thorium cycle is shown [Abbondanno 01].

Thorium natural abundance exceeds that of uranium and is widely distributed in nature as an easily exploitable resource. Unlike natural uranium, natural thorium does not contain any fissile material and is made up only of the fertile ^{232}Th isotope. ^{232}Th is likely to produce a fissile nucleus in the same way that ^{238}U produces ^{239}Pu:

$$^{232}_{90}Th + n \longrightarrow {}^{233}_{90}Th \xrightarrow{\beta^-(22min)} {}^{233}_{91}Pa \xrightarrow{\beta^-(27d)} {}^{233}_{92}U \tag{1.7}$$

A crucial difference between the two fuel cycles, that can explain why uranium fuel cycle became the first to be used commercially, is that the thorium fuel cycle needs another fissile material, either ^{235}U or ^{239}Pu, to initiate the chain reaction. Once useful quantities of ^{233}U are produced, it can either fission in situ in the fuel or could be separated and recycled into new fuel. Also, the number of neutrons produced after the absorption of a neutron in a reactor environment is larger for ^{233}U than for ^{235}U

or ^{239}Pu for thermal neutrons, opening the possibility, although technically still quite complicated, for a "thermal breeder". As it will be shown in the next Section, ^{233}U is by far the best fissile isotope for a thermal neutron spectrum and can be used for breeding in both thermal and fast reactors. That is why thorium should be reconsidered in current and future energy production technologies.

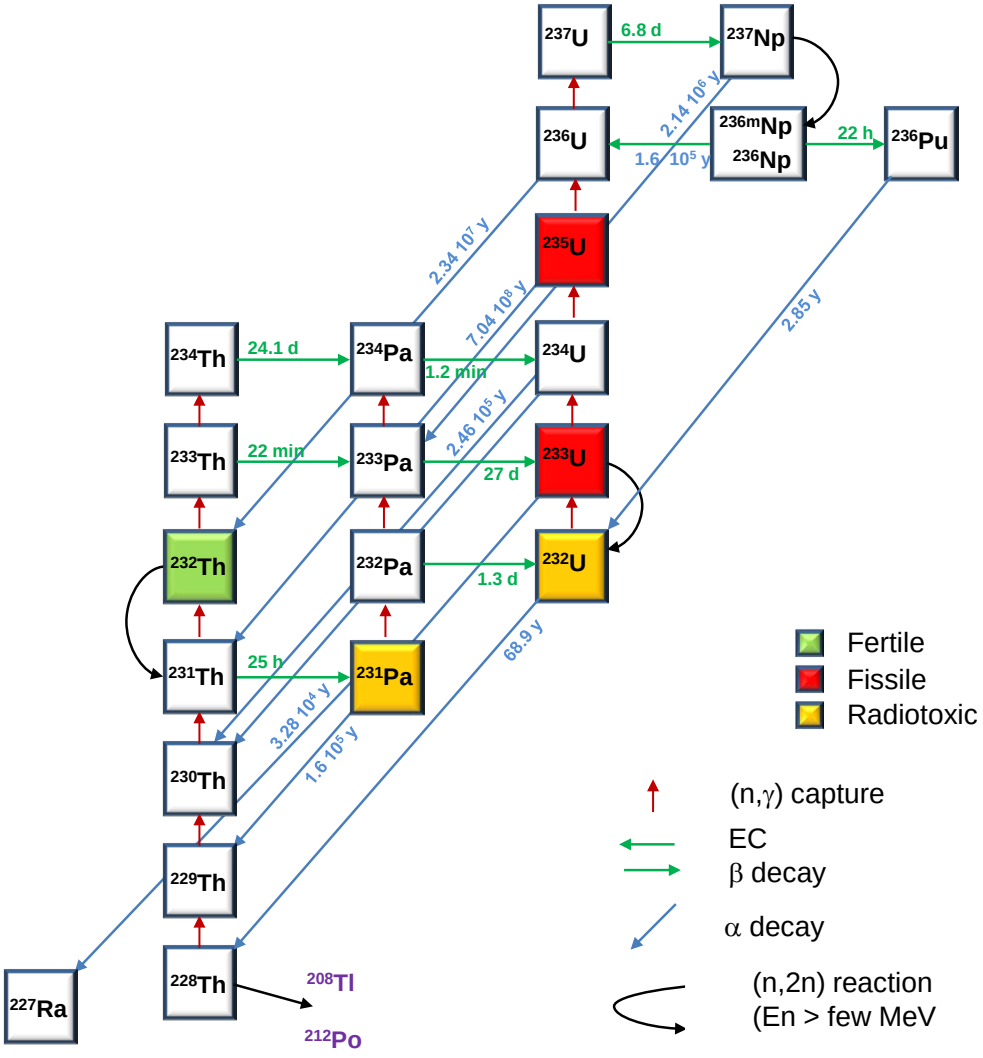

Figure 1.3: Nuclear transformations in $^{232}Th/^{233}U$ cycle [Abbondanno 01].

1.5.2 Breeding efficiency

Present reactors generate energy from the fission of ^{235}U and require around 200 tons of natural uranium to produce 1GWe of energy, equivalent to the fission of one ton of fissile material per year. With the significant increase in energy demand, these standard reactors will consume the whole estimated uranium reserve of the world in few decades. In a breeder reactor [6], the mass of fissile material remains constant, and the fertile ore is the only material to be consumed. In this case, only one ton of natural ore is needed to produce 1GWe.year. These reactors are able to achieve this performance because their neutron economy is high enough to breed more fissile fuel than they use from fertile material like ^{238}U or ^{232}Th.

Conventional reactors extract less than 1% of the total energetic potential of the uranium ore, and cannot ensure a massive and sustainable development of nuclear power in the coming centuries. Breeder reactors allow optimal use of uranium ore, by producing the fissile material from the fertile ^{238}U as shown in eq. 1.1. The two intermediate nuclei ^{239}U and ^{239}Np have short half-lives and do not play any important role in the breeding characteristics. If breeding occurs, then almost 100% of the uranium ore can be used to produce energy over several thousand years. The high fuel efficiency of breeder reactors could diminish concerns about fuel supply or energy used in mining. Moreover, the share of the ore price in the total cost of nuclear energy would be low, that could be acceptable to extract, very expensively, uranium from seawater, and satisfy the planet energy needs for several tens of thousands of years [Cohen 83, Cuttler 09]. Finally, ^{232}Th, the second natural actinide could also be used in a breeder cycle in the same way as ^{238}U (see equation 1.7). In the next section there will be discussed the physics constraints of the breeding concept and the main difference between $^{232}Th/^{233}U$ and $^{238}U/^{239}Pu$ cycles.

1.5.2.1 Breeding constraints

Breeding needs neutrons to regenerate the fissile material, and is not always possible. In order to sustain the chain reaction in a critical reactor, one neutron has to be used to induced another fission on the fissile nucleus. Let us consider one fission in a breeder reactor, which produces ν neutrons. One fissile nucleus is thus consumed by fission and $\alpha = \sigma_{cap}/\sigma_{fis}$ fissile nuclides (see eq. 1.3) are consumed by parasitic neutron capture. $(1 + \alpha)$ nuclei are consumed for one fission, and have to be regenerated by $(1 + \alpha)$ neutron captures on the fertile material, which again consumes $(1 + \alpha)$ neutrons. The neutron balance between production and absorption is then N_a given by the following approximation:

$$N_a \approx \nu - 2 * (1 + \alpha) - losses \tag{1.8}$$

6. A breeder reactor is a nuclear reactor capable to generate new fissile material at a greater rate than it consumes this material.

where *losses* represent the parasitic captures on structural materials and neutron leakage.

N_a can therefore be defined as the number of available neutrons to overgenerate the fissile material. It is important to note that, a part the losses term, the number N_a depends only on the neutronic characteristics (ν and α) of the fissile material. If N_a is close to zero or negative, the probability of regeneration is also equal to zero. Examples of the N_a values for the different cycles are given in Table 1.3 [David 13]. The number of available neutrons can be represented as a function of the energy of the incident neutron, as shown in Figure 1.4.

It can be clearly seen that N_a (without losses) is negative for $^{238}U/^{239}Pu$ cycle in the low energy region that corresponds to current reactors, and positive for fast neutron spectra. This implies that LWR reactors will not be able to reach the necessary conditions for breeding, and therefore sustainable nuclear power requires the development of new technologies.

	Thermal		Fast	
Cycle	$^{238}U/^{239}Pu$	$^{232}Th\ /^{233}U$	$^{238}U/^{239}Pu$	$^{232}Th\ /^{233}U$
Fissile	^{239}Pu	^{233}U	^{239}Pu	^{233}U
$\sigma_{(n,f)}$(barn)	90	50	1.85	2.7
$\sigma_{(n,\gamma)}$(barn)	50	6	0.5	0.27
ν	2.9	2.5	2.9	2.5
$N_a = \nu - 2*(1+\alpha)$	-0.2	0.3	0.36	0.3

Table 1.3: Available neutrons for $^{238}U/^{239}Pu$ and $^{232}Th\ /^{233}U$ cycles for thermal and fast neutrons ([David 13]).

For the $^{232}Th\ /^{233}U$ cycle, the situation is different. Figure 1.4 shows that N_a is positive in the low energy region, but the reactors based on $^{232}Th\ /^{233}U$ cycle will require a fast reprocessing to maintain $N_a > 0$ by reducing the losses term [Merle-Lucotte 08, Mathieu 06]. N_a is also positive in a fast spectrum, but less favourable for breeding than $^{238}U/^{239}Pu$ cycle. The general viability of $^{232}Th\ /^{233}U$ fuel cycle in different reactors has been confirmed by several recent studies, showing that thorium reactors can be

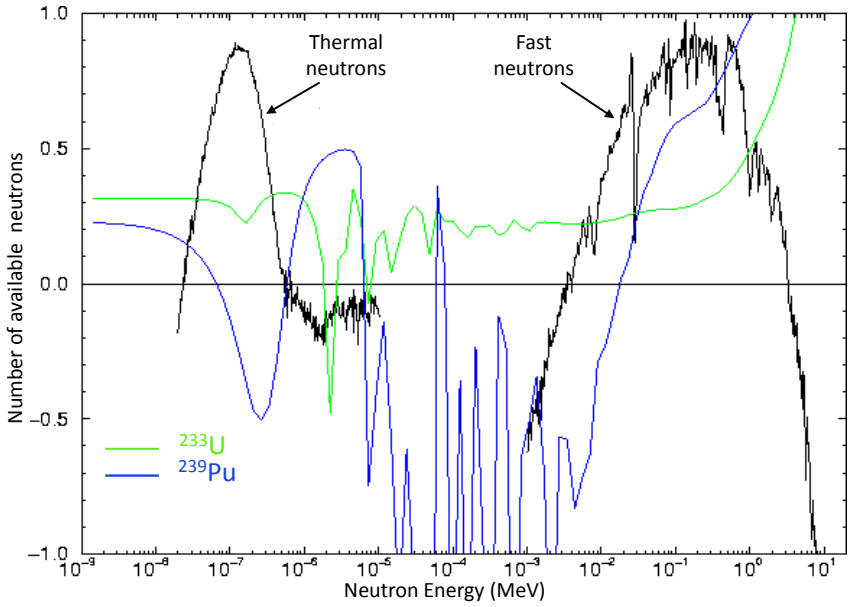

Figure 1.4: Number of neutrons available as a function of neutron energy for ^{239}Pu and ^{233}U fissile nuclei ([David 13]). For information, typical thermal and fast neutron spectra are also given.

regenerators, and even breeders [Trellue 11, Mathieu 09]. Both solutions should be taken under consideration and studied. Detailed description of fast breeder reactors based on ^{232}Th /^{233}U fuel cycle can be found in [Carminati 93, David 00].

1.5.3 Radiotoxicity

The potential radiotoxicity is calculated for different scenarios and it refers to the weighted sum of toxic ingredients of all elements contained in the spent fuel. This measure is assessed by considering it in terms of the dose (Sv) and dose factor (Sv/Bq) that take into account the metabolism of the radionuclide in the human organism once inhaled or ingested, the type and energy level of radiation, and so on. The radiotoxicity is an important estimation of the potential hazard of the nuclear waste on environment.

The radiotoxicity of the spent fuel is a function of the isotopes activity, type of radioactivity and the chemical properties of the elements. The radiotoxic sources are:

- the FP produced by nuclear fission reactions in the reactor with a $T_{1/2}$ of $\sim$ 30 years;
- the MA as part of nuclear fuel which are difficult to manage after irradiation in nuclear power plants produced by successive neutron captures;

- long lived FP

For the first couple of hundreds of years, the radiotoxicity is dominated by the short-lived FP contribution. After this time, most of the FP have decayed and the radiotoxicity becomes dominated principally by MA elements and plutonium isotopes, that are highly active radionuclides and characterized by important $T_{1/2}$, particularly plutonium. The time evolution of the radiotoxicity of HLW per unit energy produced by the reactor (ThermalGigaWatts year) for various cycles and technologies is given in Figure 1.5 [David 07].

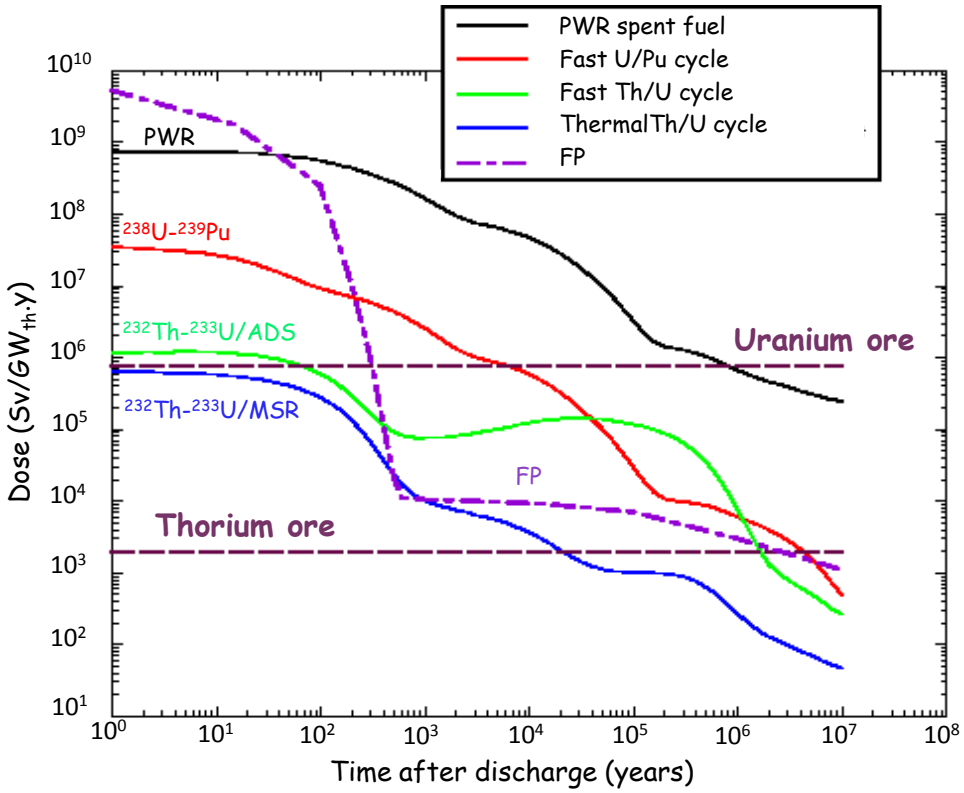

Figure 1.5: Time evolution of the radiotoxicity contribution due to the spent fuel of the main fuel cycles. Nuclear waste is due to the actinides generated during the fuel use (their quantity depending on the reactor type) and FP (their amount depending only on the quantity of energy produced) [David 07].

As seen in Figure 1.5 the radiotoxicity due to FP is roughly the same for all technologies, and dominates in the short term due to short-lived FP. After a few hundreds years, it falls to a relatively low level, much lower than the uranium ore radiotoxicity;

this is the contribution of long-lived FP. The radiotoxicity due to the spent fuel from a PWR reactor reaches the radiotoxicity level of natural uranium used by these reactors one million years after the fuel unloading. In breeder reactors based on $^{238}U/^{239}Pu$ cycle, uranium and plutonium are normally spent after fuel processing, their contribution to the radiotoxicity of the waste being insignificant (leakage during fuel processing) [David 07]. Because of this the radiotoxicity is with almost two orders of magnitude smaller than in the case of PWR reactors as illustrated in Figure 1.5.

In other words, for an equal amount of energy produced, the geological waste repositories needs will be greatly reduced with a $^{238}U/^{239}Pu$ breeder reactors than with the present nuclear-power plants. The ^{232}Th $/^{233}U$ fuel cycle presents an even better advantage, since it produces other isotopes than heavy actinides, such as ^{234}U, ^{235}U etc., much less radioactive than americium and curium isotopes. Figure 1.5 clearly shows the advantage of the ^{232}Th $/^{233}U$ cycle, where the curves for this cycle are far bellow, for thermal breeder reactor (as example for Molten Salt Reactors [Mathieu 09]) being the lowest. It reaches the radiotoxicity level of thorium ore after a little more than ten thousand years. This information is of great relevance, especially to estimate the importance of ^{232}Th $/^{233}U$ cycle and for the overall reduction of radiotoxicity.

1.5.4 Advantages and disadvantages of the $^{232}Th/^{233}U$ fuel cycle

Development of the thorium-based fuel cycle offers attractive features, mostly the reduction of radiotoxicity and a diversification option for nuclear fuel supply. Also, the use of thorium in most reactor types leads to significant safety margins. It is then important to consider a strategy to allow the implementation and the development of a fleet of thorium-based reactors.

The Advantages

- Thorium is 3 to 4 times more abundant than uranium.
- Thorium is made up only of the fertile ^{232}Th unlike natural uranium that contains ^{235}U , ^{238}U and traces of ^{234}U.
- ^{232}Th is better fertile than ^{238}U in thermal spectrum. The capture probability for thermal neutrons of ^{232}Th (7.4b) is more than two times bigger than for ^{238}U (2.7b). Therefore, a higher production of ^{233}U is possible with ^{232}Th than of ^{239}Pu with ^{238}U [IAEA 05].
- While in the $^{232}Th/^{233}U$ fuel cycle breeding is achievable with thermal, epithermal and fast neutrons, the $^{238}U/^{239}Pu$ fuel cycle can reach the conditions for breeding only with fast neutrons.

- Since the mass number of ^{232}Th is 6 units less than ^{238}U, the production of heavy nuclei like neptunium, plutonium, americium and curium, which are the major contributors to the radiotoxicity of the waste in the $^{238}U/^{239}Pu$ cycle in the long term, is drastically reduced. Figure 1.5 shows that for breeder reactors, the radiotoxicity of the waste in the thermal $^{232}Th/^{233}U$ cycle is much smaller than that of the fast $^{238}U/^{239}Pu$ cycle. For the fast $^{232}Th/^{233}U$ cycle the radiotoxicity is smaller than that of the fast $^{238}U/^{239}Pu$ cycle only during the first 10 000 years.

- The thorium fuel cycle is considered proliferation-resistant because the production of ^{233}U entails also the production of ^{232}U through (n,2n) reactions. ^{232}U has $T_{1/2} =$ 68.9 years, and decays to ^{212}Bi and ^{208}Tl, which decays with the emission of very deeply penetrating 2.6MeV $\gamma-$ray. It is thus way too difficult to manufacture a ^{233}U based nuclear weapon in the presence of ^{232}U contamination [Galperin 97].

The Disadvantages

- Because there is no fissile nucleusavailable, the acquired experience on the $^{232}Th/^{233}U$ fuel cycle is very limited as compared to the $^{238}U/^{239}Pu$ fuel cycle, and needs to be substantially increased before investing for the commercial utilisation.

- The control of a critical reactor is more delicate due to the smaller amount of delayed neutrons.

- It is very difficult to extract the thorium ore because of its direct radiological impact. As previously mentioned, the ^{232}Th-based fuels contain significant amount of ^{232}U associated with the strong 2.6MeV gamma emission. As a result, the entire fuel fabrication and reprocessing process has to be automated and to be executed in heavily shielded hot cells, leading to an increase in the cost.

- In the conversion chain of ^{232}Th to ^{233}U, the intermediate ^{233}Pa with a relatively longer $T_{1/2} = 27$ days as compared to ^{239}Np ($T_{1/2} = 2.35$ days) in the uranium fuel cycle, can capture neutrons, producing ^{234}Pa instead of decaying to the fissile ^{233}U. Neutron losses due to captures on ^{233}Pa can jeopardize breeding [Mathieu 06]. It is thereby useful to isolate ^{233}Pa from the spent fuel.

- Due to encountered technical problems but also overshadowed by the energy production of $^{238}U/^{239}Pu$ fuel cycle reactors, the effort to use $^{232}Th/^{233}U$ as alternative fuel cycle seems unlikely while uranium resources are still available.

Before the commercial use of thorium fuel cycle, many measurements, analysis, simulations and benchmark work are required. Nevertheless, the potential benefits that thorium fuel cycle may offer for the long-term nuclear scenarios is considered and evaluated as an interesting option.

1.6 Nuclear data role and need

The design, assessment and feasibility studies of potentially performant and innovative nuclear plants requires understanding the complex combinations of nuclear processes. A long chain of calculations needs to be performed and a large number of experiments must be done to obtain quantitative results for nuclear reactions, nuclear structure and nuclear decay data. Key parameters in nuclear applications such as reactor core design, heat production, shielding problems, material damage, etc., rely on accurate nuclear data.

The basic nuclear data related to the interaction of neutrons with matter (neutron transport) such as neutron cross sections, their energy dependence, emission probabilities of secondary particles (multiplicities, energies, angular distribution) etc., can be determined experimentally, or they can be predicted by dedicated nuclear-reaction codes. Therefore, the impact of neutron cross-sections accuracy is very important for nuclear waste and proliferation issues, as well as for the safety assessment of the fissile materials, reactor core and shielding of nuclear facilities.

The experimental nuclear data follow a complex process of evaluation before obtaining the "best estimated" value available for the nuclear data users community, as sketched in Figure 1.6. For each individual isotope at a particular energy of incident particles, the evaluators often combine the available experimental data with theoretical models to predict a complete set of evaluated cross-sections mandatory for reactor calculations, often for large neutron energy ranges. Also these data are of great importance in a wide range of applications such as nuclear astrophysics, nuclear medicine, food science, materials analysis, environmental monitoring etc.. All available data must be thoroughly reviewed to avoid unreliable measurements due to systematic errors or the use of obsolete methods. Sometimes, the evaluations are based directly on experimental data, but this is available only for reactions for which detailed measurements were performed [Bauge 06]. After a complete checking process with neutron transport calculation tools and suitable benchmark experiments, a complete set of evaluated cross-sections is formed, managed in a computerized way and stored in the Evaluated Nuclear Data File (ENDF) format [Group 09]. The evaluated data are then published by different nuclear-energy agencies producing evaluated data libraries like ENDF/B-VII.1 (USA), JEFF-3.1 (Europe), JENDL-4.0 (Japan), BROND-2.2 (Russia), CENDL-2 (China) used for practical applications [IAEA-NDS 13] .

The accuracy of the evaluated neutron cross sections varies from one isotope to another. These differences are due to the fact that the nuclear power plants nowadays are based on the fission process of ^{235}U and ^{239}Pu. Therefore, the accuracy of fission cross sections of ^{235}U and ^{239}Pu isotopes is better than 1% at thermal energy, while for ^{241}Pu, $^{241,242m,243}Am$ and $^{242,244,245}Cm$ the accuracy varies from 5 to 50% depending on

the energy range and the reaction channel [Aliberti 04]. For the capture and inelastic cross sections of these last isotopes the situation is even worse, very often the data are completely missing. These big disparities are related to:

- the experimental data that are in some cases incompatible, scarce or completely missing as the ones for short-lived isotopes or for nuclides that are difficult to be obtained in sufficient high purity.

- the experimental data do not cover all neutron energy ranges and the energy resolution provided is not sufficient.

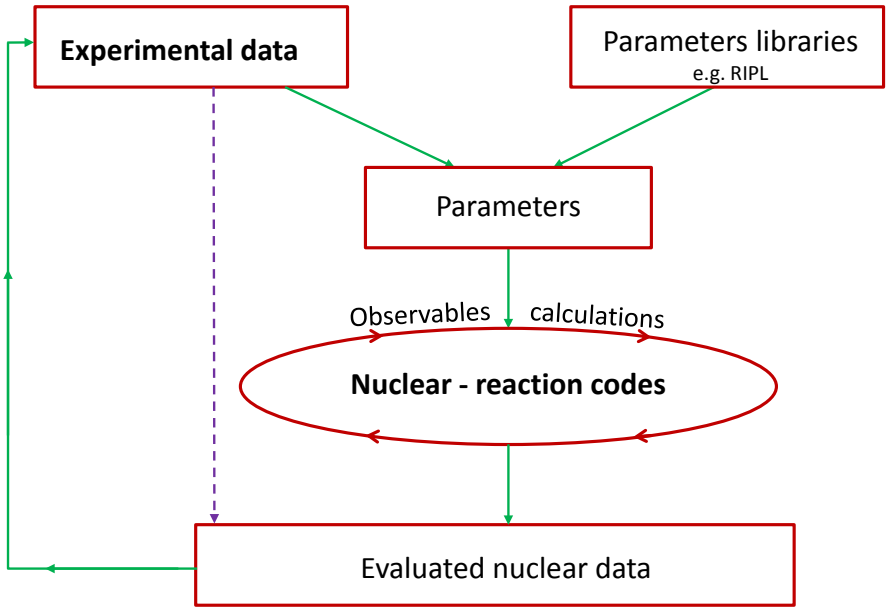

Figure 1.6: Conceptual scheme of different steps between experimental nuclear data, model parameters and evaluated nuclear data.

For this reason, the evaluators investigate the accuracy of specific data sets in order to obtain a self-consistent result. It is important to mention that accurate data are not only important for future reactors, but also for the current ones. Nuclear models are used to complement experimental data, to solve discrepancies between them and to provide coherent data of evaluated cross-sections (sometimes with big uncertainty). Usually these models depend on parameters whose values must be adjusted to reproduce the experimental data. In some cases the experimental data are insufficient to constrain the model parameters and the parameters are given by systematics [Capote 09]. Thus,

the result of the evaluation depends strongly on the evaluator decisions. Even though considerable improvement of the theoretical models has been achieved in the last years, in some cases, the experimental data are considered more reliable because the nuclear models are still not accurate enough.

To determine the priorities in the measurement of neutron-induced cross sections it is important to assess the nuclear data that play the most important role in nuclear energy applications, both for present and future systems (e.g. transmutation, generation IV nuclear reactors). Thereby, sensitivity analysis are requested where the uncertainty of a given cross section is propagated in the calculation of the quantities used in reactor calculations such as the multiplication factor(k_{eff}), the Doppler and coolant void reactivity coefficients ($\Delta\rho^{\text{Doppler}}$, $\Delta\rho^{\text{Void}}$), the reactivity loss during irradiation, the evolution of the material composition, etc.. To assess needs for nuclear data improvements, primarily but not exclusively in nuclear power technology, a High Priority Nuclear Data Request List (HPRL) [NEA-HPRL 12] was established. This list provides a guide for those planning new measurements, nuclear model calculations and data evaluation programs.

A recent sensitivity analysis has been made on the impact of neutron cross sections uncertainties on the most significant integral parameters related to the core and fuel cycle of innovative systems. The results have evidenced tight requirements for the neutron fission, capture and inelastic cross sections of an important set of isotopes. An example list of the nuclear data uncertainty objectives is presented in Table 1.4.

A selection criteria based on the impact of transmutation, the availability of neutron cross sections data, experimental difficulties involved, limitations of the methodology allows to set the priorities for further experiments. In addition, the interest for advanced technologies, neutron-induced cross sections at low energy can provide significant knowledge on nuclear properties, which is a fundamental input in nuclear structure and reaction models, as for example is the level density at neutron binding energy, that can be directly obtained from high-resolution neutron-resonance spectroscopy.

One of the HPRL requests is the reduction of the uncertainties of ^{233}U α and η parameters that are of critical importance for the evaluation of the feasibility of the reactors based on ^{232}Th cycle [Plompen 08]. In this respect, the ACEN group of CENBG decided to focus its interest on the development of an experimental set-up for the measurement of the neutron σ_{fiss} and σ_{capture} of ^{233}U from thermal to several keV energy range. Not only, the group is also is involved in MA cross-sections measurements via surrogate method [Kessedjian 10, Boutoux 12]. These measurements are part of the scientific programmes GEDEPEON and NEEDS and realised between CENBG and the IRMM European Commission collaboration participating institutes.

The work presented in this manuscript is dedicated to the development of an experimental set-up designed for the measurements of the neutron-induced σ_{fiss} and σ_{capture} of ^{233}U that will be performed at Gelina facility at IRMM.

Isotope	Energy range	Uncertainty (%)	
		Initial	Required
^{233}U capture	10 keV - 1.0 MeV	10	5
ν of ^{233}U	1 eV - 0.01 MeV	1	0.5
^{235}U capture	0 -10 MeV	7.5 - 15	<7
^{238}U inelastic	0.5 - 6 MeV	10 - 20	2 - 3
^{238}U capture	9 - 25 keV	9	1.5
^{242}Pu fission	1 eV - 6 MeV	15 - 37.2	3 -13
^{240}Pu fission	2 keV - 2.23 MeV	3.9 - 21.6	1.6 - 11.8
^{239}Pu capture	2 - 67 keV	7	3
^{241}Am capture	1.3 keV - 2 MeV	7 - 12	5
^{243}Am inelastic	1.3 keV - 2 MeV	18 - 80	2.3 - 12
^{244}Cm fission	1.3 keV - 2 MeV	30 - 50	4.6
ν of ^{244}Cm	1.3 keV - 2 MeV	5.5 - 11	3.9

Table 1.4: Examples of required data uncertainties of innovative nuclear systems, for specific energy ranges([NEA 08, Aliberti 04, Plompen 08]).

Chapter 2

Fundamental aspects of neutron induced reactions

In this chapter a review of the theoretical background required for a comprehensive understanding of the data analysis described in this document will be discussed.

The main feature of the reaction mechanisms will be explained and the concepts of neutron cross section and resonance will be introduced. We will present the principal neutron induced reactions and the energy dependence of cross-sections.

In the compound nuclear-reaction theory, a collision matrix describes the interaction process with a nucleus, but is not easily accessible due to the complexity of the nuclear potential. We will see how the so-called R-matrix formalism can bring a solution to this matter.

2.1 Reaction mechanisms

Nuclear reactions can occur when nuclei (target) are bombarded with different particles (projectiles) by means of the strong short range nuclear forces, and often, new nuclei are produced. For the same projectile and target nuclei several types of reactions may occur in different stages as shematically shown in Figure 2.1. Each stage of nuclear reactions corresponds to a reaction mechanism. The contribution of these mechanisms depends on the given reaction, the energy of the incident particle, the mass of the nuclei involved and so forth. We distinguish three types of mechanism:

- The **direct reaction** takes place at/or near the nuclear surface, nuclei make glancing contact and then separate rapidly. The projectile may exchange some energy and/or angular momentum, or have one or more nucleons transferred to it or removed from it. Such transfer reactions are generally referred to as stripping or pick-up reactions, depending on whether the incident particle has lost or acquired

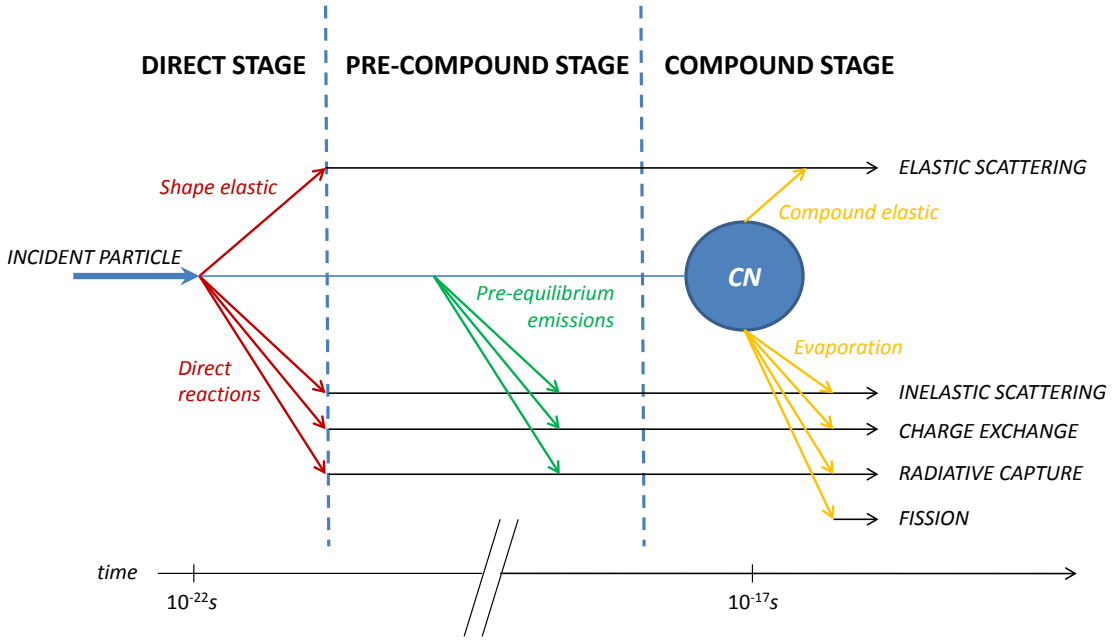

Figure 2.1: The stages of a nuclear reaction [Weisskopf 57, Feshbach 74].

nucleons in the reaction. Because it is produced by a single or double intranuclear collision, a direct transition from the entrance to the exit channel occurs in a very short time scale of about $10^{-22}s$, the time that it takes to a nucleon to cross the nucleus. If during the interaction the projectile as well as the target change only their direction but suffer no energy loss, the reaction mechanism is called shape elastic scattering. Inelastic scattering and charge transfer processes are also direct reactions.

- The **Compound-Nucleus** (CN) model was the first reaction mechanism released [Bohr 36]. The projectile shares its energy with the ensemble of the nucleons that will be in a complex nuclear state. It is a state of statistical equilibrium. That is, all the energetically possible configurations of the nucleus have equal probability to be realized. In certain configurations of the compound state, a nucleon has enough energy to escape from the nucleus. Also, the excitation energy may be concentrated on groups of particles with more or less evanescent existence in the nucleus, and charged particles may be emitted. The compound state can decay back to the incident channel, and the reaction is called compound elastic scattering, which can occur after a long time via the CN stage. The time scale of CN reactions is in the order of $10^{-14} - 10^{-18}s$, much longer than for direct reactions.

- The **pre-equilibrium** (or pre-compound) reaction takes place after the first stage of the reaction but long before the formation of the CN. The pre-equilibrium is not presented in this work (see for details [Feshbach 74, Adhikari 82]).

2.2 Neutron induced reactions

Since neutrons are electrically neutral particles they have no Coulomb barrier to overcome. Due to this fundamental property they can directly penetrate, and interact with nuclei, even at very low kinetic energies of some meV. The absence of charge also gives the neutron the possibility to cross thick materials without interacting. The probability of a neutron to interact with a nucleus is energy dependent. Small changes in neutron energy can lead to strong variations of the cross sections that are used to determine the interaction probability. The cross section is expressed in units of area (1 barn = $10^{-24} cm^2$, which is approximately the cross sectional area of an uranium nucleus). As a neutron enters a nucleus two main types of previously described reaction mechanisms can occur.

In the case of a direct reaction, the neutron can be elastic scattered and the total kinetic energy is conserved, the scattered neutron could be the same as the incident. However, the neutron can interact directly with one or a few nucleons of the target nucleus, and transfer a part of his kinetic energy, leaving the target nucleus in an excited state. This is an inelastic scattering. Also the neutron can be captured by the nucleus that become excited. Even in a state above the neutron binding energy the target nucleus will go to a stable or ground state by emitting radiations depending of the excited state achieved. α, β, γ, and protons may be emitted, or a neutron may re-emerge from the excited nucleus.

In a compound-nuclear reaction the neutron interacts with a nucleus to form a CN, which can then decay by particle emission. After the absorption of the neutron, the possible reactions are: compound elastic scattering, inelastic scattering, neutron (or radiative) capture, fission, and charge exchange. Neutron capture and the neutron-induced fission are the reactions of most interest in this work. These compound-nuclear reactions are predominant for neutrons with energies below 1MeV.

2.2.1 Compound-nuclear reactions

A complete description of the interaction between a neutron and a nucleus is very complex since it involves N-body problem. The simplified CN reaction model was first discussed by Niels Bohr considering the neutron induced reactions as a two-step process: the formation of a compound nucleus and its decay [Bohr 36]. A schematically view of the compound nucleus formation and its decay is shown in figure 2.2.

In the first step, the neutron with kinetic energy E_n in a laboratory system [1] (L.S.)

1. Because the data are measured in the laboratory reference system and the theoretical predictions are made in the center of mass (C.M.) reference system, a coordinate transformation is needed to compare theory with experiment.

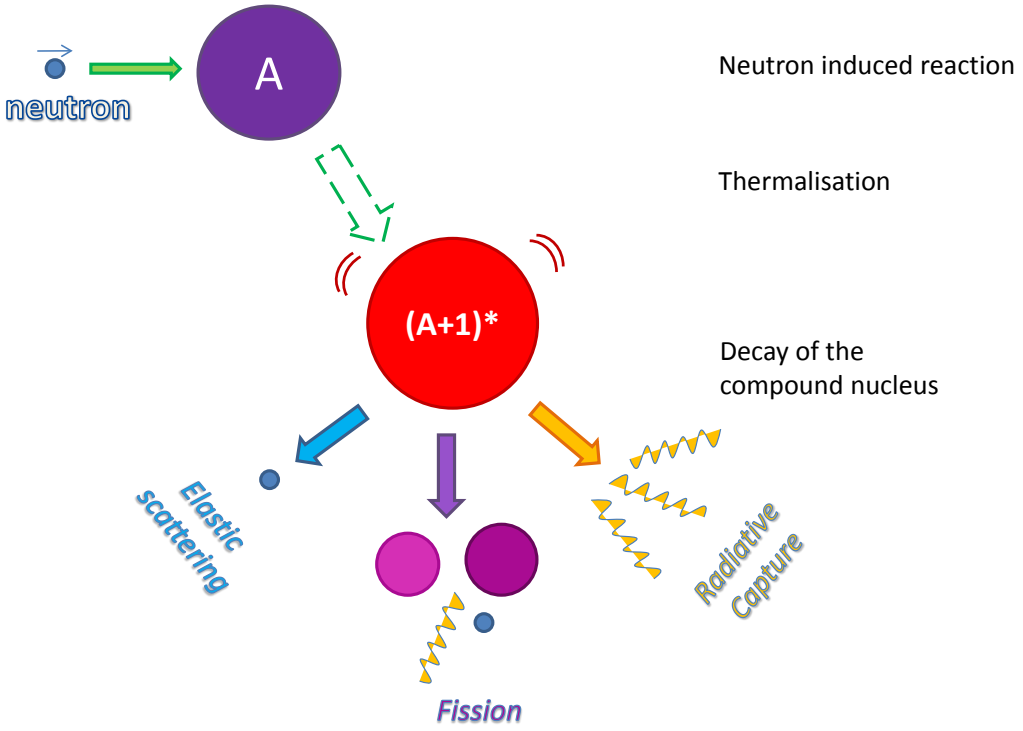

Figure 2.2: The formation and the decay of compound nucleus via neutron-induced reaction.

enters a nucleus and a CN is formed with an excitation energy E^* which is given by the following expression:

$$E^* = S_n + \frac{A}{A+1} E_n \tag{2.1}$$

where:

- S_n is the neutron binding energy of the CN,
- A is the mass of the target nucleus.

As mentioned before, the excitation energy is redistributed among all nucleons, leading to complex configurations corresponding to quasi-particle or collective states characterized by energy, spin and parity.

In the second step, the CN decays by $\gamma - ray$ emission, *neutron* emission, charged particle emission (a *proton* or an $\alpha - particle$) or fission. The way of decay and the decay probability of the CN is considered independent from the way how the CN was formed (the CN has completely lost memory of the entrance channel), but respecting conservation of energy, angular momentum and parity.

A nuclear reaction implies a transition, with a certain probability, from the initial state (the entrance channel of the projectile and the target nucleus) to the final state. The reaction products are in the exit channel. Hence, a compound nuclear reaction ${}^{A}X(n,b)Y$ can be defined as:

$$\begin{array}{ccccccccc} n & + & {}^{A}X & \longrightarrow & {}^{A+1}X^{*} & \longrightarrow & Y & + & b \\ \vec{i} & & \vec{I} & & J & & \vec{I'} & & \vec{i'} \end{array} \tag{2.2}$$

where the projectile is a neutron n, the target nucleus is ${}^{A}X$, and ${}^{A+1}X^{*}$ is the compound-nucleus with angular momentum J and parity Π at an excitation energy E^{*}. The entrance channel is defined by $c = (\alpha, l, s, J)$ where the following definitions apply:

- α represents the projectile and the target making up the channel; α includes mass (m and M), charge (z and Z), spin (i and I), and all quantum numbers for each of the two parties;
- l is the orbital angular momentum of the pair;
- s represents the spin of the entrance channel, and is the vector sum of the intrinsic target spin I and the neutron spin $i = \frac{1}{2}\hbar$: $\vec{s} = \overrightarrow{i} + \overrightarrow{I}$, with:

$$| I - i | \leq s \leq | I + i | \tag{2.3}$$

- J is the total angular momentum of the CN, given by the vector sum of the spin, and the orbital angular momentum l : $\vec{J} = \overrightarrow{l} + \overrightarrow{s}$, with:

$$| l - s | \leq J \leq | l + s | \tag{2.4}$$

The state of the CN formed has a definite parity, governed by the following equation:

$$\Pi = (-1)^{l} \pi_I \pi_i \tag{2.5}$$

Similarly, the exit channel is given with primed symbols $c' = (\alpha', l', s', J')$, with $J = J'$. The angular momentum conservation in the exit channel implies the equations 2.3 and 2.4 but with primed symbols.

An interaction may occur if the $J'^{\pi'}$ value of the exit channel is equal to the J^{π} value of the entrance channel, according to the quantum mechanics conservation law. The probability of the neutron and nucleus to produce the compound nucleus in a state characterized by an angular momentum J is given by the statistical spin factor g corresponding to:

$$g = \frac{2J+1}{(2i+1)(2I+1)} \tag{2.6}$$

For instance, the ^{233}U nucleus has the ground state spin and parity of $5/2^+$. The states of the ^{234}U compound nucleus excited by the capture of s-wave (l=0) neutrons in the ^{233}U nucleus have spin and parity 2^+ and 3^+ with statistical factors of 5/12 and 7/12 respectively.

2.3 Neutron cross sections

The simple concept of cross section (σ) in terms of area is not only useful for its illustrative purpose but also in applications where neutrons are classical point particles, nuclei are solid spheres and σ would be the cross-sectional area of each nucleus. The cross section defined as the projected area of the nucleus is a measure of probability that a neutron will hit that nucleus regardless of what happens after the collision. The variety of nuclear reactions that may occur when a neutron interacts with a specific nuclide (scattering, capture, fission, etc.) brought into evidence the definition of partial cross sections. These cross sections are very different, depending on the energy of the incident neutron and the reaction channels that are likely to occur in a CN reaction since they are related to the nuclear structure of the nucleus under the neutron bombardment. Bohr's CN idea is formalized for the neutron-induced reaction cross section of a given decay channel χ as follows:

$$\sigma_{n,\chi}(E_n) = \sum_{J\Pi} \sigma_n^{CN}(E^*, J, \Pi)\, P_\chi^{CN}(E^*, J, \Pi) \tag{2.7}$$

where:

- $\sigma_{n,\chi}(E_n)$ is the neutron-induced cross section for the reaction $^A X(n,\chi)$.
- E_n the incident neutron energy.
- E^* is the excitation energy of the CN (see eq. 2.1)
- J, Π are the spin and parity of the CN.
- $\sigma_n^{CN}(E^*, J, \Pi)$ is the formation cross section of the CN $^{A+1}X^*$ in the $\{E^*, J, \Pi\}$ state.
- $P_\chi^{CN}(E^*, J, \Pi)$ is the decay probability of the compound state with angular momentum J and parity Π for the channel of interest χ. For the present work, the relevant exit channels are: capture, fission and neutron emission.

The nomenclature for the three cross sections associated to different types of interactions is the following:

- **Scattering cross section** has a very definite meaning, being the cross section for the processes in which the only particle emitted is a neutron. There are two types:

  1. **Compound elastic scattering cross section** σ_{el} if the emitted neutron has the same kinetic energy as the incoming neutron. Unlike the shape elastic scattering that take place without the CN formation, this cross section is associated to a partial width called neutron width and written Γ_n (see Section 2.4).
  2. **Inelastic scattering cross section** σ_{inl} if the neutron has transferred part of its energy that will be emitted as $\gamma - radiation$.

- **Capture cross section** σ_{cap} is for interactions in which the neutron is absorbed by the nucleus and followed by the emission of $\gamma - rays$ until the CN reaches the ground state.

- **Fission cross section** σ_{fis} when the very excited CN starts to vibrate becoming highly deformed until it will fission into two (or more) separate fragments.

The sum of all partial cross sections is defined as the total cross section:

$$\sigma_{total} = \sigma_{cap} \ + \sigma_{scat} \ + \sigma_{fis} \ + ... \tag{2.8}$$

Even though this definition may appear simple, its exploitation, especially at low and intermediate energy regions, requires careful experimental attention.

An example of neutron-induced cross sections for ^{233}U from ENDF/B-VII.1 nuclear data library is shown in Figure 2.3, as a function of neutron energy in the range of $[10^{-8} - 25]$MeV.

Experimentally, the concept of neutron cross section can be easily explained. When a neutron flux $\Phi(neutrons/cm^2/s)$ is coming towards a very thin sample of a given isotope with surface area $A(cm^2)$, density of nuclei $N(nuclei/cm^3)$, and thickness $\Delta x(cm)$, the reaction rate $R(interactions/s)$ is given by:

$$R = \sigma \cdot \Phi \cdot (N \cdot \Delta x \cdot A) \tag{2.9}$$

where σ is the proportionality constant that has the dimension of area (cm^2) and $(N \cdot \Delta x \cdot A)$ the number of target nuclei.

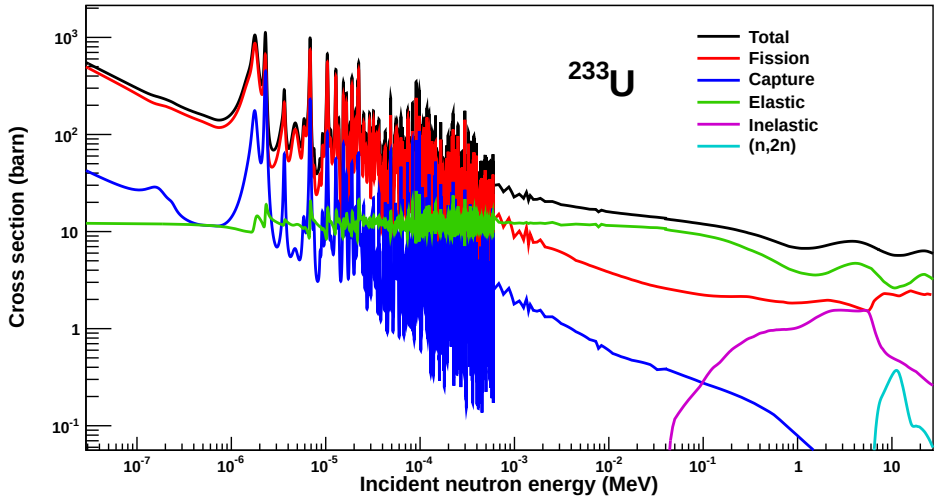

Figure 2.3: Total, fission, capture, elastic, inelastic and (n,2n) cross sections for ^{233}U isotope from ENDF/B-VII.1 nuclear data base [IAEA-NDS 13].

2.4 Neutron resonances

The CN cannot exist with an arbitrary energy content but only in definite energy states. They are related to the excitation of nuclear states in the compound nuclear system formed by the neutron and the target nucleus, at excitation energies lying above the neutron binding energy of typically several MeV. The states are called quasi-stationary levels or resonances defined by the lifetime of the corresponding excited state of the CN. The partial lifetime of these excited states is finite and satisfies the Heisenberg uncertainty principle, which states:

$$\tau = \frac{\hbar}{\Gamma_\chi} \tag{2.10}$$

where Γ_χ is the partial width for the decay through the channel χ (the resonance width).

In a heavy nucleus the number of configurations for a given E^* is very high. The CN concept states that all these configurations have the same probability. Therefore, the probability to realise one particular configuration where one nucleon escapes will be very low.

The decay probability of the excited CN for a given channel χ is equal to the ratio Γ_x/Γ, where Γ is the total width (of the resonance), that gives the total disintegration probability:

$$\Gamma = \sum_{\chi} \Gamma_{\chi} \tag{2.11}$$

The formation of the CN is decoupled from its decay, such that the reaction cross section $\sigma_{n,\chi}$ can be factored in eq. 2.7 into the product of the cross-section for forming the CN, σ_n^{CN}, times the probability of the decay via reaction χ as shown in the equation:

$$\sigma_{n,\chi} = \sigma_n^{CN} \cdot \frac{\Gamma_{\chi}}{\Gamma} \tag{2.12}$$

Even though the cross section curves look more complicated in the region of the neutron resonances than in the fast-neutron regime, as seen in Figure 2.3, each individual neutron resonance is determined by certain parameters which are properties of the nuclear excitation level represented by neutron resonance. In most of the cases the parameters needed to describe the resonance level are the neutron and $\gamma-$radiation widths (Γ_n and Γ_{γ}) and the spin of the CN. A comparison of the capture and fission cross section of ^{233}U points out that in both cases the resonances appear at the same energy (see Figure 2.3). At energies below resonance region, the cross sections are inversely proportional to the neutron velocity. Although no nuclear model exists to predict the properties of resonances, cross sections can be parametrized by the Breit-Wigner Single-Level formalism (BWSL) [Breit 36]. The simplified form of the single-level formula gives the resonance cross-section $\sigma(E)$ as a function of energy where a single level is the principal contributor in the CN formation:

$$\sigma(E) = \frac{\pi}{k^2} g \frac{\Gamma^2}{(E - E_0)^2 + \Gamma^2/4} \tag{2.13}$$

where

- Γ is the total width,
- g is the statistical spin factor, given by the eq. 2.6,
- k is the wave number in units of inverse de Broglie wavelength of the neutron,
- E is the incident energy, and
- E_0 is the excitation energy of the resonant state.

2.4.1 Resonance levels of the compound nucleus

The resonance (excitation) energy levels of the CN formed by the absorption of a neutron in nucleus ^{A}X are illustrated in Figure 2.4. The CN model was introduced by Bohr [Bohr 36] to explain the observed resonant structures. At relatively low neutron energies, the resonances are well separated and the average spacing between the neutron resonances (level distance) D is large compared to their width Γ.

With increasing excitation energy, the Γ widths of the states start to overlap and the resulting cross-sections become smoother. The properties of the resonances, like the decay widths, fluctuating from one state to another, become apparent as values averaged over many resonances. These average values now can be predicted by nuclear models, parametrized with average properties [Capote 09, Hilaire 00]. Measured cross-sections can therefore contribute at the improvement of the parametrization of these models.

At even higher excitation energies, many more decay channels open and some cross section measurements (e.g. capture cross section) become very difficult or even impossible. The level distance is much smaller than the width and the resonance structure disappears completely. Then the continuum region is reached, where the properties of neutron cross sections become much simpler since the levels are merging compared to the lower-energy resonance region. In this case, the reaction cross sections may be accessible only by nuclear model calculation.

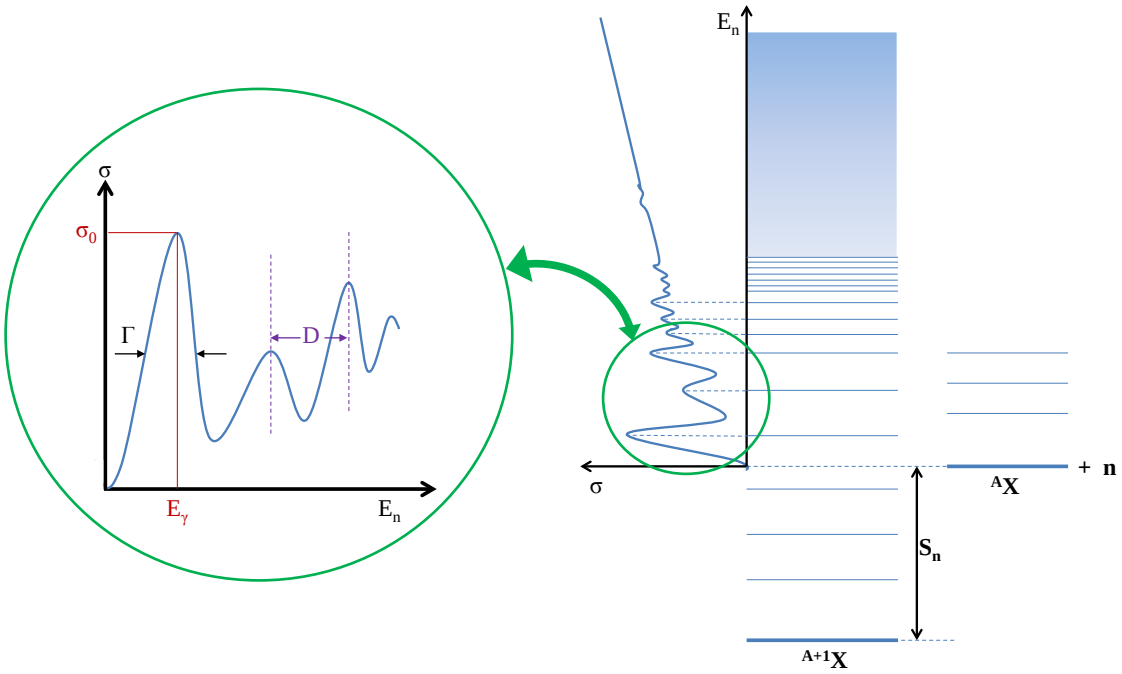

Figure 2.4: The excitation energy levels of compound nucleus formed by the absorption of a neutron and illustration of the resonance and continuum domain. The resonances observed in the reaction cross section appear as quasi-stationary levels of the CN. The parameters of the resonance are indicated for $D \ll \Gamma$.

As an example, in Figure 2.5 is shown the capture cross section of ^{233}U on a wide energy range. The resonance structures (given by resonance parameters) are very well

distinguished from the smooth cross section at high energies (parametrized by nuclear data libraries as discussed in Section 1.6). The sudden transition between these two regions is therefore not physical but related to these descriptions.

To assess the importance of the cross sections at different energies, the energy distributions of different neutron sources are also shown in the bottom of the Figure 2.5. The energy region around a few tens of meV is called thermal region and is of importance for reactor physics where moderated neutrons have Maxwell-Boltzmann distributed velocities peaked at an equivalent kinetic energy of $k_B T$. For a temperature nearly $300\,K$ this corresponds to $25.3\,meV$ (a velocity of $2200\,m/s$). The thermal cross section at $25.3\,meV$ is then an important quantity that can be measured accurately with only small amount of material in reactor experiments.

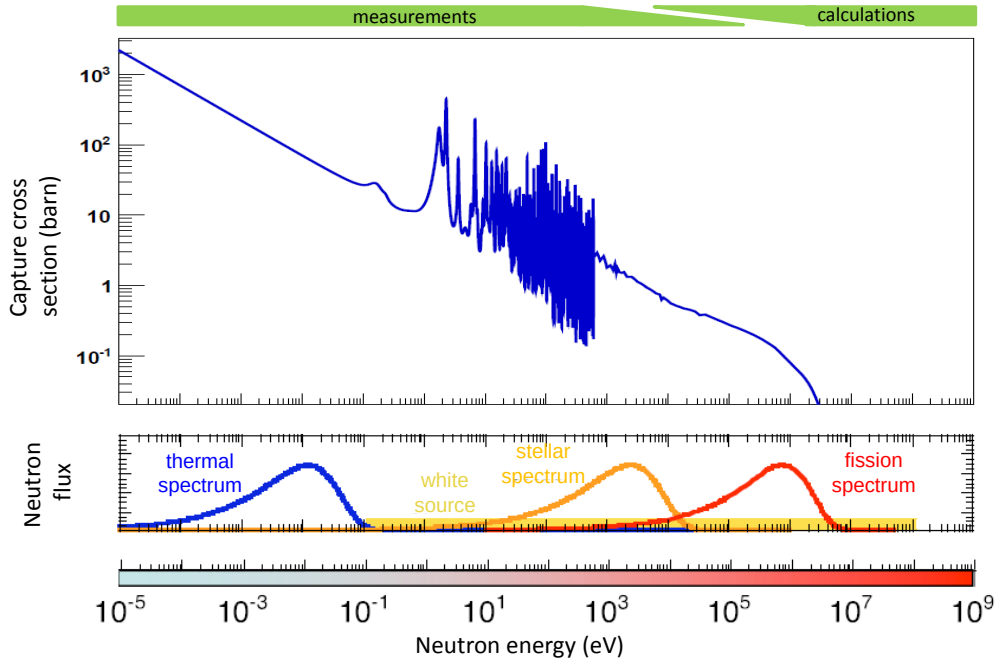

Figure 2.5: The neutron induced capture cross section of ^{233}U [IAEA-NDS 13] along with the typical energy distributions of neutron fluxes in different environments and on a wide energy range.

For the improvement of stellar models, the required input of neutron cross sections is needed in form of cross sections averaged over the neutron kinetic-energy distribution. In stellar environments the neutrons are present as a hot gas and also have a Maxwellian kinetic energy distribution with relevant temperatures $k_B T$ ranging from 5 to 100 keV [Gunsing 01, Lederer 13].

Several distribution functions describe in a satisfactory way the kinetic energy distribution of neutrons from the nuclear fission process. The neutrons from ^{233}U thermal-neutron-induced fission follow well a Maxwellian kinetic-energy distribution, peaked at about 1 MeV. This distribution is also shown in Figure 2.5.

2.4.2 Resonance cross-section

As mentioned before the cross-section of an isolated resonance can be described by BWSL formula. At low energies where neutron has zero orbital angular momentum ($l = 0$), the reaction cross-section of an isolated resonance is given by a very similar equation:

$$\sigma_\chi(E) = \frac{\pi}{k^2} g \frac{\Gamma_n \Gamma_\chi}{(E - E_0)^2 + \Gamma^2/4} \tag{2.14}$$

where E is the neutron energy, g is the statistical spin factor (see eq. 2.6), k is the wave number in units of inverse de Broglie wavelength of the neutron, E_0 is the neutron energy at the peak of the resonance, Γ_n is the neutron width, and Γ_χ is the reaction width and Γ is the total width.

Actually, for heavy nuclei the resonances are found at such low energy that only $l = 0$ is important with capture, fission and elastic scattering as the only open channels.

At high excitation energies above the neutron binding energies, for most nuclei the nuclear system is extremely complex and the properties of these excited states can not be predicted. Cross sections can therefore be determined only by measurements. For heavy nuclei the wave function which describes such a highly excited state may have as much as 10^6 parameters [Larson 08]. Also, the nuclear level density corresponding to the number of nuclear levels per MeV at an excitation energy in this region is very high. A neighbouring state characterised by a certain spin and parity can be excited by only a small change in excitation energy and may have a completely different wave function. The energy level parameters are obtained from experimental cross sections curves in a variety ways, all based on the above formula. The methods vary, depending on the relative magnitude of the scattering and capture cross-sections as well as the energy resolution available.

2.4.3 Doppler Broadening

The natural shape of a resonance does not correspond to the cross-section observed directly in an experiment. The atomic nuclei have a thermal motion, which will cause a shift in the actual kinetic energy with which the neutron interacts with the nucleus. Since the thermal motion is a statistical process with an energy distribution, the resonance

will be broadened. This effect is known as *Doppler broadening*. The effective Doppler-broadened cross-section $\sigma^D(E)$ can be obtained from the convolution of the nuclear cross section $\sigma(E)$ with an energy transfer function $S(E^{'})$, which accounts for the velocity distribution of the target nuclei:

$$\sigma^D(E) = \int dE^{'} S(E^{'}) \sigma(E - E^{'}) \tag{2.15}$$

where E is the energy of the incident neutron and $E^{'}$ is the energy of the target nucleus.

It has been shown by Lamb [Lamb 17] that the transfer function $S(E^{'})$ can be derived assuming a Maxwellian distribution of velocities for the target nuclei, similar to a monoatomic free gas or a classical solid, by introducing an effective temperature. The transfer function $S(E^{'})$ becomes:

$$S(E^{'}) = \frac{1}{\Delta_D \sqrt{\pi}} exp\left(-\frac{(E^{'} - E)}{\Delta_D^2}\right) \tag{2.16}$$

with the Doppler parameter of a Gaussian distribution at a resonance energy E_0 given by:

$$\Delta_D = \sqrt{\frac{4 k_B T_{eff} E_0}{A}} \tag{2.17}$$

where k_B is the Boltzman constant and the effective temperature is:

$$T_{eff} = \frac{3}{8}\theta coth\left(\frac{3}{8}\frac{\theta}{T}\right) \tag{2.18}$$

where θ is the Debye temperature and T is the sample temperature.

The convolution of the BWSL formula for the capture cross-section (eq. 2.14 where χ is $\gamma - ray$) with the transfer function $S(E^{'})$ (eq. 2.16) leads to an effective Doppler broadened capture cross section $\sigma^D_{capture}$:

$$\sigma^D_{capture} = \sigma_{0capture} \Psi(\beta, x) \tag{2.19}$$

with

$$\Psi(\beta, x) = \frac{1}{\beta\sqrt{\pi}} \int_{-\infty}^{\infty} dy \frac{1}{1 + y^2} exp\left(-\frac{(x - y)^2}{\beta^2}\right) \tag{2.20}$$

where $\beta = \frac{2\Delta_D}{\Gamma}$, $x = \frac{(E - E_0)}{\Gamma}$ and $y = \frac{(E^{'} - E_0)}{\Gamma}$.

Since the broadening increase with increasing temperature, the height of the resonances (the peak value of the cross-section) decreases (in a way to preserve the area under the cross-section), with a corresponding decrease of self-shielding effects [2] [Stacey 01]. This behaviour has important consequences on reactor safety, since an increase in the fuel temperature determines an increase in the effective capture or fission probability (so called feedback Doppler temperature coefficient of reactivity). The Doppler broadening is often more important than the natural line width of a resonance. For high precision cross section measurements it can be therefore favorable to cool the sample close to $T_{eff} = \frac{3}{8}\theta$.

2.4.4 Energy dependence of cross-sections

We usually distinguished three different energy region characterizing the compound nucleus reaction cross sections:

- the Thermal Energy Region → extends from a fraction of an eV down to the meV. In this region, the neutron cross-sections are smooth and their behaviour follows a decreasing $1/\sqrt{E} \sim 1/v$ shape, proportional to the time that the incident neutrons spend in the vicinity of the target nucleus.

- the Resolved Resonance Region (RRR) → located at the lower incident energies including the thermal and the epithermal regions, extends up to a few keV for heavy nuclei, and a few MeV for the lighter ones. The resonances appear well separated and their shape is entirely observable (large peaks to valley variations). The spacing between the resonances is about a few eV for heavy nuclei and a few or tens of keV for lighter or magic ones. Each resonance represents an excited state in the CN formed by the incident neutron.

- the Unresolved Resonance Region (URR) → with the increasing of the neutron energy, the spacing between the resonances decreases. Due to the important level overlap at a certain stage and also because of the degrading experimental resolution and the Doppler broadening (see Section 2.4.3) the resonances will not be resolved anymore. In addition, more and more reactions channels corresponding to threshold reactions open up.

In the RRR, the reaction cross sections can be rigorously described in terms of resonance parameters, which are the properties of the excited states mainly energy, spin

2. The presence of a sample in an neutron flux of a nuclear reactor creates a perturbation of the local neutron flux. This effect can be very important, especially if the nuclide cross-section exhibits a prominent resonance peak. To take into account the effect of the neutron flux perturbation in the sample, a resonance neutron self-shielding factor must be considered. For a given energy, this factor is the ratio of the mean fluence rate inside the sample volume to the fluence rate incident on the sample. Also it depends on the geometry and dimension of the sample, as well as on the physical and nuclear properties of the nuclide.

and parity. The physical foundation of this theory is given by the $R-matrix$ theory (see Section 2.5). The advantage of the parametrization of resonant cross sections by the $R-matrix$ formalism is that relatively few data are needed from which Doppler broadened cross sections at any temperature can be calculated.

2.5 R-matrix formalism

2.5.1 General overview

The $R-matrix$ formalism was first introduced by Wigner and Eisenbud [Wigner 46, Wigner 47] after the World War II to give a better foundation to the theory proposed by Breit and Wigner [Breit 36] for the capture of slow neutrons a few years before. An extensive and detailed overview of the $R-matrix$ theory was given by Lane and Thomas [Lane 58] and recently, Fröhner summarized the formalism together with other useful considerations on nuclear data evaluation [Frohner 00]. In the following only a brief outline of the formalism is given in order to understand the principle without giving the full details.

The theory of the R-matrix is rigorous from the mathematical point of view as well as quantum mechanics. It describes the mechanisms of nuclear reactions. Its application is limited to the interactions like the CN formation. If the wave functions of the nuclear system before and after the reaction were known, one could calculate the cross-section with the usual concepts of reaction theory. While the incoming waves are known, the reaction modifies the outgoing wave functions in a generally unknown way.

The idea behind the R-matrix formalism is to use the wave function of the nuclear system of two particles when they are so close that they form a CN. Although the wave function of the CN is extremely complicated, one can expand it in its quasi-stationary states. Matching then the incoming and outgoing waves to the internal wave function provides a way to describe the cross section of the reaction in terms of the properties of the quasi-stationary states of the CN. These properties are basically the energy, spin, parity, and a set of partial widths related to the widths of the decay modes of the CN.

This method of describing a reaction cross section using only the properties of nuclear excitation levels, is at the same time also the most important limitation. No information of the forces inside the nucleus are needed or can be extracted. The nucleus is treated as a black box where the properties of the quasi-stationary states have to be measured in order to describe the cross sections. Binary nuclear reactions proceeding from one system of two particles to another system of two particles can be described with the general R-matrix theory.

For neutron induced reactions, but also in other cases, such a reaction goes often through the formation of a CN $^{A+1}X^{*}$ (see eq. 2.2). The R-matrix formalism also

applies to direct reactions. It can also be used for charged-particle-induced reactions if the Coulomb interaction is included. But the theory is applicable only in a general way for binary reactions which is appropriate for neutron-induced reactions up to energies of several tens of MeV.

2.5.2 Theoretical considerations

In a very general way, the cross section of a two-body nuclear reaction could be calculated if the nuclear wave functions were known. The wave functions could be calculated by solving the Schrodinger equation for the nuclear system. This requires that the nuclear potential is known. When the two particles are far away, the interaction can be considered absent for neutral particles or to be the Coulomb interaction for charged particles. In these cases it is indeed possible to calculate the wave functions.

When the two particles are so close to each other that a nuclear reaction takes place, the potential of the interaction is extremely complicated. For certain energy ranges and reactions this potential can still be approximated or calculated [Bauge 01] and the wave functions and cross sections can be calculated. In other cases however, and especially in the RRR, the complexity of the reacting system does not allow this.

As mentioned before, the R-matrix principle is to consider that the reaction process can be split up into two geometrical regions for each channel. The boundary between these regions is a parameter known as the channel radius $a_c = a_0 A^{1/3}$. This radius is chosen large enough so that, in the external region, when a neutron is far away from the nucleus, the interaction between them is negligible due to the short range of nuclear forces; hence, they can be treated as two independent systems with known wave functions.

At short distances, smaller than the channel radius a_c, all nucleons involved in the reaction are close to each other and form a unique system, the CN. Although the wave function of the CN is extremely complicated, it can be expanded as a linear combination of its quasi-stationary states without solving explicitly the Schrödinger equation of the system.

In the external region, at distances larger than a_c, the potential is zero for neutral particles or is the Coulomb interaction for charged particles and the Schrödinger equation of the system can be solved. The properties of the quasi-stationary states of the CN are taken together in the R-matrix. The values and derivatives of the wave functions at the boundary of the internal and external region assure a smooth wave function and the cross sections can be calculated. The exact internal wave function is not needed, only the values and derivatives at the nuclear surface.

From information on low-energy resonances, the R-matrix theory offers an efficient way for accurately parametrizing not only resonances but also the non-resonant part

of low-energy cross sections with a small number of parameters [Lane 58]. An important advantage is that most of these parameters have a physical meaning. The other aspect of the R-matrix theory is that it can provide a simple and elegant way for solving the Schrödinger equation in the internal region and opened the way to accurate methods for the cross-sections determination in the RRR. It is especially competitive in coupled-channel problems with large numbers of open channels where a direct numerical integration may become unstable. An additional advantage is that narrow resonances which can escape a purely numerical treatment are easily studied.

2.5.3 The R-Matrix application for RRR

R-Matrix formalism is very useful for the determination of the resonance parameters from experimental data. The cross sections can be reproduced using the resonance parameters, namely: resonance energy E_0, total angular momentum (resonance spin) J, orbital momentum of the incoming neutron l, resonance total width Γ, the always present neutron width Γ_n, and other partial widths like the radiative width Γ_γ or fission width Γ_f. The spin determines the statistical factor g of the resonance.

To determine the resonance parameters different types of experiments can be performed: transmission, elastic scattering and capture measurements [Frohner 66]. To extract the resonance parameters from experimental data it is very important to understand the relation between the experimental observable and the resonance parameters and to identified a combination of complementary measurements that should be performed to determine the resonance parameters. In practice several difficulties arise in order to obtain the experimental observable. One must do corrections for the Doppler broadening, which effects the self shielding term, for the detector resolution and multiple scattering corrections for the partial cross sections measurements.

In conclusion, the R-Matrix analysis is used to set out the resonance parameters from a measured resonance and to adjust them function of Doppler coefficient and energy resolution of the detector.

Chapter 3

Review of nuclear data on ^{233}U

High accuracy fission and capture cross section data of ^{233}U are very important for the design and development of new systems for energy production and nuclear waste transmutation, based on the lighter $^{232}Th/^{233}U$ fuel cycle. For this isotope, the existing data are scarce or present discrepancies are too large to meet the current requests.

In this chapter the assessment of the available evaluated and experimental neutron-induced cross-sections of ^{233}U will be presented. The discussion will focus on the capture and fission cross sections of ^{233}U in the Resolved Resonance Region (RRR).

3.1 General overview

Most of the previous neutron cross-section measurements of ^{233}U in the thermal region and the RRR were performed before 1975. In the 1930s and 1940s, cross-section measurements where performed using neutrons from accelerators and early reactors. Activation measurements with and without Cd using devices such as the pile oscillators [1] provided thermal-spectrum-averaged cross sections [Kukavadse 55]. Neutron choppers [2] using the time-of-flight (TOF) method (see Section 4.2) provided sufficient energy resolution to measure resonance energy cross sections up to 100 eV [Moore 60]. After the 1950s, monoenergetic neutron beams were produced by nuclear reactions with positive

1. The pile oscillator is an instrument which causes periodic variations of the neutron intensity in a pile. A realization of the pile oscillator is for instance an absorbing material that moves back and forth in a field of thermal neutrons such as that existing in a chain reactor. In the vicinity of the absorber there is a depression in the neutron flux and the motion of this depression past a nearby ion chamber produces an oscillating signal whose amplitude is proportional to the total neutron-absorption cross-section of the sample. The instrument constitutes a means of determining unknown neutron-absorption cross-sections by making comparisons with samples for which accurate direct measurements have been made.

2. A device that interrupts the output beam of neutrons from a nuclear reactor mechanically, to provide bursts or pulses of neutrons for research purposes.

ion accelerators that made possible to obtain cross sections within the keV to MeV energy range. Pulsed accelerators for electrons and protons were used to produce intense bursts of neutrons, which considerably enhanced the number of the TOF measurements [Brooks 66, Weston 68]. Since the 1970s, cross sections have been mainly obtained by the pulsed-accelerator TOF method [Blons 73, Guber 00]. Recently, the pulsed spallation source at CERN has been used for TOF cross-section measurements where its intense neutron pulses is suited for both high energy-resolution and high neutron-intensity measurements [Berthoumieux 07, Calviani 09].

Despite all the measurements done so far, the uncertainties of the available data in different energy ranges are still bigger than what is needed for design calculations of nuclear facilities based on the $^{232}Th/^{233}U$ fuel cycle and the nuclear criticality safety analysis of fuel storage. With the renewed interest in new power reactors, for which these requirements are essential, the activity on neutron cross-section measurements of ^{233}U will continue to rise.

3.2 Fission cross-section data

The fission cross section of ^{233}U has been widely measured in different laboratories. One common feature of these measurements is that they were done using different normalization methods: relative to the standard $^{235}U(n, f)$ cross section [Carlson 09], normalized to thermal cross-section of ^{233}U or normalized via other indirect methods (see for example table IV of Deruyter and Wagemans [Deruyter 74]). The normalization method is a critical issue in most of experiments because often, the reference samples are not measured simultaneously and different energy ranges are measured at different time intervals with different experimental arrangements.

Large discrepancies among experimental data, sometimes bigger than 50% in some energy ranges [Deruyter 74], show that these data could not be used to improve the description of the cross-section parameters in the RRR, important for an accurate estimation of the self-shielding effects in reactor simulations [Guimaraes 00].

3.2.1 Evaluated fission cross-section data

Even though the ENDF group [Group 09] (see Section 1.6) is using basically the same experimental data sets, the evaluated data of standard libraries are sometimes different, depending on how the evaluation has been done. To predict a complete set of evaluated cross-sections, some calculations require knowledge of the cross-section values derived from different experiments for which, sometimes, no data exist. Thus, the result on the evaluation depends strongly on the decisions adopted by the evaluator.

An important difference between evaluated libraries is the upper limit of the RRR, the region where the resonances are still clearly identified. In particular, while in the American ENDF/B-VII.1 [Chadwick 11] and the Japanese JENDL-4.0 [Shibata 11] evaluated databases the RRR reaches up to 600 eV, the European JEFF-3.1 and the previous Japanese JENDL-3.3 have a limit at 150 eV. In the case of the previous ENDF/B-VI library, this limit is even lower, at 60 eV.

In the most recent evaluation for ^{233}U in the RRR included in ENDF/B-VII.1 (from thermal to 600 eV [Leal 01]), the most relevant measurement that is used as the primary data was the one performed at Oak Ridge Electron Linear Accelerator Pulsed Source (ORELA) [Guber 00]. This evaluation brought a large improvement compared to the previous evaluations by extending the energy range up to 600 eV and allowing accurate calculation of the cross-section. For the most recent evaluation in JENDL-4.0 [Iwamoto 09], the resolved resonance-parameters evaluation was taken from Leal. This is the reason why there are no significant differences between these two evaluations. A comparison between the evaluated fission cross-section of ^{233}U around the RRR can be seen in Figure 3.1.

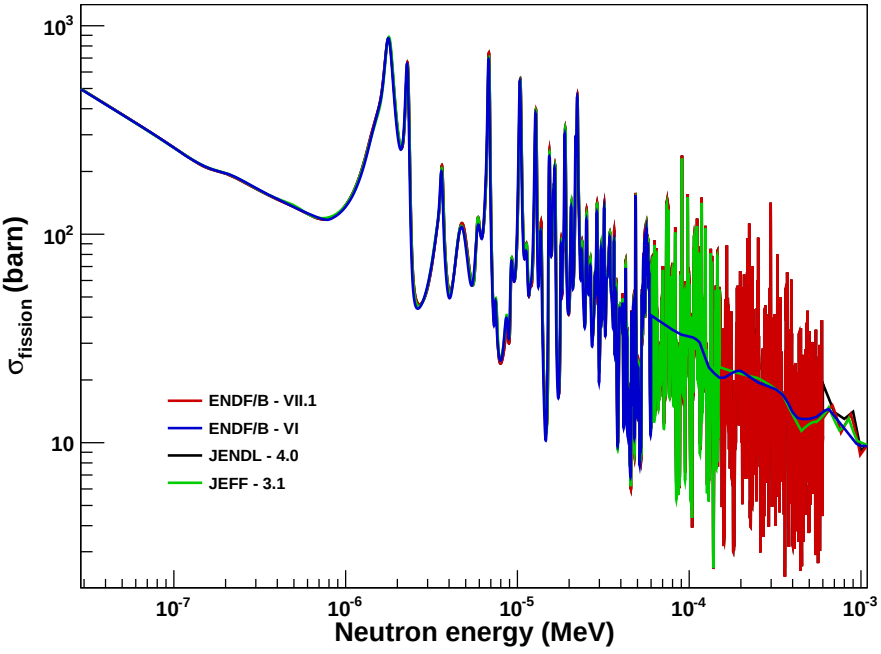

Figure 3.1: Overview of the ^{233}U fission cross-section from different evaluated libraries.

For an accurate calculation of self-shielding factors it is important to reproduce the exact shape of the experimental cross-section, especially for those which show strong

fluctuations. Therefore accurate resonance parameters are needed in the RRR for the determination of these factors. However, the available experimental information is at present insufficient and, as it will be shown in the following sections, strong discrepancies still exist among evaluated nuclear data.

3.2.2 Experimental fission cross-section data

Several sets of experimental data of ^{233}U fission cross-section are available in the RRR, but only few can be used to obtain the parameters needed for the resonance analysis. The evaluations relied only on the experiments with good energy resolution and with reduced errors, also considered as benchmark experiments. Therefore, the selected experimental data used as example in this work are the ones employed by evaluators as well as the most high-quality recent ones, not included in the evaluations yet. Also, these data were obtained using the TOF technique with a pulsed neutron source, in a large neutron energy range, with completely different experimental set-up conditions and at different neutron facilities.

3.2.2.1 Weston experiment performed in 1968

One important set of data were obtained in 1968 by Weston et al. [Weston 68] at the electron linear accelerator of the Rensselaer Polytechnic Institute (RPI) which included simultaneous measurement of the capture and fission cross-section of ^{233}U. The measuring station was located at a distance of $25.24\,m$ from the moderator. Different beam filters were used along the neutron drift tube to absorb or scatter neutrons which corresponded to certain resonance energies (e.g. Cd or ^{10}B for the neutrons below $\sim 0.4\,eV$). The experimental set-up was made of a large liquid-scintillator tank that detected both capture and fission events in the ^{233}U via their associated prompt $\gamma - rays$ and an ionisation chamber (IC) to detect the fission fragments. The IC consisted of 21 Al plates of $12.7\,\mu m - thick$ coated on both sides with $0.5\,mg/cm^2$ of ^{233}U to a diameter of $7.35\,cm$. The chamber was positioned in the center of the scintillator. The tank scintillator was approximately a sphere of $1.25\,m$ in diameter filled with xylene solution to which $\sim 6\%$ by volume of trimethyl borate has been added to reduce the $\gamma - ray$ background caused by neutrons scattered into the liquid. Also to minimize the effect of slow neutrons scattered toward the IC from the scintillator, the beam traversed the tank in a tube lined with $2\,cm$ thick Li^6H. The schematic view of the experimental set-up is presented in Figure 3.2. The relative flux through the IC was measured by a parallel-plate BF_3 chamber, placed $1\,m$ in front of the scintillation tank.

The $^{233}U(n,f)$ cross-section was determined from $0.4\,eV$ to $2\,keV$ neutron energy. Because the efficiency of the scintillator to detect capture and fission events and the efficiency of the IC for the fission events were not determined with sufficient accuracy,

these parameters were derived from a normalization of the data by using the total cross-section of Pattenden and Harvey [Pattenden 63] with an accuracy of $\sim 2-3\%$.

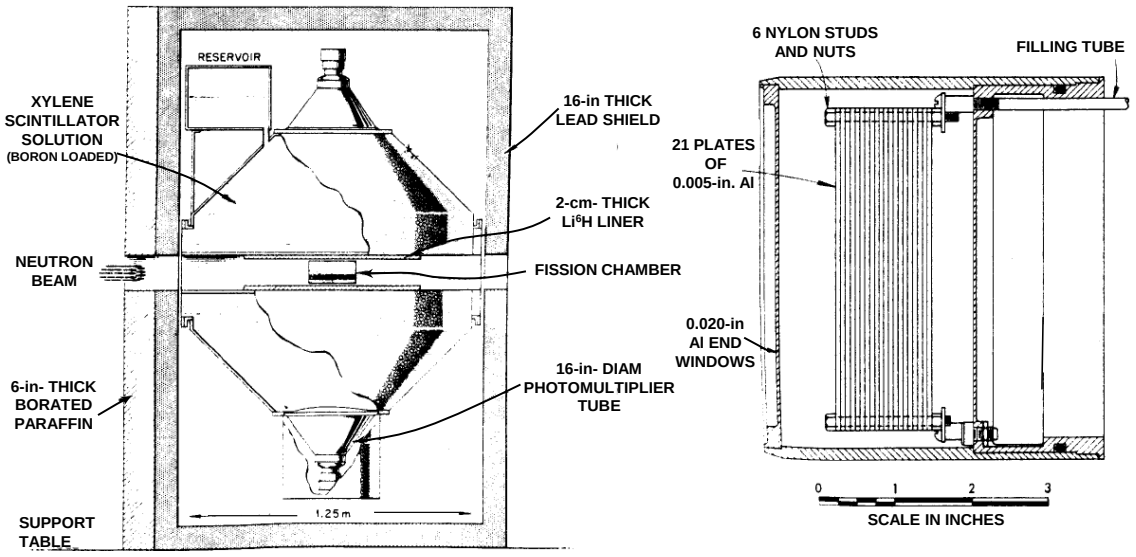

Figure 3.2: Schematic view of the experimental set-up, liquid-scintillator tank and fission chamber. Detail of the ^{233}U fission ionisation chamber on the right [Weston 68].

3.2.2.2 Wagemans experiment done in 1988

Another relevant measurement of the fission cross-section of ^{233}U was performed in 1988 at GELINA accelerator at the $8.2\,m$ flight path by Wagemans et al. [Wagemans 88]. An evaporated layer of $25\,\mu g$ of $^{6}LiF/cm^2$ used for the neutron flux determination, and the ^{233}U target were mounted back to back in the center of a vacuum chamber of $50\,cm$ in diameter. The ^{233}U sample was evaporated homogeneously with a thickness of only $40\,\mu g/cm^2$, chosen in such way to minimize the self-absorption effects. The $^{6}Li(n,\alpha)t$ particles and the fission fragments were detected in a compact geometry with two $20\,cm^2$ large gold-silicon surface-barrier detectors positioned in parallel and placed outside the neutron beam. The experimental arrangement and collimation of the flight path are shown in Figure 3.3.

The data for the fission cross section of ^{233}U were obtained only in one measurement from thermal to $20\,eV$ energy range. A normalisation was done in the thermal region relative to the thermal fission cross-section value proposed by the ENDF/B-VI evaluated library, i.e. 531.14 $\pm$ 0.25% barn. The results were in a very good agreement with the

previous data of Deruyter et al. [Deruyter 74] obtained also at GELINA in 1974, using the same method and experimental area.

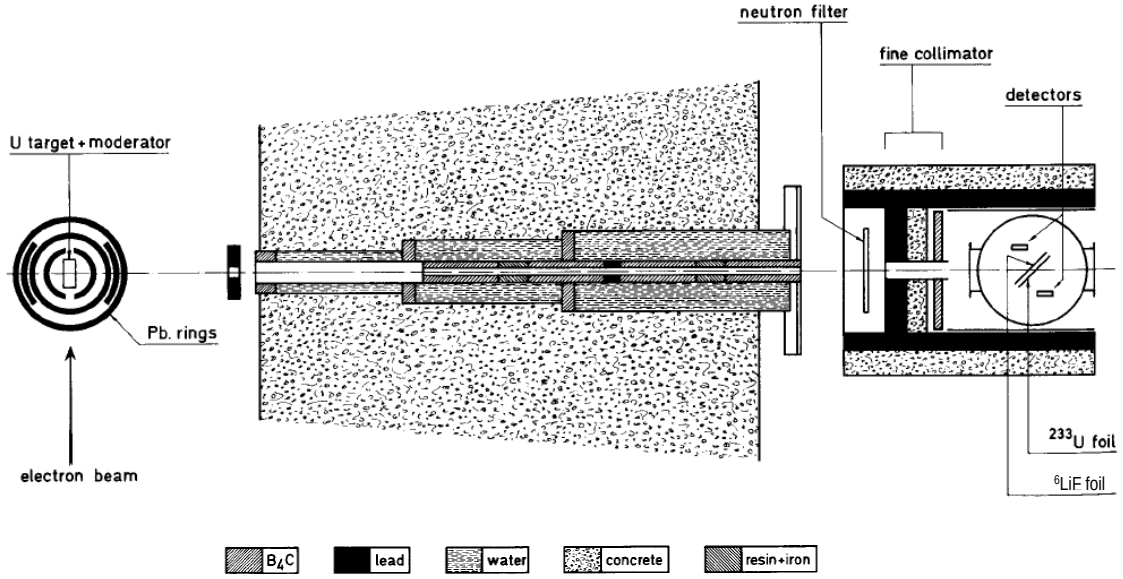

Figure 3.3: Experimental set-up and the collimation arrangement at GELINA from 1988 [Wagemans 88].

3.2.2.3 Guber experiments accomplished in 1999 and 2000

Because most of the older data showed large discrepancies due to poor experimental energy resolution, and thus did not cover the neutron-energy range important for the nuclear criticality and design calculations, two measurements were performed by Guber et al. [Guber 00][Guber 01] at the Oak Ridge Electron Linear Accelerator (ORELA) in 1999 and 2000: fission cross-section measurements and neutron transmission measurements [3] of ^{233}U at the flight path of $80\,m$ with an experimental energy resolution much better than any of the previous measurements.

The fission cross-section was determined over the $0.4\,eV - 700\,keV$ energy range using an IC centered at $81.237\,m$ from the neutron source. For the neutron flux determination, a ^{6}Li-loaded glass scintillation detector was mounted in the neutron beam at $1.423\,m$ in front of the IC. The IC used in the experiment was similar to that used by Weston [Weston 68] (see left of the Figure 3.2) but with twice the amount of fissile material.

3. Transmission measurements are the simplest and also the most accurate type of cross-section measurements [Schillebeeckx 12b]. Also no correction for detector efficiency is required, no data normalization is needed but only good transmission geometry is requested (good collimation that all detected neutrons must cross the sample and all neutrons scattered by the sample should not reach the detector).

The IC contained a total of 2.11 g of uranium with an isotopic composition of 99.997 % of ^{233}U. The samples where prepared as U_3O_8 layers with a diameter 7.6 cm, coated on Al plates of 12.7 $\mu m - thick$. Nineteen Al plates were coated on both sides and two end plates on one side only. In this arrangement, the ^{233}U sample thickness was of 0.000120 $atoms/b$. The plates were connected electrically to form ten identical fission chambers. Two separate runs were made, first one for the low energy range by using a cadmium filter in the beam to absorb the neutrons below 0.4 eV and the second one which covered the neutron energy range from 10 $eV - 700\,keV$ by using a ^{10}B filter in the beam.

Since the measurement of Guber [Guber 00] was not an absolute measurement, the data have been normalized to the results from Deruytter and Wagemans [Deruyter 74], following their suggestion to integrate the cross section in the 8.1 $eV - 17.6\,eV$ neutron-energy range. The proposed value was revised in 1988 by Wagemans to 965.2 $b \cdot eV$ [Wagemans 88], which is the value used by Guber.

For the transmission measurement of ^{233}U high-purity metallic samples with an enrichment of 99.76% were used. The samples were mounted in a cryogenic device at 9 m from the neutron source and cooled down to 11 K. Cooling to this low temperature reduced the Doppler broadening of individual resonances and improved the separation of resonances significantly. The results of this two measurements allowed the extension of the resonance analysis up to 600 eV while the URR covers the energy range [600 $eV - 40\,keV$] [Leal 01] (see Figure 3.1).

3.2.2.4 Calviani experiment carried out in 2009

The most recent data of the ^{233}U fission cross-section were obtained in 2009 by Calviani et al. [Calviani 09] at the innovative facility n_TOF at the European Organization for Nuclear Research (CERN) [Abbondanno 02], but they have not been used in the evaluations yet. The main characteristic of the n_TOF neutron beam is the high instantaneous neutron flux ($10^5 n/cm^2/pulse$ at 200 m), which leads to a large reduction of the background related to the natural radioactivity of the sample, and the low background achieved with the massive concrete and iron shielding walls placed along the flight path. The experimental area was located at a distance of 185 m from the target. The fission detector was a Fast Ionisation Chamber (FIC) [Calviani 08] that consists of three ionisation chambers. Each chamber consists of three electrods, one 100 $\mu m - thick$ Al cathode placed between two 15 $\mu m - thick$ Al anode foils at 5 mm distance from the cathod. The cathode was plated on both sides with the sample material. The samples were prepared as U_3O_8 layers by means of painting technique [Drapchinsky 99]. The diameter of the sample deposit was 8 cm, identical to the aperture of the neutron beam. The detector was operated with a gas mixture of 90% Ar and 10% CF_4 at 720 $mbar$-pressure. Four ^{233}U samples of different thicknesses ($3.83\,10^{-7} atoms/b$, $3.85\,10^{-7} atoms/b$ $4.04\,10^{-7} atoms/b$

and $4.13\,10^{-7} atoms/b$), and two ^{235}U samples ($7.75\,10^{-7} atoms/b$, $8.45\,10^{-7} atoms/b$) were used in the measurement. Figure 3.4 shows two pictures of the FIC chamber and its schematic representation. To discriminate fission fragments from the high α background of the ^{233}U sample, a threshold in a pulse-height spectra was used. The background related to the scattered neutrons was found to be negligible. The $^{233}U(n,f)$ cross-section was determined from thermal neutron energy to $1\,MeV$. Also, the data were not normalized to any previous $^{233}U(n,f)$ results, but to the standard $^{235}U(n,f)$ cross-section measured in the same experiment. The value of 534.8 ± 0.2 barns for fission cross section at thermal energy was found in agreement within 1% with the ENDF/B-VII.1 value of 530.70 barns. In the RRR the agreement with ENDF/B-VII.1 is the best compared to other measurements. Important advantages of these data are the accuracy of the cross-section with systematic uncertainties of 3.3% in the RRR, the wide energy range covered and the high energy resolution which can contribute significantly to the analysis of the fission cross-section of ^{233}U above the current limits in the evaluated data library.

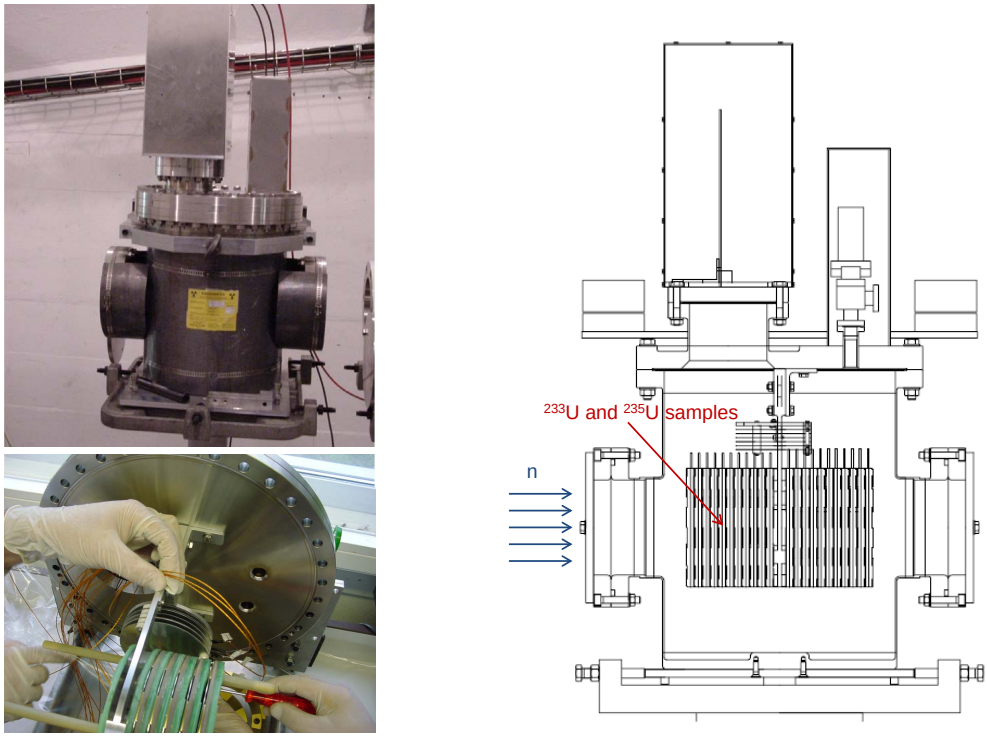

Figure 3.4: FIC chamber which contains the ^{233}U and ^{235}U samples (upper left panel) and a picture of the inside of FIC during assembly (bottom left panel). Schematic view of the FIC on the right [Calviani 08].

3.2.2.5 Comparison between experimental and evaluated data

Figure 3.5 shows a comparison between the fission cross-sections of ^{233}U obtained in the experiments presented above together with the latest ENDF/B-VII.1 and JEFF-3.1 evaluated libraries in the RRR. One can see rather good agreement in shape between the experimental data and the evaluations. Looking into detail, sizable discrepancies in terms of resonance amplitude and energy can be noticed. This effect can be better observed for selected resonances like the ones illustrated in Figures 3.6 and 3.7 in two different energy regions. For the first two resonances of $^{233}U(n,f)$ cross-section, in the eV region, the most recent cross-section data from Calviani [Calviani 09] are 10% higher than the previous ones obtained by Guber [Guber 00], shifted to the right from Weston [Weston 68] and to the left from Wagemans, while a good agreement can be observed with the evaluated libraries, in particular with JEFF-3.1. On the contrary, Calviani's data confirm the results of Guber around $90\,eV$, with a small difference noticed only for the resonance energy. A striking agreement is observed in this energy region with the ENDF/B-VII.1 database, while discrepancies with Weston data are clearly noticed.

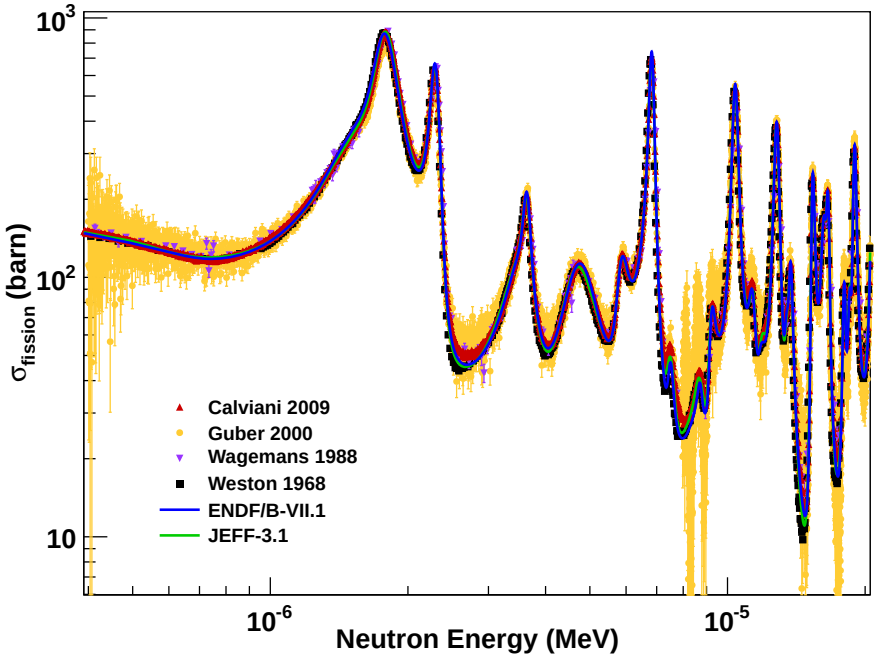

Figure 3.5: Evaluated ENDF/B-VII.1 and JEFF-3.1 $^{233}U(n,f)$ cross-section in the RRR compared with four experimental data [Calviani 09, Guber 01, Wagemans 88, Weston 68] obtained by different methods and experimental set-up conditions, at different neutron facilities.

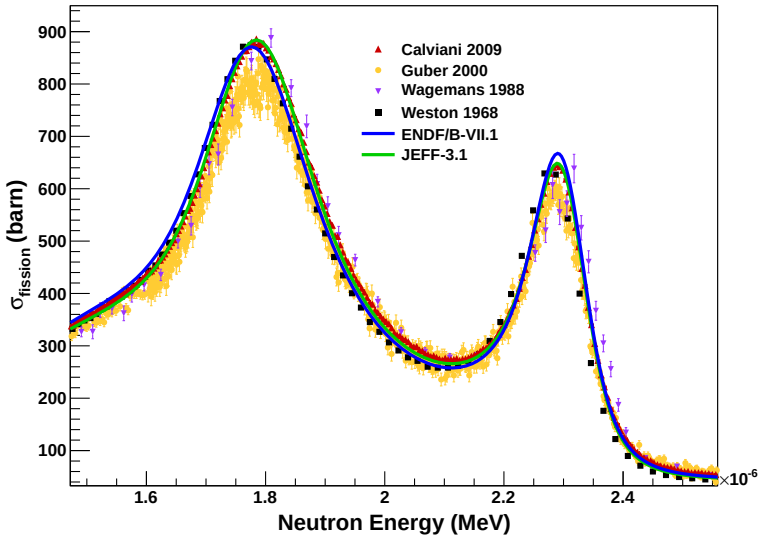

Figure 3.6: The first two resonances in the $^{233}U(n, f)$ cross-section. Comparison between different experimental data from EXFOR and evaluated data from ENDF/B-VII.1 and JEFF-3.1. The lower cross-section value in Guber's data is most probably due to self-shielding effects, not corrected in that experiment.

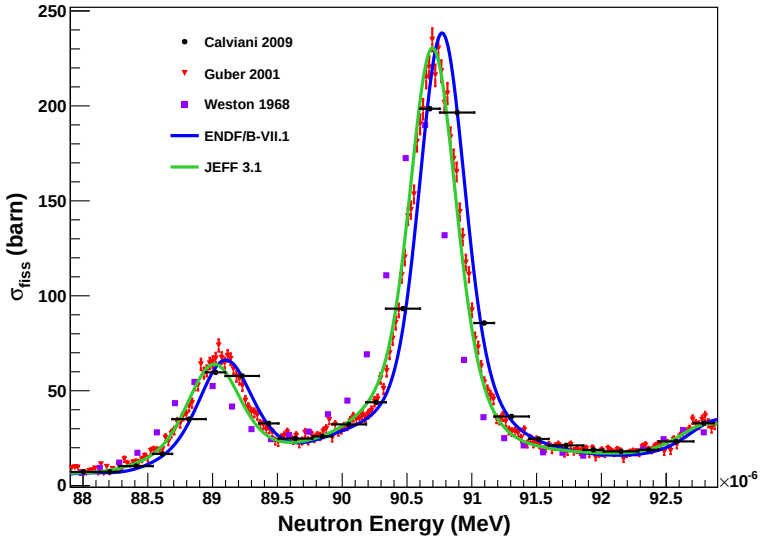

Figure 3.7: Comparison for selected resonances in the $^{233}U(n, f)$ cross-section around $90\,eV$. Large discrepancies between experimental data and between evaluations are observed in this case.

One important feature of Calviani's data is that they have been obtained with a high neutron energy resolution at the n_TOF facility that enabled to extend the limit of the resonance region. Compared with other results, the only previous measurement that shows a comparable resolution are Guber's data. This is evident in Figure 3.8 where the data, especially those obtained by Calviani and Guber, show well resolved resonance structures above $600\,eV$, whereas in Weston measurement, these resonances are reported as few broad peaks in TOF spectrum. Merging these data will allow to achieve more accurate determination of the resonance parameters and probably to extend the resonance region beyond the present limit, leading to more accurate calculation of self-shielding effects in reactors based on the $^{232}Th\ /^{233}U$ fuel cycle.

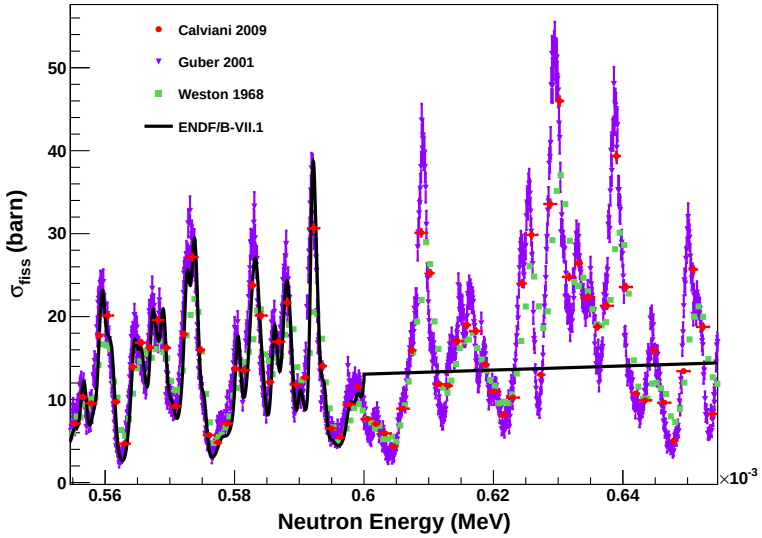

Figure 3.8: Comparison between experimental data that show resonance structures above the current limit of the RRR in the ENDF/B-VII.1 for the $^{233}U(n,f)$ cross-section. The good TOF resolution of Calviani and Guber experiments improves the description of the data.

3.3 Capture cross-section data

Measurements of neutron-induced capture cross-section of ^{233}U is very complicated due to the $\gamma - rays$ originating from neutron induced fission. Typically, FF detectors are employed to identify the neutron-induced fission reaction and remove it from the analysis of capture data. This requires that actinides samples to be thin enough to achieve a high FF detection efficiency. On the other hand, the thin sample compromises the counting statistics of the measurements. As a result, the residual spectrum remains

contaminated with both prompt fission $\gamma-rays$ and delayed $\gamma-rays$ that follow $\beta-decay$ of fission products. In addition, the neutron scattering background and the background associated with the neutron beam facilities need to be subtracted. This removal of several background components results in large uncertainties and, if not performed accurately, in the end leads to systematic errors. Therefore, the few existing capture cross-section measurements are mainly old and may be subject to these errors. For the thermal-energy range there are more data available (see for example data from M. J.Cabell [Cabell 71]) than for the RRR and in the fast region (the only data in the RRR are from F. D. Brooks [Brooks 66], L. W. Weston [Weston 68] and E. Berthoumieux [Berthoumieux 07]) and from J. C. Hopkins [Hopkins 62] in the fast region), all indexed in EXFOR [McLane 05].

3.3.1 Evaluated capture cross-section data

The data used in the latest evaluation for the capture cross-section of ^{233}U are mainly from the measurement performed by Guber [Guber 00, Guber 01]. Even though Guber's measurement was done only for fission and transmission data, the capture cross section was deduced. Also, since the last simultaneous measurement of capture and fission cross-sections has been recently performed (see Section 3.3.2.3), it was therefore not included in the last evaluation done for the $^{233}U(n,\gamma)$ cross-section by Leal in 2001 [Leal 01]. A comparison between the capture cross-section of ^{233}U from different database libraries in the vicinity of the RRR is shown in Figure 3.9. One can notice bigger discrepancies among evaluations than for the fission cross-section of ^{233}U (see Figure 3.1). This effect is due to the lack and/or the discrepancies between the experimental data of capture cross section of ^{233}U in this energy region.

3.3.2 Experimental capture cross-section data

Up to now there are only three measurements in the RRR for the neutron capture cross-section of ^{233}U. All these measurements were performed simultaneously with the fission cross-section, in the same neutron flux, and thus have the same energy resolution. The main differences between them are the neutron-energy resolution and the limitation of the neutron energy regions.

3.3.2.1 Brooks experiment done in 1966

The first significant measurement of the capture cross section of ^{233}U was performed in 1966 by Brooks et al. [Brooks 66] at the Harwell Linear accelerator up to $10\,eV$ with a poor energy resolution. There are no details on the sample configuration except that there were metal discs of several thicknesses and the data were given for various flight paths and timing channel widths. Therefore these data will not be considered in the following.

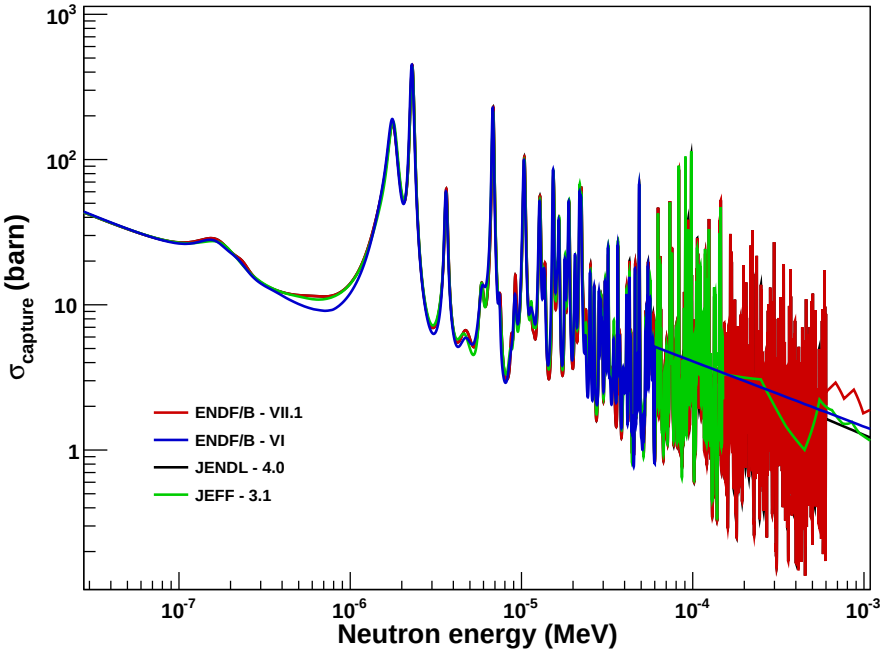

Figure 3.9: Comparison between evaluated capture cross-section of ^{233}U from different libraries.

3.3.2.2 Weston experiment performed in 1968

The next measurement was done in 1968 by Weston et al. [Weston 68] and details of the experimental set-up and samples characteristics were presented in Section 3.2. Let us recall that Weston measurement was performed with two detector types: liquid scintillator tank detector to measure the prompt $\gamma - rays$ produced in capture reactions, and IC to detect fission fragments produced in fission reactions (see Figure 3.2). To discriminate between $\gamma - rays$ associated with fission and $\gamma - rays$ produced in capture reactions the VETO method was used: the $\gamma - rays$ detected in coincidence with the FF correspond to a fission event, and the capture event is identify by putting a VETO on FF. A similar technique is being developed at Los Alamos Neutron Science Center (LANSCE) using Detector for Advanced Neutron Capture Experiments (DANCE) [Bredeweg 07], but there are no reported data on ^{233}U so far. This technique is also used in our work and will be described in detail later. The statistical accuracy of the capture data was poor compared with the fission data. Also, different evaluators concluded that the capture cross section was too small between the resonances due to a possible overestimation of the background correction made by Weston. Nevertheless, accurate fit of the data were possible in the energy range below $30\,eV$. Above this energy, the data were still considered by evaluators because of the presence of strong narrow resonances

with enough statistical accuracy at the peaks.

3.3.2.3 Berthoumieux experiment carried out in 2007

The most recent measurement was performed in 2007 at the n_TOF facility by Berthoumieux et al. [Berthoumieux 07] at CERN using a recently constructed Total Absorption Calorimeter (TAC) [Guerrero 09]. The TAC has a high detection efficiency for capture events of nearly 100% and is based on 40 BaF_2 crystals shaped as hexagonal and pentagonal pyramids which form a spherical shell with 10 cm inner radius and 15 cm thickness. Although the BaF_2 features a small neutron sensitivity, each crystal was covered by a teflon light reflector layer, an aluminium foil and a final cover with ^{10}B loaded carbon fiber capsule to reduce this source of background. The sample used in this measurement consisted of 108 mg of U_3U_8, which corresponds to 91 mg of ^{233}U, placed in the center of the TAC and surrounded by neutron absorber made of $C_{12}H_{20}O_4(^6Li)_2$. The ^{233}U mass was deposited on an aluminum backing and encapsulated with titanium. The sample assembly of 1 cm in diameter can be seen is Figure 3.10 together with the sample holder made of a kapton foil used to center the sample inside the TAC to avoid the interaction of the neutron beam with structural materials. The measurements were performed at the 185 m flight path. The $^{233}U(n,\gamma)$ cross-section was determined from 0.7 eV to 20 eV neutron energy.

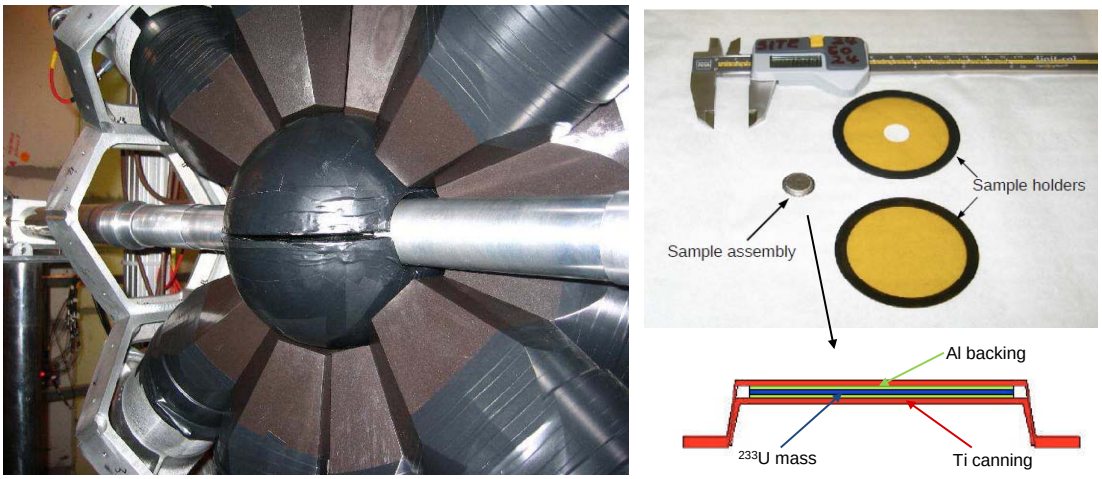

Figure 3.10: Layout of the experimental set-up at n_TOF/CERN. View of one of the TAC half hemispheres with the neutron absorber in the center, the ^{10}B loaded carbon fiber capsules and the neutron beam line [Berthoumieux 07]. The sample assembly and holders layout is shown on the right.

The method used was the shape analysis of the TAC energy response which provides the information for reconstructing the $\gamma - cascades$ from neutron-induced capture and

fission events properly. Using the capture and fission cross-sections of ^{233}U data from ENDF/B-VII.1 evaluation Berthoumieux selected a resonance in fission which is not present in capture around $4.5\,eV$. The fission-only response was obtained by subtracting the TAC energy response in the vicinity of this resonance. By selecting another resonance present in both capture and fission cross-sections, like the one around $6.8\,eV$, and applying the same principle, the capture and fission spectrum can be extracted. Considering that the signal above $8\,MeV$ can only be attributed to fission ($S_n = 6.845\,MeV$ for ^{233}U) and subtracting the previously obtained fission response, the TAC response to capture-only was obtained. The next step was the efficiency determination for the capture events that consisted in a simulation of the TAC with GEANT4 toolkit [Agostinelli 03] including $\gamma - ray$ cascade generation model [TAIN 02]. For fission events the TAC efficiency was not determined but was considered to be 100%.

Preliminary results were published [Berthoumieux 07] and indexed in EXFOR data base. Due to the background from fission $\gamma - rays$ the accuracy was limited to only 10%. Such an accuracy is remarkable with respect to previous measurements, but still not sufficient, taking into account the nuclear data requirements in the field of nuclear technologies [NEA 08, Plompen 08]. Also, they concluded that the capture cross section data of Weston are overestimated by up to 20% in the RRR region. New data analysis has been recently performed using the calorimetric shape decomposition method [4] which lead to data with improved accuracy and an extended energy range up to $1\,keV$ [Carrapico 12a, Carrapico 12b], but are not yet indexed in EXFOR.

3.3.2.4 Comparison between experimental and evaluated data

A comparison between the selected set of data on the capture cross-section of ^{233}U coming from the experiments described above and evaluated libraries is shown in Figure 3.11. The experimental data are in good agreement in shape, except for the first resonance where Berthoumieux contribution is $\sim 10\%$ lower than Weston, as illustrated in Figure 3.12. Also, in the low energy region Berthoumieux resonances show a deeper fall-off that could be attributed to the better resolution of the n_TOF facility compared to the RPI facility according to [Berthoumieux 07].

In the same time, the ENDF/B-VI evaluated data are in a good agreement with Weston data, while Berthoumieux data are in a better agreement with the most recent evaluations ENDF/B-VII.1. These agreements may be easily explained since ENDF/B-VI evaluation was done using Weston experimental data and Berthoumieux data were

4. The contributions of the different reactions are discriminated solely by the TAC energy response, the shape of the total energy distribution in the TAC, to which capture and fission events contribute linearly and independent from each other. It only requires to know the open channels and the respective energy deposition spectra since they describe the specific physics of each reaction. Even if the mean energy deposition for capture and fission are similar, the shape of both spectra are different.

obtained by normalisation to ENDF/B-VII.1 (see Section 3.3.2.3). This can be better observed for selected resonances in two different energy regions shown in Figures 3.12 and 3.13. The accuracy of the energy points of TOF spectrum depends mainly on the accuracy of the length of the flight path and of the detector time resolution [Schillebeeckx 12b]. Therefore, the resonances could be slightly shifted when comparing independent experiments. This may be the reason why Weston capture data are slightly shifted to the right in comparison with Berthoumieux data.

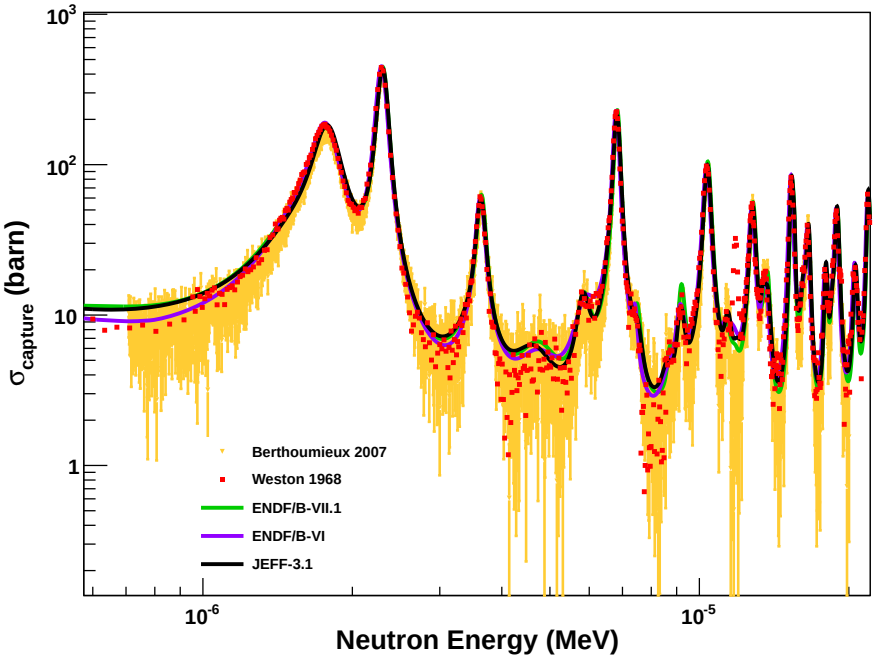

Figure 3.11: Comparison between the only existing experimental data of neutron capture cross-section of ^{233}U [Berthoumieux 07, Weston 68] and the evaluation of nuclear data libraries ENDF/B-VII.1, ENDF/B-VI and JEFF-3.1 in the energy range from $0.6eV$ to $20eV$.

Looking at Figure 3.13, a resonance can be seen in Weston data around $11.8\,eV$ but not in Berthoumieux data and neither reported in the evaluations. Even though the data of Weston were the only capture data of ^{233}U existed at the moment of the last evaluation, ENDF/B-VII.1 does not show any evidence that this resonance may be one of the $^{233}U(n,\gamma)$ cross-section. The origin of this resonance is not clear, but it can be related to a contamination of the sample.

Compared to the fission cross-section of ^{233}U where experimental data exist above the current limit of the RRR in the ENDF/B-VII.1, for the capture cross-section of ^{233}U,

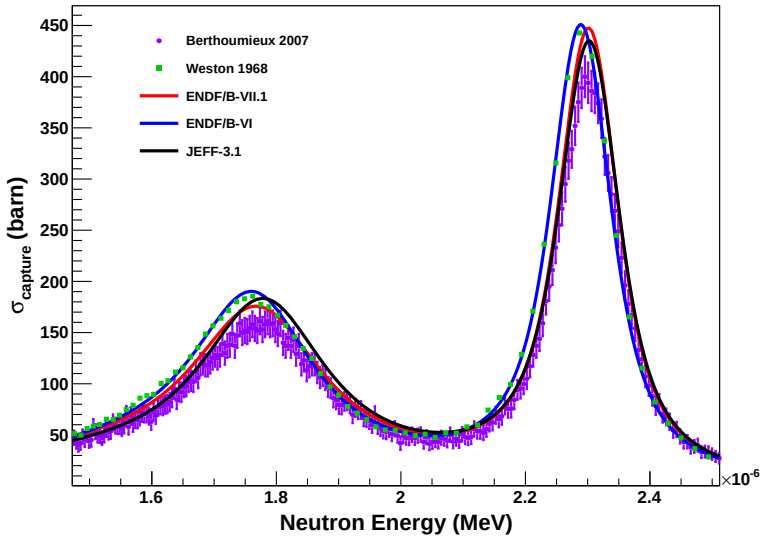

Figure 3.12: The first two resonances in the $^{233}U(n,\gamma)$ cross-section. Comparison between experimental data [Berthoumieux 07, Weston 68] and evaluated data ENDF/B-VII.1, ENDF/B-VI and JEFF-3.1.

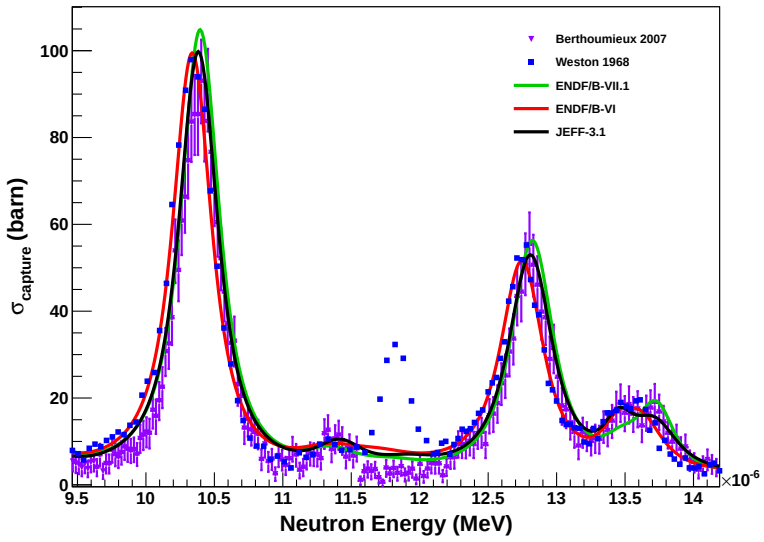

Figure 3.13: Comparison for selected resonances in the $^{233}U(n,\gamma)$ cross-section around $11.8eV$. Large discrepancies between experimental and evaluated data are noticed in this case. A resonance is also seen in Weston data, but not in the most recent data obtained by Berthoumiex and neither in the evaluations.

only Weston data can be exploited so far. This can be noticed in Figure 3.14 where the data show resonance structures above $600eV$, but not as well resolved as for fission (see Figure 3.8).

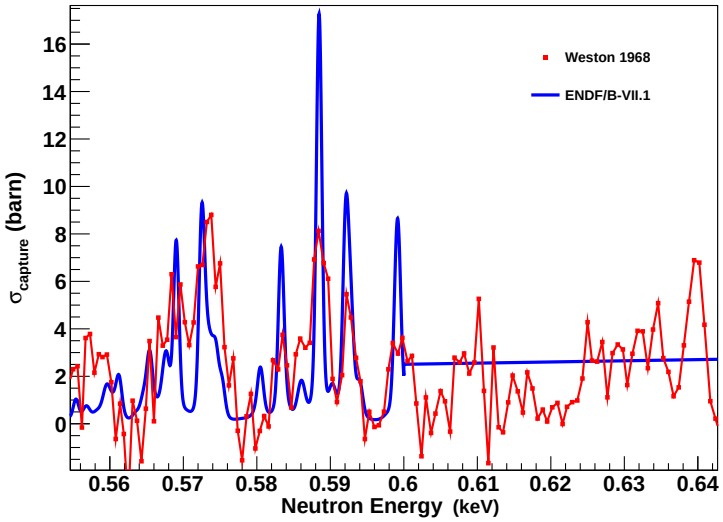

Figure 3.14: Comparison between experimental data that shows resonance structures above the current limit of the RRR in the ENDF/B-VII.1 for the $^{233}U(n,\gamma)$ cross-section.

3.4 Alpha ratio of ^{233}U

In practice, the procedure to determine the α ratio can be a very difficult task. Capture cross-section measurements for fissile nuclei such as ^{233}U are considerably more complicated than fission ones. As already mentioned, capture cross-section measurements rely on detection of the emitted $\gamma - rays$ which in this case include the $\gamma - rays$ emitted by the de-excitation of the fission fragments. Therefore, it is necessary to separate the two contributions. Further, the natural activity contribute with a significant $\alpha - pile - up$ which complicates measurements with fission anti-coincidence arrangement. That is why only two benchmark experimental data exist for the capture cross-section of ^{233}U carried out at an interval of almost 40 years.

The neutron fission and capture cross-sections of ^{233}U are of critical importance in the design of breeder reactors using $^{232}Th/^{233}U$ fuel cycle. Since the breeding ratio (the average number of fissile atoms created per fission event) in such reactors is not large, close to 1, it is of great economic importance to know the fraction of the neutrons produced by fission that are lost to capture in ^{233}U.

Let us recall equation 3.1 that gives the number of neutrons used for breeding, N_a, called available neutrons:

$$N_a = \nu - 2 * (1 + \alpha) - losses \tag{3.1}$$

where ν is the average number of neutrons produced per fission of ^{233}U and α is the fission to capture cross-section ratio of ^{233}U.

Examples of the N_a values for the two different cycles for thermal and fast neutrons are given in Section 1.5.2, see Table 1.3.

α parameter is not determined only by a simple ratio between capture and fission data, it involves an adjustment of data and a calculation of the associated uncertainties. An example of the α ratio determination is presented in the following using the results obtained in experiments presented in the previous sections 3.2 and 3.3. An overview of differences between experimental data and evaluations in the RRR for the α ratio of ^{233}U is shown in Figure 3.15. While at low energy, below $3eV$ the average difference between experimental cross-section is within 10% (see Figure 3.16), a much smaller discrepancy of up to 3% in average exists in the region between $3eV$ and $20eV$ (see Figure 3.17). The same behaviour can be observed for the evaluated data. As already pointed out, the unknown resonance present only in Weston capture cross-section data has to be well interpreted not to lead to miscalculations of the α ratio illustrated in Figure 3.17.

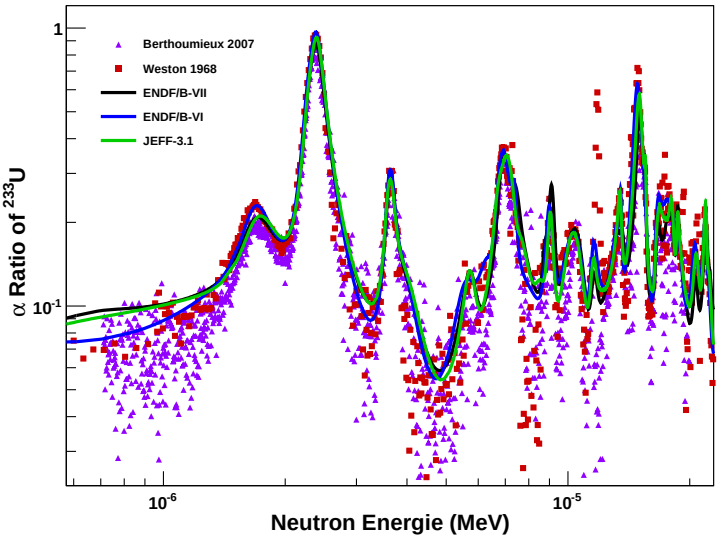

Figure 3.15: Comparison between the experimental and the evaluated α ratio of ^{233}U in the RRR.

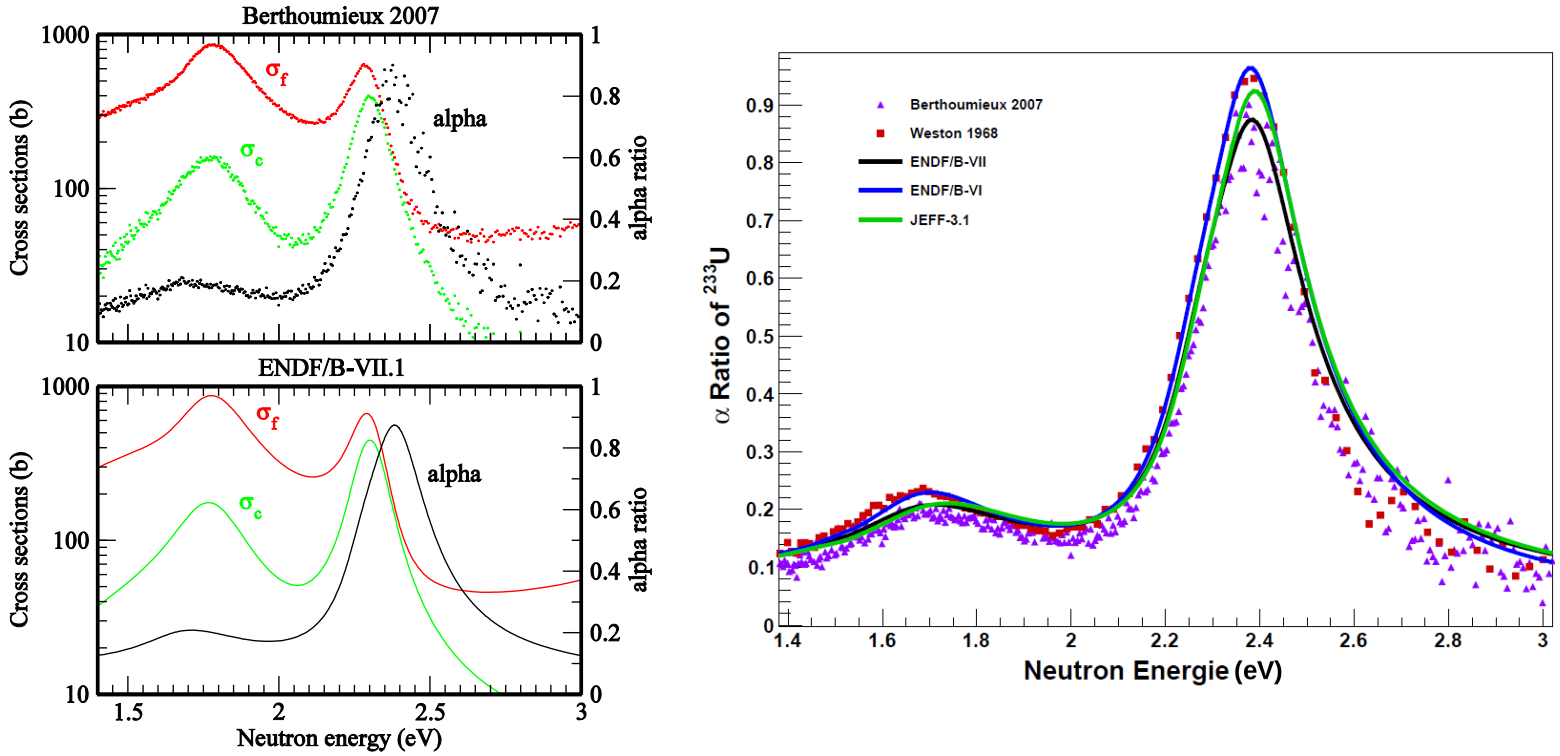

Figure 3.16: On the left it is shown the $^{233}U(n,f)$ and $^{233}U(n,\gamma)$ cross sections with the associated α ratio determined using Berthoumieux data (left up) and ENDF/B-VII.1 data (left down) for the first two resonances. On the right a comparison between α ratio derived from different experimental and evaluated data of ^{233}U for the first two resonances. The lower α ratio value from the results of Berthoumieux may be attributed to the better energy resolution of the n_TOF facility compared to the RPI facility according to [Berthoumieux 07].

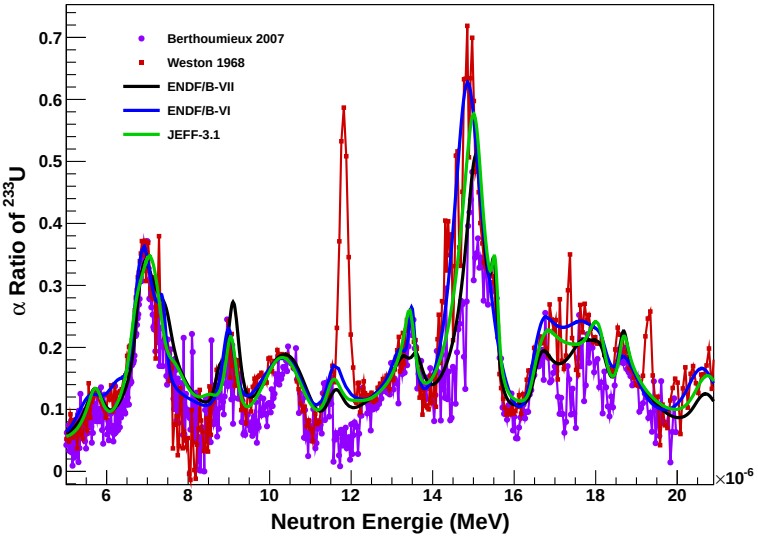

Figure 3.17: Comparison between experimental data and evaluations of the α ratio of ^{233}U around $12eV$. Large discrepancies between experimental data and evaluated libraries are observed, as well as the unknown resonance present only in Weston data.

3.5 Summary and context of our experiment

The most representative experimental data for ^{233}U from thermal energy to the RRR are listed in Table 3.1. Some of these experimental data were used in the most recent evaluation made by Leal [Leal 01] for ^{233}U in the RRR for the ENDF/BVII.1 library and are marked with a star ($\star$). One can notice that the only measurements dedicated to capture in the RRR region at that time and considered in the evaluation were the ones done by Weston [Weston 68, Weston 70]. The evaluation also included Guber's high resolution transmission and fission cross-section data obtained at ORELA [Guber 00, Guber 01] in addition to other experimental data. Before this evaluation, the resonance analysis was done up to $150eV$ and could not be extended because of the lack of high-resolution data above this energy. This evaluation extended the energy range to $600eV$ and improved the accuracy of the parameters, taking advantage of the improved experimental conditions of the ORNL transmission and fission data.

The observed differences of the neutron-induced fission cross-section of ^{233}U with respect to the evaluated databases are significant especially from thermal energy to the RRR, of interest for reactors, in particular the epithermal ones based on $^{232}Th/^{233}U$ fuel cycle. The origin of these discrepancies resides in the choice of the evaluators when selecting experimental data on which the evaluation analysis is based, as well as in

adjustments of cross-section operated in order to be compatible with critical benchmarks, which rely on parameters such as k_{eff} [Leal 01]. In the particular case of ENDF/B-VII.1, Leal found that for the energy range above $100\,eV$, a better prediction of some experimentally determined k_{eff} values required a systematic decrease of the evaluated cross-sections values by $\sim 8\%$, away from the data of Guber but towards the results of Weston. This explains why the latest evaluation in ENDF/B-VII.1 underestimates also the data obtained at n_TOF by Calviani [Calviani 09] that are in agreement within 2% with the data of Guber. Therefore, a revision of the evaluated cross-sections is needed, at least below $600eV$.

Neutron-induced capture cross-section measurements of ^{233}U are very complicated, therefore only few experiments were performed. These measurements require bigger improvements especially due to all experimental difficulties and because is also time consuming. Nevertheless, the most recent data for ^{233}U show good agreement with the latest evaluation, as well as the possibility of extending the RRR, and also offer, for the first time, information in the unresolved resonance region above $1\,keV$. Moreover, a measurement in a high flux, with high energy resolution and broad neutron spectrum source lead to lower uncertainties and smaller discrepancies between neutron energy regions.

An underestimation or a misinterpretation of the experimental results in this energy region may have some important influences on reactor calculations and on α ratio estimation for the $^{232}Th/^{233}U$ fuel cycle. The R-matrix analysis of the most recent data presented in the Sections 3.2 and 3.3 is nevertheless very useful for reliable calculations of the resonance self-shielding [Guimaraes 00]. It is important to stress that more accurate resonance data are of great importance to improve the predictions of the Doppler reactivity coefficient of advanced reactor systems that use ^{233}U as fuel [Ganesan 04].

As a conclusion, we believe that these findings lead to the motivation and justification of the present work, especially in the case of neutron-induced capture cross-section of ^{233}U where the number of experimental data in the RRR is so reduced. New measurements of capture cross-section of ^{233}U are foreseen to be obtained at n_TOF where a successful test experiment for a simultaneous measurement of neutron-induced capture and fission of ^{235}U was recently performed [Guerrero 12].

Reference	Energy Region Analyzed (eV)	Main features
⋆ Moore et al., 1960 [Moore 60]	$0.02 - 15.0$	Transmission, chopper, TOF 15.66 m Sample 0.0037 and 0.0213 atom/b
Hopkins and Diven, 1962 [Hopkins 62]	$3.00e4 - 1.00e6$	Capture to fission ratio, n beam from$^3H(p,n)^3He$ and$^7Li(p,n)^7Be$ reactions, Samples: pallets packed into aluminium cans
⋆ Pattenden and Harvey, 1963 [Pattenden 63]	$0.08 - 15.0$	Transmission, chopper, TOF 45 m, Sample 0.00057, 0.00308, 0.01219 atom/b
Brooks et al., 1966 [Brooks 66]	$0.35 - 10.0$	Simultaneous measurements of capture and fission, Linac TOF
⋆ Weston et al., 1968 [Weston 68]	$1.0 - 2.05e3$	Simultaneous measurements of capture and fission, Linac TOF 25.24 m
Cabell et al. 1970 [Cabell 71]	$0.00253 - 1.0$	Mass spectrometric measurements, 2 years irradiation at Pluto reactor
⋆ Weston et al., 1970 [Weston 70]	$0.02 - 1.00e6$	Simultaneous measurements of capture and fission, Linac TOF 25.6 m
⋆ Blons, 1973 [Blons 73]	$4.0 - 600.0$	Fission, Linac TOF 50.1 m, Sample at liquid nitrogen temperature
⋆ Deruyter Wagemans, 1974 [Deruyter 74]	$0.02 - 15.0$	Fission, Linac TOF 8.1 m
⋆ Harvey et. al., 1979 [Harvey 79]	$0.02 - 1.2$	Transmission, Linac TOF 17.9 m, Sample 0.00605 and 0.0031 atom/b
⋆ Wagemans et al., 1988 [Wagemans 88]	$0.002 - 1.0$	Fission, Linac TOF 8.1 m
⋆ Guber et al., 2000 [Guber 00]	$0.4 - 200.0$	Transmission, Linac TOF 80 m, Total sample thickness 0.000120 atom/b, ^{10}Cd filter
⋆ Guber et al., 2000 [Guber 00]	$8.0 - 7.00e5$	Transmission, Linac TOF 80 m, Total sample thickness 0.000120 atom/b, ^{10}B filter
⋆ Guber et al., 2001 [Guber 01]	$0.6 - 3.00e5$	Transmission, Linac TOF 80 m, Sample temperature 11K, Total sample thikness 0.000293 atom/b
Berthoumieux, 2007 [Berthoumieux 07]	$0.708 - 1.00e3$	Simultaneous measurements of capture and fission, Spallation TOF 185 m
Calviani, 2009	$0.0034 - 1.00e6$	Fission, Spallation TOF 185 m

Table 3.1: The most significant measurements of ^{233}U cross sections.

Method and experimental set-up

Chapter 4

$^{233}U(n,f)$ and $^{233}U(n,\gamma)$ cross section measurements

There is not a standard method that could be applicable for the measurement of (n,γ) cross sections. For a selective group of actinides, in particular for the ^{233}U isotope in this work, where the neutron-induced fission reaction competes with the neutron capture reaction at all neutron energies, additional signature is needed to distinguish between fission and capture $\gamma-$rays. This can be accomplished by introducing a detector system to tag fission fragments and thus establish a unique signature for the fission event.

The main objective of this work is the development of an experimental set-up to improve the knowledge of the capture and fission cross sections of ^{233}U in the RRR. For the measurement of (n,γ) cross sections of highly radioactive, fissile nuclei with high accuracy, a new experimental set-up was developed and tested at CENBG in Bordeaux that will allow us to achieve such goal. The measurements will be performed at the GEel LINear Accelerator (GELINA) neutron time-of-flight facility in Belgium, where neutron cross sections can be measured over a wide energy range with high energy resolution. The new set-up consists of an fission detector which is a dedicated multi-plate high efficiency fission ionization chamber (IC). The chamber is surounded with six liquid scintillators filled with deuterated benzene C_6D_6 that are used for the detection of the prompt fission neutrons and the prompt γ -rays from the neutron capture reaction.

In this chapter the method employed for the measurement of neutron induced cross sections of highly radioactive nuclide, will be presented. Details about the experimental set-up for $^{233}U(n,f)$ and $^{233}U(n,\gamma)$ cross sections measurements are discussed and the relation between experimental observables and theoretical estimations are given. We will start by presenting a short description of Gelina facility.

4.1 Time-of-flight facility GELINA

In the so-called resolved resonance region (RRR), which is the energy range where the nuclear level spacing is larger than the Doppler and experimentally broadened natural level widths, a very good resolution in neutron energy is needed to resolve the resonance structure of the cross section. Such high resolution measurements are usually performed at pulsed white neutron beams using accelerators, combined with the Time-Of-Flight (TOF) neutron energy measurement technique. The GEel LINear Accelerator (GELINA) [Mondelaers 06] of the IRMM in Belgium provides a pulsed white neutron spectrum with an extremely good time resolution for fission and capture measurements. A similar facility is the Oak RidgE Linear Accelerator (ORELA) [Pering 69, Bigelow 06] available at the Oak Ridge National Laboratory in USA. Alternatively to electron accelerator-based neutron sources, like GELINA and ORELA, spallation sources using very high energy proton accelerator can be used, such as the n-TOF facility installed at the synchrotron of CERN [Rubbia 99].

Gelina is a multi-user TOF facility, serving up to 12 different experiments simultaneously, and providing a white neutron source, with an energy range between 1 meV and 20 MeV. It comprises four major elements: a linear electron accelerator, a post-accelerating beam compression magnet system, a mercury-cooled rotary uranium target and several flight paths. An image of Gelina flight paths can be seen in Figure 4.1.

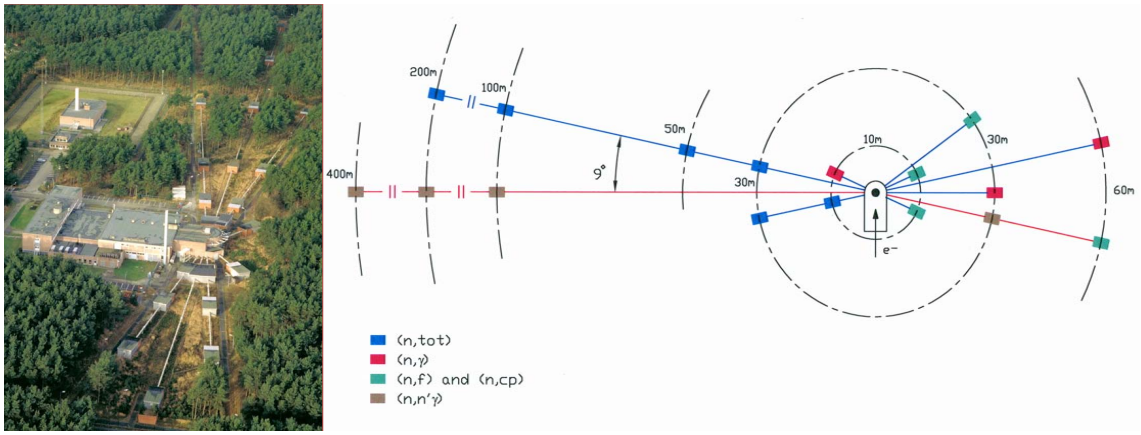

Figure 4.1: Gelina site on the left picture. A schematic view of the flight paths on the right. Neutron measurements can be performed simultaneously at 12 flight paths with lengths ranging from 10 up to 400 m, located in radial direction from the target [Mondelaers 06]. Many types of neutron cross section measurements are possible: transmission experiments, as well as capture, fission, elastic and inelastic cross section experiments.

Intense pulsed electron beams, at repetition rates from 40 to 800 Hz and with peak currents up to 12 A in a 10 ns time interval, are accelerated to a maximum energy of 150 MeV in a linear electron accelerator. The electron bunches are compressed to a duration of less than 1 ns (and peak currents of up to 120 A respectively) by a specially designed post-acceleration compression magnet [Tronc 85]. These high-energy electrons generate Bremsstralung $\gamma-$rays in a uranium target, where neutrons are mainly produced by (γ, n) and (γ, f) reactions [Salome 81]. Uranium was chosen as target material because it favours the production of photons in Bremsstrahlung process and neutrons by photon-induced nuclear reactions. Above ~ 30 MeV electron energy, the neutron production rate is nearly proportional to the electron beam power.

The target delivers an average neutron intensity of $3.4 \cdot 10^{13}$ neutrons/s. The fast neutrons obtained are subsequently moderated by two water-filled beryllium containers placed above and below the uranium target, as shown in Figure 4.2. Water is a good neutron moderator due to the small mass number and the very large neutron scattering cross section of hydrogen. Using appropriate collimators, either the direct (fast) neutron spectum with very good resolution, or the moderated (slow) neutron spectrum with a reduced resolution, may be used. The partially moderated neutrons have an $\sim 1/E$ energy dependence plus a Maxwellian peak at thermal energy as illustrated on the left side of the Figure 4.3. Based on the required energy range in a particular measurement station, shadow bars are properly placed between the source and the flight path to shield unwanted neutrons. Further adjustments of the spectral shape is done with movable filters. The total neutron output is continuously monitored by several BF_3 proportional counters placed at different positions around the target hall. These monitors measure the energy-integrated neutron flux and are used to monitor the stability of the accelerator and to normalize the spectra to the same total neutron intensity.

Figure 4.3 shows the absolute neutron flux of the moderated neutron spectrum at a 10 m flight path that was measured in the energy range from 25 meV to 200 keV with the accelerator operating at 40 Hz [Borella 05]. The results are compared with the MCNP code [Briesmeister 00] calculations [Flaska 04]. On the right side of the figure is shown the comparison of similar calculations with the absolute neutron flux of the unmoderated neutron spectrum in energy range from 200 keV to 20 MeV with the accelerator operating at 800 Hz [Mihailescu 04]. The experimental data were obtained from measurements using ionisation chamber based on the $^{10}B(n, \alpha)$ and $^{235}U(n, f)$ reactions. At long flight paths the high operating frequency limits the application in the low energy domain due to the influence of so-called "overlap neutrons". The slow neutrons from a previous pulse overlap with the fast neutrons of the present pulse. These are neutrons of previous burst reaching the detector when the next burst is already produced. To eliminate the influence of slow neutrons from previous accelerator cycle, anti-overlap filters are used.

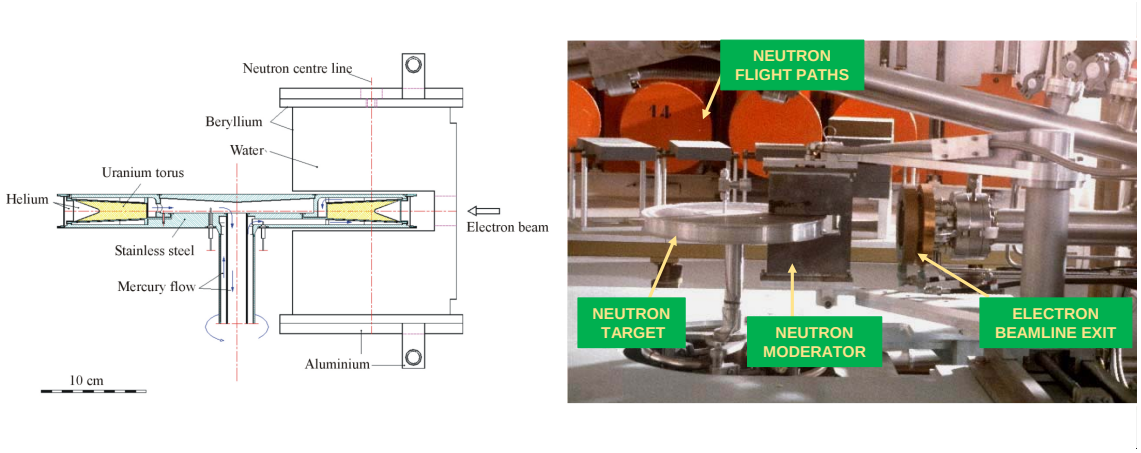

Figure 4.2: Scheme of neutron producing target (on the left) and a picture of the disk shaped uranium rotating target with moderators above and below, collimators and shadow bars and the neutron shutters, leading to the flight paths (on the right).

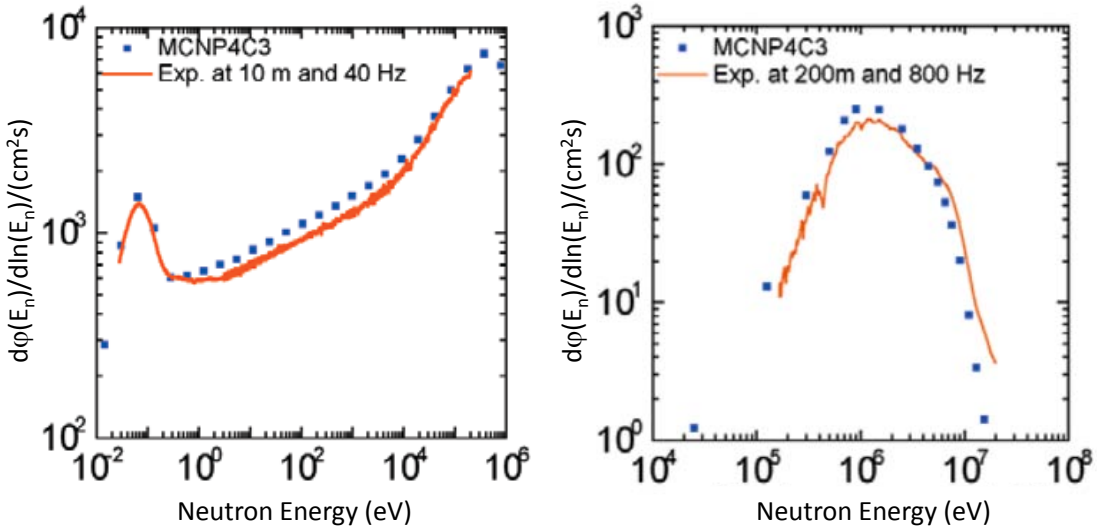

Figure 4.3: The absolute neutron flux per unit lethargy of the neutron spectrum at 30 m distance from the uranium target with and without moderator with the accelerator operating at 800 Hz (on the left) and in energy range from 200 keV to 20 MeV with the accelerator operating at 800 Hz on the right. The experimental data are compared with the results of Monte Carlo simulations reported by Flaska [Flaska 04].

The distribution of the moderated neutron flux at Gelina can be represented by a Maxwellian distribution whit a peak energy about 50 meV, plus a tail of partially moderated neutrons.

To perform high-resolution cross-section measurements an accurate knowledge of neutron energy is essential. At Gelina, the determination of neutron energy is based on the Time-of-Flight (TOF) method (see next Section). This powerful method allows for the study of neutron induced capture, fission and secondary particle production reactions.

4.2 Time-of-flight method

There exist several methods to measure the total and partial neutron cross sections of highly radioactive nuclides. All of them require a neutron source and a sample as isotopically pure as possible. Cross sections can be measured at specific energies using monoenergetic neutron beams, or in the form of point-wise cross sections or average values using continuous energy neutron beam. In most cases, the neutron source is driven by a pulsed particle accelerator using protons or electrons, while pulsed research reactors also can be successfully employed for this purpose. The most complete measurements are those of the point-wise cross-section for all open reaction channels in a wide energy range, that is only possible by applying the time-of-flight (TOF) technique.

The principle of neutron TOF is based on the pulsed neutron source which produces at a time t_0, typically in few nanoseconds, neutrons in a broad energy spectrum. The TOF method relies on a direct relation between the energy of the neutron and the time (time-of-flight) that it needs to travel a given distance L. For reaction cross-sections measurements a sample is placed in a neutron beam at a distance L ranging from a few centimeters to several hundreds of meters for high energy resolution measurements, and the reaction products are detected (like fission fragments, alpha particles, capture $\gamma-$rays or scattered neutrons). The detection of a reaction determines the arrival time of the neutron t_n at the sample and therefore its velocity by:

$$v = \frac{L}{t} \tag{4.1}$$

where $t = t_n - t_0$ is the TOF of the neutron who had induced the reaction.

The kinetic energy E_n of the neutron with a velocity v and momentum $p = m \cdot v$ is given by the relativistic expression:

$$E_n = E_{tot} - mc^2 = \sqrt{c^2p^2 + m^2c^4} - mc^2 = mc^2 \cdot (\gamma - 1) \tag{4.2}$$

where c is the speed of light and γ represents the relativistic Lorentz factor:

$$\gamma = \frac{1}{\sqrt{1-(v/c)^2}} \tag{4.3}$$

At low energies where $v \ll c$ and therefore $\gamma \to 1$, the relativistic expression can be conveniently written as a series of expansion of γ as:

$$\gamma = 1 + \frac{1}{2}\frac{v^2}{c^2} + \frac{3}{2}\left(\frac{v^2}{c^2}\right)^2 + \frac{5}{16}\left(\frac{v^2}{c^2}\right)^3 + O\left(\frac{v^2}{c^2}\right)^4 \tag{4.4}$$

For resolved resonances the first two terms of the series expansion of the relativistic expression are usually sufficient, which results in the classical definition of kinetic energy:

$$E_n \approx \frac{1}{2}mv^2 = \alpha^2\frac{L^2}{t^2} \tag{4.5}$$

Considering the definition of speed of light $c = 299\,792\,458\,m/s$ and taking $m_n = 939.6\,MeV/c^2$for neutron mass, we obtain $\alpha = 72.2983\,\mu s\sqrt{eV}/m$.

The corresponding energy resolution of a TOF spectrometer is obtained by derivation of eq. 4.5:

$$\frac{\triangle E}{E} = 2\sqrt{\left(\frac{\triangle T}{t}\right)^2 + \left(\frac{\triangle L}{L}\right)^2} = 2\sqrt{\left(\frac{\triangle T}{72.3L}\right)^2 + \left(\frac{\triangle L}{L}\right)^2} \tag{4.6}$$

The neutron energy resolution in a TOF method is affected by the following uncertainty sources:

- the time resolution of the acquisition system (detector and time coder),
- the duration of the neutron burst,
- the dimensions of the neutron source,
- the sample dimensions and position, and
- the neutron multiple scattering in the neutron source and in the sample.

The first two sources influence the time resolution $\left(\frac{\triangle T}{t}\right)$ and the last three the uncertainty of the flight path-lenght $\left(\frac{\triangle L}{L}\right)$. It results that for a good neutron energy resolution, the measurement should be done at a longer flight-path length and with detectors of a good time resolution. For the neutron source, special efforts were done to reduce the neutron burst length in order to least affect the time resolution [Tronc 85].

Experimentally, the neutron TOF is determined from the difference between the arrival time and start signal. The latter depends on the characteristics of the neutron beam.

For a continuous neutron beam produced in a reactor, the start signal is given by a chopper. At accelerator facilities, the use of chopper can be avoided since the start signal is provided by the pulsed charge-particle beam. The arrival time in transmission measurements is given by the neutron detector, while in capture measurements it is obtained from the detection of prompt $\gamma-$rays emitted in capture reaction. The principle of the TOF method is shown in Figure 4.4.

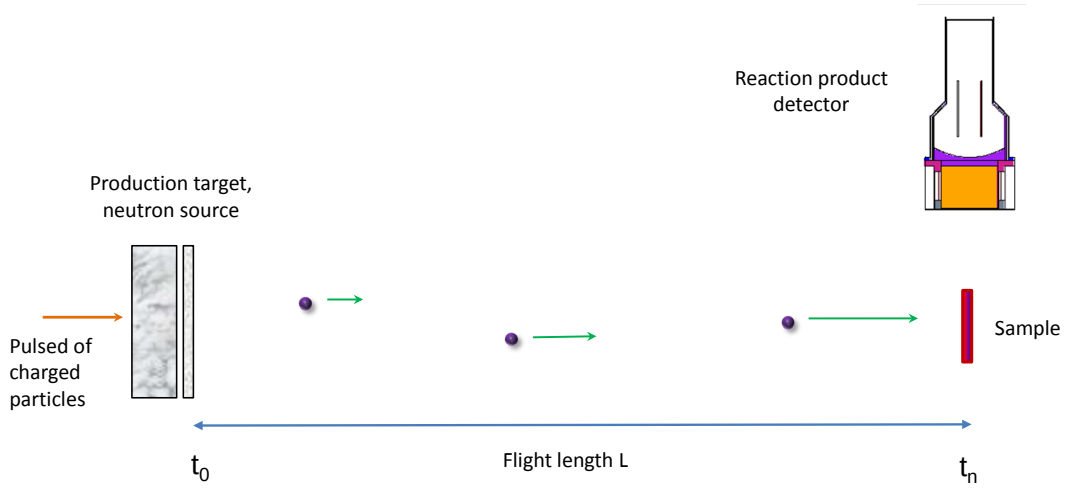

Figure 4.4: The principle of time-of-flight method

4.3 Flight path description

In this work, the capture and fission measurements will be performed at the flight path No. 1 at 10 m from the moderator. The angle between the flight path and the normal to the moderator for this flight path is 12^0. A detailed description of the experimental arrangement is shown in Figure 4.5.

A 115.2 mm thick natural sulphur filter is permanently installed to reduce the influence of the γ-flash [1] and to continuously monitor the background at 102.71 keV. The collimating system is mainly composed of lead collimators. At about 1 m from the ^{233}U sample and just in front of the ^{10}B ionisation chamber (used for the monitoring the neutron flux) is placed a shielding construction, consisting of Boron-oxide and paraffin together with a 10 cm thick lead wall, to reduce the background from scattered neutrons. An air-conditioning system is continuously functioning to keep the samples at

1. The biggest contribution to the in-beam component comes from γ-rays directly propagating from the target. Although the uranium target is designed to stop the electrons and bremsstrahlung photons, an intense prompt flash, called γ-flash, leaks from the target.

constant temperature and to reduce the electronic drifts due to temperature changes. To determine the resonances for $^{233}U(n,\gamma)$ in the RRR with a statistical uncertainty better than 1% the beam time of the measurement was estimated at several months with the accelerator operating at 800 Hz frequency.

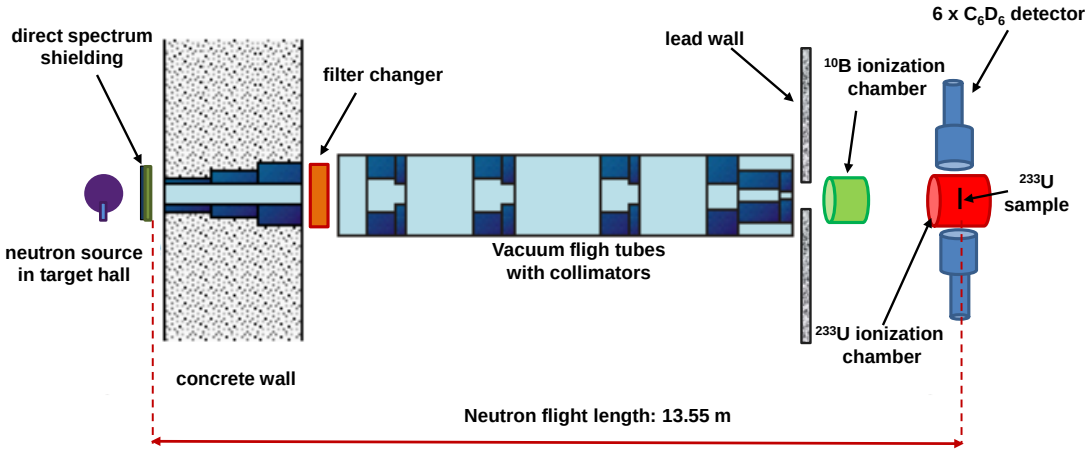

Figure 4.5: Detailed description of the experimental arrangement for the neutron-induced fission and capture cross sections of ^{233}U at the Gelina accelerator at the 10 m flight path.

4.4 Theoretical considerations of experimental observable

The R-Matrix formalism, as mentioned in Section 2.5, is a nuclear reaction formalism that is particularly suited for the parametrisation of resonance structured cross sections. The R-matrix formalism links the properties of excited states of the compound-nucleus, such as energy, spin, parity and partial reaction widths, to the cross sections. Its assumption that the photon channels have only a diagonal contributing to the width matrix is justified by the great number of radiative channels and practically random signs of their width amplitudes.

Accurate cross sections can only be parametrized by codes like SAMMY [Moxon 91] and REFIT [Larson 08] based on R-matrix analysis. These codes include corrections for various experimental effects such as inhomogeneities, self-shielding, multiple scattering, Doppler broadening, response of the TOF spectrometer, neutron sensitivity of the capture detection system and $\gamma-$ray attenuation in the sample and a full R-matrix analysis can be performed.

In a reaction cross-section measurement in the RRR, the quantity of interest is the reaction yield, which is the fraction of the neutron beam inducing a reaction in a sample. The theoretical reaction yield $Y_{r,X}$ resulting from a neutron induced reaction(n,r) with a nuclide ${}^{A}X$, can be expressed as a sum of primary $Y_{0,X}$ and multiple interaction events $Y_{m,X}$:

$$Y_{r,X} = Y_{0,X} + Y_{m,X} \tag{4.7}$$

The latter are due to a (n,r) reaction after at least one neutron scattering in the sample. For a parallel uniform neutron beam and a homogeneous sample placed perpendicular to the neutron beam, the primary yield $Y_{0,X}$ is given by:

$$Y_{0,X} = \left(1 - e^{-\sum\limits_{j} n_j \overline{\sigma_{tot,j}}}\right) \frac{n_X \overline{\sigma_{r,X}}}{\sum\limits_{j} n_j \overline{\sigma_{tot,j}}} \tag{4.8}$$

where

- n_j is the overall sample thickness (i. e. the number of atoms per unit area of all nuclides in the sample),
- $\overline{\sigma_{tot,j}}$ is the Doppler broadened total cross-section,
- $\overline{\sigma_{r,X}}$ is the Doppler broadened reaction cross section, and
- n_X is the specificsample thickness (i. e.the number of atoms per unit area of nuclide ${}^{A}X$).

Only for very thin samples and/or small cross sections, where $\sum\limits_{j} n_j \overline{\sigma_{tot,j}} \ll 1$, the reaction yield is directly proportional to the reaction cross-section with $Y_{r,X} \approx n_X \overline{\sigma_{r,X}}$.

The thickness is expressed in atoms per barn (at/b) and is given by the following relation:

$$n_X = \frac{m}{A \cdot S \cdot 10^{24}} N_A \tag{4.9}$$

where m is the mass in grams, A is the atomic number, S is the sample surface in cm^2 and $N_A = 6.022 \cdot 10^{23} mol^{-1}$ is the the Avogadro number. The advantage of expressing the thickness in at/b is that the neutron interaction probability in the sample is given by the product of the neutron cross-section and the thickness.

The calculation of the reaction yield, in particular the contribution of the multiple interaction events is one of the most complex parts of the resonance shape analysis codes like SAMMY and REFIT.

4.5 Reaction cross section measurements

Figure 4.6 show how an incident neutron beam with a flux $\phi_0(E_n)$ is attenuated by interaction with a sample of thickness n_X containing nuclide ^AX. The effective thickness of the sample seen by the incident neutron beam is between x and $x+dx$. The outgoing flux $\phi(E_n)$ is related to the incoming one by the total neutron cross section $\sigma_{tot,X}$ via the formula:

$$\phi(E_n, x) = \phi_0(E_n) \cdot e^{-\rho \cdot x \cdot \sigma_{tot,X}(E_n)} \tag{4.10}$$

where ρ is the sample density in at/cm^{-3} and x is the sample thickness in cm.

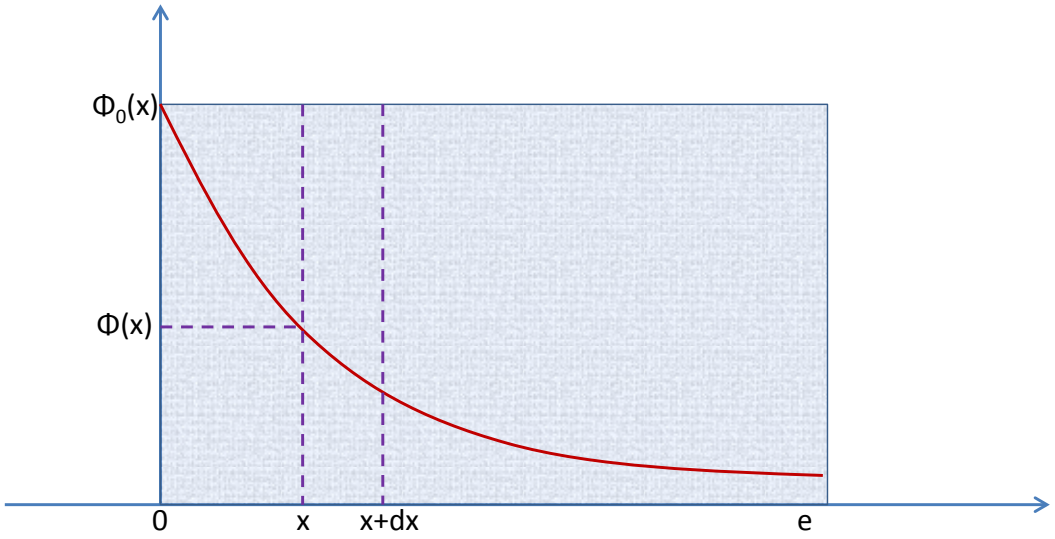

Figure 4.6: Neutron flux attenuation versus thickness e (in cm) of attenuating material.

The number of interactions $N_{r,X}(E_n)$ in a reaction cross section experiment due to the presence of nuclide ^AX in a sample, which is placed perpendicular to the parallel incident neutron beam, is given by:

$$N_{r,X}(E_n, x) \cdot dx = \phi(E_n, x) \cdot \sigma_{r,X}(E_n) \cdot \rho \cdot S \cdot dx = \phi(E_n) \cdot e^{-\rho \cdot x \cdot \sigma_{tot,X}(E_n)} \cdot \sigma_{r,X} \cdot \rho \cdot S \cdot dx \tag{4.11}$$

where:

- S is the sample surface, and
- $\sigma_{r,X}(E_n)$ the reaction cross-section of the nuclide ^AX.

The total number of interactions in the sample can be expressed as:

$$N_{r,X}\left(E_n\right) = \int_0^e N_{r,X}\left(E_n\right) \cdot dx$$

$$N_{r,X}\left(E_n\right) = \phi_0\left(E_n\right) \cdot \frac{\sigma_{r,X}}{\sigma_{tot,X}}\left(E_n\right) \cdot S \cdot \left[1 - e^{-n_X \cdot \sigma_{tot,X}(E_n)}\right] \tag{4.12}$$

The partial reaction yield $Y_{r,X}\left(E_n\right)$ defined as the fraction of the neutron beam that undergoes a (n,r) reaction in a sample can be defined as:

$$Y_{r,X}\left(E_n\right) = \frac{C_{r,X}\left(E_n\right)}{\epsilon_r\left(E_n\right) \cdot \phi_0\left(E_n\right) \cdot S} = \left(1 - e^{-n_X \sigma_{tot,X}}\right) \frac{\sigma_{r,X}}{\sigma_{tot,X}}\left(E_n\right) \tag{4.13}$$

where the expected count rate (the experimental number of interactions) $C_{r,X}(E_n)$ in a reaction cross section experiment is defined by:

$$C_{r,X}\left(E_n\right) = \epsilon_r\left(E_n\right) \cdot N_{r,X}\left(E_n\right) \tag{4.14}$$

and ϵ_r is the intrinsic detection efficiency of the detector defined as the efficiency of the detection system to detect an event resulting from a (n,r) reaction with nuclide ${}^{A}X$.

The count rate is related to the partial reaction yield $Y_{r,X}\left(E_n\right)$ by the following expression:

$$C_{r,X}\left(E_n\right) = \epsilon_r\left(E_n\right) \cdot S \cdot Y_{r,X}\left(E_n\right) \cdot \phi(E_n) \tag{4.15}$$

The partial reaction yield not only depends on the partial cross section but also on the total cross section. In a thin sample approximation (with $n_X \sigma_{tot,X} \ll 1$), the reaction cross-section is obtained from the ratio between the reaction count rate and the flux measurement:

$$\sigma_{r,X}(E_n) = \frac{C_{r,X}\left(E_n\right)}{n_X \cdot \epsilon_r \cdot S \cdot \phi(E_n)} \tag{4.16}$$

Therefore, the determination of the partial cross-section requires an additional measurement of the neutron flux and a very good knowledge of the detection efficiency for the partial reaction event.

4.5.1 Principle of the $^{233}U(n,f)$ cross section measurement

4.5.1.1 General presentation

The fission measurement is carried out with a compact ionisation chamber based on the direct detection of the fission fragments (FF) produced in fission reactions.

The ionisation chamber has been designed and built to meet the following requirements:

- to minimize the material in and around the neutron beam, and in particular, to reduce the thickness of the electrodes, windows, sample layers and to use material with compositions that minimize neutron interactions,

- to obtain a fast charge collection time, in order to allow reliable operation at very high instantaneous counting rates. This is needed due to the strongα-radioactivity of the sample.

The measurement of energy deposited in gas by the FF produced in a thin target of fissile material is one of the standard techniques for the measurement of neutron-induced fission cross-section, as well as for neutron flux measurements as we will discuss in section 4.5.1.4. The sensitive volume of the ionizing particles is in physical contact with the fissile deposit, so that the solid-angle coverage is very close to 2π. Due to different effects of the fission process (multiplicity and kinematics), the number of detected FF is equal to the total number of fission reactions.

Fission ionisation chambers operate in the ionisation regime, where the signal is strictly related to the charge produced by ionization in the gas. The FF loses energy due to Coulomb interactions with the atoms and molecules of the gas, and the number of the electron-ion pairs created is proportional to the energy of the fragment. This happens when the distance between electrodes is larger than the range and the electric field between the electrodes is sufficiently high to collect all the charges produced by the ionization and low enough to prevent the production of secondary pairs. Since the charge state of the FF decreases with decreasing velocity, their specific energy losts dE/dx decreases as they slow down in the medium: an opposite behaviour to that of lighter particles like α particles or protons, for which the energy loss becomes most significant at the end of the range. Therefore, it is important that the separation between FF and lighter particles to be as large as possible, avoiding also the problem when FF deposits low energy similar to α particle. The distance between the anode and cathode and the gas pressure in the IC are chosen so that the signals produced by the FF are larger than those produced by any other competing reaction. A simple amplitude threshold, which corresponds to a deposited energy threshold, is therefore sufficient to discriminate fission events from signals related to the natural radioactivity of the samples, in particular α-particle decay.

In the case of highly radioactive isotopes, such as ^{241}Am and ^{245}Cm, the probability of superposition of the signals generated by two or more α-particles becomes significant. This is also the case for ^{233}U even though is less radioactive. Such a pile-up may be misinterpreted as a FF signal or, in general, a particle that has lost a great amount of energy. To avoid the pile-up effect, a thin sample (reduced mass) must be used and a fast detector as well. The pile-up effect is strongly dependent on the time response of the chamber, which is related to the electron drift time (rise time) in the gap between the anode and cathode. Several parameters determine the behaviour of the IC, as the gas pressure or the high voltage between the electrodes. The impact of these parameters has been studied to find the ideal operating point: a good energy separation between α/ FF and a good timing resolution. In the present measurement, a charge collection time of 50 ns, corresponding to an electron drift velocity of 12 cm/μs in the 0.5 cm gap between the electrodes, and the absence of Frisch grid [2], make the IC detector very fast, and therefore, suitable for measurements of very highly radioactive isotopes.

4.5.1.2 Ionisation chamber detector

In order to minimize the contribution from neutron-induced background by the IC itself (scattered/capture of IC components), a new IC was designed and build at CENBG in Bordeaux. The IC has a cylindrical shape of 18.6 cm long and 20.3 cm outer diameter and is made of high purity aluminum (aluminum 1050A with 99.9% ^{27}Al purity) with the entrance and exit windows for the neutron beam of 200 μm thickness. Typically, the FF detectors are used to identified the neutron induced fission reaction events and to separate them during the analysis from those of capture reaction. This requires samples thin enough to achieve a high FF detection. Because the thin target diminishes the statistics of the measurements, we will use 10 thin targets to enlarge the amount of the material. For the same reason, to maximize the amount of the ^{233}U material without increasing the thickness of the layer, the diameter of the uranium deposit is 6 cm. The chamber is operating with a continuous flow of mixture of Argon (90%) and Methan (10%) at atmospheric pressure as detector gas, designed for measurement of highly α-active isotopes. Also, in order to have similar flight path length (L) and similar target-$\gamma-$detectors distance, the IC is therefore an assembly of 10 parallel-plates fission chambers with 5 mm spacing between electrodes, to be in a compact geometry. The IC is therefore an assembly of 10 parallel-plates fission chambers with 5 mm spacing between electrodes. The ^{233}U samples required for this experiment are prepared at IRMM (Belgium) by electro-deposition technique on 50 μm thick high purity Al foil with a diameter of 12 cm stretched on aluminium ring. The uranium samples are placed in the center of the cathode. Obviously the material used for the backing should be as thin as

2. Used in some ionisation chambers to remove the dependence of the pulse amplitude on the position of interaction. It is placed between the two electrodes of the chambers and it is constituted by a grid maintained at an intermediate potential between the two electrodes and made to be as transparent as possible to electrons.

reasonable possible and made out of material with low neutron interaction probability. The plates are electrically isolated, having a separate signal connector for each of them, and assembled along the direction of the neutron beam. The anodes of the IC are biased to 100 V high voltage with a power supply system. The cathode signals are connected to the input of fast charge amplifiers. The chamber, shown in Figure 4.7, was operated only with ^{233}U samples and ^{252}Cf, which is a spontaneously fissioning isotope. The ^{233}U samples have an activity of the order of MBq. This is why the samples mounting in the ionisation chamber has to be operated in a dedicated ventilation system suitably equipped for handling unsealed radioactive sources, as requested by the radioprotection department at CENBG.

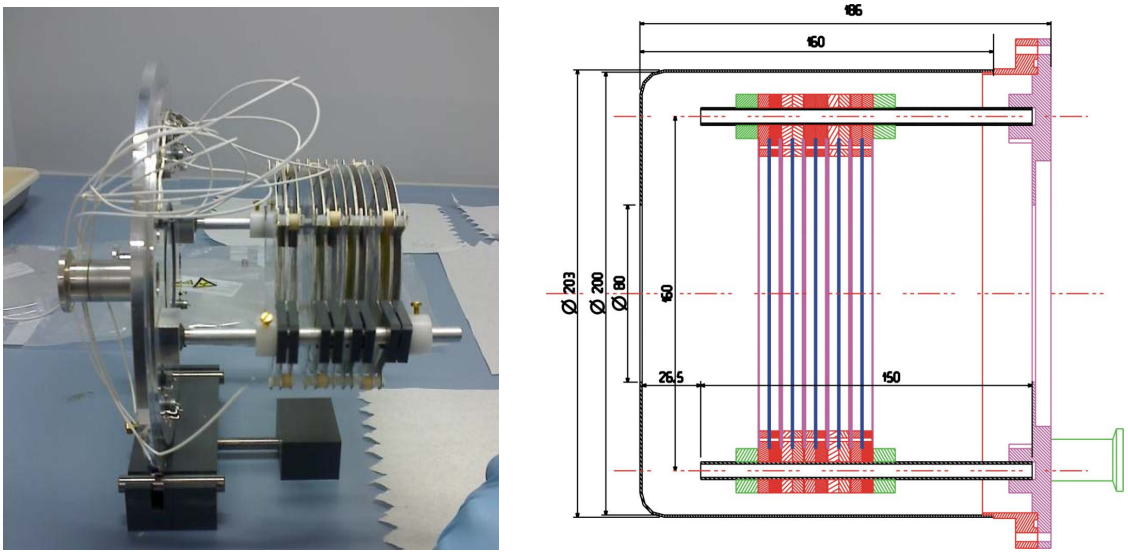

Figure 4.7: Photo of the inside of the ionisation chamber with three ^{233}U samples taken during the assembly. A detailed schematic view of the ionisation chamber on the right.

4.5.1.3 Experimental fission cross section of ^{233}U

Experimentally, the neutron-induced fission cross-section of ^{233}U is extracted from the following expression of the measured fission yield $Y_{fis,U}(E_n)$, according to eqs. 4.13, and valid in the assumption of negligible multiple scattering:

$$Y_{fis,U}(E_n) = \frac{C_{fis,U}(E_n)}{\epsilon_{IC} \cdot \phi(E_n) \cdot S} = \left(1 - e^{-n_U \sigma_{tot,U}}\right) \frac{\sigma_{fis,U}}{\sigma_{tot,U}}(E_n) \tag{4.17}$$

where:

- ϵ_{IC} is the efficiency of the IC to detect the FF resulting from $^{233}U(n,f)$ reactions,
- S is the effective surface of the ^{233}U sample,
- n_U is the thickness of the ^{233}U sample,
- $\sigma_{fis,U}(E_n)$ is the fission cross-section of ^{233}U,
- $\sigma_{tot,U}(E_n)$ is the total cross-section of ^{233}U,
- $C_{fis,U}(E_n)$ is the fission count rate defined by:

$$C_{fis,U}(E_n) = \phi(E_n) \cdot S \cdot Y_{fis,U}(E_n) \cdot \epsilon_{IC} \tag{4.18}$$

The accurate determination of the fission cross-section requires a precise knowledge of the detector performances, in particular of its efficiency ϵ_{IC}. The method used in our experiment for the determination of ϵ_{IC} will be discussed later in Section 4.6. For the analysis of any reaction cross-section measurement the absolute $\phi'(E_n)$ or relative $\phi(E_n)$ neutron flux as a function of neutron energy is also required. This measurement is detailed in the next section. Such measurements rely on neutron cross section well known. Details about standard cross sections for neutron-induced reactions can be found in [Carlson 09]. Additional cross section standards at 0.0253 eV neutron energy or at a velocity of 2200 m/s are given in [Holden 89].

4.5.1.4 Neutron flux measurement

In the region below a few hundred keV flux measurements are predominantly based on the $^{6}Li(n,\alpha)^{7}Li$ and $^{10}B(n,\alpha)^{7}Li$ reactions. At energies above 0.5 MeV the $^{235}U(n,f)$ reaction is mostly used. The $^{238}U(n,f)$ reaction is especially useful in the MeV region, because the cross-section has a threshold near 1 MeV eliminating the influence of low-energy neutrons. Most of the time, very thin layers of the target material are used in ionisation chambers and thus the thin target approximation could be applied.

At Gelina, the $^{10}B(n,\alpha)^{7}Li$ reaction is used as a neutron converting reaction in combination with an ionisation chamber. This standard reaction is used to determine the energy dependence of the neutron flux for fission and capture measurements below the keV region at Gelina facility [Borella 05, Borella 06, Borella 07a]. The ^{10}B chamber is a Frisch gridded ionisation chamber, whit three back-to-back layers of ^{10}B evaporated on a 30 μm thick aluminium backing with a total thickness of about $1.25 \cdot 10^{-5}$at/b and a diameter of 84 mm. A schematic representation and technical details of the ^{10}B chamber are shown in Figure 4.8. The chamber is operating with a mixture of Argon (90%) and Methan (10%) at 1 .0 atm pressure like the IC designed for fission measurements.

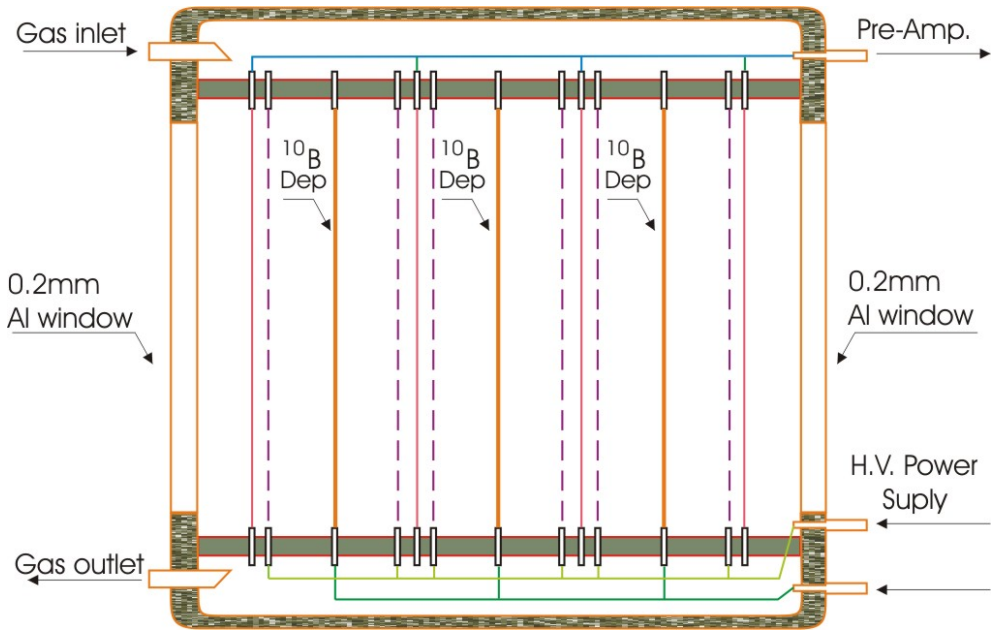

Figure 4.8: Schematic view of the Frisch gridded ^{10}B ionisation chamber used for the neutron flux measurements.

One of the reaction product is stopped in the cathode, and the particle emitted by the ^{10}B layers loses its energy by ionisation of the gas atoms. Under the influence of the electric field, the positive ions are accelerated toward the cathode and the electrons toward the anode. The gas multiplication process takes place between the grid and the anode. The signal pulse at the anode is proportional to the total number of ion-electron pairs formed along the track of the incident particle, when becomes independent of their original position.

Using the definition given in eq. 4.13, the partial reaction yield $Y_{\alpha,B}(E_n)$ for $^{10}B(n,\alpha)^7Li$ reaction will be:

$$Y_{\alpha,B}(E_n) = \frac{C_{\alpha,B}(E_n)}{\epsilon_{\alpha,B}(E_n)\cdot\phi'(E_n)\cdot S} = \left(1 - e^{-n_B\sigma_{tot,B}}\right)\frac{\sigma_{\alpha,B}}{\sigma_{tot,B}}(E_n) \tag{4.19}$$

with :

- $C_{\alpha,B}(E_n)$ the count rate of the ^{10}B sample,
- $\epsilon_{\alpha,B}(E_n)$ the efficiency of the ^{10}B ionisation chamber,
- $\phi'(E_n)$ is the neutron flux impinging the ^{10}B sample,
- S the effective surface of the sample seen by the neutron beam,

- n_B the thickness of the ^{10}B sample (at/b),
- $\sigma_{\alpha,B}$ the α cross-section of ^{10}B,
- $\sigma_{tot,B}$ the total cross section of ^{10}B .

The neutron flux measured using the ^{10}B ionisation chamber can be determined as:

$$\phi'(E_n) = \frac{C_{\alpha,B}(E_n)}{\epsilon_{\alpha,B}(E_n) \cdot S \cdot Y_{\alpha,B}(E_n)} \tag{4.20}$$

4.5.1.5 Estimation of neutron flux relative to the ^{233}U ionisation chamber

The neutron flux impinging the ^{233}U sample $\phi(E_n)$, is monitored with information provided by the ^{10}B ionisation chamber. Nevertheless, this flux is slightly different than the one measured with the ^{10}B ionisation chamber $\phi'(E_n)$. The two fission chambers are cylindrical and made of aluminum. They have different dimensions and the aluminum plates and end windows of the chambers have different thicknesses. That is why we use Al_1 as the notation for the ^{10}B ionisation chamber and Al_2 for the ^{233}U ionisation chamber as shown in Figure 4.9. The ^{10}B chamber is placed approximately 1 m prior to the fission and capture detection system. The $^{10}B(n,\alpha)$ standard reaction is used to determine the energy dependence of the neutron flux below the keV region.

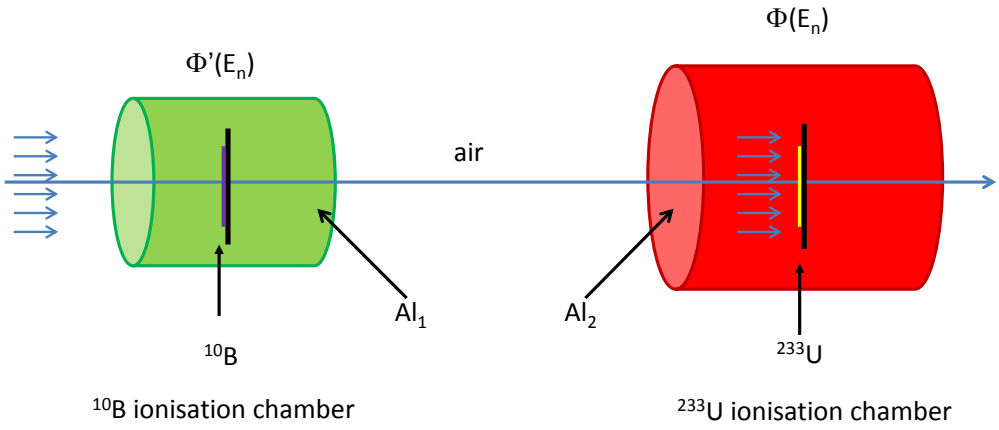

Figure 4.9: Experimental set-up for the energy dependence of the neutron flux $\phi'(E_n)$ measurement at Gelina using a ^{10}B ionisation chamber and the neutron flux $\phi(E_n)$ in the ^{233}U ionisation chamber.

The neutron flux $\phi(E_n)$ impinging on ^{233}U sample is given by $\phi'(E_n)$ attenuated by several layers of materials:

$$\phi(E_n) = \phi'(E_n) \cdot e^{-n_B \sigma_{tot,B}} \cdot e^{-n_{Al_1} \cdot \sigma_{tot,Al}} \cdot e^{-n_{air} \cdot \sigma_{tot,air}} \cdot e^{-n_{Al_2} \cdot \sigma_{tot,Al}}$$

$$\phi(E_n) = K_{air} \cdot K_{Al} \cdot \phi'(E_n) \cdot e^{-n_B \sigma_{tot,B}} \tag{4.21}$$

where $Al = Al_1 + Al_2$ in cm, K_{air} and K_{Al} are the attenuation factors for air and aluminum which can be measured or estimated by the MCNP simulation code [Briesmeister 00].

For neutron energies below 150 keV, the neutron flux attenuation factor through an aluminum foil of 50 μm thickness and ^{233}U sample of 400 $\mu g/cm^2$ was found to be negligible between the entrance and exit of the fission chambers ^{233}U-aluminum foils assembly. Therefore, the neutron flux at the entrance and end window in the ^{233}U fission chambers is considered uniform.

4.5.2 Principle of the $^{233}U(n,\gamma)$ cross section measurement

4.5.2.1 General presentation

As explained in section 2, in a neutron capture reaction, the compound nucleus decays to its ground state through the emission of one or several γ-rays. Measurements of the capture cross-section σ_γ rely on the detection of the prompt γ-rays emitted in the (n,γ) reaction. Reviews on capture cross section measurements and exhaustive discussion of the various techniques and the corresponding detectors can be found in [Chrien 61, Gayther 82, Corvi 94]. In this work we will briefly describe the techniques that are still in use and concentrate mainly on the technique applied in the RRR, i. e. the use of the total energy detection principle using the Pulse Height Weighting Technique (PHWT) with C_6D_6 detectors.

The ideal detection system for neutron capture cross section measurements in the RRR must satisfy the following requirements:

- the detector should have a very good time resolution,
- the sensitivity to scattered neutrons should be low, and
- the detection efficiency for the capture event should be independent of the particular γ-ray emission (independent of the shape and multiplicity [3] of the gamma spectrum).

Three main types of neutron capture detectors can be distinguished: high-resolution γ-ray detector, total absorption detectors and total energy detectors.

3. The multiplicity is defined as the total number of transitions needed to reach the ground state. For the majority of nuclei at E^* close to S_n, the γ-multiplicity can vary between 2 and 6.

4.5.2.2 High resolution γ-ray detectors

The most used detectors in γ-ray spectroscopy are the scintillators (NaI, BaF_2, BGO) and the semiconductor diodes (Ge(Li), Si(Li), HPGe). From these detectors the best energy resolution is obtained for the germanium detectors.

Using high-resolution γ-ray detector, the capture cross-section is determined by measuring all primary γ-rays depopulating the capture state [Saito 03] or alternatively, by measuring all γ-rays feeding the ground state proposed by [Coceva 94]. Certainly, this technique is applicable only for the nuclei with relatively simple and well known level scheme for which all capture γ-rays are known and can be resolved. Due to a relatively high Ge(n, γ) cross section, germanium detectors are sensitive to neutrons. In addition, the time resolution of these detectors is about 10 ns, even using special selection criteria [Mihailescu 04]. Therefore, germanium detectors are not suitable for capture measurements in a high neutron flux, the main effect on the detector performance being an increase of the leakage current that leads to a degradation of the energy resolution. However, germanium detectors are used for resonance spin and parity assignment, based on the low-level population method and on primary γ-ray intensities [Gunsing 97][Zanini 00].

4.5.2.3 Total absorption detectors

The total absorption detectors rely on the collection of all γ-rays emitted in a capture event. The ideal detector for such measurements is a 4π-detector that surrounds the sample in order to absorb the complete γ-rays cascade with an efficiency of nearly 100%. The most advanced detector for neutron capture experiments is the DANCE detector at Los Alamos Neutron Science Center [Reifarth 05]. It consists of up to 160 inorganic high-density BaF_2 crystals. These crystals detect γ-rays following neutron capture with high efficiency (about 86% at 1 MeV). The γ-cascade detection efficiency is around 98%. Its high segmentation enables gamma multiplicity measurements and high counting rate. The fast timing allows precise γ-γ coincidence and TOF measurements. Similar 4π BaF_2 arrays have been build at CERN (n_TOF) [Guerrero 09] and at Forschungszentrum Karlsruhe for capture measurement up to 220 keV [Heil 01]. Due to the difference of multiplicity and total energy of the detected cascades originating from (n, γ), $(n, n'\gamma)$, and $(n, f\gamma)$ events, most of the contaminant reactions can be removed. For the same reason, it is also possible to distinguish the "internal" γ-rays coming from the barium itself. The main drawback of this kind of 4π-detector is the overwhelming cost.

4.5.2.4 Total energy detectors

The total energy detection principle is based on the use of a low efficiency detection system with a γ-ray detection efficiency ϵ_γ which is assumed to be proportional to the γ-ray energy E_γ:

$$\epsilon_\gamma = k \cdot E_\gamma \tag{4.22}$$

When the γ-ray detection efficiency of such a detector is very small ($\epsilon_\gamma \ll 1$), such that essentially only one γ-ray out of the capture cascade is registered at a time, the efficiency to detect a capture event can be approximated by:

$$\epsilon_c = 1 - \prod_i (1 - \epsilon_{\gamma_i}) \approx \sum_i \epsilon_{\gamma_i} \tag{4.23}$$

with i the number of γ-rays emitted during the capture event.

Under these conditions, the detection efficiency for a capture event ϵ_c is directly proportional to the total energy released in the capture event E^* (the sum of the neutron binding S_n and the neutron kinetic energy E_n in the center of mass):

$$\epsilon_c \approx k \sum_i E_{\gamma_i} = k \cdot E^* = k(E_n + S_n) \tag{4.24}$$

The probability of detecting a capture even ϵ_c is then independent of the actual cascade path. The determination of the radiative capture in this way is known as total energy detection principle.

In practice, the proportionality factor is known for the so-called Moxon-Rae detector by a proper design of the detector [Moxon 91]. In this detector the capture γ-rays eject electrons from a layer of the element, usually made of carbon, called convector. These electrons are then detected by a very thin plastic scintillator. The linear dependence of the efficiency of the γ-energy is determined by the linearity of the convolution between the electron production cross-section and the electron transmission converter. However, the use of these type of detectors has been abandoned due to the non-proportionality bellow 1 MeV, the strong influence on the final response of the photon transport in the sample and the low efficiency [Corvi 94].

An alternative to the Maxon-Rae detector is the Pulse Height Weighting Technique (PHWT) by means of the so-called Weighting-Function (WF). This technique was first applied by Macklin and Gibbons using C_6F_6 detectors [Macklin 67]. The idea is to use non-proportional detectors and achieve the proportionality of the detection efficiency with energy mathematically by weighting the response function of the detector with an appropriate function. Nowadays this technique is often used in neutron-induced capture cross-section measurements but with less neutron sensitive C_6D_6 detectors, e.g. at Gelina (IRMM) [Borella 07b], at n_TOF (CERN) [Plag 03, TAIN 02], and by CENBG group [Wilson 03, Boyer 06].

4.5.2.5 Experimental capture cross section of ^{233}U

The quantity determined in a neutron capture experiment is the capture yield, i. e. the fraction of neutrons incident on a sample, which undergo a (n,γ) interaction. The capture yield $Y_{capt,U}(E_n)$, with $Y_{capt,U}(E_n) \in (0,1)$, according to eq. 4.13, for the first interaction can be written as:

$$Y_{\gamma,U}(E_n) = \left(1 - e^{-n_U \sigma_{tot,U}}\right) \frac{\sigma_{\gamma,U}}{\sigma_{tot,U}}(E_n) \approx \begin{cases} n_U \sigma_{\gamma,U} & if \quad n_U \sigma_{tot,U} \ll 1 \\ \sigma_{\gamma,U}/\sigma_{tot,U} & if \quad n_U \sigma_{tot,U} \gg 1 \end{cases} \tag{4.25}$$

where $\sigma_{\gamma,U}$ is the capture cross-section of ^{233}U.

The two limiting cases are approximations for thin and thick samples, respectively. Additional terms must be added to this yield coming from neutrons that are scattered one or more times in the sample and surroundings and subsequently captured. This multiple scattering effect has to be taken into account in the R-matrix analysis code. Since the efficiency and solid angle of the capture detector do not exceed a few percent, the measured TOF spectra need to be normalized by a factor N. The parameters determining the normalization factor are difficult to be defined in an absolute way. Therefore, it is preferable to be deduced from capture measurements at energies where capture yield is accurately known. At Gelina facility, three methods can be applied:

- normalization at thermal neutron energy, for capture reactions where the thermal capture cross-section is known with high precision [Brusegan 79]. This normally change the experimental conditions if the experiment is taking place at a longer flight path since is needed a lower operating frequency of the accelerator.

- normalization to one ore more resonances of the nucleus under investigation. When the radiation width dominates the total natural line width, one can determine the capture area from transmission measurements. One needs a resonance with $\Gamma_n \ll \Gamma_\gamma$ that is strong enough to be observed in a transmission measurement, such as the 1.15 keV resonance of ^{56}Fe [Perey 86] and the 2.25 keV resonance of ^{60}Ni [Corvi 02].

- normalization using the so-called "saturated" resonance method. This refers to a resonance, where the thick sample approximation is valid in the peak of the resonance and where the capture yield is no more proportional to the capture cross section but to the ratio of the capture and the total cross section. The measured resonance shape has then a flat top and from this characteristic shape the normalization constant can be extracted. Often an isotope does not have such a large resonance or is not available as a thick sample. For a resonance with a capture width much larger than the neutron width, the normalization is almost independent of the resonance

parameters [Corvi 02, Borella 03]. In this case the normalization is determined by measuring the first saturated resonance of ^{197}Au (at 4.9 eV) or of ^{109}Ag (at 5.1 eV). Since only the strong, saturated resonance needs to be recorded, the normalization measurement with gold or silver lasts in general much shorter than the actual measurement.

Applying the last method, when it is possible, to a resonance belonging to the same isotope as the one under investigation, has the advantage that all the experimental conditions remain unchanged and no auxiliary measurements are required. This is referred as an internal normalization. Consequently, systematic uncertainties due to geometry and in some cases to the WF are largely reduced. This was demonstrated in the study of the $^{232}Th(n,\gamma)$ reaction [Borella 06].

4.5.2.6 C_6D_6 γ-ray detectors

Since neither neutrons nor γ-rays are charged particles their detection efficiency is low and it is difficult to discriminate between them especially when they are both present. Neutron induced capture cross section measurements in the resonance region are mostly done using γ-ray detectors with good timing characteristics and with low sensitivity to neutrons such as C_6D_6 liquid scintillators [Wilson 03, Borella 07b]. Nevertheless, neurons may scattered in the liquid scintillator, and the recoil nuclei may be detected, but since the pulse widths for neutrons are wider in time than for γ-rays thus doing that the neutrons emitted after fission to be discriminated using the difference in detected pulse shape. The energy resolution of this type of detectors does not allow the selection of the individual primary γ-rays because they interact with the detector via the Compton scattering process. The purpose of this detector is to accurately determine the number of (n,γ) events produced in a target by counting the γ-ray cascades using the WF method as mentioned in Section 4.5.2.4.

Neutron capture experiments with C_6D_6 scintillation detectors for the prompt capture γ-ray cascade [Plag 03, Borella 07b] rely on the validity of the PHWT, by which the detection efficiency becomes independent of the cascade multiplicity. Application of the PHWT requires both the time of arrival and the energy deposited in the γ -ray detector for each recorded event [Borella 05].

These detectors are unique for their very low sensitivity to scattered neutrons as compared to other γ-ray detectors. The latest reports on C_6D_6 detectors said that they have the lowest neutron sensitivity that has ever been achieved [Koehler 00, Plag 03]. Also, C_6D_6 scintillators are known for their very good Pulse Shape Discrimination (PSD) proprieties that allow neutron-γ discrimination. This technique is used in this work and the principle is detailed in many references, as [Chalupka 77, Perkins 79].

Because of the very low atomic numbers of the components of the scintillating material (C and D), Compton scattering is the predominant γ process inside the scintillator cavity

cell. Considering the conservation of the liner momentum and total energy we can obtain the equation of the Compton scattering:

$$E_\gamma = \frac{E_\gamma}{1 + (E_0/mc^2)(1 - cos\theta)} \tag{4.26}$$

where:

- E_0 and E_γ are the energies of the incident and scattered photon respectively,
- $m_e.c^2$ = 0,511 MeV is the rest energy of the electron, and
- θ is the angle of deflection for the photon (see Figure 4.10).

The amount of energy exchanged varies with angle, and is given by the formula:

$$E_{e^-} = E_0 - E_\gamma = \frac{E_\gamma^2(1 - cos\theta)}{mc^2 + E_\gamma(1 - cos\theta)} \tag{4.27}$$

When θ approaches zero, no energy is transferred to the electron. The maximum amount of energy is transferred when θ approaches π and is called the Compton edge.

Consequently, C_6D_6 detectors are clearly not suitable as γ-ray spectrometers: the output response for a given input γ-ray is a distribution covering all energies (the Compton plateau) up to the maximum energy of the Compton electron, the Compton edge. Note that the photoelectric peak is invisible. Figure 4.10(b) shows the response for a γ-ray with E_0=661 keV.

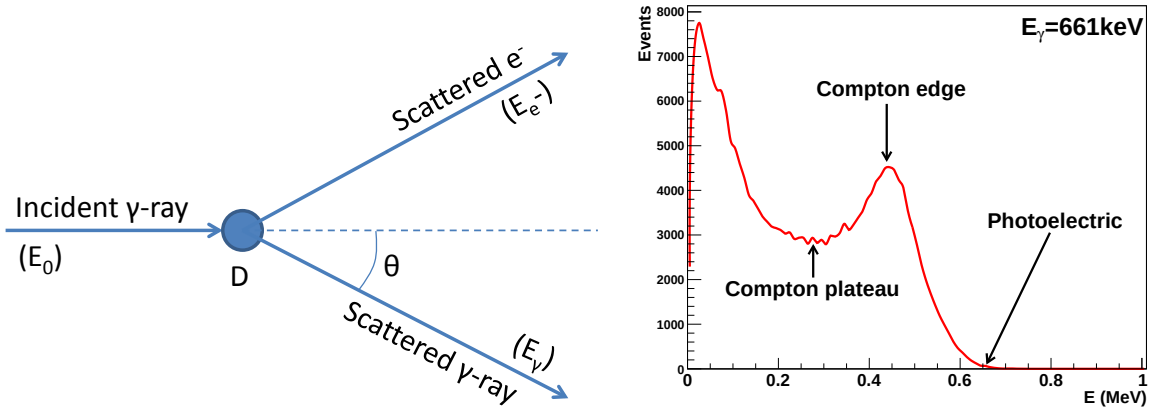

(a) (b)

Figure 4.10: (a) Compton scattering diagram (b) Example of an experimental energy spectrum for an incident γ-ray E_0=661 keV obtained with C_6D_6 scintillator.

The detection of the γ-rays produced in the $^{233}U(n,\gamma)$ reaction event is accomplished by an efficient array of six cylindrical C_6D_6 detectors, placed around the ^{233}U IC, perpendicular to the neutron beam. The distance between the center of target and the C_6D_6 is about 12 cm. Each scintillator cell cavity has a diameter of 106 mm diameter and a thickness of 76.2 mm. Additional technical data are given in Appendix B.1. Each C_6D_6 detector consists of a liquid scintillating organic material which is optically coupled to a photomultiplier via a light guide as illustrated in Figure 4.11.

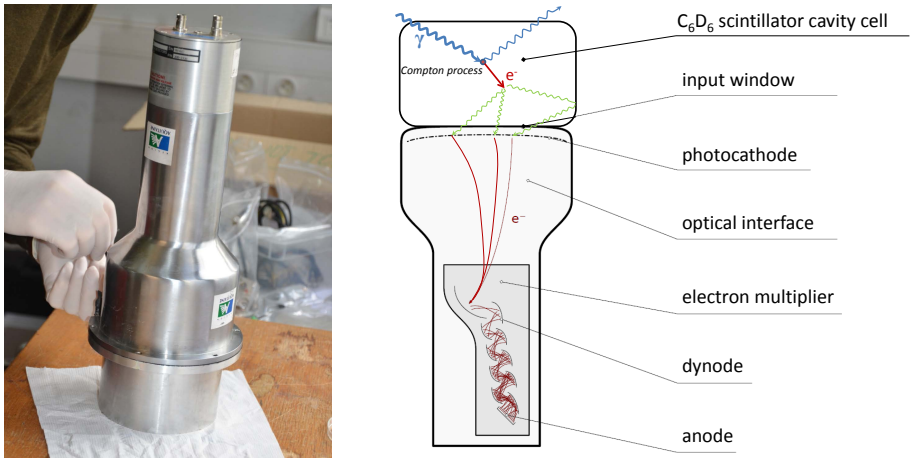

(a) (b)

Figure 4.11: (a) Picture of one C_6D_6 detector used in our experiment: a module consists of a C_6D_6 cavity cell, a photomultiplier tube and a voltage divider. (b) Generation of the electronic signal in the anode for a Compton event.

However, in contrast to a total absorption 4π-detector, it is not possible with C_6D_6 detectors to distinguish whether the detected γ-rays originate from the (n,γ) reaction, the radioactive background, or from competing reaction channels, e.g. from fission or inelastic scattering.

4.5.2.7 Background contribution

The background is one of the most important characteristics that has to be considered at TOF Gelina facility, since it may strongly affect the capture cross-section measurements.

Two types of background sources are present at Gelina: the accelerator background, related to the configuration of the beam line and to the neutron production method (present only with the beam of the experimental flight path), and a sample-related background. The first one is an intrinsic characteristic of the facility and is independent

of the single measurement done, while the second one strictly depends on the sample being measured. The various background components act differently, depending on the type of detector used in measurements and type of reaction, e.g. in particular, neutron capture measurements are greatly affected by the γ-ray background while fission set-up is very sensitive to the neutron background and relatively intenseγ-rays.

The background related on the sample for capture measurements consists of tree contributions [Schillebeeckx 12b]:

- a time dependent component due to ambient radiation and possible long-lived radioactivity in the sample and surroundings,
- a time dependent component dependent on the experimental set-up but independent of the sample, and
- a time dependent component depending on the sample characteristics.

The first component can be estimated with a good accuracy from measurements just after the accelerator is switched off, or in a TOF region where the neutron flux is negligible. The background as a function of TOF can be determined by a proper combination of the operating frequency and filters, applying the black resonance technique. Ideally, the black resonances have a large capture to scattering cross-section ratio and a total width that is larger than the resolution. The elements which can be used as black resonance filters are Cd, Ag, W, Mo, Co, Al, Na and S. Unfortunately, the presence of both the sample and black resonance filter will alter the background [Syme 82]. Nevertheless, the best accuracy is obtained by measurements with fixed background filters in the beam [Borella 07b, Lampoudis 13]. Using fixed background filters the impact of the material placed in the beam can be taken into account and the stability of background level can be controlled at any time.

The second component results from the neutrons which are scattered by the experimental set-up assembly inside the measurement flight station and by scattered neutrons at the other flight paths. The neutron sensitivity of the C_6D_6 detectors is defined as the probability that a scattered neutron from the environment is captured in the assembly, creating a signal relative to the γ-ray detection probability. One has to distinguished between a direct and a delayed component:

- the direct or prompt component originates from scattered neutrons that cause an immediate capture reaction in the detector assembly.
- the delayed component is due to neutrons that scatter from the aluminum, enter the detector or measuring station and slow down in the construction material of the detector or the experimental set-up before they create a capture reaction in the detector.

These contributions can be subtracted from measurements without a sample in the beam. More details are given at the end of this section in the aluminum contribution paragraph.

The last component is the most difficult one to be quantified. The principle is the same like in the case of second component, but this component depends on the neutron and γ-ray scattering proprieties of the sample itself. In this case, the neutron sensitivity is the detector response due to neutrons which are scattered from the sample and create a capture reaction in the sample-detector environment, an information that it cannot be determined experimentally with the experimental set-up used by us, but it can be evaluated by MCNP or Geant4 simulation codes.

Since potential scattering is always present and for all resonances $\Gamma_n > 0$, neutron scattering always occurs. This contribution cannot be determined experimentally. One way to estimate the background due to scattered neutrons by ^{233}U is by additional measurements with material for which the contribution due to capture can be neglected, e. g. heavy element ^{208}Pb (capture cross section is rather low and the reaction rate in the keV region is almost entirely due to sample scattered in-beam γ-rays) or carbon [Schillebeeckx 12a]. To separate the direct from the delayed component several measurements using various black resonance filters are required.

The sample dependent background due to the neutron sensitivity of the detection system is a systematic effect which can create a substantial bias if is not correctly into account in the data reduction or analysis. The best solution is to reduce as much as possible the neutron sensitivity by a proper design of the detection system [Plag 03] and to avoid scattering material close to the detection system. That is way the experimental set-up use in the $^{233}U(n,f)$ and $^{233}U(n,\gamma)$ cross sections measurements was specially design to reduce the neutron sensitivity effect.

The second and third components may be influenced by overlap neutrons. This impact depends on the operating frequency and overlap filter that is used [Macklin 91].

Aluminum contribution

One important measurement that has to be done is the measurement of the neutron background without the sample in the neutron beam, in particular the one related to the neutron induced capture and elastic scattering from the IC detector windows and electrodes. The yield and experimental count rate for (n,γ) reaction on ^{27}Al foil is:

$$Y_{\gamma,Al}(E_n) = \frac{C_{\gamma,Al}(E_n)}{\epsilon_{\gamma,Al}(E_n)\cdot\phi(E_n)\cdot S} = \left(1 - e^{-n_{Al}\sigma_{tot,Al}}\right)\frac{\sigma_{\gamma,Al}}{\sigma_{tot,Al}}(E_n) \tag{4.28}$$

$$C_{\gamma,Al}(E_n) = \epsilon_{\gamma,Al}(E_n)\cdot\phi(E_n)\cdot S\cdot Y_{\gamma,Al}(E_n) \tag{4.29}$$

where:

- $\epsilon_{\gamma,Al}(E_n)$ is the efficiency of the C_6D_6 detector to detect a γ-ray event coming from neutrons captured by Al material,
- n_{Al} is the thickness of the ^{27}Al foil (at/b),
- $\sigma_{\gamma,Al}$ is the capture cross-section of ^{27}Al, and
- $\sigma_{tot,Al}$ is the total cross section of ^{27}Al.

The yield and experimental count rate for (n,n) reaction on ^{27}Al foil is:

$$Y_{n,Al}(E_n) = \frac{C_{n,Al}(E_n)}{\epsilon_{n,Al}(E_n)\cdot\phi(E_n)\cdot S} = \left(1 - e^{-n_{Al}\sigma_{tot,Al}}\right)\frac{\sigma_{n,Al}}{\sigma_{tot,Al}}(E_n) \tag{4.30}$$

$$C_{n,Al}(E_n) = \epsilon_{n,Al}(E_n)\cdot\phi(E_n)\cdot S\cdot Y_{n,Al}(E_n) \tag{4.31}$$

where:

- $\epsilon_{\gamma,Al}(E_n)$ is the efficiency of the C_6D_6 detector to detect a γ-ray event coming from neutrons scattered by Al material, and
- $\sigma_{n,Al}$ is the neutron cross-section of ^{27}Al.

The total background contribution from ^{27}Al neutron-induce reactions seen by the C_6D_6 detectors will be:

$$C_{Al}^{n,\gamma}(E_n) = \phi(E_n)\cdot S\cdot\left[Y_{\gamma,Al}(E_n)\cdot\epsilon_{\gamma,Al}(E_n) + Y_{n,Al}(E_n)\cdot\epsilon_{n,Al}(E_n)\right] \tag{4.32}$$

These contributions can be easily subtracted from the data of interest by doing a background measurement using identical aluminium foil like the ones for the ^{233}U sample (the "dummy" chamber) and placed in the same geometry inside the fission ionisation chamber. Since the background is very strong when compared to the signal of interest, the background measurement with the "dummy" chamber should last as long as the ^{233}U measurement.

4.5.2.8 The VETO method for the capture cross section of ^{233}U

Neutron capture measurements on fissile actinides are complicated by the presence of prompt γ-rays arising from low energy neutron-induced fission, which competes with neutron capture.

The challenging issue in this experiment is the discrimination between γ-rays coming from fission and γ-rays coming from capture reaction. As mentioned before, the γ-rays produced in capture reaction are detected by an efficient array of C_6D_6 scintillators. Fission events are obtained by doing a coincidence measurement between the FF detected in the IC and the prompt γ-rays detected by the C_6D_6 detectors. The capture events are identified with anti-coincidence measurement, a VETO with the FF. The VETO method is not ideal since the FF detection is not 100 %. Indeed, some FF are affected by back scattering or self-absorption in the target itself. The undetected fission event will then be interpreted as capture event. A correction has to be applied with respect to the efficiency of the IC that should be high and known with a high precision.

The experimental set-up prepared for the neutron capture of ^{233}U measurement together with a scheme of the VETO method are illustrated in Figure 4.12. The block diagram of the electronics used for this experiment in a reduced geometry, for only 4 fission chambers (4 ^{233}U samples) and 4 C_6D_6 detectors, is shown in Figure 4.13 for the read out of the fission chambers and C_6D_6 detectors.

Neutron reactions of ^{233}U in this experiment

The experimental count rate for the prompt fission neutrons $C_U^{n-fis}(E_n)$ and prompt fission γ-rays $C_U^{\gamma-fis}(E_n)$ $^{233}U(n,\gamma f)$, $^{233}U(n,nf)$ are obtained from:

$$C_U^{\gamma-fis}(E_n) = \epsilon_{\gamma-fis,U}(E_n) \cdot \phi(E_n) \cdot S \cdot Y_{fis,U}(E_n) \tag{4.33}$$

$$C_U^{n-fis}(E_n) = \epsilon_{n-fis,U}(E_n) \cdot \phi(E_n) \cdot S \cdot Y_{fis,U}(E_n) \tag{4.34}$$

where

- $\epsilon_{\gamma-fis}(E_n)$ is the efficiency of the C_6D_6 detector to detect a γ-ray event coming from fission event,
- $\epsilon_{n-fis}(E_n)$ is the efficiency of detecting γ-ray event coming from the prompt fission neutron event, which is removed by VETO, and
- $Y_{fis,U}(E_n)$ is the fission yield given by eq. 4.17.

Therefore these fission γ-rays has to be corrected from the capture spectrum.

Another contribution is the elastic scattering $^{233}U(n,n)$. The count rate in this reaction is:

$$C_{n,U}\left(E_n\right) = \epsilon_{n,U}\left(E_n\right) \cdot \phi\left(E_n\right) \cdot S \cdot Y_{n,U}\left(E_n\right) \tag{4.35}$$

where

- $\epsilon_{n,U}\left(E_n\right)$ is the efficiency of the C_6D_6 detector to detect a γ-ray event coming from fneutron scattering on ^{233}U, and
- $Y_{n,U}\left(E_n\right)$ is the elastic scattering yield given by a similar equation as for the fission yield eq. 4.17.

The total contribution of ^{233}U will be given by:

$$C_U^{n,\gamma}\left(E_n\right) = \phi\left(E_n\right) \cdot S \cdot [\epsilon_{n,U}\left(E_n\right) \cdot Y_{n,U}\left(E_n\right) +$$

$$+ Y_{fis,U}\left(E_n\right) \cdot (\epsilon_{\gamma-fis,U}(E_n) + \epsilon_{n-fis,U}(E_n))\,] \tag{4.36}$$

Coincidence relation

Using the VETO technique, as some fission events are not detected by IC, the γ-fission coincidence count rate is obtained as following:

$$C_U^{coinc}\left(E_n\right) = \phi\left(E_n\right) \cdot S \cdot Y_{fis,U}\left(E_n\right) \cdot (\epsilon_{\gamma-fis,U}\left(E_n\right) + \epsilon_{n-fis,U}\left(E_n\right)) \cdot \epsilon_{IC} \tag{4.37}$$

where we remember that ϵ_{IC} is the efficiency of the IC.

If $\epsilon_{IC}$is known, from this equation we can obtain the fission yield:

$$Y_{fis,U}\left(E_n\right) \cdot (\epsilon_{\gamma-fis,U}\left(E_n\right) + \epsilon_{n-fis,U}\left(E_n\right) = \frac{C_U^{coinc}\left(E_n\right)}{\epsilon_{IC} \cdot \phi\left(E_n\right) \cdot S} \tag{4.38}$$

Anti-coincidence relations

Finally, the γ-fission anti-coincidence count rate is obtained as:

$$C_0^{anti-coinc}\left(E_n\right) = \phi\left(E_n\right) \cdot S \cdot [(1-\epsilon_{IC}) \cdot (\epsilon_{\gamma-fis,U}\left(E_n\right) + \epsilon_{n-fis,U}\left(E_n\right)) \cdot Y_{fis,U}\left(E_n\right)$$

$$+ Y_{\gamma,U}\left(E_n\right) \cdot \epsilon_{\gamma,U}\left(E_n\right) + Y_{n,U}\left(E_n\right) \cdot \epsilon_{n,U}\left(E_n\right)$$

$$+ Y_{\gamma,Al}\left(E_n\right) \cdot \epsilon_{\gamma,Al}\left(E_n\right) + Y_{n,Al}\left(E_n\right) \cdot \epsilon_{n,Al}\left(E_n\right)\,] \tag{4.39}$$

The first line represents the γ-ray contribution from undetected fission events, the second line is the γ-ray contribution from capture and scattering neutrons on ^{233}U, and the third line is the γ-ray contribution due to capture and scattered neutrons on ^{27}Al.

The latest terms will be subtracted from the C_6D_6 spectrum obtained in anti-coincidence measurement thanks the dummy chamber measurement. It is necessary to consider a correction factor k_{Al} that reflects the difference between the measurement with the ^{233}U samples in the ionisation chamber and the measurement with only the aluminium layers. Consequently, aluminum background subtraction anti-coincidence count rate will be:

$$C_1^{anti-coinc}(E_n) = C_0^{anti-coinc}(E_n) - k_{Al} \cdot C_{Al}^{n,\gamma}(E_n) =$$

$$= \phi(E_n) \cdot S \cdot [\,(1-\epsilon_{IC}) \cdot (\epsilon_{\gamma-fis,U}(E_n) + \epsilon_{n-fis,U}(E_n)) \cdot Y_{fis,U}(E_n)$$

$$+ Y_{\gamma,U}(E_n) \cdot \epsilon_{\gamma,U}(E_n) + Y_{n,U}(E_n) \cdot \epsilon_{n,U}(E_n)\,] \tag{4.40}$$

The capture count rate from eq. 4.40 can then be corrected for undetected fission contribution:

$$C_2^{anti-coinc}(E_n) = C_1^{anti-coinc}(E_n) - C_U^{coinc}(E_n)\left(\frac{1-\epsilon_{IC}}{\epsilon_{IC}}\right)$$

$$C_2^{anti-coinc}(E_n) = \phi(E_n) \cdot S \cdot (Y_{\gamma,U}(E_n) \cdot \epsilon_{\gamma,U}(E_n) + Y_{n,U}(E_n) \cdot \epsilon_{n,U}(E_n)) \tag{4.41}$$

One can see that all parasitic terms but $Y_{n,U}(E_n) \cdot \epsilon_{n,U}(E_n)$can be subtracted from the measurements. This last parasitic term cannot be measured directly. That is why it has to be minimized by using a non-neutron sensitive set-up.

If the ϵ_{IC} is perfectly known, the undetected fission subtraction is accurate. But since there are 5 to 20 more γ-rays coming from fission than from capture 1% of uncertainty on efficiency of the IC induces 5-20% of uncertainty on capture cross section. For certain energies, where only the fission resonance is present and no capture resonance, the fission γ-ray contribution is much higher. In this case, 1% of uncertainty of ϵ_{IC} will induce 30-50% of uncertainty on capture cross section. Therefore this parameter has to be determined with a very good precision.

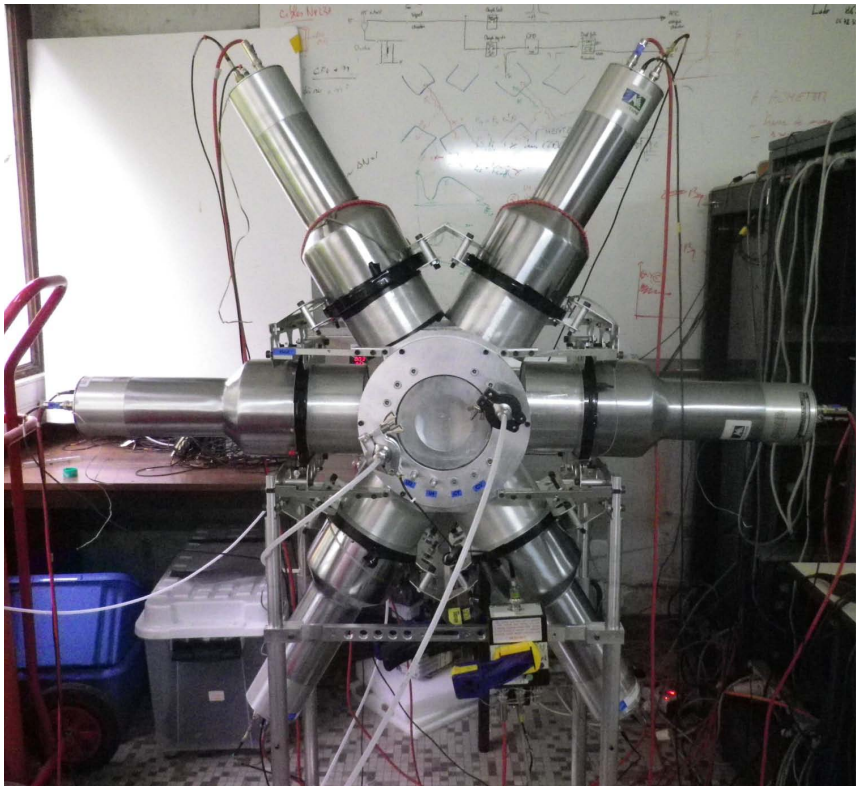

(a)

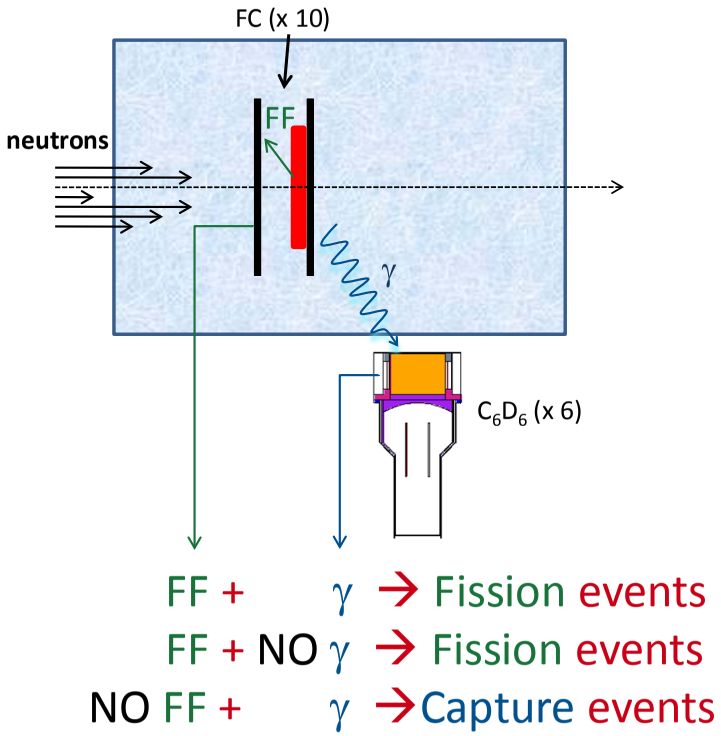

(b)

Figure 4.12: (a) The detection set-up for the measurements of the neutron-induced fission and capture cross sections composed of six C_6D_6 detectors positioned around the IC. (b) The VETO Principal: capture to fission discrimination diagram.

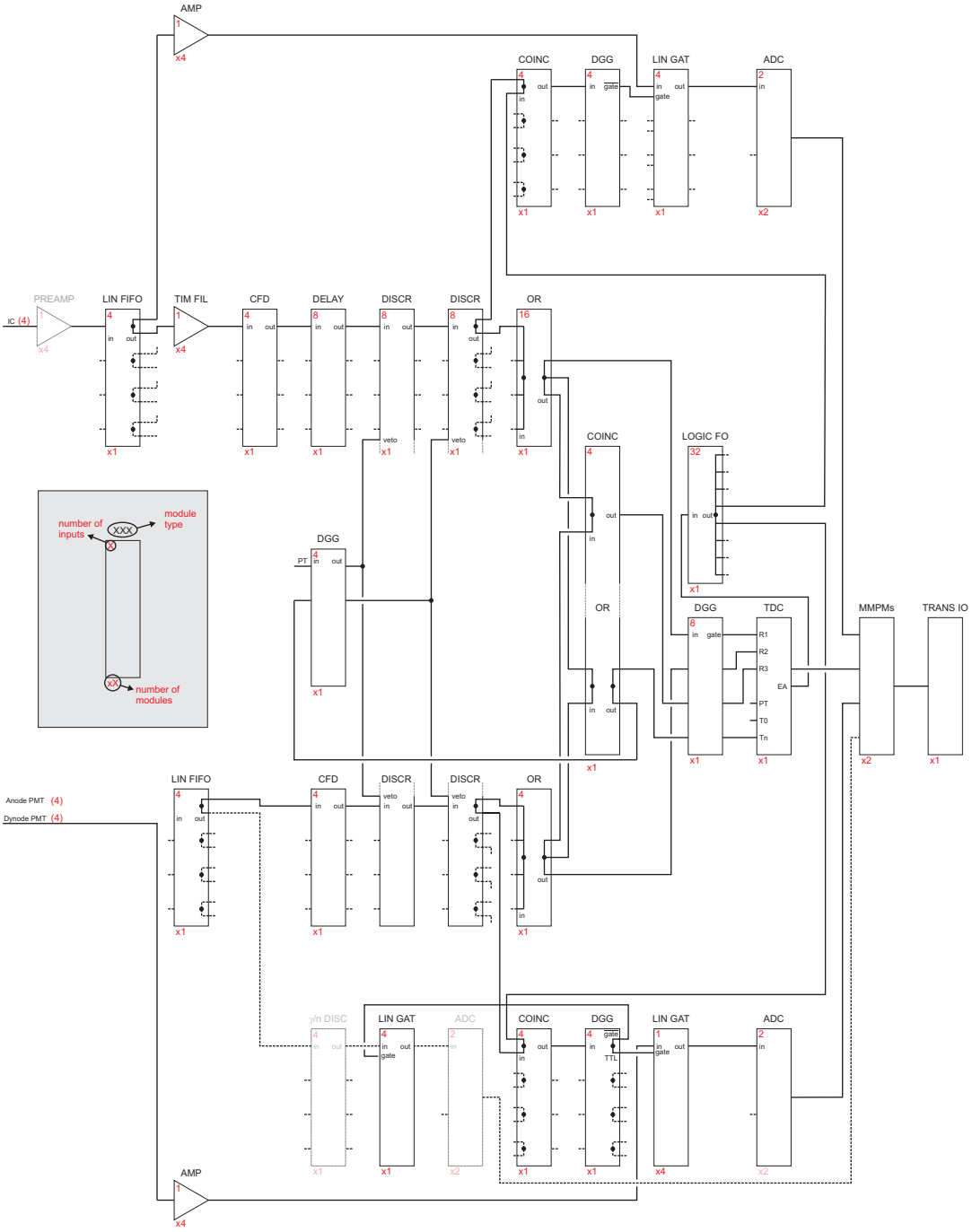

Figure 4.13: Details about the electronics used for the test experiments in reduced geometry, for only 4 fission chambers in the IC and 4 C_6D_6 detectors

4.6 Efficiency of the IC

In fission experiments, the accurate determination of the fission efficiency is rather difficult, especially when using fission detectors of efficiency close to 100 %. The efficiency is limited by the back scattering and self-absorption of the fission fragments (FF) in the target. Therefore the efficiency of the IC is less than 100%, implying that some fission events remain undetected and some of them will be interpreted as capture events.

There are different methods to determine the efficiency of ionisation chamber. The fission efficiency is often determined by using known fission cross section if the neutron flux is given. However, in some cases, the fission cross section is not well known and the neutron flux cannot be measured with sufficient accuracy.

4.6.1 Method for spontaneous fissioning samples

The simplest method to determine the efficiency of an ionisation chamber is applied to spontaneously fissioning nuclei like ^{252}Cf, where the reaction rate depends only on the amount of material. The isotopic contents of a sample can easily be obtained via α-spectrometry. The most important premise for high-resolution α-spectrometry is the availability of good sources. One of the most critical aspects of the sample preparation process is ensuring the uniformity, dryness and thickness of the sample test source. These parameters control the resolution of all the α-peaks that are measured.

Most of these properties apply for sources to be assayed with Si-detectors or in gridded ionisation chambers. The efficiency is determined from the formula:

$$\epsilon_{IC} = \frac{N'_{FF-det}}{N'_{spont.fiss}} = \frac{N'_{FF-det}}{\frac{Y_{sf}}{1-Y_{sf}}} \cdot \frac{\epsilon_\alpha}{N'_{\alpha-det}} \tag{4.42}$$

where

- N_{FF-det} is the number of detected FF,
- $N_{spont.fiss}$ is the number of spontaneous fission emitted by the source,
- Y_{sf} is the proportion of fission decays from the source,
- ϵ_α is the detection efficiency of alpha particles,
- $N_{\alpha-det}$ is the number of alpha particles detected, and
- the prime symbols indicate the quantities subject to dead-time correction.

The main uncertainty sources of this method are the solid angle of the α-spectrometer and the dead-time correction of the fission measurement. For certain nuclei, the spontaneous fission yield may also be a significant source of uncertainty. For example, the yield of ^{252}Cf is known with a 0.25% uncertainty and the one of ^{240}Pu with 3.5% [Tuli 01]. The efficiency uncertainty, using this method, is not better than 1%.

4.6.2 The extrapolation method

For fissile nuclei, the determination of the FF emission angle can be done by extrapolating missing FF using a gridded ionisation chamber. A Frisch Grided Ionization Chamber (FGIC) can been used as FF detector to determine the FF emission angle. In the plane defined by the variables $cos\theta$, it is possible to identify an area A which is unaffected by particle back-scattering and self-absorption. Events belonging to this area show an isotropic angular distribution, which, extrapolated to $\theta = 90^0$, yields the true source strength [Jørgensen 84]. An example of this application is shown in Figure 4.14 [Castineira 13b]. In this situation the uncertainty of the efficiency of the grid ionisation chamber is not better than 1%.

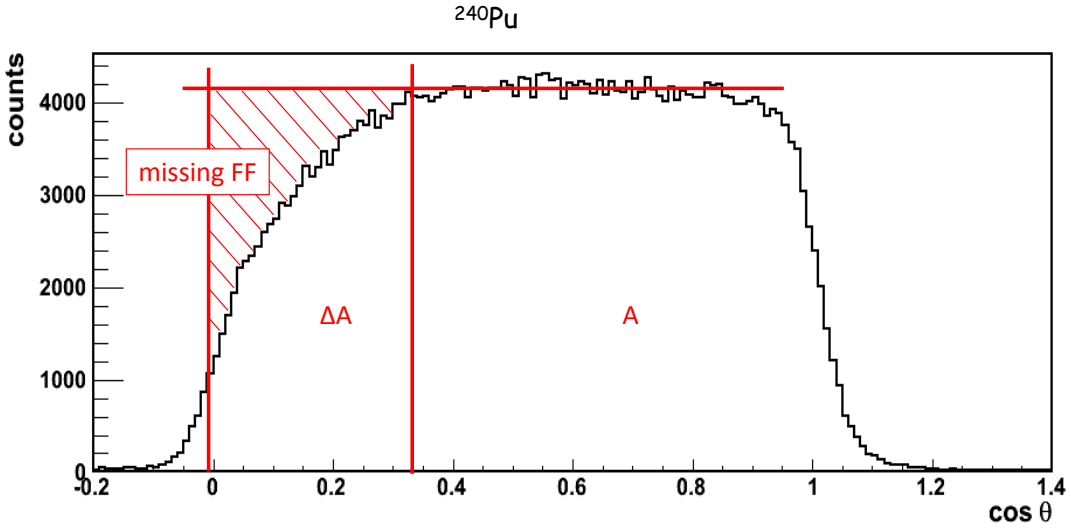

Figure 4.14: The rectangular shape of the $cos\theta$ distribution for ^{240}Pu sample and integrated over all FF obtained with a FGIC detector [Castineira 13b]. The angular distribution of the FF should be uniform along the $cos\theta$ axis.

4.6.3 The ratio method

The ratio method is based on determination of the efficiency of an ionisation chamber relative to standard materials. This method has been extensively used for nearly all experiments of the neutron induce fission and capture cross section of radioactive nuclei, which is a well established standard in the neutron energy range from 0.15 eV to 200 MeV [Carlson 09]. This method, has the advantage of using FGIC detectors in a back-to-back geometry, therefore there is no need of determining the neutron flux impinging the sample under study since it can be assumed to be the same for both sample and the reference material [Castineira 13a]. The IC efficiency is determined using the following equation:

$$\epsilon_{IC} = \frac{N_{FF-det}}{N_{fiss}} = \frac{N'_{FF-det}}{N_{at} \cdot \sigma \cdot \phi} \tag{4.43}$$

where the number of atoms (N_{at}) in the sample are determined by α-spectrometry, and the flux is obtained with a reference material:

$$\phi = \frac{N_{FF-det-ref}}{N_{at-ref} \cdot \sigma_{ref} \cdot \epsilon_{IC-ref}} \tag{4.44}$$

If the ratio method is applied to radioactive standard material, with N_{at-ref} obtained also via α-spectrometry, the efficiency will be defined by:

$$\epsilon_{IC} = \left(\frac{N_{FF-det}}{\frac{N'_{\alpha-det}}{\lambda \cdot \epsilon_\alpha} \cdot \sigma} \right)_{target} / \left(\frac{N_{FF-det}}{\frac{N'_{\alpha-det}}{\lambda \cdot \epsilon_\alpha} \cdot \sigma \cdot \epsilon_{IC}} \right)_{reference} \tag{4.45}$$

It can be noticed that lots of uncertainty sources can be found in this equation. An important uncertainty is the cross-section of the target, that usually is obtained from ENDF [IAEA-NDS 13] with an associated uncertainty. Other sources of uncertainty are coming from α-spectrometry, the dead time normalization, the half-life of the isotope, and the efficiency of the ionisation chamber for the reference material. Using this method, the uncertainty of the efficiency is in the range of few percents.

4.6.4 The prompt fission neutrons method

Another method to determine the fission efficiency is based on the detection of prompt fission neutrons emitted by the FF in coincidence and not with the fission tagging detector (prompt fission neutrons method). This method is much simpler and more accurate

since the number of uncertainty sources is considerably reduced (no reference material, sample mass, solid angle emission or half-life and isotope content needed). The estimation of the IC efficiency is derived from the pulse height spectra from fission events (prompt fission neutrons and prompt γ-rays) in the C_6D_6 scintillators.

$$\epsilon_{IC} = \frac{N_{n-coinc-FF}}{N_{n-total}} \tag{4.46}$$

where

- $N_{n-coinc-FF}$ is the number of neutrons detected in coincidence with a FF, and
- $N_{n-total}$ is the total number of neutrons detected.

Since these quantities are measured in the same experiment, no dead time correction is required. Nevertheless, one has to carefully verify that the detected prompt fission neutrons are free from any contamination (e. g. scattered beam neutrons or wrongly discriminated γ-rays). This requires, however a good discrimination of neutrons and any γ-rays, since it has been shown that a small amount of γ-rays mis-interpreted as neutrons dramatically reduces the quality of multiple scattering-rejection [Ljungvall 04]. Using the prompt fission neutrons method, the accuracy is significantly better, with an uncertainty for the efficiency of the ionisation chamber much less than 1% as we will see later in Section 5.4.

Data analysis

Chapter 5

Data analysis and interpretation

The measurement of the capture cross section of ^{233}U is a very complex and complicated experiment. Most of the issues in this measurement are also of major importance like the efficiency of the IC or the α-FF discrimination. Other difficulties are related to a proper correction of the backround from the neutron capture in experimental setup which requires additional measurements. Therefore, it is important to measure, found, check and solve every parameter before a full scale experiment could be carried out. This chapter describes the procedures followed in the analysis of different experimental results obtained from various tests realized.

5.1 IC response for ^{252}Cf

The energy deposition in gas of α-particles and FF was obtained using a ^{252}Cf source. The sample is an electrodeposited californium oxide of 20 μg with a diameter of 5.04 mm, centered on nickel-clad platinum foil and fixed to the supporting foil by diffusion-bonding at 1000°C so that in high vacuum conditions loss by flaking is prevented. The sample is covered with 50 $\mu g/cm^2$ gold to prevent loss of ^{252}Cf by recoil or sputtering. The activity of the sample is of 370 kBq. The technical details of the sample assembly are given in Figure 5.1. The source was placed in the midle of the IC and fixed on pure aluminium support with a diameter of 10.6 cm.

The pulse high spectrum of fission events obtained with the IC only (without coincidence with the C_6D_6 detectors) and using the ^{252}Cf source is shown in Figure 5.2. The heavy/light parts of the usual FF distribution cannot be seen because of the poor energy resolution, since the width of the IC was chosen to maximize the compactness of the device. The shape is characteristic of FF incomplete energy deposition caused by a path much shorter than the range. This is also because the IC has no Frisch grid, which prevent to discriminated between emission angle. The steep increase at the begining is due to FF emitted normal to the target and with the shortest range in the IC (the

distance between the electrods is 5 mm). Their energy deposition is then quite low. As the emission angle increases, the path lenght and the energy deposition increase too. Furthermore, most FF exit at a grazing angle, so their path lenght is longer than the range. But some of them can be partially absorbed but the sample.

Indeed, one has to realize that such a target is very particular:

- the active sample (^{252}Cf) is much thinner than one atomic layer
- the 50 $\mu g/cm^2$ of gold represents few tenth of nanometers

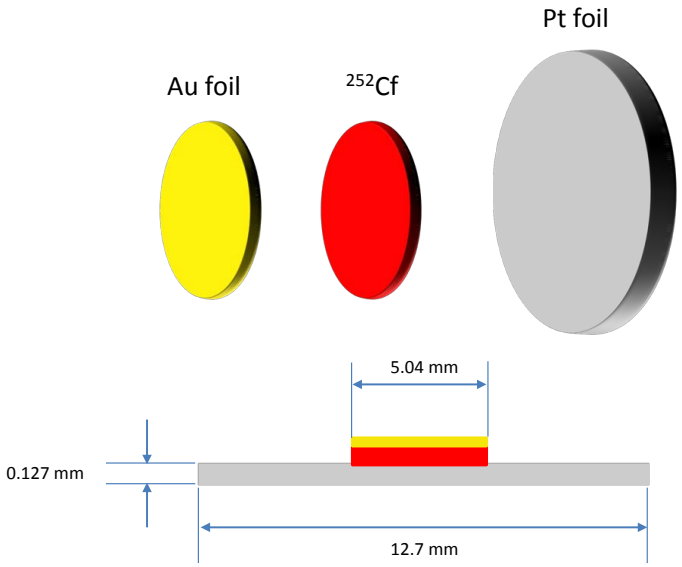

Figure 5.1: The ^{252}Cf spontaneous fission sample technical details.

So the target+gold layer is several orders of magnitude smaller than the backing roughness (peaks, steps, cracks... in the order of micrometer). Depending on the emission point and angle, a FF may lose a small or large part of its energy in the target/gold/backing. The energy deposited in the gas greatly varies, covering all the energy range.

Also an α-particle background is present at low energies, with a typical α energy of 6 MeV ^{252}Cf, whereas the FF energy is an order of magnitude larger. The α-peak forms with FF a deep valley, that we will refer to as the α-FF valley. A detailed description of the pulse height distribution from the IC obtained with ^{252}Cf source is illustrated in Figure 5.3. As previously mentioned, the bottom of the valley is due to FF emitted at grazing angles. The α-pile-up gives a hight-energy tail on the α-peak that reduces the

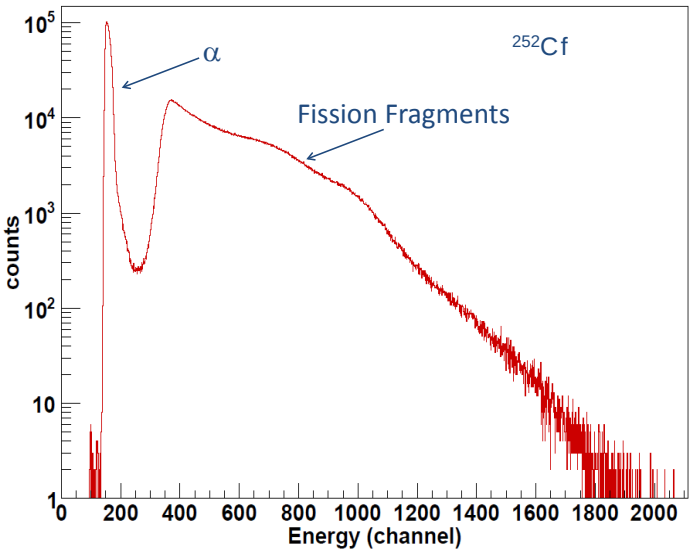

Figure 5.2: Pulse height distribution from the ionisation chamber measurement of ^{252}Cf spontaneous source. The peak at the channel 150 is caused by alpha particles, while the broad distribution above 300 channel is caused by fission fragments.

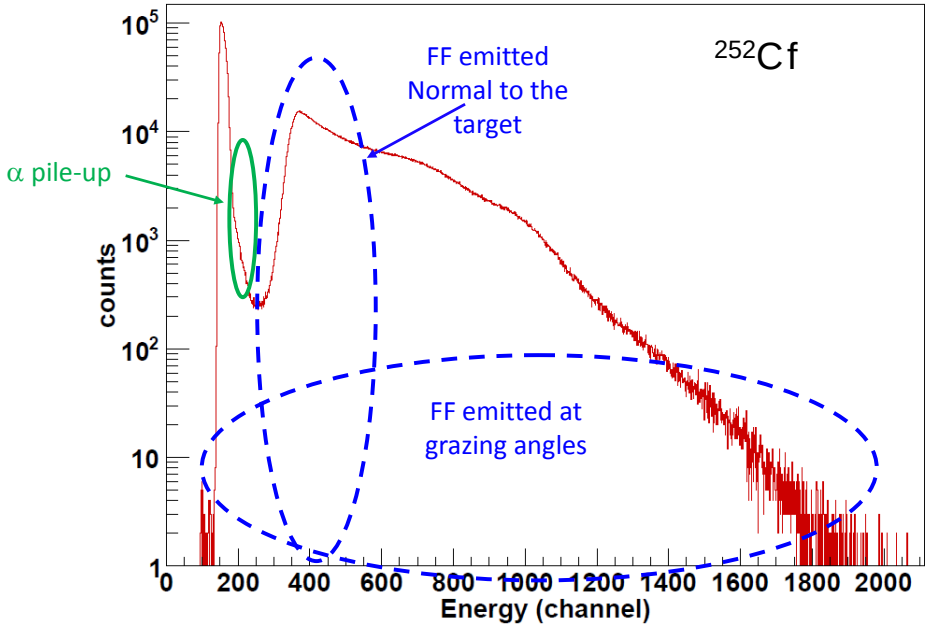

Figure 5.3: Detailed description of the pulse height distribution from the ionisation chamber obtained using ^{252}Cf source. The angular FF distribution and the α-pile-up position are indicated.

width of the α-FF valley, which can even vanish completly. With ^{233}U a much higher α-activity will cause a reduction of the α-FF valley, as will be presented in Section 5.5.

5.2 Detector simulations

The principle of the capture measurement relies on the detection of the γ-rays emitted during the interaction between the neutron beam and the sample. As mentioned before, the lower neutron sensitivity of the C_6D_6 detectors is of advantage, especially since the contribution on γ-rays spectra of neutron scattered on sample is difficult to estimate and subtract. The use of Weighting Functions requires a completes modelisation of the experimental setup to be done, in order to simulate the response of the system. This was done with Monte Carlo simulation code Geant4 [Agostinelli 03]. It includes photon and electron transport in the sample and the experimental set-up.

To obtain reliable results, a detailed geometric description of the sample and the detectors and all the other elements of the experimental assembly influencing the response was reproduced in the simulation. We included not only the active detection volume, but also the aluminum canning, the boron free quartz window, the photo-multiplier (PM), the μ-metal shield which covers the PM to provide an electomagnetic insulation and the flexible teflon tube [1]. All these materials are of great importance for the simulation of the neutron sensitivity [Plag 03, Borella 07b]. Plag et al. discussed in detail the various components contributing to the neutron sensitivity and reported that C_6D_6 detector has the lowest neutron sensitivity that has ever been achieved at this time. The detailed modelled geometry of the experimental set-up is shown in Figure 5.4.

5.2.1 γ-ray efficiency of the C_6D_6 detectors

The simulated response of each detector was treated separately but considering the whole environment. The simulated response $R_{sim}(E_{sim}, E_\gamma)$ represents the energy deposited in the detector, E_{sim}, by a γ-ray of initial energy E_γ. The deposited energy distribution in the sensitive detector volume was simulated for monoenergetic 11 γ-ray energies E_γ in the range from 0.1 to 10 MeV. For each energy, $1 \cdot 10^7$ photons were isotropically emitted starting randomly from the sample volume with a radial probability distribution. In Figure 5.5 is shown a set of simulated responses. One can notice various contributions to the shape of the detector response. While both the photoelectric and Compton effects decrease with increasing γ-ray energy, the pair production increases with increasing energy. The latter process, where the photon can be annihilated in the

1. the teflon tube serves as an expansion volume to compensate the thermal expansion of the C_6D_6

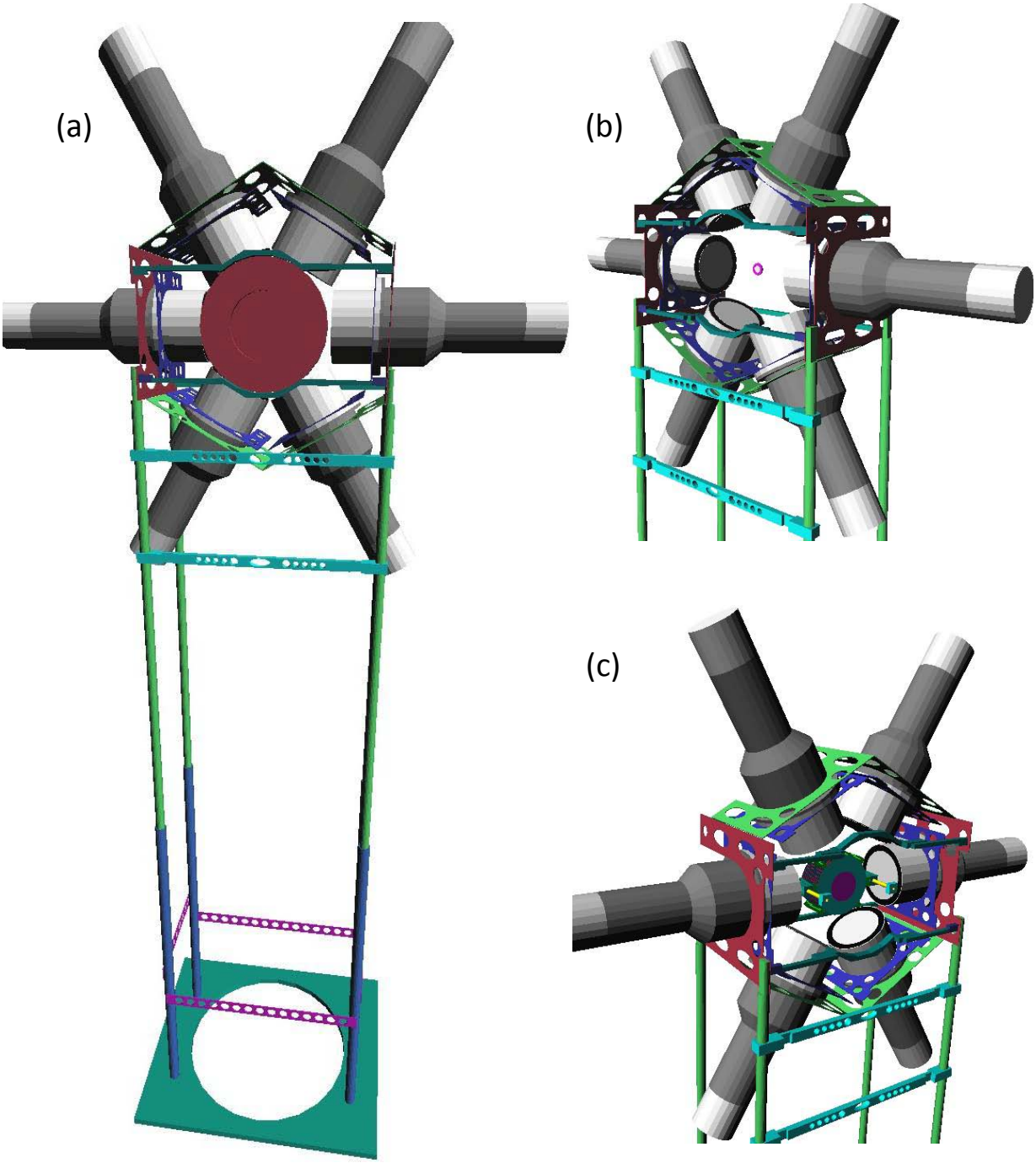

Figure 5.4: Simulation of the complete experimental set-up (a). Details of the experiment when using a point like source (b) or with the ^{233}U targets in the IC (c).

strong nuclear electric field with the formation of an e^-/e^+ pair, is specially characterized by the energy located at $(E_\gamma - 2m_e c^2)$ which corresponds to the double escape peak where both the annihilation photons escape the detector.

As can be seen in the Figure 5.5, simulated response cannot be directly compared with experimental spectra since it does not take into account the experimental resolution. For this purpose, the final response function $R_d(E_d, E_\gamma)$ was obtained by the convolution of the simulated response $R_{sim}(E_{sim}, E_\gamma)$ by a Gaussian function $G(E_d, E_{simu})$ representing the energy resolution function of the detector [Borella 07b]. The detector response function $R_d(E_d, E_\gamma)$ can be written as:

$$R_d(E_d, E_\gamma) = \int R_{sim}(E_{sim}, E_\gamma) \cdot G(E_d, E_{sim}) dE_{sim} \tag{5.1}$$

with the probability that a γ-ray with an energy E_γ results in an observed deposited energy E_d. Figure 5.6 illustrates the final response functions $R_d(E_d, E_\gamma)$ for a set of incident γ-ray energies E_γ. The Gaussian width is energy dependent and therefore, must be determined experimentally in a procedure called resolution calibration. Usually, the resolution broadening of the C_6D_6 scintillators as a function of the deposited energy E_d (in MeV) is given by the relation:

$$\sigma^2_{exp}(E_d) = \left[a + b \cdot E_d + c \cdot E_d^2\right] \tag{5.2}$$

where the free parameters were obtained by a least square fitting procedure from the experimental energy resolution.

5.2.2 Energy and resolution calibration using γ-γ coincidence technique

After the simulations are performed, the next step for the PHWT is to compare the results with the experimental data. This requires the calibration and determination of the resolution of the scintillators.

The usual calibration method of the scintillators is to find the Compton edge. Due to poor resolution of these detectors, it is not easy to be determined. Usually is found at about 80% of the tail of the Compton edge. The resolution function is obtained by the convolution of the simulated spectrum with a Gaussian function adjusted to the experimental spectrum, a similar procedure as discussed in [**?**]. At γ-ray energies below 2.6 MeV standard radio-active sources can be used to determine the response function of the detector. For higher energies the (p,γ) induced reactions on light nuclei

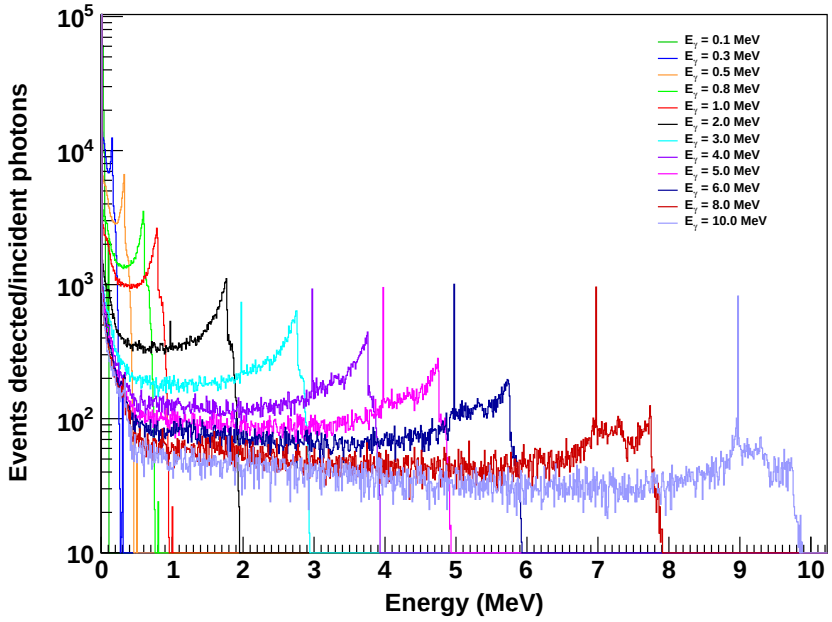

Figure 5.5: Simulated response function of different monoenergetic sources

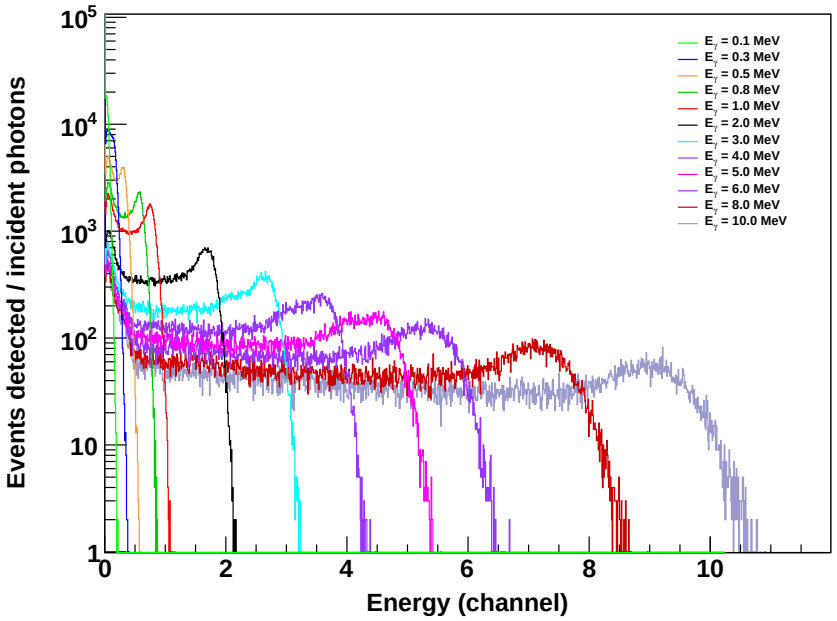

Figure 5.6: Simulated response function

[Gayther 82, Corvi 91, Wilson 03] or capture γ-ray spectra from selected resonances of nuclei near close shells may be used [Perey 86, Borella 05].

Another method to determine the calibration and the resolution function for scintillators can be established by the γ-γ coincidence technique, a similar procedure as described by [Smith 68, Knox 72]. The principle is to measure the Compton effect in coincidence with another detector located at backward angle. Since the energy deposited is dependent of the angle, the γ-γ coincidence with the detector located at 180° will give a precise energy (i. e. the theoretical energy of the Compton edge). The energy resolution can be obtained more easily by fitting the coincidence Compton edge with a Gaussian function. Figure 5.7 shows simulated response using ^{137}Cs source of one scintillator in coincidence with the other five, placed in the geometry which will be used in the final experiment. As expected, the coincidence between the detectors placed at 180° gives the Compton edge located at its theoretical position and the smallest width. A shift and a broadening can be seen on the Compton edge in the other coincidence spectra. Figure 5.8 presents the same simulation for ^{60}Co source. Even for such a source emitting multipleγ-rays, the coincidence method allow to obtain separated Compton edge peaks.

In this work spectra obtained for several standard γ-sources were compared with results from simulations. Figure 5.9 presents the experimental spectra of ^{137}Cs source in single event and in coincidence with a detector at 180°. As can be seen the coincidence spectrum is much easier to calibrate since a narrow peak appears. For the same reason the resolution function is easy to be determined with a simple Gaussian fit. Figure 5.10 shows the same measurement with the^{60}Co source, where the two Compton edges can be discriminated in coincidence method.

This method is a very powerful for the energy and resolution accurate calibration, but like all coincidence methods, it requires long time measurement, or quite intense sources (i.e. in our case several tens of kBq). Nevertheless, thanks to the good energy resolution, the measurement of several sources can be performed in the same time. In addition, this method is less adapted to compact geometries, but is well suited to our symmetrical configuration.

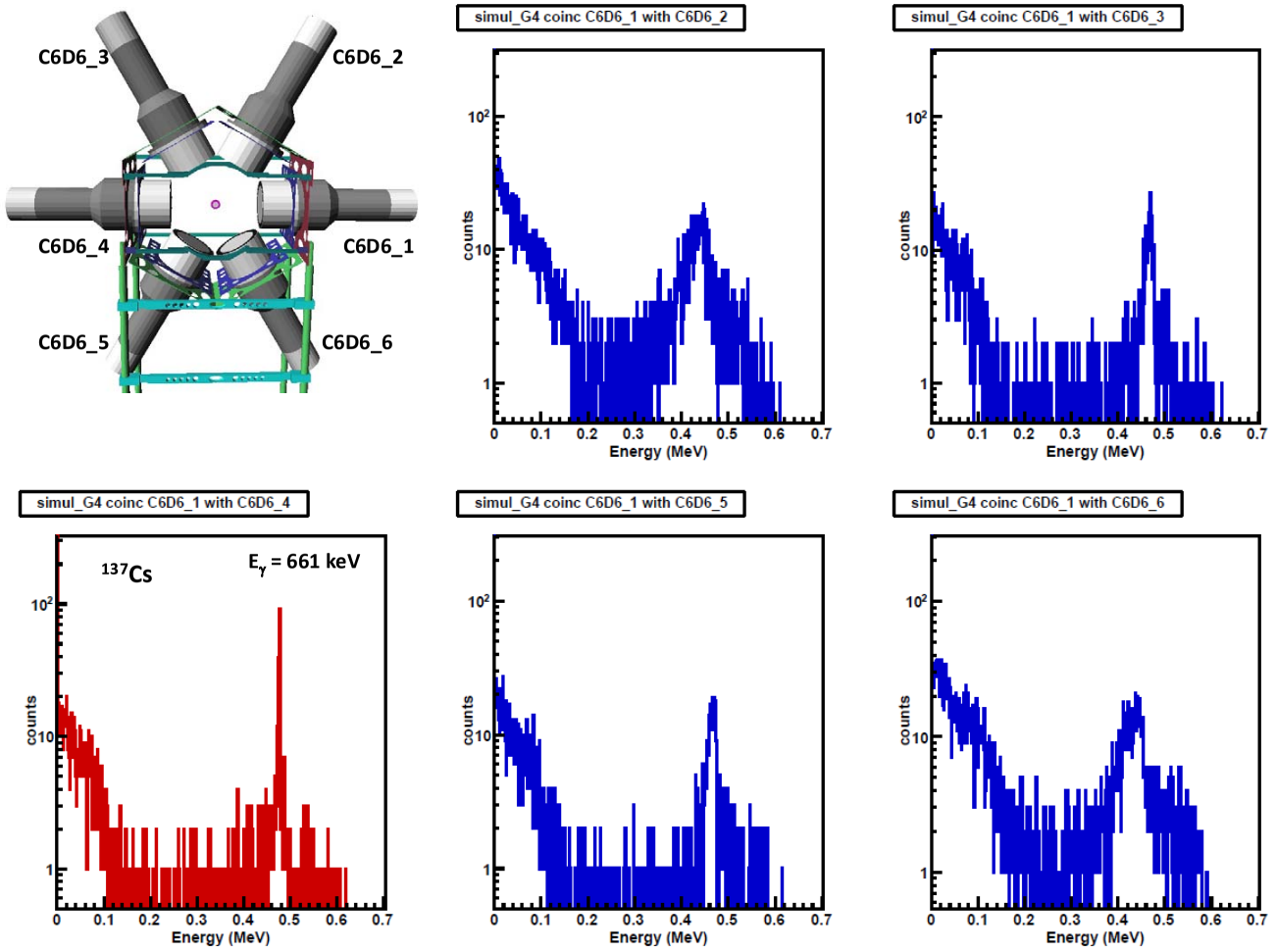

Figure 5.7: Simulated coincidence spectra with ^{137}Cs point like source (10^7 particles). The energy of the γ-ray is 661 keV and the corresponding Compton edge is 477 keV.

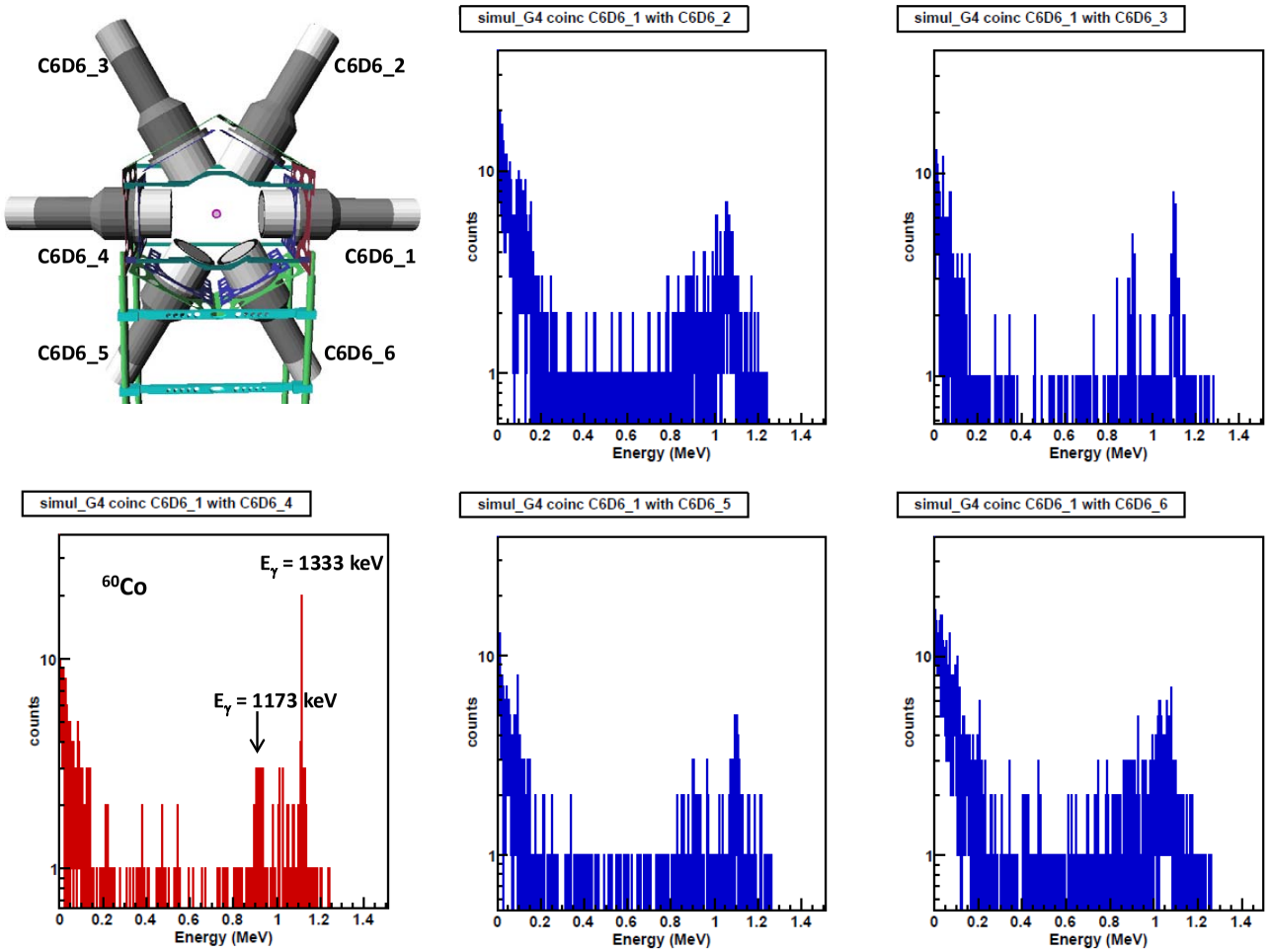

Figure 5.8: Simulated coincidence spectra with ^{60}Co point like source (10^7 particles). The energy of the γ-rays are 1173 keV and 1333 keV and the corresponding Compton edges are 963 keV and 1119 keV respectively.

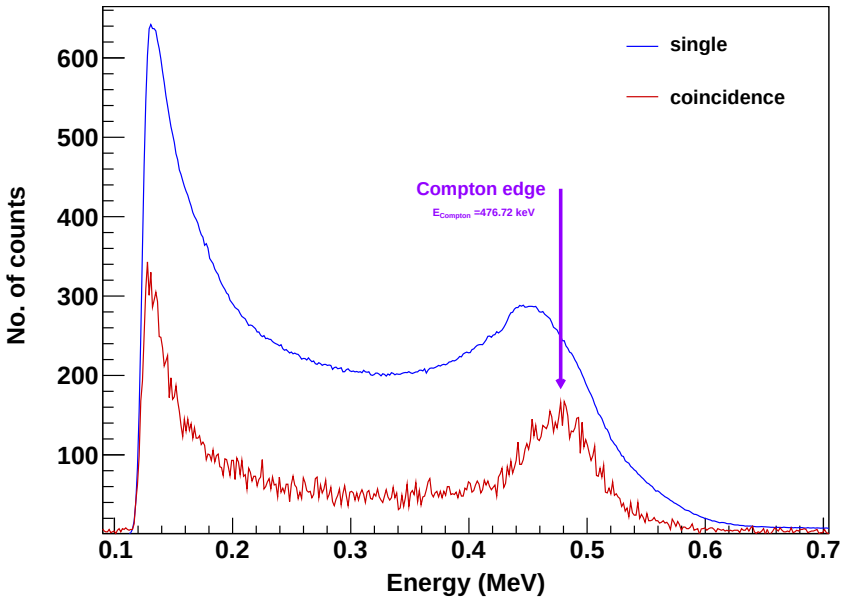

Figure 5.9: Comparison between single and coincidence spectrum for ^{137}Cs source.

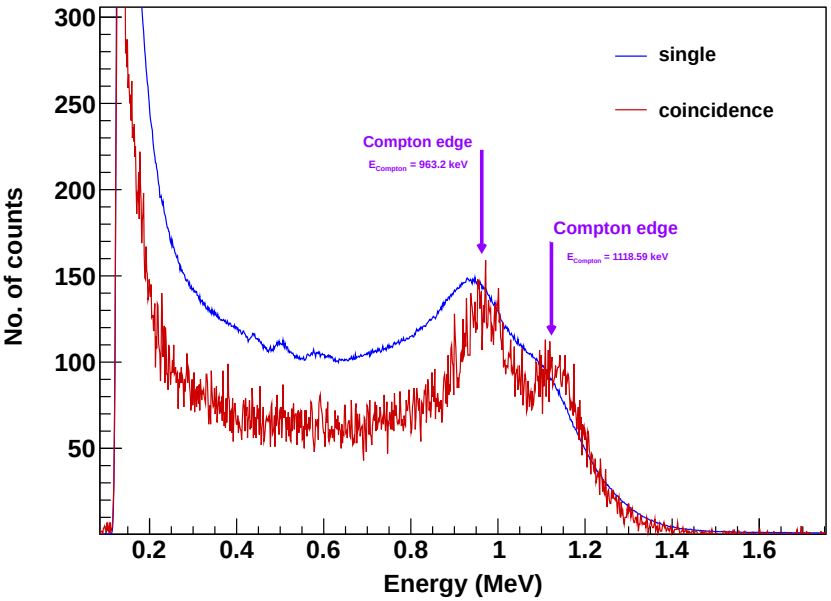

Figure 5.10: Comparison between single and coincidence spectrum for ^{60}Co source.

5.3 Preliminary experiment at Gelina

The first test of the experimental set-up was done at the TOF facility pulsed neutron source Gelina at IRMM. The main purpose of this experiment was :

- to test the electronics scheme
- to determine the response of the experimental set-up
- to test the Ionization Chamber with ^{233}U

The measurement was performed in a reduced geometry using only two C_6D_6 detectors and ^{233}U targets at the 10 m flight path station (center of the IC at 13.55m). As mentioned in previous chapter, this flight length is needed for the required high quality data in the RRR. The beam diameter was fixed to 8 cm, using a combination of Li-carbonate, copper, nickel and lead collimators, to be sure we cover all the deposit diameter. To reduce the contribution of overlap neutrons we have used the Ag and Cd filters placed in the neutron beam for background measurement. The black resonance of cadmium at 0.2 eV allowed to get an estimation of the background in this whole lower energy region by removing completely all thermal neutrons, and among them any overlapping neutrons coming from the previous pulse.

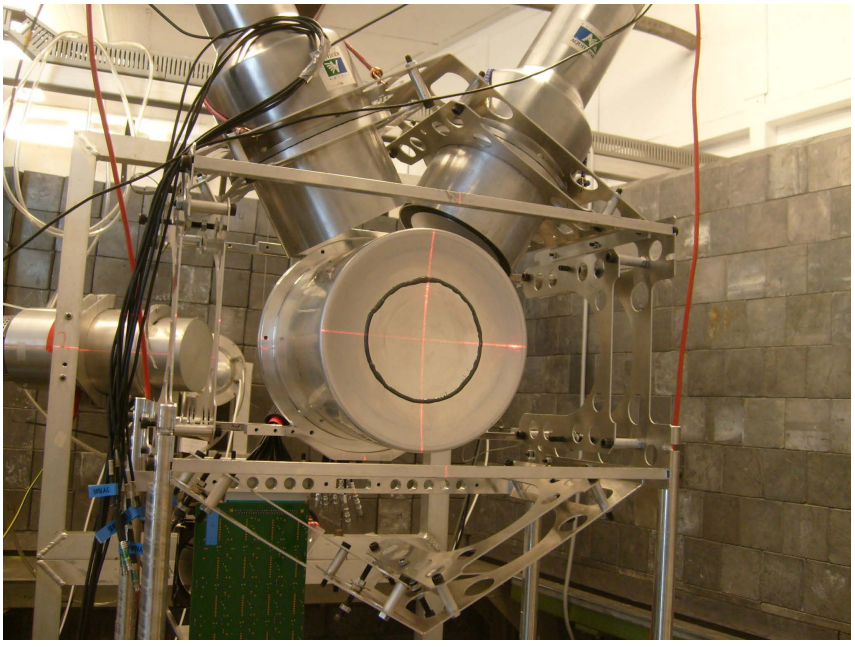

Figure 5.11: Experimental set-up used at Gelina facility for the preliminary test experiment using different ^{233}U targets in the IC and only two C_6D_6 detectors

5.3.1 Sample description

For this experiment we used four ^{233}U samples of different thicknesses. The samples were prepared by electrodeposition technique at IRMM. The chemical formula of the deposit is $U(OH)_4$. Each deposit was heated for 1 min at 100 ^0C to strengthen the adherence. The possibility of preparing actinide deposits is, however, dependent on the preparation of high-quality actinide powders without water residue. More details about the production process of the targets can be found in [Pauwels 91, Ingelbrecht 97]. This technique is used to prepare targets for cross section measurements, for FF studies and also for targets used as fission foils. In this case high-accuracy characterisation is obtained by low-geometry α-counting and isotope dilution mass spectrometry.

The samples consist of ^{233}U material in the form of a thin hydroxide coating, with thicknesses ranging between 50 and 375 $\mu g/cm^2$, electrodeposited on aluminum foil support of 50 μm. An example of one of the ^{233}U sample used in this measurement is shown in Figure 5.12. The thickness, mass and activity of the deposit for each sample used in this test are given in Table 5.1.

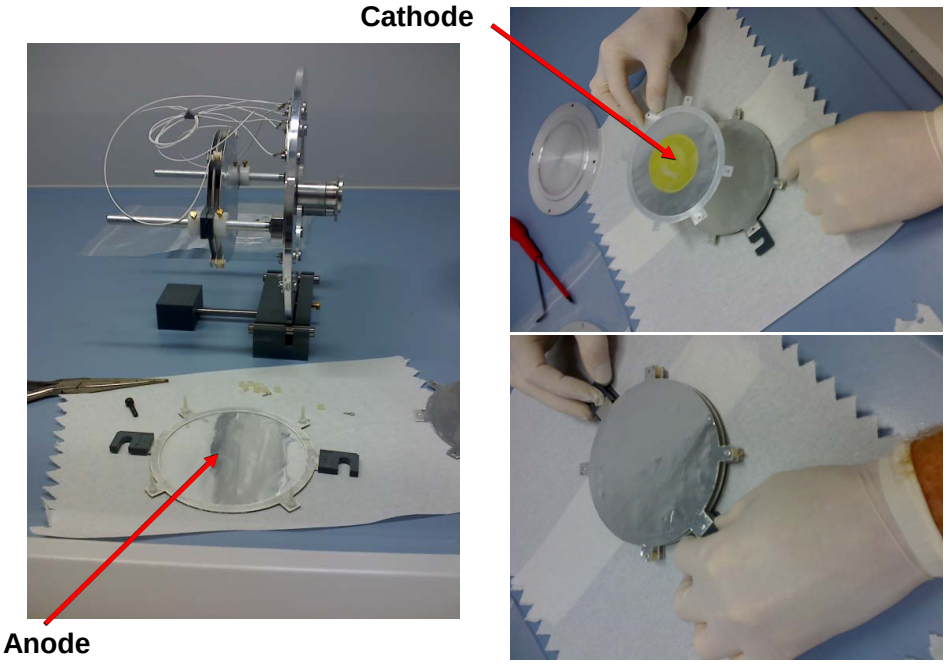

Figure 5.12: Example of the ^{233}U samples used in the IC for the experimental set-up test at Gelina. The diameter of all the targets deposit is 6 cm.

Few weeks after the GELINA test experiments, it appeared that the thickest target showed signs of leakages. It is probably due to the aerial suspension of microscopic flakes

Sample	Density ($\mu g/cm^2$)	Mass (g)	Activity (MBq)
No. 1	373	10.546	3.76
No. 2	246.9	6.98	2.49
No. 3	148.2	4.19	1.50
No. 4	63	1.781	0.64

Table 5.1: Characteristics of the sample used for the experimental set-up test measurements.

and dust of ^{233}U. Considering this fact, such a high thickness have not been taken into consideration anymore.

5.3.2 IC response using ^{233}U samples

The first attempt of the experimental test was to check the good separation between $\alpha-$FF in the pulse height spectra of the IC. For this we used different ^{233}U samples. The spectra are shown in Figure 5.13. Comparing these three spectra, it can be noticed that in the case of the thickest sample (no 1), the FF emitted at grazing angles are losing more energy in the target itself: there are more FF in the valley and less at high energy.

Also, the activity of the samples play an important role in the α-pile up. The α peak is much broader with the 3.7 MBq target, and it nearly fills the $\alpha-$FF valley. This test was done with a shaping time set at $0.5\mu s$. Considering these result, for a better separation between $\alpha-$FF, a shorter shaping time and/or a moderately thick target should be used.

5.3.3 Detection system response

The entire response of the detection system is shown on Figure 5.14. It includes TOF spectrum of: the total events, all γ-ray spectrum, fission spectrum and prompt γ-ray (coincidence between IC and C_6D_6). It is important to mention that these runs were not intended for analysis but only to study the response of the detectors and electronics used for the VETO method.

The TOF of the IC response (blue spectrum) shows peaks which correspond to the specific fission resonances of ^{233}U. The first two broad resonances of ^{233}U around 2 eV can be seen on the right. The resonance structure is also seen in the γ-ray coincidence spectrum (green spectrum), because of prompt fission γ-rays. It allows us to extract the

C_6D_6 detection efficiency for fission events: 4.5% for one detector, which experimentally confirms the "single" detection assumption used for the Weighting Functions technique (see Section 4.5.2.4).

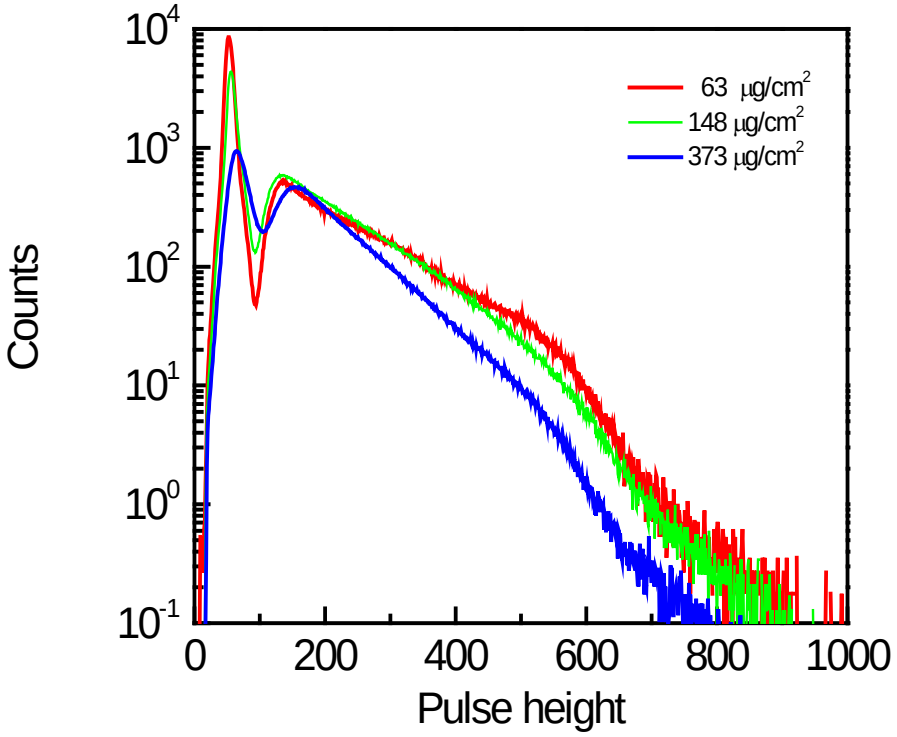

Figure 5.13: Pulse height fission spectra of the IC for three different ^{233}U target layers

One can see that prompt fission γ-rays are very low in comparison with the total amount of γ-rays detected by the scintillators (red spectrum). Indeed, the γ background is very high on such facility at such short distance. The subtraction of this background is a very important and delicate step of every capture cross section measurement. That is why background measurement has to last as long as the cross section measurement.

The multi-plate IC showed a very high stability with respect to the gamma flash. The good performance of IC is reflected by the fission spectrum as a function of neutron energy. One can see some of well known resonances of ^{233}U and the energy resolution at low energy is rather good. At high energy, some resonances can also be noticed even above the ENDF/B-VII RRR limit, but less resoluted. To improve the energy resolution in this energy region another strategy has to be considered, by placing the entire experimental set-up at a longer flight path.

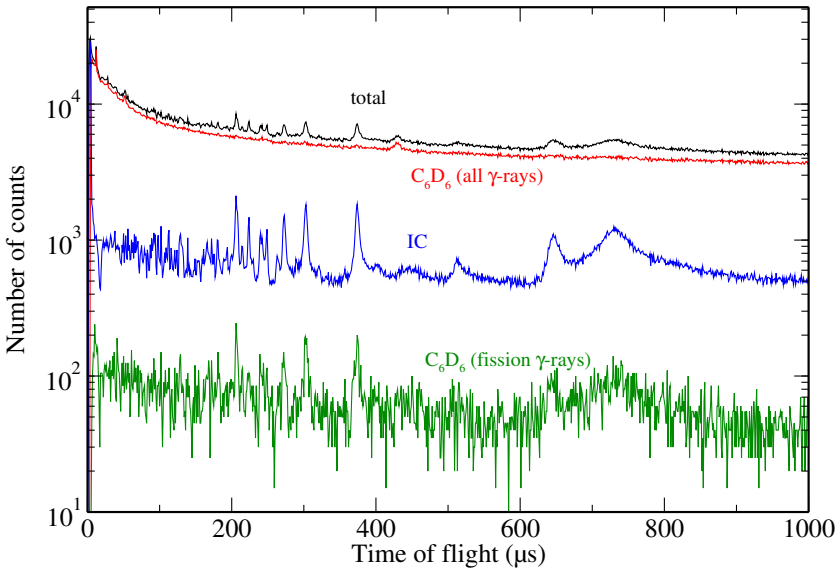

Figure 5.14: TOF spectra of the total events, all γ-ray spectrum, fission spectrum and prompt γ-ray (coincidence between IC and C_6D_6). This run lasted only 2 minutes.

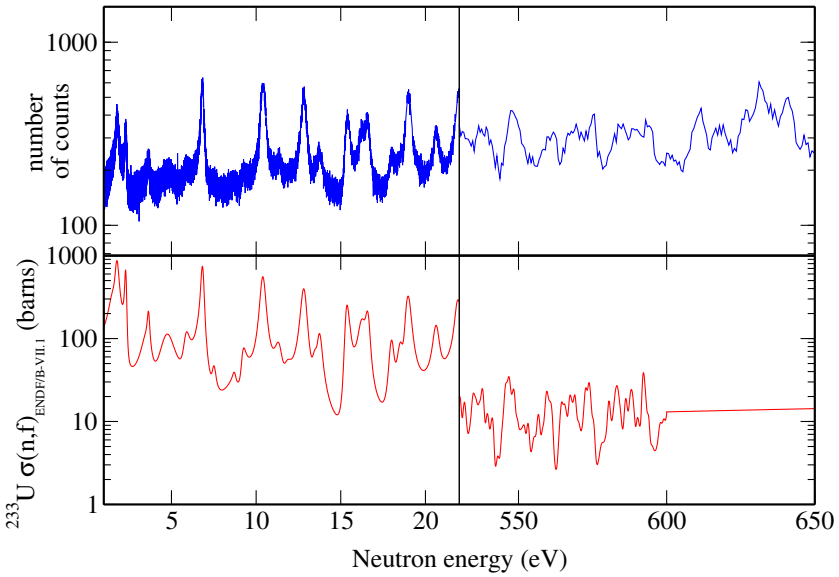

Figure 5.15: Fission count rate obtained with the thick ^{233}U sample compared to ENDF/B-VII evaluation. The run lasted 8 hours.

5.4 Experimental method for efficiency of the IC

The efficiency of the IC is specific of the target/source used. It was measured for a ^{252}Cf sample which decays by α-emission and spontaneous fission, giving rise to both a typical fission products and neutrons.

5.4.1 Event selection

To identify the fission events, the FF have to be carefully selected without including α-particles. Indeed, we are interested in the γ-rays coming from fission events. α-particles included in the selection would induce a systematic error. And FF below the threshold are responsible for the IC efficiency, ε_{IC}, to be lower than 100% (they represent $1-\varepsilon_{IC}$), and can be corrected. To achieve a clear α-FF discrimination, a deep and wide valley is therefore required. It implies that less FF are lost (i.e an efficiency closer to 100%) and that this proportion is much less sensitive to a threshold drift (due to electronic, temperature...). In Figure 5.2 a very good separation in energy between α-particles and FF can be observed, with a large and flat valley. As previously stated, FF in the bottom of the valley are specific of the target. So the depth of the valley cannot be really improved by a IC optimization, as it is the case for its width.

The IC efficiency was determined using the prompt neutron method that has been explained previously in Section 4.6.4. For completeness, we recall how the efficiency of the IC is obtained experimentally:

$$\epsilon_{IC} = \frac{N_{n-coinc-FF}}{N_{n-total}} \tag{5.3}$$

where:

- $N_{n-coinc-FF}$ is the number of neutrons detected in coincidence with a FF, and
- $N_{n-total}$ is the total number of prompt neutron detected.

The selection of prompt neutrons detected in the C_6D_6 scintillator is made by using the pulse shape discrimination (PSD) method. A typical bi-dimensional diagram showing how this selection is applied is presented in Figure 5.16. The separation between γ-rays and neutrons is observed without any γ-detection threshold. Because at low energies the discrimination is not perfect, one prefer to make the neutron selection starting from an energy where the separation between γ-rays and neutrons is clear. The total number of prompt neutrons $N_{n-total}$ considered in equation 5.3 is the number of neutron events selected in the contour obtained from the PSD versus energy spectrum.

5.4.2 IC efficiency analysis

The number of neutrons detected in coincidence with a FF $N_{n-coinc-FF}$ for each of the C_6D_6 detector is determined from the coincidence spectra, as shown in Figure 5.17 where a threshold was chosen at channel 240 to be sure that only the neutrons-FF coincidence is selected. Also, the shape of the coincidence spectra in comparison with the height pulse spectra in a single event (the black spectra), has changed. This behaviour will be discussed later. The efficiency measured aimed to be used in the cross section measurement. The threshold for the efficiency measurement has then to be the same as the one used for fission tagging. Figure 5.18 illustrates the threshold selection by showing a spectra close-up at low energy.

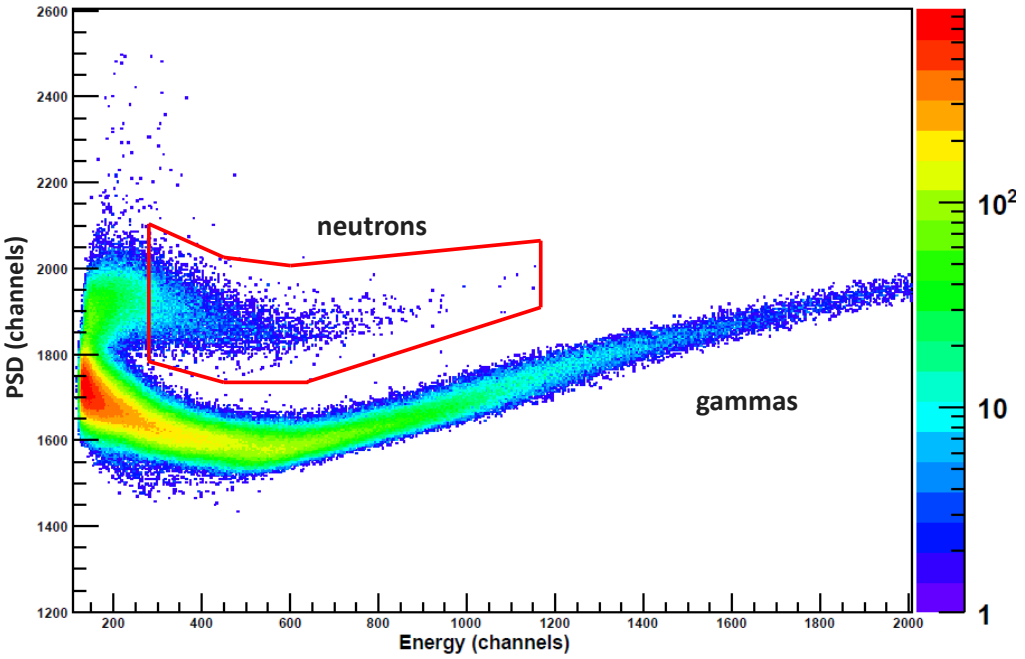

Figure 5.16: Qualitative view of the bi-dimensional plot of energy deposited in C_6D_6 detector versus Pulse Shape Discrimination (PSD) obtained with ^{252}Cf source. The contour represents the selection of prompt fission neutrons coming from the spontaneous fission process.

The efficiency of the IC obtained using six similar C_6D_6 detectors and the ^{252}Cf fissile spontaneous source is shown in Figure 5.19. The error bars shown here are only statistical, and are greatly reduced by the strong correlation existing between the observables. The average value of the efficiency was found to be 97.92 % with an uncertainty of 0.10%.

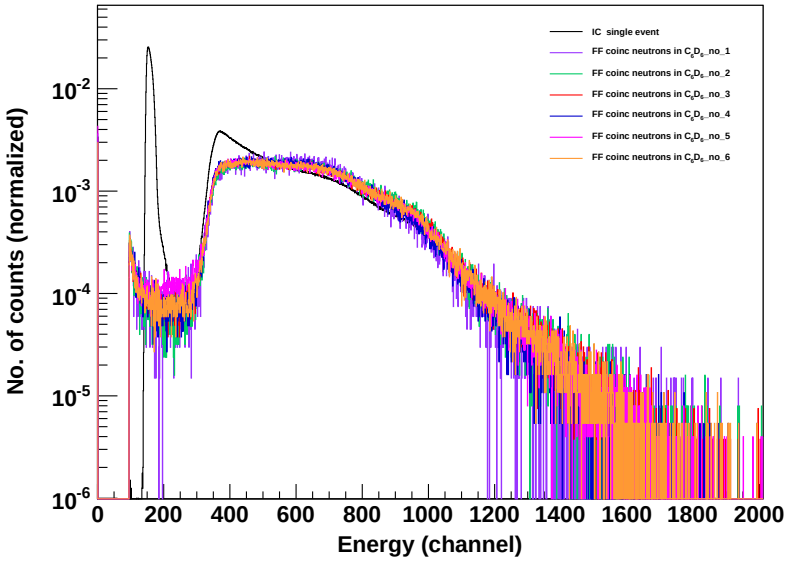

Figure 5.17: IC spectrum in a single event and IC spectra obtained in coincidence with the six C_6D_6 detectors placed around the IC as shown in Figure 4.12.

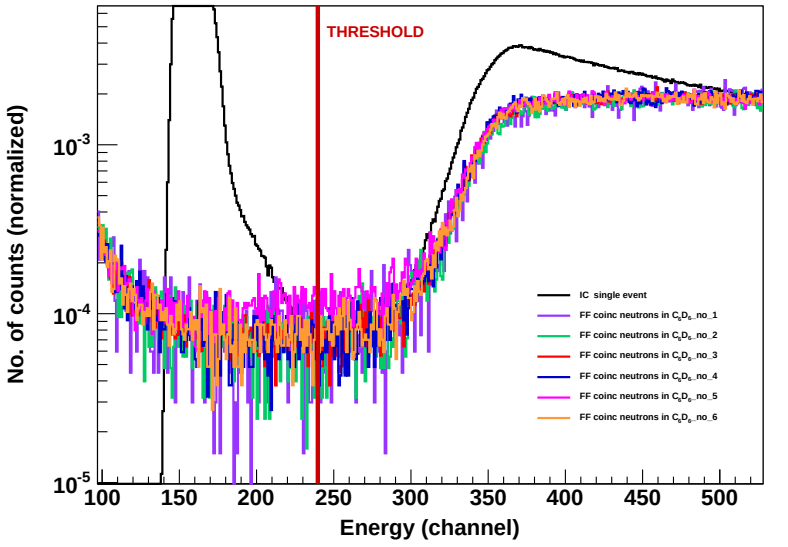

Figure 5.18: The threshold selection in the neutrons-FF coincidence spectra.

This result was obtained by eliminating detector C_6D_6_no 5, which shows an abnormal behaviour during the experiment. This behaviour is noticed in the coincidence spectra (see Figure 5.18), where for this detector, the number of FF detected at low energies, which are found just under the channel 300, is greater than in the case of other detectors, where the coincidence spectra are matches. This explains the lower value of the efficiency when using the this detector.

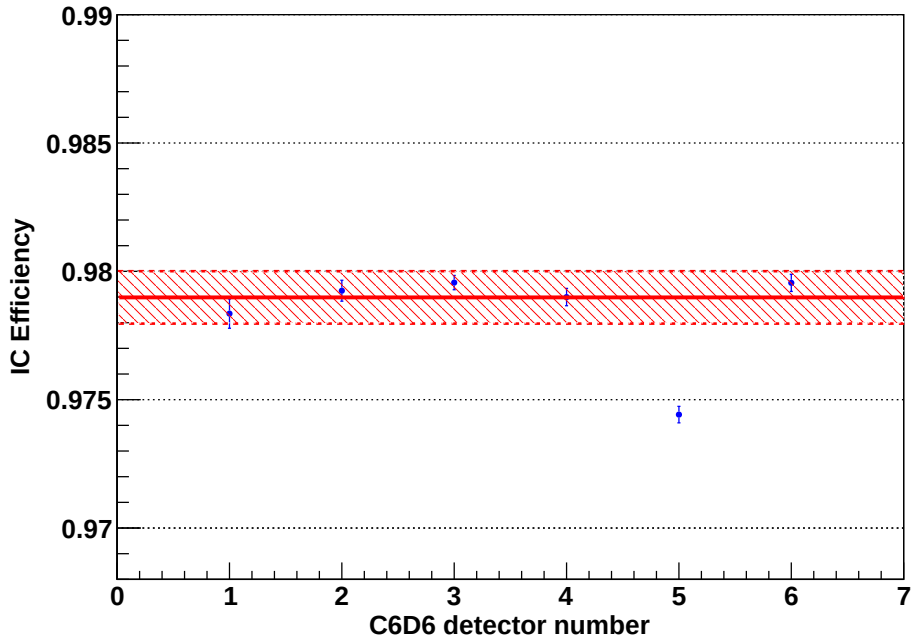

Figure 5.19: Ionisation chamber efficiency obtained with the C_6D_6 detectors in standard position.

As mentioned in the previous chapter, the measurement method is valid if there are only fission prompt neutrons in the neutron contour. For the first measurement, the background neutrons (from cosmic rays interacting in the high atmosphere) was found to be negligible in comparison with the prompt neutrons. The assumption has revealed to be false for the following experiment, as will be discussed in Section 5.4.4.

Furthermore, since the measurement is made in the same experiment no dead time correction is needed. In the first approach, the efficiency of the IC does not depend on the set-up geometry, on neutron contour selection (no energy calibration needed), on the background or on the neutron multiplicity (even for cold fission).

5.4.3 Efficiency function of C_6D_6 angle

The first experimental results, in which the geometrical set-up was set with the C_6D_6 detectors placed at $\phi = 90^0$ from the IC and ^{252}Cf source, lead to the conclusion that other different geometries like placing the C_6D_6 detectors at different angles need to be studied. Therefore two of the six C_6D_6 detectors, where placed at different angles and distances from the ^{252}Cf source and the other four were maintained in the same previously geometry conditions. The positions and angle chosen for this study are given in Table 5.2.

C_6D_6 detector	Position 1 (cm)	Position 2 (cm)	Position 3 (cm)	Position 4 (cm)	Position 5 (cm)
C_6D_6_1	12	12	12	12	12
C_6D_6_2	12	12	12	12	12
C_6D_6_3	12	12	12	12	12
C_6D_6_4	12	12 (ϕ=0°)	24 (ϕ=0°)	44 (ϕ=0°)	87 (ϕ=0°)
C_6D_6_5	12	12	12	12	12
C_6D_6_6	12	16 (ϕ=45°)	35 (ϕ=45°)	68 (ϕ=45°)	96 (ϕ=45°)

Table 5.2: The positions of the six C_6D_6 detectors used in the measurement of the efficiency of the IC. The distance represents the distance between the center of the target and the end cap of the C_6D_6 detector. When the angle is not mention the phi is by default at 90.

The efficiencies of the IC obtained in coincidence with the C_6D_6 detectors at 90°, in five different runs, are shown in Figure 5.20. The discrepancies are much larger than the statistical uncertainties. It may be due to a slight change in experimental conditions (temperature, shifts in the electronics, etc.) as these experiments took place in a relatively long period of time, with a time difference of approximately 5 days between each experiment. The second run of C_6D_6_1 (red point) is clearly abnormal and will not be taken into consideration in the following. Except for this point and the efficiencies obtained in coincidence with detector C_6D_6_5, a very good reproducibility of the results is obtained, with an efficiency average value of 97.95% with an uncertainty of 0.10%.

The efficiency measured with C_6D_6 at different angle (C_6D_6_4 and C_6D_6_6 respectively at $\phi = 0^0$ and 45^0) are presented in 5.21. One can notice a significant increase

of the efficiency, which is due to a kinematic effect. The neutrons emitted by FF are slightly focused at forward angles on the same direction as the FF, due to the velocity of the fragments. Therefore they have a higher probability of detection in the C_6D_6 detector located in the same direction. Such a focusing effect affects the coincidence spectrum of FF, as can be seen in Figure 5.22. When FF are detected in coincidence with the $C_6D_6\_4$ at $\phi = 0^0$, FF emitted normal to the target are favored (the green spectra where a higher peak around the channel 370 can be observed). On the contrary, an increased proportion of FF emitted at grazing angles (with a high energy deposition or in the α-FF valley) can be noticed on the coincidence with the $C_6D_6\_4$ at $\phi = 90^0$ (the blue spectrum), where a flatted shape of the spectrum is observed.

The efficiency is related to the number of FF below the threshold. 5.23 shows a close-up view at low energy of the FF spectra in coincidence. As can be seen, the alpha peak has disappeared since no neutron is correlated to the α-decay. The shape of the valley can then be easily analysed : there are less FF below the threshold (i.e emitted at grazing angle) when in coincidence with neutron detected at $\phi = 0^0$ or 45^0 than at 90^0. It confirms the focusing effect and induces a higher efficiency.

This explanation was also confirmed by simulations. The aim was to simulate the FF emission and transport in the IC, as well as the neutron emission and transport to the scintillator. A spontaneously fissioning ^{252}Cf source was considered, with the same characteristics as the one that we have used in the experiment and described in Section 5.1. The FF mass and energy distributions were determined using the GEF code [Schmidt], which treats spontaneous fission and fission up to an excitation energy of about 100 MeV. The energy losses in the different materials were calculated considering the stopping power tables [Nortiicliffe 70] and their flight path. The induced charge signal was inferred from the deposited energy in the gas, taking into account the averaged position between the electrodes. The neutron emission from FF was simulated with respect to the energy distribution and multiplicity taken from [Bowman 63, Jørgensen 88], and with conservation of the total kinetic energy and angular-momentum.

The simulation results are shown in Figure 5.24. One can see the same features than in the experimental spectra: FF in coincidence with neutron detected at $\phi = 90^0$, are more likely detected at high energy or in the $\alpha-$FF valley. It induces more FF below the threshold, and a lower efficiency measured at this scintillator angle.

To obtain the best estimate of the real IC efficiency, one has to take into account this angular dependency. The average value over the cosines distribution (isotropic emission of the FF) gives an efficiency of 98.4% with an uncertainty of 0.2%.

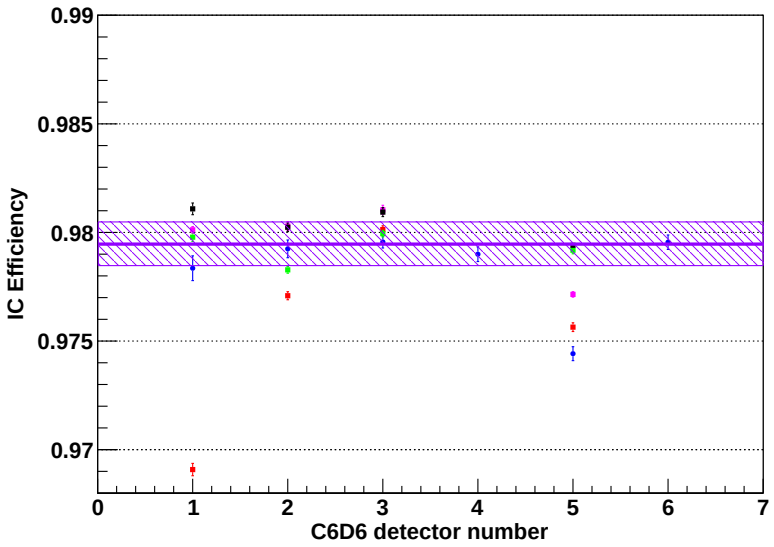

Figure 5.20: Efficiency of the IC obtained in different runs made at approximately 5 days time interval between them. This study was performed in order to see the stability of the electronic system.

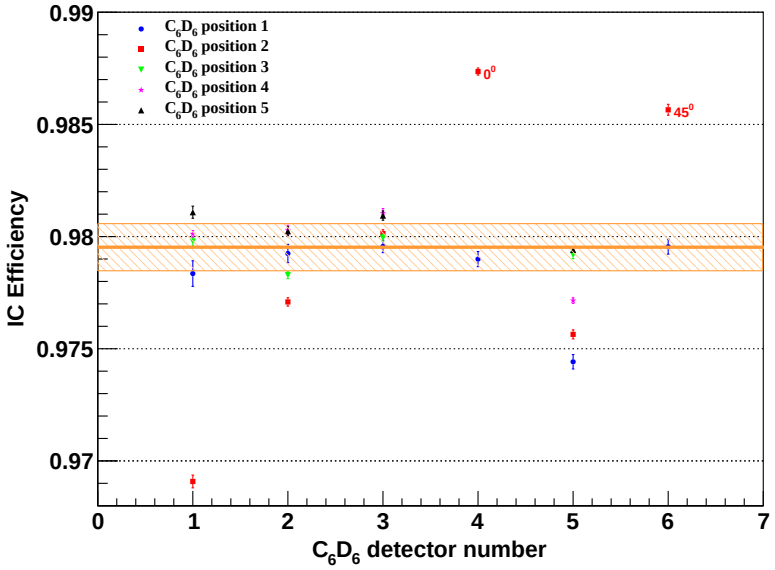

Figure 5.21: Efficiency of the IC obtained in five different runs and geometries. C_6D_6_1, C_6D_6_2, C_6D_6_3,C_6D_6_5 have been maintained in standard position around the IC at $\phi = 90^0$, and detectors C_6D_6_4 and C_6D_6_6 were placed at $\phi = 0^0$ and $\phi = 45^0$ respectively.

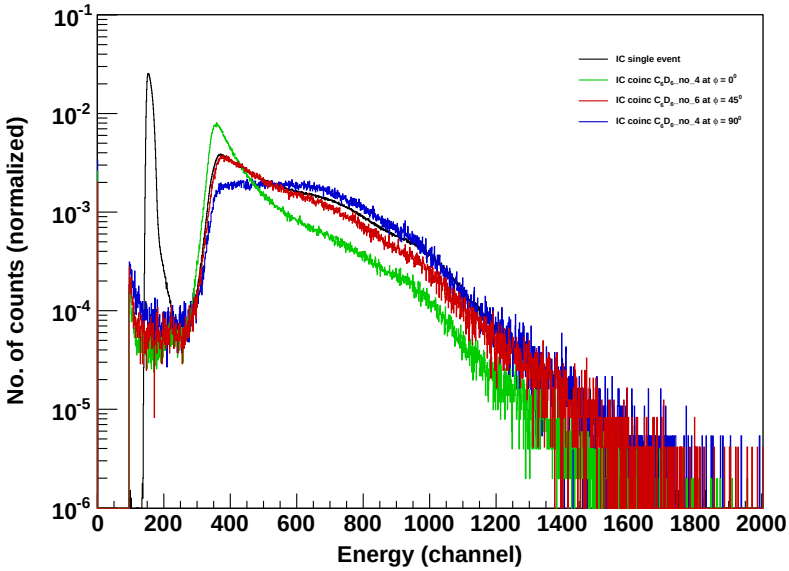

Figure 5.22: Spectra of IC in single event and in coincidence with three C_6D_6 scintillators, placed in different geometries. The IC spectra is normalized to the same number of FF. The coincidence spectrum are obtained in coincidence with C_6D_6_4 in position 1 at $\phi = 0$, and in position 2 at $\phi = 90^0$. The same coincidence was obtained with C_6D_6_6 in position 2 at $\phi = 45^0$.

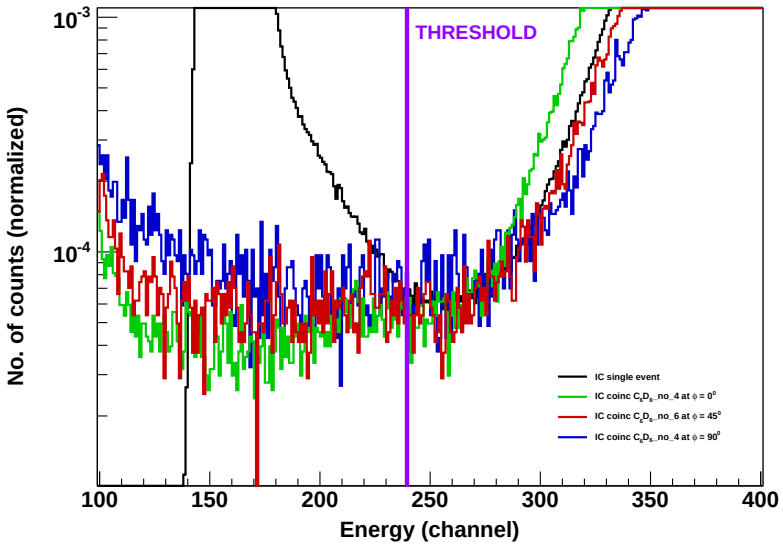

Figure 5.23: Zoom of spectrum of IC in single event and in coincidence with different C_6D_6 scintillators near the IC threshold selection.

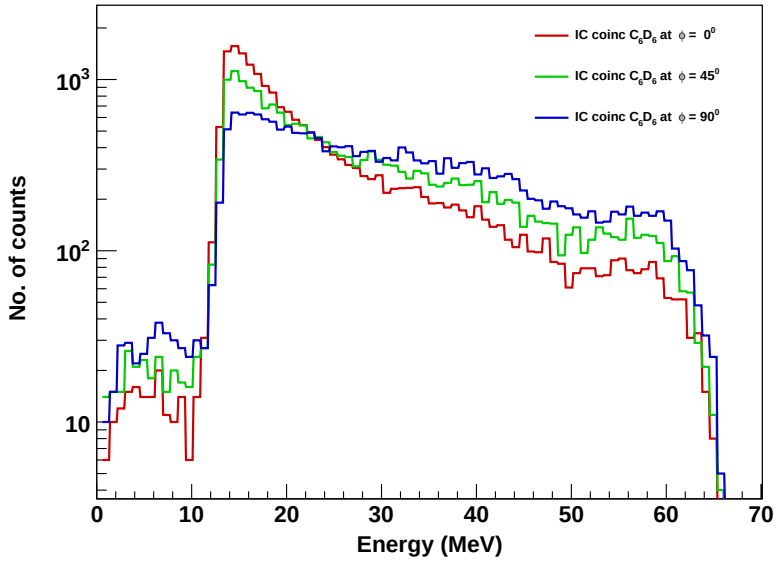

Figure 5.24: The coincidence spectra obtained from a simulated IC response in coincidence with three C_6D_6 detectors placed at various angles from a spontaneously fission ^{252}Cf source

5.4.4 Efficiency function of C_6D_6 energy threshold and distance

Other factors my influence the real efficiency of the IC. Additional studies were undertaken, like the C_6D_6 threshold energy dependence which is shown in Figure 5.25. The study is shown for position2 of the C_6D_6 detectors, where two of them where placed at different angles from the ^{252}Cf source. The neutron energy is indirectly obtained from the γ-ray energy calibration study for each C_6D_6 detectors. As previously mentioned, in the first approach, the background contribution does not influence the efficiency evaluation in the standard position, where the analysis was made considering all the neutron contour. Therefore, increasing the energy threshold in the neutron selection (see Figure 5.16), a decrease of efficiency can be noticed for all detectors. As expected, this effect is more visible for detector C_6D_6_no1 and C_6D_6_no5, since, as previously mentioned, C_6D_6_no5 had an abnormal behavior in all positions and the efficiency found in coincidence with detector C_6D_6_no1 for this run-position2, was shifted (see Figure 5.20). For the other four detectors, the efficiency slightly decrease with the energy. A layout of the efficiency obtained with these last detectors is presented in Figure 5.26. Normally, a linear behaviour was expected, but the influence of the cosmic neutron background leads to a lower efficiency. In Figure 5.27 is illustrated the prompt neutron spectrum obtained with with ^{252}Cf source (red spectrum) and the neutron background spectrum obtained in standard configuration. It can be observed that the neutron rates do not decrease in the same manner as function of energy. It implies that the background becomes more

important with increasing energy. The total number of single neutrons will increased leading, according to equation 5.3, to a decrease of the efficiency. This could explains why the efficiency is slightly lower when the threshold is higher. Nevertheless it will be confirmed in a new experimental campaign. The study of efficiency function of distance is illustrated in Figure 5.28. The principle is exactly the same as for energy threshold. The longer the distance between source and scintillator, the lower the prompt neutron counting rates is. Therefore, the neutron background contribution is then becoming more important.

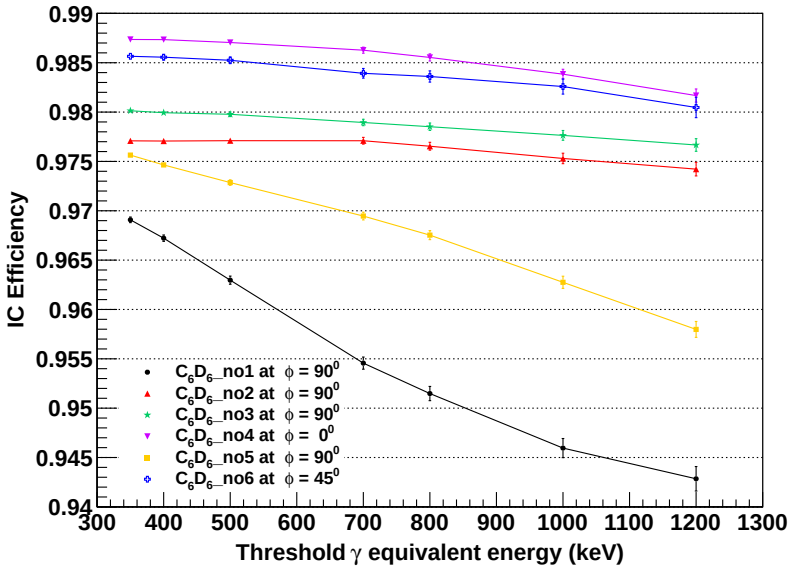

Figure 5.25: Study of the efficiency function of neutron energy threshold for the six C_6D_6 scintillators placed in position2.

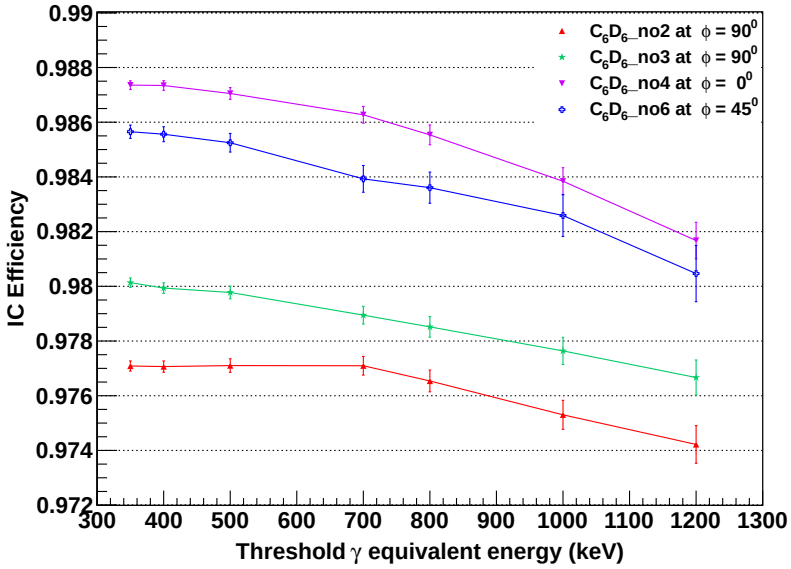

Figure 5.26: Layout of efficiency study function of neutron energy threshold for the C_6D_6 detectors which were correctly functioning.

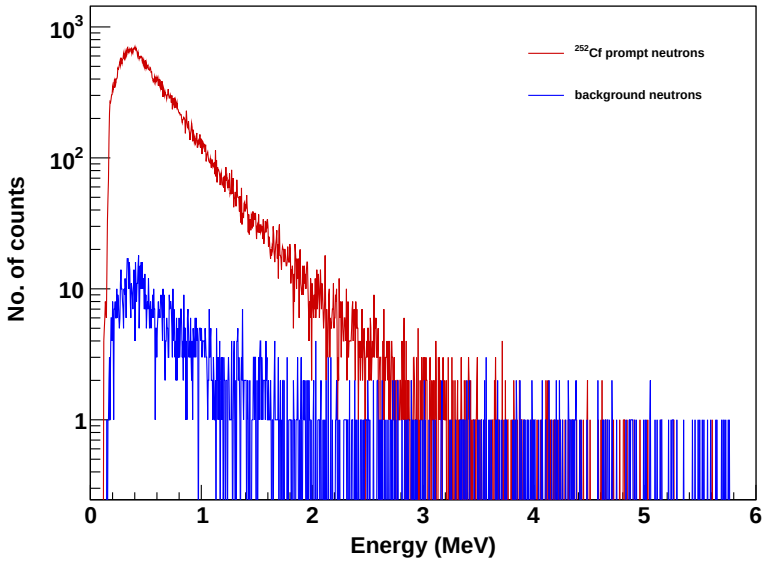

Figure 5.27: Comparison between the prompt fission spectrum obtained with ^{252}Cf source and the background neutron spectrum.

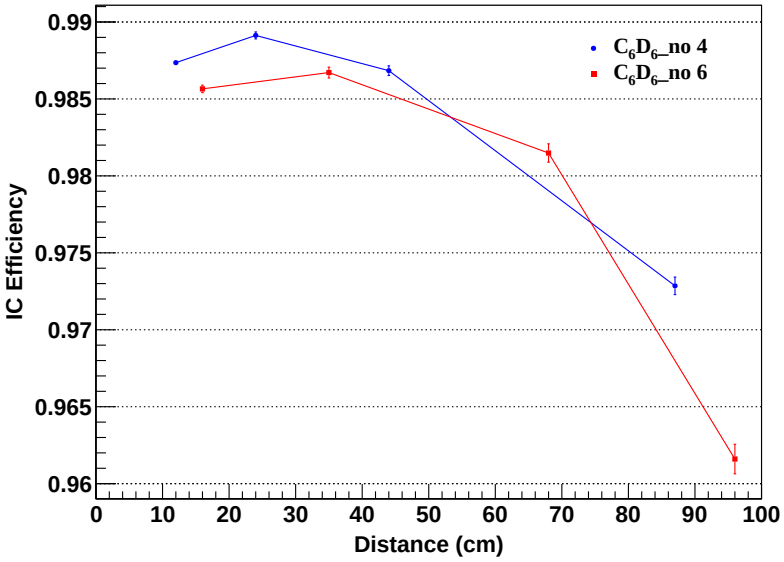

Figure 5.28: Study of the efficiency function of energy threshold in C_6D_6 scintillators.

5.5 Efficiency of the IC with ^{233}U

The straightforward measurement with ^{252}Cf source is very advantageous since no neutron beam is needed, and is very useful for testing the response of the experimental set-up. Even though we have obtained very good results for the efficiency of the IC using this source, the efficiency is specific for the ^{252}Cf isotope, and therefore not enough for the final experiment of the measurement of the fission and capture cross sections of the ^{233}U. It is important to mention that the efficiency measurement of the IC with ^{233}U will be performed during the final experiment. The prompt fission neutrons from different samples could not be separated from the ten fission chambers, therefore we will only obtain a mean value of the efficiency. This averaged result will be applied to the total fission rate (all FF detected) giving the same information as if the fission chambers were analyzed one by one. Nevertheless, a measurement of the efficiency using one ^{233}U sample is useful and will give information about possible issues that could arise. That is why a test was carried out at AIFIRA facility (Applications Interdisciplinaires des Faisceaux d'Ions en Région Aquitaine).

The sample used in this study was the ^{233}U sample no.2 from the Table 5.1, with an α-activity of 2.49 MBq. The ion beam facility is equipped with a single stage electrostatic accelerator designed by the HVEE Europe company (3,5 MV Singletron). It can deliver up to 50 μA beams of light ions (H^+, D^+, He^+). Production of fast mono-energetic neutrons (100 keV - 6.5 MeV and up to 20 MeV) is performed using (p, Li), (p, T), (D, D)

and (D, T) nuclear reactions.

Considering the low fission cross-section at high energy, the principle of the experiment was to produce fast neutrons with energy below 1 MeV via $^{7}Li(p,n)^{7}Be$ reaction, and reduce their energy with a paraffin moderator. The Li target (LiF chemical form) had a thickness of 440 $\mu g/cm^2$ and was fixed on copper support (radius of 2.5 cm anf 0.5 mm thickness). The proton beam is stopped in the copper material therefore the target was continuously air-cooled to dissipate heat. Although, the global temperature of the backing was kept below 10°C, the beam intensity has been limited to $4\mu A$, to avoid hot spots and target degradation. To maximise the neutron production, the proton energy was set to 2.3 MeV (the resonance energy) with a neutron initial energy of 573 keV [Liskien 75]. The neutrons were thermalized using a 5 cm block of paraffin and a lead shielding was disposed to attenuate the γ-rays coming from the target and paraffin. Pictures of the experimental set-up are shown in Figure 5.32.

We have obtained the pulse height spectrum of the IC with ^{233}U and a good separation α-FF is observed, especially when considering the high activity of the sample compared to the one of ^{252}Cf previously studied. The spectrum is shown in Figure 5.29. One important objective of this experiment was the determination of the efficiency of the IC with ^{233}U sample. This part could not be achieved due to an unexpected high background which was impossible to be completely removed. This background was due to high energy γ-rays (up to 10 MeV) from F(p,γ) and Cu(n,γ) reactions on the target. Also, the 2.2 MeVγ-rays from H(n,γ) in paraffin and an important background from the 511keV γ-rays produced by the lead shielding which was added during the experiment to remove most of the high energy γ-rays. Moreover, the shielding was not the same for all the detectors since was constructed during the experiment and no preliminary calculations were performed. Simulations of the neutron flux obtained with this shielding is shown in Figure 5.30 with two different source particles, neutrons (a) and high energy γ-rays (b). It can be noticed that the shielding was effective but the γ-ray flux was still to high for a clean measurement.

It is important to note that the PSD is not properly working when an significant γ-ray flux is present. Therefore a good separation between prompt neutrons and γ-rays was impossible to be obtained. The PSD response of one of the C_6D_6 detector is shown in Figure 5.31. For comparison, the PSD response using ^{252}Cf source is presented, where the prompt neutrons are very well disentangled from γ-rays. Therefore, we have obtained completely discrepant efficiencies values for the four C_6D_6detectors and therefore these results could not be considered conclusive.

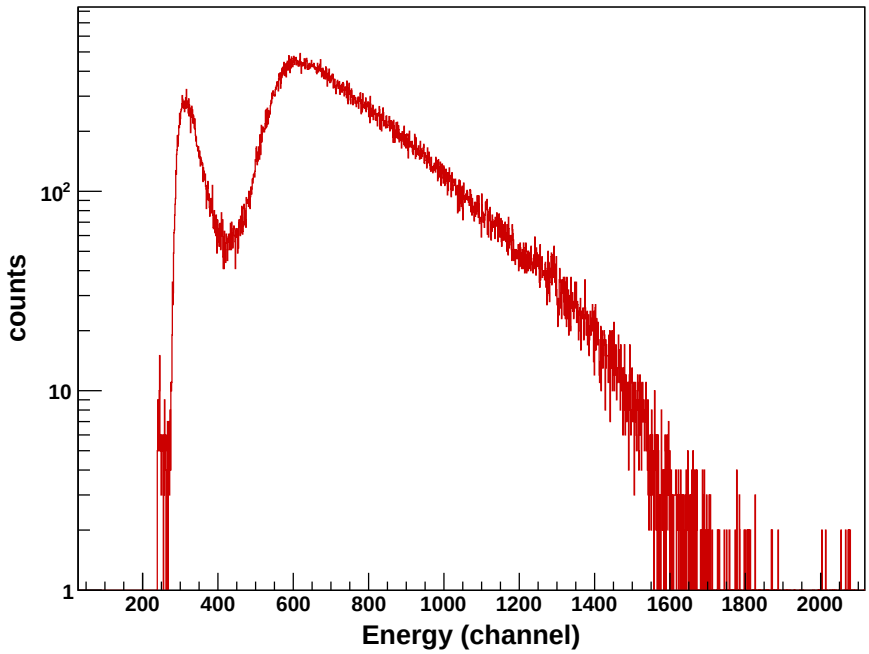

Figure 5.29: The pulse height fission spectra of the IC obtained with ^{233}U sample in thermalized neutrons at AIFIRA facility.

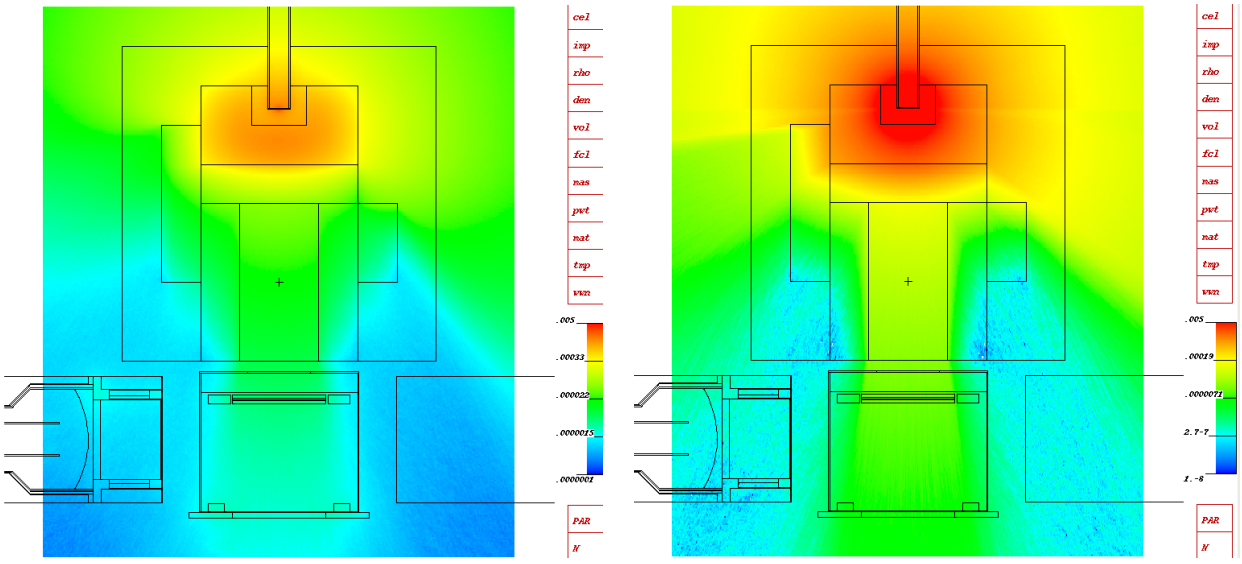

(a) (b)

Figure 5.30: Simulation of the γ-ray flux from neutron source (a) and high energyγ-ray source (b)

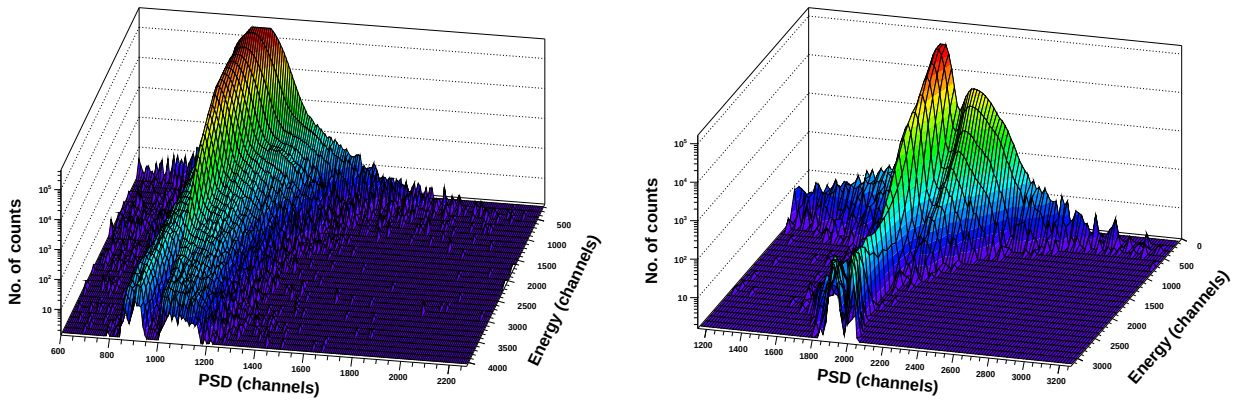

Figure 5.31: Pulse shape discrimination obtained in the case of ^{233}U target at AIFIRA facility (left), and spontaneously fissile ^{252}Cf source (right).

5.6 Neutron-gamma discrimination at Gelina

It is important to check the experimental conditions for the efficiency measurement for the final experiment are not as inappropriate as on the AIFIRA facility. At Gelina, the neutron flux is obtained in a completely different way:

- the neutrons are produced in burst, therefore, the the γ-rays produced in the same time (gamma-flash) and traveling faster than neutrons can be avoided ,
- the C_6D_6 detectors do not see the neutron moderator since the beam is collimated with a heavy shielding as presented in Figure 4.5.

In order to verify a good and clean separation between prompt fission neutrons and γ-rays, one test experiment was performed. This experiment was done using a similar experimental set-up already in placed at the facility composed of an ^{235}U ionisation chamber, two large C_6D_6 detectors and the same electronic system, as shown in Figure 5.33. Even though the sample and the experimental configuration are different from ^{233}U experiment , the results are still characteristic for our objective.

The PSD discrimination is presented in Figure 5.34. The prompt neutrons are clearly visible, but the separation is not as good as in ^{252}Cf experiment. As previously mentioned, the efficiency method is accurate only if the background in neutron selection could be neglected or subtracted. As a conclusion, for the final experiment, the gamma shielding will have to be adjusted to enhance the n-γ discrimination.

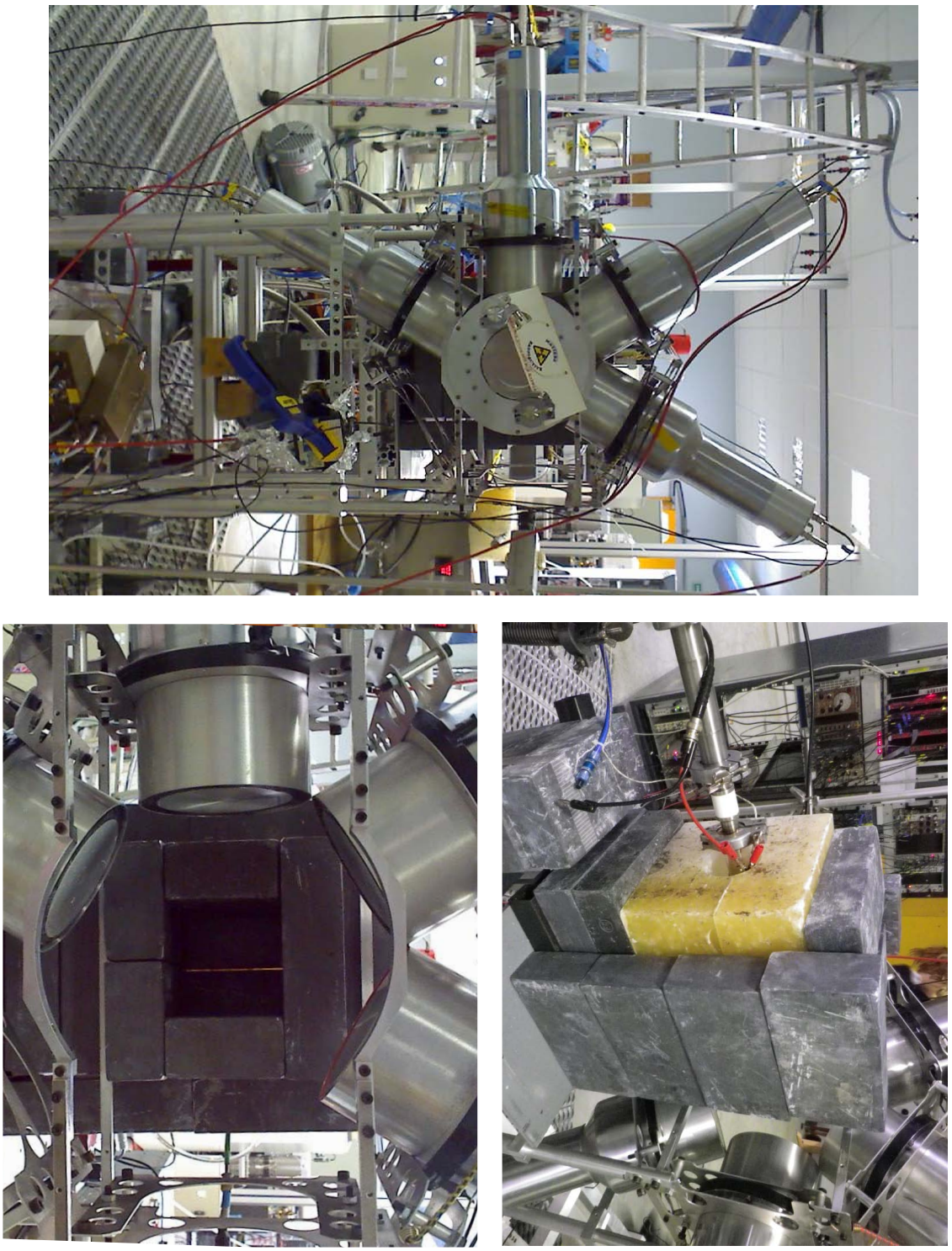

Figure 5.32: Experimental set-up used for the efficiency of the IC measurement using ^{233}U target at AIFIRA facility at CENBG.

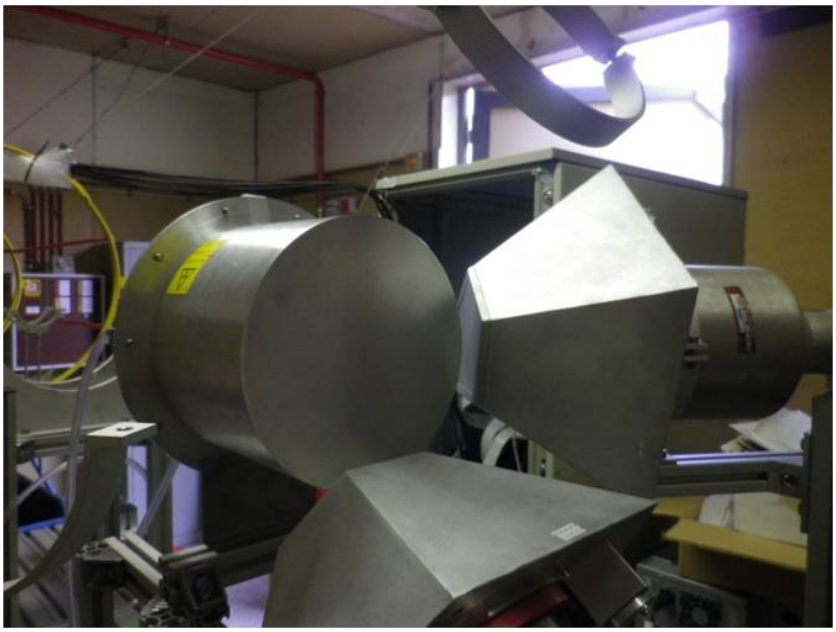

Figure 5.33: Picture of the experimental set-up for PSD response function prompt fission neutrons and γ-ray discrimination at Gelina.

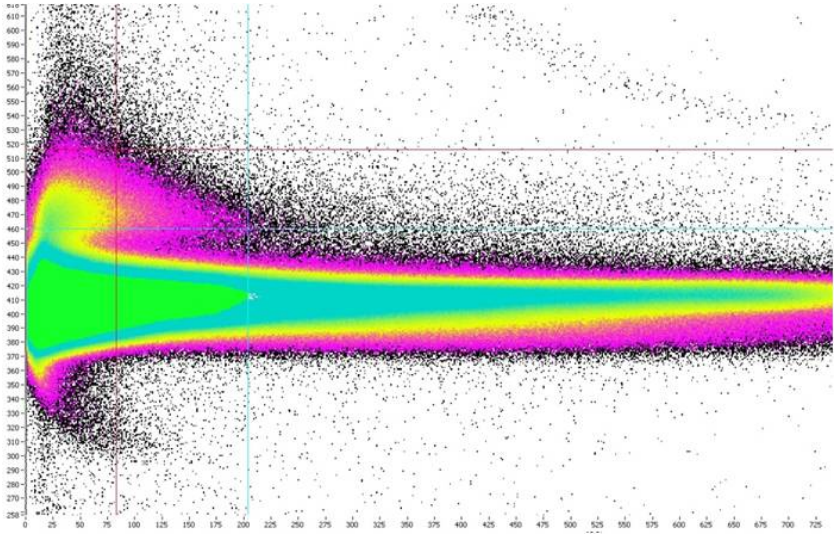

Figure 5.34: PSD function response. A good prompt fission neutrons and γ-rays discrimination using ^{235}U source.

Conclusion

At present there are considerable doubts about the future of nuclear power. Two main issues affect the sustainable use of nuclear fission for energy production: safety (the risks of accidents with serious consequences, which was not part of this thesis) and the nuclear waste. The second and the prior concern for this industry, even on the short term, is the radioactive nuclear waste generated during the operation of nuclear power plants, in particular the high-level waste that has the most dangerous level of radioactivity and needs to be kept isolated into a final disposal. A significant contribution to the high-level radioactive waste comes from minor actinides, in particular americium, neptunium and curium, which are produced during multiple captures and radioactive decays in current nuclear reactors. A possible solution for the nuclear waste disposal could come from partitioning, transmutation and waste-reduction technologies. These possibilities could be achieved with innovative nuclear reactor systems currently being developed, such as subcritical ADS or critical future Generation IV nuclear reactors. A renewed interest in the ^{232}Th /^{233}U fuel cycle was observed, since the actinides produced by this cycle are less radiotoxic than the ones produced by the currently used $^{238}U/^{239}Pu$ cycle. Also, the number of neutrons produced after the capture of a neutron in a reactor environment is larger for ^{233}U than for ^{235}U or ^{239}Pu for thermal neutrons, opening the possibility, although technically still quite complicated, for a thermal breeder. ^{233}U is by far the best fissile isotope for a thermal neutron spectrum and can be used for breeding in both thermal and fast reactors. Nevertheless, the design and development of new systems for energy production and nuclear waste transmutation based on the thorium cycle require improved knowledge of key parameters, like the capture cross-section of ^{233}U, and not only with high accuracy but over the ENDF/B-VII energy range limits.

Accurate capture cross section measurements of ^{233}U are complicated due to difficulties associated with the use of a radioactive sample with several open neutron-reaction channels in the energy range of interest. Important difficulties are due to the γ-ray background generated by the competing neutron-induced fission reaction. In addition, the backgrounds due to neutron scattering and to the neutron beam facility are very high and need to be subtracted. This removal of several background components results in large uncertainties and, if not performed correctly, in the end leads to systematic errors. Therefore, the few existing capture cross-section measurements for ^{233}U are mainly old

and may suffer from these errors. The only two benchmark experimental data for the capture cross-section of ^{233}U obtained by Weston and Berthoumieux were carried out at different TOF facilities using completely different methods at an interval of almost 40 years distance. The overview of differences between experimental data and evaluations in the RRR for capture cross-section of ^{233}U showed clearly that new experimental data are required to solve some inconsistencies. New measurements of capture cross-section of ^{233}U are foreseen to be obtained at n_TOF where a successful test experiment for a simultaneous measurement of neutron-induced capture and fission of ^{235}U was recently performed.

The aim of this work was the development of an experimental set-up dedicated to a simultaneous measurement of the neutron-induced capture and fission cross sections of ^{233}U in the RRR. This set-up was designed, assembled and optimized at CENBG in Bordeaux in the frame of this thesis. The final measurements will be performed at Gelina neutron TOF facility in Belgium, where neutron cross sections can be measured over a wide energy range with high energy resolution. The fission detector consists of a dedicated multi-plate high-efficiency ionization chamber (IC). The γ-rays produced in capture reactions are detected by an array of six C_6D_6 scintillators which surrounds the IC. The challenging issue in this experiment is the discrimination between γ-rays coming from fission and γ-rays coming from the capture reaction. Fission events are identified by doing a coincidence measurement between the FF detected in the IC and the prompt γ-rays detected by the C_6D_6 detectors. The capture events are selected by imposing an anti-coincidence with the IC. Therefore, the IC will act as a VETO for the scintillators. The VETO method is not ideal since the FF detection efficiency is not 100%. Indeed, some FF are affected by back scattering or self-absorption in the target. The undetected fission events will be interpreted as a capture event. This background can be corrected if the efficiency of the IC is known. Moreover, since there are 5 to 20 more γ-rays coming from fission events than from capture events, 1% uncertainty in efficiency of the IC induces 5-20% of uncertainty on the capture cross section. Therefore, this key parameter should be determined with a high precision.

An accurate efficiency of the IC requires a very good discrimination between α and fission fragments (FF) in the pulse-height spectrum of the chamber is required which may be difficult to obtain because of the high $\alpha-$activity of ^{233}U which induces significant pile-up in the IC.

Another difficulty in this measurement is the neutron sensitivity. Indeed, a neutron can be scattered by the experimental set-up and be captured by the surrounding material. This background event is then interpreted as a capture event. To reduce the interactions of the neutron beam with the IC and to minimize the production of background by the experimental set-up, the amount of the material used in to support the γ-detectors and the IC was minimized and highly pure aluminum was used.

The first measurement campaign with the complete experimental set-up was made using a ^{252}Cf source. Several parameters have been studied to determine the behaviour of the IC (gas pressure, high voltage and the distance between the electrodes) in order to find the ideal operation point: a good energy separation between α-FF and a good timing resolution. This source was also necessary to set the electronics that allow the pulse shape discrimination between the γ-rays and neutrons in the C_6D_6 detectors.

To achieve a high FF detection efficiency thin samples are required. On the other hand, a thin sample compromises the counting statistics of the measurement. Therefore, to increase the amount of material, 10 fission chambers will be used. The choice of the sample thickness was made after the first test of the IC using four ^{233}U samples of different thicknesses (63-373 $\mu g/cm^2$) at the TOF facility Gelina at the IRMM. The activity of the ^{233}U samples was much higher than that of ^{252}Cf . Therefore, the α-pile-up gave a high-energy tail on the α-peak which reduced the width of the valley considerably. A compromise between the stability of the sample deposit, a good separation α-FF and the counting statistics, led us to choose for the final experiment the $247\mu g/cm^2$ sample thickness. Also, this experiment allowed us to test the electronics and to determine the response of the experimental set-up. The good performance of the IC was reflected by the fission yield as function of neutron energy. Well known resonances were easily identified at low energy with a good energy resolved. At high energy, some resonances were noticed even above the RRR limit of ENDF/B-VII evaluations, but less resolute. The resonance structures were also observed in γ-coincidence spectrum. This measurement allowed us to determine the efficiency of the C_6D_6 detectors for fission events : 4.5% per detector, which experimentally confirms the "single" detection assumption needed for the validation of Weighting Function technique.

The IC efficiency was determined using the prompt-fission neutrons method. These neutrons are detected via their scattering in the liquid scintillators, and can be disentangle from γ-rays through Pulse Shape Discrimination method. The IC efficiency is then given by the ratio between the number of detected prompt neutrons in coincidence or not with the FF. The efficiency of the IC is specific of the target/source used. The measurements were performed using a ^{252}Cf source. To identify the fission events, the FF have been carefully selected without including α-particles which can induce a systematic error. The number of prompt neutron events was determined via PSD method by making a neutron selection in the PSD versus energy spectrum, carefully discriminating from γ-rays. The average value of the efficiency was found to be 97.95 % with an uncertainty of 0.10%. The uncertainty is greatly reduced by the strong correlation existing between the observables. The advantages of this method is that no dead time correction is required since the measurements are made in the same experiment. Nevertheless, additional measurements have been done for the efficiency determination. In particular we studied the efficiency as a function of the C_6D_6 detectors angles. The efficiencies determined with the C_6D_6 detectors placed at $\phi = 0^0$ and 45^0 were found to be significantly

increased, due to kinematic effects of the prompt-fission neutron emission. This impact was also confirmed by Monte Carlo simulations. Therefore, to obtain the best estimate of the real IC efficiency, the angular dependency has to be considered. The average value over the cosines distribution (isotropic emission of the FF) gives then an efficiency of 98.4% with 0.2% uncertainty, 0.5% higher than the "standard measurement". Other factors may influence the measured efficiency of the IC. Studies of the dependence of the efficiency function of the threshold energy in the C_6D_6 detector showed that the efficiency slightly decreases although a constant behaviour was expected. This effect can be attributed to a weak neutron background. The same behaviour was observed when varying the distance between the source and the scintillator. This effect may be also explained by the reduced fraction of prompt-neutron counting rates at higher energies. A longer neutron background measurement needs to be performed to completely confirm our assumptions.

To conclude, our results show a very good response of the IC using the ^{252}Cf sample. This sample was used to set and optimize the IC features. A very good discrimination between the prompt neutrons and γ-rays was achieved using six C_6D_6 detectors associated with the PSD method. The prompt fission neutrons method used for the determination of the efficiency of the IC is robust. Accurate results are obtained with the experimental set-up developed at CENBG. To avoid systematic errors on the efficiency of the IC, leading to a significant error on the capture cross-section determination in the final experiment, additional C_6D_6 detectors will be placed at 45°.

In the case of ^{233}U different experiments were carried out. A good discrimination between α and fission fragments was obtained which allowed us to choose the most appropriate thickness for in the final experiment. During the measurements made at AIFIRA we noticed that the important γ-ray background contribution can cause a serious disturbance in the C_6D_6 detectors PSD, making impossible the efficiency determination. Nevertheless, at Gelina the background contribution is low enough to achieve a proper discrimination between the prompt neutrons and γ-rays. In addition, the results obtained at this facility show that the experimental set-up is nearly free from any neutron capturing contaminants, and the time resolution of the IC is satisfying.

The experimental set-up is very well functioning and is ready for the final measurement of the fission and capture cross sections of the ^{233}U which will be performed at Gelina. The production of the ten ^{233}U targets by the IRMM may take some time. Meanwhile, an experiment with ^{235}U targets (easier to produce) is foreseen to control the experimental set-up developed at CENBG and the VETO method since ^{235}U is a very well known standard.

Annexes

Annexe A

Technical data : CENBG Ionisation Chamber

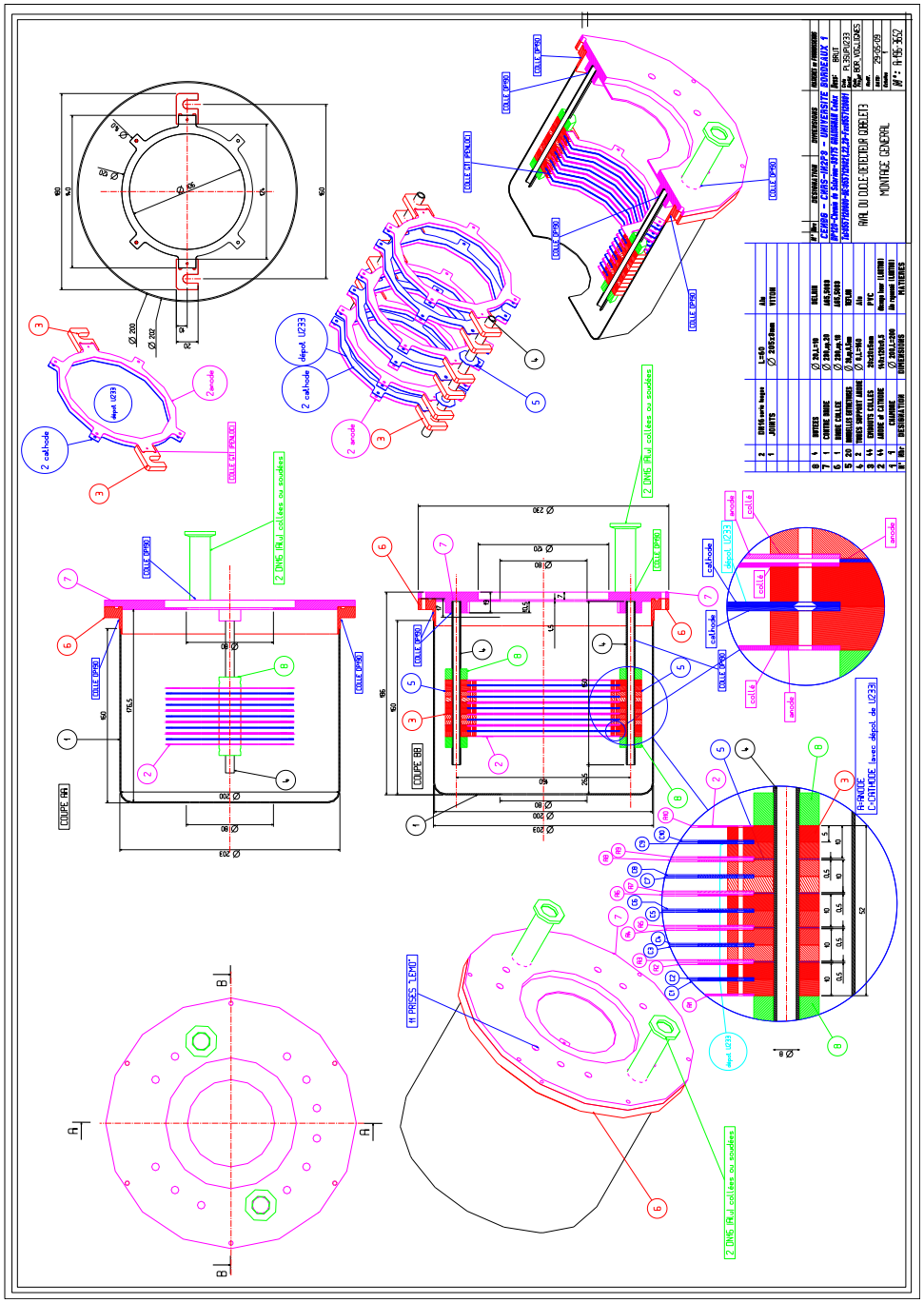

Figure A.1: Engineering drawing of the ionisatoion chamber detector.

Annexe B

Technical data : BICRON C6D6 scintillator

Saint Gobain Crystals (BC-537)	
General Technical Data	
Density (20°C)	0.954 g/cc
Refractive index	1.5
Scintillation Properties	
Wavelength of maximum emission	425 nm
Decay time	2.8 ns
Atomic composition	
No. of D Atoms per cc	4.06×10^{22}
No. of H Atoms per cc	3.55×10^{20}
No. of C Atoms per cc	4.10×10^{22}

Table B.1: C_6D_6 detector technical data

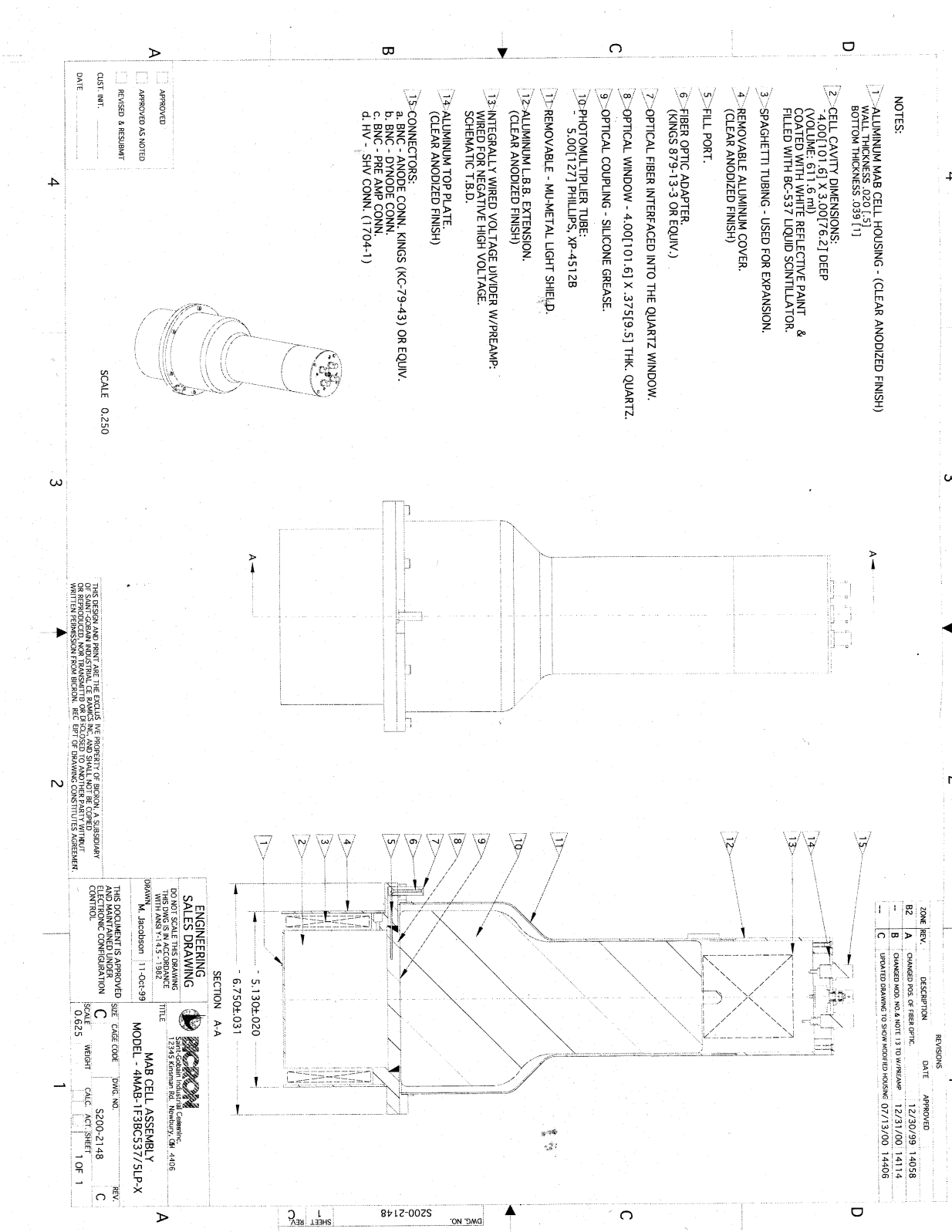

Figure B.1: Engineering drawing of a BICRON C_6D_6 detector.

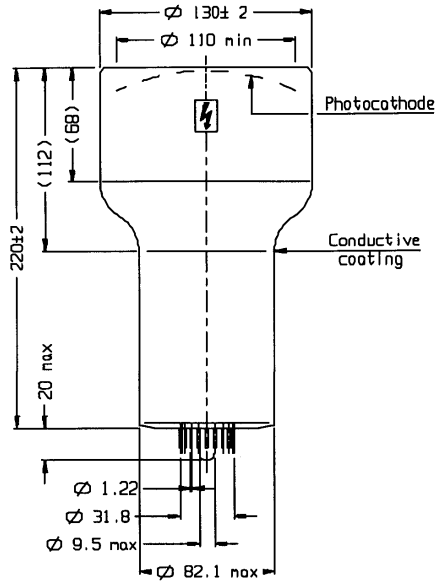

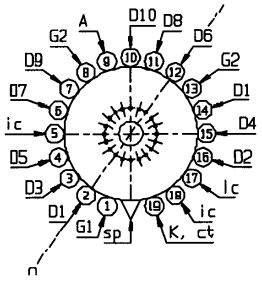

ref.: 99900645
sp: short pin
Ic: internally connected
n: plane of symmetry of the multiplier

K: cathode Dn: dynode
Gn: focusing electrode
A: anode Ct : coating

Typical gain curve

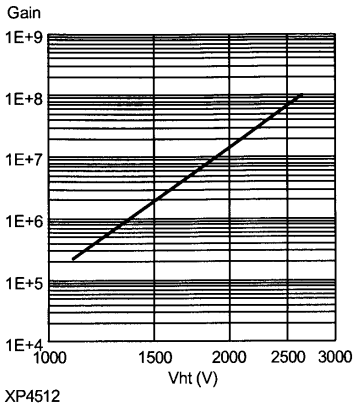

XP4512

Typical spectral characteristics

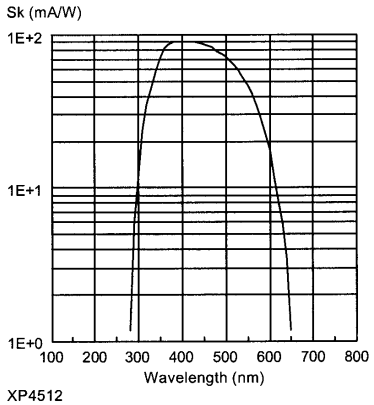

XP4512

Accessories

Socket : FE2019
Mu-metal shield: MS175

PHOTONIS imaging sensors

Figure B.2: Specification of the XP4512 photomultiplier tube.

Bibliographie

[Abbondanno 01] U. Abbondanno & al. *Measurements of Fission Cross Sections for the Isotopes relevant to the Thorium Fuel Cycle*. CERN-INTC-2001-025, no. 25, pages 1–23, 2001. www

[Abbondanno 02] U. Abbondanno, G. Aerts & al. *CERN n-TOF Facility : Performance Report*. CERN/INTC-O-011,INTC-2002-037, no. 53, pages 220–153, 2002. www

[Adhikari 82] S. K. Adhikari. *Exit doorway states in nuclear reactions*. Phys. Rev. C 27, no. 1, 1982.

[Agostinelli 03] S. Agostinelli, J. Allisonas, K. Amakoe, J. Apostolakisa, H. Araujoaj, P. Arcel & al. *Geant4 — a simulation toolkit*. Nucl. Instr. and Meth. A, no. 506, pages 250–303, July 2003. www

[Aliberti 04] G. Aliberti, G. Palmiotti, M. Salvatores & C. G. Stenberg. *Impact of Nuclear Data Uncertainties on Transmutation of Actinides in Accelerator-Driven Assemblies*. Nucl. Sci. and Eng., vol. 146, pages 13–50, 2004. www

[ANDRA 12] Agence nationale pour la gestion des déchets radioactifs ANDRA. *INVENTAIRE NATIONAL des matières et déchets radioactifs*. ANDRA - Inventaire national, no. 466, November 2012. www

[Bauge 01] E. Bauge, J. P. Delaroche & Giro. M. *Lane-consistent, semimicroscopic nucleon-nucleus optical model*. Phys. Rev. C, no. 63, page 024607, Jan. 2001. www

[Bauge 06] E. Bauge & S. Hilaire. *Modélisation et Evaluation de Données*. Proc. Ecole Joliot-Curie de Physique Nucléaire, no. 25, pages 127–166, Sept. 2006. www

[Berthoumieux 07] E. Berthoumieux & al. *Simultaneous measurement of the neutron capture and fission yields of* ^{233}U. Proc. Conf. on Nucl. Data for Sci. and Technology, Nice, no. 1, pages 571–574, 2007.

[Bigelow 06] T.S. Bigelow, C. Ausmus, D.R. Brashear, K.H. Guber, J.A. Harvey, P.E. Koehler, R.B. Overton, J.A. White & V.M. Cauley. *Recent operation of the ORELA electron LINAC at ORNL for neutron cross-*

section research. Proc. of LINAC, no. 21, pages 79–81, June 2006. www

[Blokhintsev 55] D. V. Blokhintsev & Walter H. Zinn. *Experience with Nuclear Power Plants.* Bulletin of the Atomic Scientists, vol. 11, no. 7, pages 273–921, September 1955.

[Blons 73] J. Blons. *High Resolution Measurements of Neutron-Induced Fission Cross Sections for ^{233}U, ^{235}U, ^{239}Pu and ^{241}Pu Below 30 keV.* Nucl. Sci. Eng., no. 51, page 130, 1973.

[Bohr 36] Niels Bohr. *Neutron Capture and Nuclear Constitution.* Nature, no. 137, pages 334–348, 1936. www

[Borella 03] A. Borella, A. Brusegan, P. Schillebeeckx, K. Volev, G. Aerts & F. Gunsin. *High Resolution Cross Section Measurements at GELINA in Support of Ads and P& T.* Proc. Int. Workshop on P&T and ADS Develoment, pages 1–10, October 2003. www

[Borella 05] Alessandro Borella. *Determination of the neutron resonance parameters for ^{206}Pb and the thermal neutron capture cross section for ^{206}Pb and ^{209}Bi.* PhD thesis, Ghent University, Belgium, pages 1–181, January 2005.

[Borella 06] A. Borella, Volev K., Brusegan A., Schillebeeckx P., Corvi F., Koyumdjieva N., Janeva N. & Lukyanov A. A. *Determination of the $^{206}Th(n, \gamma)$ cross section from 4 to 140 keV at GELINA.* Nucl. Sci. Eng., no. 152, pages 1–14, 2006. www

[Borella 07a] A. Borella, G. Aerts, F. Gunsing, M. Moxon, P. Schillebeeckx & R. Wynants. *High-resolution neutron transmission and capture measurements of the nucleus 206Pb.* Phys. Rev. C, no. 76, pages 014605–18, July 2007. www

[Borella 07b] A. Borella, G. Aerts, F. Gunsing, M. Moxon, P. Schillebeeckx & R. Wynants. *The use of C6D6 detectors for neutron induced capture cross-section measurements in the resonance region.* Nucl. Instr. and Meth. A, no. 577, pages 626–640, March 2007. www

[Boutoux 12] G. Boutoux, B. Jurado, V. Méot, O. Roig, L. Mathieu, M. Aïche, G. Barreau, N. Capellan, I. Companis, S. Czajkowski, K.-H. Schmidt, J.T. Burked, A. Bail, J.M. Daugas, T. Faul, P. Morel, N. Pillet, C. Théroine, X. Derkx, O. Sérot, I. Matéa & L. Tassan-Got. *Study of the surrogate-reaction method applied to neutron-induced capture cross sections.* Phys. Lett. B, no. 712, pages 319–325, 2012. www

[Bowman 63] H.R. Bowman, J.C.D. Milton, S.G. Thompson & W.J. Swiatecki. *Further studies of the prompt neutrons from the spontaneous fission*

of ^{252}*Cf.* Physical Review, no. 129, pages 2133–2147, March 1963. www

[Boyer 06] S. Boyer, D. Dassie, J.N. Wilson, M. Aiche, G. Barreau, S. Czajkowski, C. Grosjean, A. Guiral, B. Haas, B. Osmanov, G. Aerts, E.Berthoumieux, F. Gunsing, Ch. Theisen, N. Thiolliere & L. Perrot. *Determination of the 233Pa(n,gamma) capture cross section up to neutron energies of 1 MeV using the transfer reaction 232Th(3He,p)234Pa.* Nuclear Physics A, vol. 775, no. 3-4, pages 175 – 187, 2006. www

[Bredeweg 07] T. A. Bredeweg & al. *Simultaneous measurement of (n, γ) and (n, fission) cross sections with the DANCE 4π BaF_2 array.* Nucl. Instrum. Methods Phys. Res. B, no. 261, pages 7986–989, Aug. 2007. www

[Breit 36] G. Breit & E. Wigner. *Capture of Slow Neutrons.* Phys. Rev., no. 49, pages 519–544, Feb. 1936. www

[Briant 57] R. C. Briant & A. M. Weinberg. *Aircraft Nuclear Propulsion Reactor.* Nucl. Sci. and Eng., vol. 2, pages 795–8538, 1957.

[Briesmeister 00] J. F. Briesmeister. *MCNP- A General Monte Carlo N-Particle Transport Code-Version 4C2.* LA-13709-M, Los Alamos National Laboratory, 2000. www

[Brooks 66] F. Brooks & al. *Eta and Neutron Cross Sections of* ^{239} *Pu and* ^{233}*U.* United Kingdom Atomic Energy Research Establisment, Harwell, Berks., England,Tech. Rep. AERE-M-1709,, 1966.

[Brusegan 79] A. Brusegan, F. Corvi, G. Rohr, R. Shelley & T. Van der Veen. *Neutron Capture Cross Section Measurements of Fe-54 and Fe-56.* Proc. Int. Conf. Nuclear Cross Sections for Tech. Bull.Am.Phys.Soc., no. 7, page 867, 1979.

[Burghrr 11] P. Burghrr, P. Eckle, S. Hirschberg & E. Cazzoli. *Final Repport on Severe Accident Risks including Key Indicators.* Seventh Framework Programme, Project No 213744, 2011. www

[Cabell 71] M. J. Cabell & M. Wilkins. *The thermal neutro capture cross-section of* ^{233}*U.* J. Inorg. Nucl. Chem, no. 33, pages 3972–3974, 1971. www

[Calviani 08] M. Calviani & al. *A fast ionization chamber for fission cross-section measurements at n-TOF.* Nucl. Instr. and Meth. A, no. 594, pages 220–227, June 2008. www

[Calviani 09] M. Calviani & al. *High-accuracy* ^{233}*U(n,f) cross-section measurement at the white-neutron source n-TOF from near-thermal to 1 MeV neutron energy.* Phys. Rev. C, no. 80, page 044604, April 2009. www

[Capote 09] R. Capote, M. Herman, P. Oblozinsky, P. G. Young, S. Goriely, T. Belgya, A. V. Ignatyuk, A. J. Koning, S. Hilaire, V. A. Plujko, M. Avrigeanu, O. Bersillon, M. B. Chadwick, T. Fukahori, Zhigang Ge, Yinlu Han, S. Kailas, J. Kopecky, V. M. Maslov, G. Reffo, M. Sin, E. Sh. Soukhovitskii & P. Talou. *RIPL – Reference Input Parameter Library for Calculation of Nuclear Reactions and Nuclear Data Evaluations*. IAEA-TECDOC, no. 110, pages 3107–3214, Dec. 2009. www

[Carlson 09] A. D. Carlson, V.G. Pronyaev, D. L. Smith, N. M. Larson, Zhenpeng Chen, F. J. Hale G. M.and Hambsch, E. V. Gai, Soo-Youl Oh, S. A. Badikov, T. Kawano, H. M. Hofmann, H. Vonach & S. TagesenKukavadse. *International Evaluation of Neutron Cross Section Standards*. Nucl. Data Sheets, no. 110, pages 3215–3324, 2009. www

[Carminati 93] F. Carminati, R. Klapisch, I. P. Revol, Ch. Roche, A. Rubiol & C. Rubbia. *An energy amplifier for cleaner and inexhaustible nuclear energy production driven by a particle beam accelerator*. CERN/AT/93-47 (ET), pages 1–74, Sept. 1993. www

[Carrapico 12a] C. Carrapico. *Measurement of the ^{233}U neutron capture cross section at the n TOF facility at CERN*. PhD Thesis, Universidade técnica de Lisboa, Instituto Superior Ténico, Aug. 2012. www

[Carrapico 12b] C. Carrapico & al. *Neutron induced capture and fission discrimination using calorimetric shape decomposition*. Nucl. Instr. and Meth. A, no. 704, pages 60–67, Nov. 2012. www

[Castineira 13a] P. Salvador Castineira, , R. Bevilacqu, T. Brys, F.-J. Hambsch, S. Oberstedt, C. Pretel & M. Vidali. *Measurement of the $^{240,242}Pu$ neutron-induced fission cross sections*. Physics Procedia, no. 47, pages 150–155, 2013. www

[Castineira 13b] P. Salvador Castineira, J. Hambsch, C. Pretel, T. Bryś S. OberstedtI & M. Vidali. *Measurement of the $^{240,242}Pu$ neutron-induced fission cross sections*. Proc. Fission 2013, Caen, Juin 2013. www

[CEA 12] CEA. *Mémento sur l'énergie*. Commissariat à l'énergie atomique et aux énergies alternative, CEA Saclay, pages 1–110, 2012. www

[Chadwick 32] J. Chadwick. *The Existence of a Neutron*. Proc. Roy. Soc. A, London, vol. 136, no. 830, pages 692–708, May 1932. www

[Chadwick 11] M. B. Chadwick, M. Herman & al. *ENDF/B-VII.1 Nuclear Data for Science and Technology : Cross Sections, Covariances, Fission Product Yields and Decay Data*. Nuclear Data Sheets, no. 112, pages 2887–2996, Dec. 2011. www

[Chalupka 77] A. Chalupka, G. Stengl & H. Vonach. *Temperature dependence of the pulse shape discrimination properties of NE 213.* Nuclear Instruments and Methods, vol. 144, no. 2, pages 167 – 169, 1977. www

[Chrien 61] R. E. Chrien. *Neutron capture cross section measurement techniques.* Ann of Phys., no. 12, pages 331–340, Dec. 1961.

[Coceva 94] C. Coceva. *Radiative transitions from neutron capture in ^{53}Cr resonances.* Il Nuovo Cimento A, no. 107, pages 85–116, January 1994. www

[Cockcroft 56] Sir John Cockcroft. *Calder Hall Nuclear Station.* The Engineer, October 1956. www

[Cohen 83] Bernard L. Cohen. *Breeder reactors : A renewable energy source.* Am. J. Phys., no. 51, page 1, 1983. www

[Coleman 12] N. M. Coleman, L. R. Abramson & F. A. Coleman. *Estimated lag time in global carbon emissions and CO2 concentrations produced by commercial nuclear power through 2009 with projections through 2030.* Health Phys., no. 102, pages 326–360, March 2012. www

[Commission 08] European Commission. *Climate Change : Commission Welcomes Final Adoption of Europe's Climate and Energy Package.* Press Release, 2008.

[Corvi 91] F. Corvi, G. Fioni, F. Gasperini & P.B. Smith. *The weighting function of a neutron capture detection system.* Nucl. Sci. Eng., no. 107, pages 272–281, January 1991. www

[Corvi 94] F. Corvi. *The measurement of neutron capture cross section via prompt gamma-ray detection.* Proc. Spec. Meeting on Measurment, Calculation and Evaporation of Photon Production Data, ANL-83-4Argon National Laboratory, Report NEA/NSC/DOC(95), no. 1, pages 225–246, Nov. 1994.

[Corvi 02] F. Corvi, G. Fioni, F. Gunsing, P. Mutti & L. Zaninin. *Resonance neutron capture in ^{60}Ni below 450 keV.* Nucl. Phys. A, no. 697, pages 581–610, August 2002. www

[Cuttler 09] Jerry M. Cuttler & Myron Pollycove. *NUCLEAR ENERGY AND HEALTH And the Benefits of Low-Dose Radiation Hormesis.* Am. J. Phys., no. 7, pages 52–89, 2009. www

[David 00] S. David, A. Billebaud, M. E. Brandan, R. Brissot, A. Giorni, D. Heuer, J. M. Loiseaux, O. Meplan, H. Nifenecker, J. B. Viano & J. P. Schapira. *Fast subcritical hybrid reactors for energy production : evolution of physical parameters and induced radiotoxicities.* Nucl. Instr. and Meth. A, no. 443, pages 510–530, Oct. 2000.

[David 07] S. David, A. Huffer & H. Nifenecker. *Revisiting the thorium-uranium nuclear fuel cycle.* Europhysics News, no. 38, pages 24–27, April 2007. www

[David 13] S. David. *Y'a-t-il un intérêt à développer le cycle thorium ?* Proc. Prospectives 2100, Mars 2013. www

[Deruyter 74] A. J. Deruyter & C. Wagemans. *Measurement and normalization of the relative U-233 fission cross-section in the low resonance region.* Nucl. Sci. and Eng., no. 54, page 423, 1974.

[Drapchinsky 99] L.V. Drapchinsky, T. E Kuzmina & S. M. Solovieval. *Practice of using the multiple painting method.* Nucl. Instr. and Meth. A, no. 438, pages 116–118, Dec. 1999. www

[Einstein 05] A. Einstein. *Zur Elektrodynamik bewegter Körper.* Annalen der Physik, Berlin, vol. 322, no. 10, pages 891–921, November 1905. www

[Felder 09] F. A. Felder. *A critical assessment of energy accident studies.* Energy Policy, vol. 37, no. 12, pages 5744–5751, December 2009. www

[Fermi 46] Enrico Fermi. *The Development of the First Chain Reaction Pile.* American Philosophical Society, vol. 90, pages 20–24, January 1946.

[Feshbach 74] H. Feshbach. *Doorway states and pre-equilibrium reactions.* Rev. Mod. Phys., vol. 46, no. 1, pages 1–5, Jan 1974.

[Flaska 04] M. Flaska, A. Borella, D. Lathouwers, L. C. Mihailescu, W. Mondelaers, A. J. M. Plompen, H. van Damb & T. H. J. J. van der Hagen. *Modeling of the GELINA neutron target using coupled electron–photon–neutron transport with the MCNP4C3 code.* Nucl. Instr. and Meth. A, no. 531, pages 392–406, January 2004. www

[Frohner 66] F. H. Frohner, E. Haddad, M. Lopez & S. J. Friesenhahn. *Accuracy of Neutron Resonance Parameters from Combined Area and Self-Indication Ratio Measurements.* Proc. Conf on Neutron Cross Section Technology, Washington D. C., pages 55–66, March 1966.

[Frohner 00] F. H. Frohner. *Evaluation and Analysis of Nuclear Resonance Data.* JEFF Report 18 NEA OECD, 2000. www

[Galperin 97] Alex Galperin, Paul Reichert & Alvin Radkowsky. *Thorium fuel for light water reactors—reducing proliferation potential of nuclear power fuel cycle.* Sci. and Global Security, no. 6, pages 265–290, 1997. www

[Ganesan 04] S. Ganesan. *New Reactor Concepts and New Nuclear Data Needed to Develop Them.* Proc. Conf. on Nucl.Data for Sci. and Technology, Santa Fe, USA, pages 1411–1416, 2004. www

[Garcia-Sanz 99] J. M. Garcia-Sanz & al. *Isotopic Composition Simulation of the Sequence of Discharges from a Thorium TRU's, Lead Cooled, ADS.*

Proc. Int. Conf. on Acc. Driven Transm. Tech. Appl., ADTTA, 1999. www

[Gayther 82] D. B. Gayther & R. B. Thom. *Prompt gamma ray detectors for the measurement of neutron capture cross section.* Proc. of the NEANDC/NEACRP Argon National Laboratory, ANL-83-4 NEANDC(US), no. 214, pages 205–217, 1982.

[Group 09] Members of the Cross Sections Evaluation Working Group. *ENDF-6 Formats Manual.* Brookhaven National Laboratory, Upton, NY 11973-5000, USA, vol. 102, no. 2, June 2009. www

[Guber 00] K. H. Guber, R. R. Spencer, L. C. Leal, J. A. Harvey, N. W. Hill, G. Dossantos & D. C. Sayer R. O.and Larson. *New High-Resolution Fission Cross-Section Measurements of ^{233}U in the 0.4-eV to 700-keV Range.* Nucl. Sci. Eng., no. 135, pages 141–149, Nov. 2000.

[Guber 01] K. H. Guber, R. R. Spencer, L. C. Leal, J. A. Harvey, J. A. Koehler, H. Sayer R. O.and Derrien, T. E. Valentive, V. M. Pierce & T. A. Lewis. *New High-Resolution Transmission Measurements of ^{233}U Using a Cooled Sample at the Temperature T = 11K.* Nucl. Sci. Eng., no. 139, pages 111–117, Feb. 2001.

[Guerrero 09] G. Guerrero & al. *The n-TOF Total Absorption Calorimeter for neutron capture measurements at CERN.* Nucl. Instr. and Meth. A, no. 608, pages 424–433, September 2009. www

[Guerrero 12] G. Guerrero & al. *Simultaneous measurement of neutron-induced capture and fission reactions at CERN.* Eur. Phys. J. A, no. 48, pages 1–9, March 2012. www

[Guimaraes 00] F. B. Guimaraes, L. C. Leal, H. Derrien & N. M. Larson. *Test of Pseudo Resonance Representation in the keV Range for ^{235}U for Self-Shielding Parameter Calculations.* Trans. ANS, no. 83, pages 223–224, 2000.

[Gunsing 97] F. Gunsing, K. Athanassopulos, F. Corviand H. Postma, Yu. P. Popov & E. I. Sharapov. *Spins of resonances in reactions of neutrons with ^{238} U and ^{113}Cd.* Phys. Rev. C, no. 56, pages 1266–1275, Sept. 1997. www

[Gunsing 01] F. Gunsing, A. Leprêtre, C. Mounier, C. Raepsaet, C. Bastian, F. Corvi & J. Gonzalez. *Stellar neutron capture cross section of ^{99}Tc.* Nuclear Physics A, no. 688, pages 496c–498c, 2001. www

[Hahn 38] Von O. Hahn & F. Strassmann. *Über die Entstehung yon Radiumisotopen aus Uran durch Bestrahlen mit schnellen und verlangsamten Neutronen.* Naturwissenschaften, vol. 26, no. 46, pages 755–756, November 1938. www

[Hahn 39] Von O. Hahn & F. Strassmann. *Über den Nachweis und das Verhalten der bei der Bestrahlung des Urans mittels Neutronen entstehenden Erdalkalimetalle (Concerning the Existence of Alkaline Earth Metals Resulting from Neutron Irradiation of Uranium).* Naturwissenschaften, vol. 27, no. 46, pages 11–15, January 1939. www

[Harvey 79] J. A. Harvey, C. L. Moore & N. W. Hill. *Neutron total cross section of ^{233}U from 0.01 to 1.0 eV.* Oak Ridge National Lab., TN (USA), Tech. Rep. CONF-791058-73, Jan. 1979.

[Heil 01] M. Heil, R. Reifarth, M. M. Fowler, R. C. Haight, F. Kappeler, R. S. Rundberg, E. H. Seabury, J. L. Ullmann, J. B. Wilhelmy & K. Wisshak. *A 4π BaF_2 detector for (n, γ) cross-section measurements at a spallation neutron source.* Nucl. Instr. and Meth. A, no. 459, pages 229–246, Feb. 2001. www

[Hilaire 00] S. Hilaire. *Level Densities.* Proc. Nucl.Data and Nucl. React., pages 1–15, March 2000. www

[Holden 89] Norman E. Holden & Kristen A. Holden. *Re-examination of 2200 metre/second cross section experiments for NEUTRON CAPTURE AND FISSION STANDARDS.* Pure and Appl. Chem., no. 61, pages 1505–1510, 1989. www

[Hopkins 62] J. C. Hopkins & B. C. Diven. *Neutron capture to fission ratios in ^{233}U, ^{235}U,^{233}Pu.* Nucl. Sci. Eng., no. 12, pages 169–177, 1962.

[IAEA-NDS 13] IAEA-NDS. *Evaluated Nuclear Data File (ENDF).* 2013. www

[IAEA 04] Internation Atomic Energy Agency IAEA. *Implications of Partitioning and Transmutation in Radioactive Waste Management.* IAEA Technical Reports Series, no. 435, 2004. www

[IAEA 05] Internation Atomic Energy Agency IAEA. *Thorium fuel cycle — Potential benefits and challenges.* IAEA-TECDOC-1450, pages 1–113, 2005. www

[IAEA 09] Internation Atomic Energy Agency IAEA. *Classification of nuclear waste.* IAEA Safty Standars, Vienna, no. GSG-1, November 2009. www

[IEA 11a] Internation Energy Annual IEA. *Energy for all - Financing access for the poor.* Energy Information Administration, DOE/EIA-0484, 2011. www

[IEA 11b] Internation Energy Annual IEA. *International Energy Outlook.* Energy Information Administration, DOE/EIA-0484, 2011. www

[IEA 11c] Internation Energy Annual IEA. *World Energy Statistics.* OECD/IEA, 2011. www

[Ingelbrecht 97] C. Ingelbrecht, A. Moens, R. Eykens & A. Dean. *Improved electrodeposited actinide layers.* Nucl. Instr. and Meth. A, no. 397, pages 34–38, September 1997. www

[IPCC 12] The Intergovernmental Panel on Climate Change IPCC. *Special Report. Managing the Risks of Extreme Events and Disasters to Advance Climate Change Adaptation.* CAMBRIDGE UNIVERSITY PRESS, ISBN 978-1-107-60780-4 Paperback, 2012. www

[Iwamoto 09] Osamu Iwamoto, Tsuneo Nakagawa, Naohiko Otsuka & Satoshi Chiba. *JENDL Actinoid File 2008.* Journal of Nucl. Sci. and Tech., no. 59, pages 510–528, Feb. 2009. www

[Jaramillo 07] Paulina Jaramillo, W. Michaeland Griffin & H. Scott Matthews. *Comparative Life-Cycle Air Emissions of Coal, Domestic Natural Gas, LNG, and SNG for Electricity Generation.* Environ. Sci. Technol., no. 41, pages 6290–6296, July 2007. www

[Jørgensen 84] C. Budtz Jørgensen & H. H. Knitter. *A precise method for charged particle counting employing energy and angle information from gridded ion chambers.* Nucl. Instr. and Meth. A, no. 223, pages 295–302, June 1984. www

[Jørgensen 88] C. Budtz Jørgensen & H. H. Knitter. *Simultaneous investigation of fission fragments and neutrons in* ^{252}*Cf.* Nuclear Physics A, no. 490, pages 307–328, 1988. www

[Kessedjian 10] G. Kessedjian, B. Jurado, M. Aiche, G. Barreau, A. Bidaud, S. Czajkowski, D. Dassié, B. Haas, L. Mathieu, L. Audouin, N. Capellan, L. Tassan-Got, J.N. Wilson, E. Berthoumieux, F. Gunsing & al. *Neutron-induced fission cross sections of short-lived actinides with the surrogate reaction method.* Phys. Lett. B, no. 692, pages 297–301, 2010. www

[Kharecha 13] A. Pushker Kharecha & E. James. *Prevented Mortality and Greenhouse Gas Emissions from Historical and Projected Nuclear Power.* Environ. Sci. Technol., no. 47, pages 4889–4895, March 2013. www

[Knox 72] H. H. Knox & T. G. Miller. *A technique for determining bias settings for organic scintillators.* Nucl. Instr. and Meth., no. 101, pages 519–525, June 1972. www

[Koehler 00] P. E. Koehler, R. R. Winters, K. H. Guber, T. Rauscher, J. A. Harvey, S. Raman, R. R. Spencer, J. C. Blackmon, D. C. Larson, D. W. Bardayan & T. A. Lewis. *High-resolution neutron capture and transmission measurements, and the stellar neutron-capture cross section of* ^{88}*Sr.* Phys. Rev. C, no. 62, pages 055803–15, November 2000. www

[Kukavadse 55] G. M Kukavadse, L. L. Goldin, M. P. Anikina & B. W. Ershler. *Determination of the absorption cross section and of the radiative capture cross section of ^{233}U for pile neutrons.* Proc. Conf. 1st UN Conf.Peaceful Uses Atomic Energy, Geneva, no. 4, page 230, 1955.

[Lamb 17] H. Lamb. *On Waves in an Elastic Plate.* Proc. Roy. Soc. London, no. 93, pages 114–128, 1917. www

[Lampoudis 13] C. Lampoudis, S. Kopecky, O. Bouland, F. Gunsing, G. Noguere, A. J. M. Plompen, C. Sage, P. Schillebeeckx & R. Wynants. *Neutron transmission and capture cross section measurements for ^{241}Am at the GELINA facility.* Eur. Phys. Journal, no. 198, pages 128–186, August 2013. www

[Lane 58] A. M. Lane & R. G. Thomas. *R-matrix theory of nuclear reactions.* Rev. Mod. Phys., no. 30, pages 257–353, April 1958. www

[Larson 08] M. Nancy Larson. *Multilevel R-MATRIX fits to neutron data using Bayes' equations.* ORNL/TM-9179/R8, ENDF-364/R2, pages 1–720, Oct. 2008. www

[Leal 01] L. C. Leal, H. Derrien, J. A. Harvey, K. H. Guber, N. M. Larson & R. R. Spencer. *R-matrix resonance analysis and statistical properties of the resonance parameters of ^{233}U in the neutron energy range from thermal to 600 eV.* ORNL/TM-2000/372, page 59, March 2001. www

[Lederer 13] C. Lederer & al. (*nTOFCollaboration*). *Neutron Capture Cross Section of Unstable ^{63}Ni : Implications for Stellar Nucleosynthesis.* Phys. Rev. Lett., no. 110, pages 022501–022511, Jan. 2013. www

[Lensa 08] Werner von Lensa, Nahim Rabbi & Matthias Rossbach. *RED-IMPACT Impact of Partitioning, Transmutation and Waste Reduction Technologies on the Final Nuclear Waste Disposal.* Forschungszentrum Jülich, 2008. www

[Lenzen 08] Manfred Lenzen. *Life cycle energy and greenhouse gas emissions of nuclear energy : A review.* Energy Convergs. and Manage., no. 49, pages 2178–2199, August 2008. www

[Lenzen 12] Manfred Lenzen & Roberto Schaeffer. *Historical and potential future contributions of power technologies to global warming.* Climatic Change, no. 112, pages 601–632, August 2012. www

[Liskien 75] Horst Liskien & Arno Paulsen. *Neutron production cross sections and energies for the reactions $^{7}Li(p,n)^{7}Be$ and $^{7}Li(p,n)^{7}Be^{*}$.* Atomic Data and Nuclear Data Tables, no. 15, pages 57–84, January 1975. www

[Ljungvall 04] Joa Ljungvall, Marcin Palacz & Johan Nyberg. *Monte Carlo simulations of the Neutron Wall detector system.* Nucl. Instr. and Meth. A, no. 528, pages 741–762, August 2004. www

[Macklin 67] R. L. Macklin & J. H. Gibbons. *Capture-Cross-Section Studies for 30—220-keV Neutrons Using a New Technique.* Phys. Rev., vol. 159, no. 4, pages 1007–1012, Jul 1967.

[Macklin 91] R. L. Macklin, R.B. Pereza, G. de Saussure & R. W. Ingle. *High energy resolution measurement of the 238U neutron capture yield from 1 to 100 keV.* Annals of Nucl. En., vol. 18, no. 10, pages 567–583, 1991. www

[Markandya 07] Anil Markandya & Paul Wilkinson. *Electricity generation and health.* The Lancet, no. 370, pages 979–990, Sept. 2007. www

[Mathieu 06] D. Mathieu L.and D. Heuer, R. Brissot, C. Garzenne, C. Le Brun & D.and al. Lecarpentier. *The thorium molten salt reactor : Moving on from the MSBR.* Prog. in Nucl. Energy, no. 48, page 664–679, Sept. 2006. www

[Mathieu 09] L. Mathieu, D. Heuer, E. Merle-Lucotte, E. Brissot, C. Le Brun & al. *Possible Configurations for the Thorium Molten Salt Reactor and Advantages of the Fast Nonmoderated Version.* Nucl. Sci.and Eng, no. 161, pages 78–89, 2009. www

[McLane 05] Victoria McLane. *EXFOR Basics, A Short Guide to the Nuclear Reaction Data Exchange Format.* Technical report, International Atomic Energy Agency, page 70, 2005. www

[Meitner 39] Lise Meitner & O. R. Frisch. *Disintegration of Uranium by Neutrons : a New Type of Nuclear Reaction.* Nature, vol. 143, no. 3615, pages 239–240, February 1939. www

[Merle-Lucotte 08] Elsa Merle-Lucotte, Ludovic Mathieu, Daniel Heuer, Véronique Ghetta & al. *Influence of the Processing and Salt Composition on the Thorium Molten Salt Reactor.* Nucl. Technol., no. 163, pages 358–365, 2008. www

[Mihailescu 04] L. C. Mihailescu, L. Olah, C. Borcea & A. J. M. Plompen. *A new HPGe setup at Gelina for measurement of gamma-ray production cross-sections from inelastic neutron scattering.* Nucl. Instr. and Meth. A, no. 531, pages 375–391, January 2004. www

[Mondelaers 06] W. Mondelaers & P. Schillebeeckx. *GELINA, a neutron time-of-flight facility for high-resolution neutron data measurement.* Notiziario Neutroni e Luce di Sincrotrone, no. 2, pages 19–25, June 2006. www

[Moore 60] M. S. Moore, L. G. Miller & O. D. Simpson. *Slow Neutron Total and Fission Cross Sections of ^{233}U.* Phys. Rev., no. 118, pages 714–717, May 1960. www

[Moxon 91] M. C. Moxon & J. B. Brisland. *GEEL REFIT, A least squares fitting program for resonance analysis of neutron transmission and capture data computer code.* AEA-InTec-0630, AEA Technology, no. 6, Oct. 1991.

[Nations 04] United Nations. *World Population to 2300.* United Nations, ST/ESA/SER.A/236, 2004. www

[NEA-HPRL 12] NEA-HPRL. *Nuclear Data High Priority Request List.* NEA/WPEC, 2012. www

[NEA 08] NEA. *Uncertainty and target accuracy assessment for innovative systems using recent covariance data evaluations.* NEA/WPEC-26, 2008. www

[NEI 12a] NEI. *Nuclear Energy Around the World.* World Statistics, 2012. www

[NEI 12b] NEI. *World Nuclear Industry Handbook.* Global Trade Media, 2012. www

[Nifenecker 03] N. Nifenecker, O. Meplan & S. David. *Accelerator Driven Subcritical Reactors (Series in Fundamental and Applied Nuclear Physics).* Institute of Physics Publishing, London, pages 1–316, June 2003. www

[Nortiicliffe 70] L. C. Nortiicliffe & R. F. Sctlilling. *Range and Stopping-Power Tables for Heavy Ions.* Nucl.Data Tables A, no. A7, pages 233–463, 1970. www

[Pattenden 63] N. J. Pattenden & J. A. Harve. *Measurement of the Total Cross Section of ^{233}U from 0.07 to 10,000 eV.* Nucl. Sci. Eng., no. 17, pages 404–415, 1963.

[Pauwels 91] J. Pauwels. *Specific nuclear target preparation and characterization techniques used at CBNM.* Nucl. Instr. and Meth. B, no. 56/57, pages 938–941, May 1991. www

[Perey 86] F. G. Perey. *Status of the Parameters of the 1.15-keV Resonance of ^{56}Fe.* Proc. of the Intern. Conf. on Nucl. Data for Basic and Applied Science, no. 697, pages 1523–1529, May 1986. www

[Pering 69] N.C. Pering & T.A. Lewis. *Performance of a 140 MeV High Current Short Pulse LINAC at ORNL.* Trans Nuc. Sci., no. 16, pages 316–320, June 1969. www

[Perkins 79] L.J. Perkins & Malcolm C. Scott. *The application of pulse shape discrimination in NE 213 to neutron spectrometry.* Nuclear Instruments and Methods, vol. 166, no. 3, pages 451 – 464, 1979. www

[Plag 03] R. Plag, M. Heil, F. Kappeler, P. Pavlopoulos, R. Reifarth & K. Wisshak. *An optimized C6D6 detector for studies of resonance-dominated (n,γ) cross-sections*. Nuclear Instruments and Methods in Physics Research Section A : Accelerators, Spectrometers, Detectors and Associated Equipment, vol. 496, no. 2-3, pages 425 – 436, 2003. www

[Plompen 08] A.J.M. Plompen, T. Fukahori, H. Henriksson, A. Ignatyuk, T. Iwasaki, G. Manturov, R. D. McKnight, G. Rimpault & D. L. Smith. *The NEA High Priority Nuclear Data Request List for future needs*. EDP Science, vol. 2, no. 202, pages 765–768, 2008. www

[Reifarth 05] R. Reifarth, E.-I. Esch, A. Alpizar-Vicente, E.M. Bond, T.A. Bredeweg, S.E. Glover, U. Greife, R. Hatarik, R.C. Haight, A. Kronenberg & al. *(n,γ) measurements on radioactive isotopes with DANCE*. Nucl. Instr. and Meth. B, no. 241, pages 176–179, August 2005. www

[Rosental 70] M. W. Rosental & al. *Molten Salt Reactor - Hystory, Status, and Potential*. Nuclear application and technology, vol. 8, pages 107–117, February 1970. www

[Rubbia 95] C. Rubbia, J. A. Rubio, S. Buono, F. Carminati, N. Fiètier, J. Galvez, C. Gelès, Y. Kadi, R. Klapisch, P. Mandrillon, J.P. Revol & Ch. Roche. *Conceptual design of a fast neutron operated high power energy amplifier*. Tech. Rep. CERN/AT/95-44 (ET), pages 1–241, 1995. www

[Rubbia 99] C. Rubbia, A. Samuel, D. Bouvet-Bensimon, S. Buono, R. Cappi, P. Cennini, C. Gelès, I. Goulas, Y. Kadi, P. Pavlopoulos, J. P. Charles, A. Tzima & V. Vlachoudis. *A high resolution spallation driven facility at the CERN-PS to measure neutron cross sections in the interval from 1 eV to 250 MeV : a relative performance assessment*. CERN/LHC/98-02 (EET)-Add. 1, pages 1–14, June 1999. www

[Rutherford 19] E. Rutherford. *Collisions of alpha Particles with Light Atoms. IV. An Anomalous Effect in Nitrogen*. Philosophical Magazine and Journal of Science, Series 6, vol. 27, pages 581–587, 1919. www

[Saito 03] K. Saito, M. Igashira, T. Ohsaki, T. Obara & H. Sekimoto. *Measurement of Cross Sections of the ^{210}Po Production Reaction by keV-Neutron Capture of ^{209}Bi*. Proc. Nippon Genshiryoku Kenkyujo JAERI Conf., no. 1, pages 133–137, Nov. 2003. www

[Salome 81] J.M. Salome & R. Cools. *Neutron producing targets at GELINA*. Nucl. Instr. and Meth. A, no. 179, pages 13–19, January 1981. www

[Schillebeeckx 12a] P. Schillebeeckx. Private Communication, 2012.

[Schillebeeckx 12b] P. Schillebeeckx, B. Beckera, Y. Danonb, K. Guberc & al. *Determination of Resonance Parameters and their Covariances from Neutron Induced Reaction Cross Section Data.* Nuclear Data Sheets, no. 113, pages 3054–3100, Dec. 2012. www

[Schmidt] Karl-Heinz Schmidt & Beatriz Jurado. *GEF, A GEneral description of the Fission process.* www

[Semenov 83] B. A Semenov. *Nuclear power in the Soviet Union.* IAEA Bulletin, vol. 25, no. 2, pages 47–59, 1983. www

[Shibata 11] Keiichi Shibata, Osamu Iwamoto, Tsuneo Nakagawa & al. *JENDL-4.0 : A New Library for Nuclear Science and Engineering.* Journal of Nucl. Sci. and Tech., no. 48, pages 1–30, Sept. 2011. www

[Smith 68] D. L. Smith, R. G. Polk & T. G. Miller. *Measurement of the response of several organic scintillators to electrons, protons and deuterons.* Nucl. Instr. and Meth., no. 64, pages 157–166, September 1968. www

[Stacey 01] Weston M. Stacey. *Nuclear Reactor Physics.* Wiley-Interscience, New York, page 706, 2001. www

[Syme 82] D. B. Syme. *The black and white filter method for background determination in neutron time-of-flight spectrometry.* Nucl. Instr. and Meth. A, no. 198, pages 357–364, July 1982. www

[TAIN 02] Jose L. TAIN, Frank GUNSING, Daniel CANO-OTT, Nicola COLONNA & al. *Accuracy of the Pulse Height Weighting Technique for Capture Cross Section Measurements.* J. Nucl. Sci. Techn, Sup. 2, pages 689–692, 2002. www

[Trellue 11] H. Trellue, C. Bathke & P. Sadasivan. *Neutronics and material attractiveness for PWR thorium systems using Monte Carlo techniques.* Progress in Nuclear Energy, no. 53, pages 698–707, 2011. www

[Tronc 85] D. Tronc, J.M. Salomé & K.H. Böckhoff. *A new pulse compression system for intense relativistic electron beams.* Nucl. Instr. and Meth. A, no. 228, pages 217–227, January 1985. www

[Tuli 01] Jagdish K. Tuli. *Evaluated Nuclear Structure Data File-A Manual for Preparation of Data Sets.* BNL-NCS-51655-01/02-Rev, no. 2, Feb. 2001. www

[Wagemans 88] C. Wagemans, P. Schillebeecks, A.J. Deruytter & R. Barthelemy. *Subthermal Fission Cross-section Measurements for ^{233}U, ^{235}U, ^{239}Pu.* Conf.on Nucl.Data For Sci.and Technol.,Mito, no. 1, page 91, May 1988. www

[Weisskopf 57] F. Weisskopf Victor. *Nuclear Physics.* Rev. Mod. Phys., no. 29, pages 174–179, April 1957. www

[Weston 68] L. W. Weston, R. Gwin, G. deSaussure, R. R. Fullwood & R. W. Hockenbury. *Measurement of the Fission and Capture Cross Section for ^{233}U in the Energy Region 0.4 to 2000 eV.* Nucl. Sci. Eng., no. 34, pages 1–12, 1968.

[Weston 70] L. W. Weston, R. Gwin, deSaussure, R. W. Ingle, J. H. Todd, C. W. Craven, R. W. Hockenbury & R. C. Block. *Neutron Fission and Capture Cross-Section Measurements for Uranium-233 in the Energy Region 0.02 to 1 eV.* Nucl. Sci. Eng., no. 42, pages 143–154, 1970.

[WHO 08] World Health Organization WHO & United Nations Children's Fund UNICEF. *Progress on Drinking Water and Sanitation-Special focus on sanitation.* WHO Library Cataloguing-in-Publication Data, ISBN 978 92 806 4313 8, 2008. www

[Wigner 46] Eugene P. Wigner. *Resonance reactions.* Phys. Rev., no. 70, pages 606–618, Nov. 1946. www

[Wigner 47] E. P. Wigner & L. Eisenbud. *Higher angular momenta and long range interaction in resonance reactions.* Phys. Rev., no. 72, pages 29–41, Jul. 1947. www

[Wilson 03] J.N. Wilson. *Measurements of (n,γ) neutron capture cross-sections with liquid scintillator detectors.* Nucl. Instr. Meth. A, vol. 511, no. 388, pages 388 – 399, 2003. www

[Zanini 00] L. Zanini, F. Becvár, F. Corvi, I. Honzátko, H. Postma & I. Tomandl. *Neutron capture gamma-ray spectroscopy with ^{107}Ag, ^{109}Ag and ^{115}In, for parity violation and nuclear structure studies.* Proc.Conf. on Nuclear Data for Science and Technology, SantaFe, New Mexico, USA, no. 529, pages 719–721, Sept. 2000. www

Résumé

^{233}U est le noyau fissile produit dans le cycle du combustible $^{232}Th/^{233}U$ qui a été proposé comme une alternative plus sûre et plus propre du cycle $^{238}U/^{239}Pu$. La connaissance précise de la section efficace de capture de neutrons de cet isotope est requise avec une haute précision pour la conception et le développement de réacteurs utilisant ce cycle du combustible. Les deux seuls jeux de données expérimentales fiables pour la section efficace de capture de l'^{233}U montrent des écarts important allant jusqu'à 20%. Ces différences peuvent être dues à des incertitudes systématiques associées à l'efficacité du détecteur, la correction du temps mort, la soustraction du bruit de fond et le phénomène d'empilement de signaux causé par la forte activité α de l'échantillon. Un dispositif expérimental dédié a la mesure simultanée des sections efficaces de fission et de capture des noyaux fissiles radioactifs a été conçu, assemblé et optimisé au CENBG dans le cadre de ce travail. La mesure sera effectuée à l'installation de temps de vol de neutrons Gelina de l'IRMM, où les sections efficaces neutroniques peuvent être mesurées sur une large gamme d'énergie avec une haute résolution énergetique. Le détecteur de fission se compose d'une chambre à ionisation (CI) multi-plaque de haute efficacité. Les rayons γ produits dans les réactions de capture sont détectés par un ensemble de six scintillateurs C_6D_6 entourant la CI. Dans ces mesures, les rayons γ de la capture radiative sont masqués par le grand nombre de rayons γ de fission, ce qui représente le problème le plus delicat. Ces γ parasites doivent être soustraits par la détection des événements de fission avec une efficacité très bien connue (méthode de VETO). Une détermination précise de cette efficacité est assez difficile. Dans ce travail, nous avons soigneusement étudié la méthode des neutrons prompts de fission pour la mesure de l'efficacité de la CI, apportant un éclairage nouveau sur la méthode, ce qui a permi d'obtenir une excellente precision sur l'efficacité de détection des fission d'une source de ^{252}Cf. Avec cette même source, plusieurs paramètres (pression du gaz, haute tension et la distance entre les électrodes) ont été étudiés afin de déterminer le comportement de la CI et de trouver le point de fonctionnement idéal : une bonne séparation énergétique entre les particules α et les fragments de fission (FF) et une bonne résolution temporelle. Une bonne séparation α-FF a également été obtenue avec une cible d'^{233}U tres radioactive. De plus, l'analyse de forme de signaux entre les rayons γ et les neutrons dans les détecteurs C_6D_6 a été observée à Gelina dans des conditions expérimentales réalistes. Pour conclure, le dispositif expérimental et la méthode de VETO ont été soigneusement vérifiés et validés, ouvrant la voie à la mesure future des sections efficaces de capture et fission d'^{233}U.

Mots clés : cycle thorium, sections efficaces neutronique de fission et de capture, isotope fissile, développement d'un dispositif expérimental pour la détection des neutrons et γ, scintillateurs C_6D_6, chambre à ionisation, mesure de l'efficacité, méthode VETO, simulations Geant4.

Abstract

^{233}U is the fissile nucleus produced in $^{232}Th/^{233}U$ fuel cycle which has been proposed as a safer and cleaner alternative to the $^{238}U/^{239}Pu$ cycle. The accurate knowledge of the neutron capture cross-section of this isotope is needed with high-precision for design and development of this fuel cycle. The only two reliable experimental data for the capture cross-section of ^{233}U show discrepancies up to 20%. These differences may be due to systematic uncertainties associated with the detector efficiency, dead-time effects, background subtraction and signal pile-up caused by the α-activity of the sample. A special experimental set-up for simultaneous measurement of fission and capture cross sections of radioactive fissile nuclei was designed, assembled and optimized at CENBG in the frame of this work. The measurement will be performed at the Gelina neutron time-of-flight facility at IRMM, where neutron cross sections can be measured over a wide energy range with high energy resolution. The fission detector consists of a multi-plate high-efficiency ionization chamber (IC). The γ-rays produced in capture reactions are detected by an array of six C_6D_6 scintillators surrounding the IC. In these measurements the radiative capture γ-rays are hidden in large background of fission γ-rays that represents a challenging issue. The latter has then to be subtracted by detecting fission events with a very well known efficiency (VETO method). An accurate determination of this efficiency is rather difficult. In this work we have thoroughly investigated the prompt-fission-neutrons method for the IC efficiency measurement, providing new insights on this method. Thanks to this study the IC efficiency was determined with a very low uncertainty. Using a ^{252}Cf source, several parameters (gas pressure, high voltage and the distance between the electrodes) have been studied to determine the behaviour of the IC in order to find the ideal operation point: a good energy separation between α-particles and fission fragments (FF) and a good timing resolution. A good α-FF separation has been obtained with a highly radioactive ^{233}U target. Also, the pulse-shape discrimination between γ-rays and neutrons in the C_6D_6 detectors was observed at Gelina under realistic experimental conditions. To conclude, the experimental set-up and the VETO method have been carefully checked and validated, opening the way to future measurements of the capture and fission cross sections of ^{233}U.

Keywords: thorium cycle, neutron-induced capture and fission cross sections, fissile isotope, development of experimental set-up for neutron and gamma detection, C_6D_6 scintillators, ionisation chamber, efficiency measurement, VETO method, Geant4 simulations.